**UNIVERSITÀ DEGLI STUDI DI NAPOLI FEDERICO II**

**Scuola Politecnica e delle Scienze di Base**

**Corso di Dottorato in Ingegneria Industriale (XXIX Ciclo)**

**Dipartimento di Ingegneria Industriale**

**Tesi di Dottorato**

# Modelling and Acoustic Optimization of an Intake System for an Internal Combustion Engine

**Danilo D'Agostino**

**COORDINATORE**

**Ch.mo Prof. Ing. Michele Grassi**

**TUTORI**

**Ch.mo Prof. Ing. Fabio Bozza**
**Ing. Daniela Siano**

**Anno 2017**

*To my parents…*

# Acknowledgements

*I am very grateful to my friends and colleagues Roberto Aiello and Maria Antonietta Panza for the very interesting discussions on sociological and scientific topics and with whom I have shared three incredible, unbelievable years. Their presence has been very important in this path of both personal and professional growth.*

*My sincere thanks go to PhD Luigi Teodosio for his friendship and for the very valuable time we spent together talking about various matters.*

*Thanks to my supervisors, Daniela Siano, who gave me the opportunity to start such journey in the research environment, and prof. Fabio Bozza for his technical teachings and his support related to the performed activities.*

*Thanks to all the people I have met during the PhD, for their support, encouragement and suggestions.*

*Last but not the least, a special thank goes to my family and friends, for their unconditioned, priceless love and presence.*

*Thanks to Claudia, for being as she is and for her support and understanding during all these years.*

# Abbreviations

| | |
|---|---|
| CAE | Computer Aided Design |
| 1D | One-Dimensional |
| 3D | Three-Dimensional |
| TL | Transmission Loss |
| SI engine | Spark Ignition engine |
| GA | Genetic Algorithm |
| IPFM | Interior Penalty Function Method |
| EPFM | Exterior Penalty Function Method |
| FDM | Feasible Direction Method |
| FE | Finite Element |
| OSPL | Overall Sound Pressure Level |
| IL | Infinite Element |
| NR | Noise Reduction |
| PDE | Partial Differential Equation |
| CAD | Computer Aided Design |
| IE | Infinite Element |
| TM | Transfer Matrix |
| FSI | Fluid-Structure Interaction |
| CFD | Computational Fluid Dynamic |
| IVO | Inlet Valve Opening |
| VVA | Variable Valve Actuator |
| WOT | Wide Open Throttle |
| RANS | Reynolds Average Navier-Stokes |
| OASPL | Overall A-weighted Sound Pressure Level |

| | |
|---|---|
| SPL | Sound Pressure Level |

# Contents

# Introduction

## Introduction

Noise is recognized as having a significantly adverse effects on our everyday lives, including interference with communication, sleep disturbance, annoyance responses, performance effects as well as health through psycho-physiological effects. As an everyday example, noise induced annoyance is a very important problem occurring when people are constantly exposed to a noise source, regardless of its intensity. Such evidence has been recognized by product designers engineers within the world's most innovative and successful companies, which try to incorporate effective noise mitigation measures into their product design process. Such new project aspect has become extremely important in the automotive industry too and it is possible to state that there is a strong competition among automotive manufacturers to generally reduce the radiated noise levels.

In fact, nowadays, the concept of client perception quality of a vehicle, which represents the prior target behind the production strategies of cars manufacturers, is quite changed with respect to a dozen of years ago. In particular, among the factors identifying the quality of a vehicle, the concept of delivered sound represents a critical aspect that manufacturers are focusing on, in order to be more competitive on the global market. As matter of fact, poor sound quality can give the impression of poor vehicle build quality or, for a customer point of view, can give the idea that there is something wrong with the operations of the vehicle, as if something is not working properly and is going to break. More precisely, the term sound quality refers to whether sounds are pleasant or annoying. For example, if a properly tuned engine noise is something that may be appreciated by customers, on the other hand it may strongly reduce the global comfort. Consequently, every vehicle component is not only designed in order to ensure the achievements of its specific goal but also considering the impact on the vehicle's overall sound quality. Such a new design philosophy is becoming more and more important as it is also testified by the increase in the noise emission standards (e.g. Regulation (EU) N° 540/2014).

So, it may be stated that the acoustic project of a vehicle, considering all the components it is made of, must satisfy a trade-off between acoustic comfort and perceived sound. However, as schematically depicted in Figure 1, within a vehicle various noise sources are involved such as powertrain noise, aerodynamic noise, rolling noise etc..

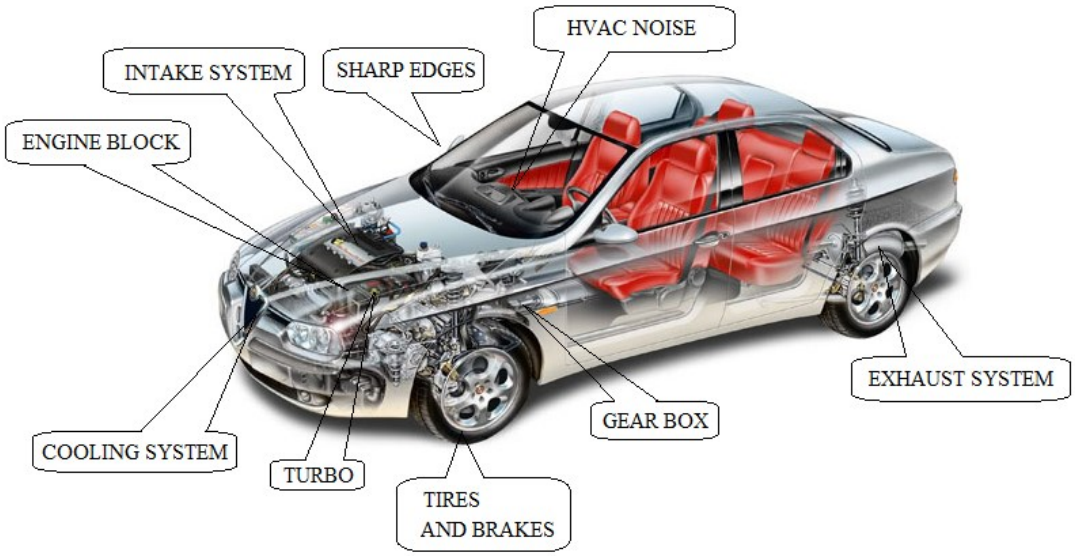


Figure 1 – Noise sources embedded within a modern vehicle.

Among these, the most prominent noise source, with particular regard to the low vehicle speed, is certainly represented by the powertrain induced noise. Here, the various subcomponents may be distinguished such as engine block, transmission, drive shaft and so on. Each of the above mentioned subsystems must satisfy requirements related to engine performances, vehicle drivability together with another important mandatory target represented by attention to noise emissions. Focusing on the engine related noise, the most prominent is certainly represented by the gas-dynamic noise emitted by both the intake and the exhaust systems, because they represent the direct transmission path of high amplitude acoustic waves to the external ambient.

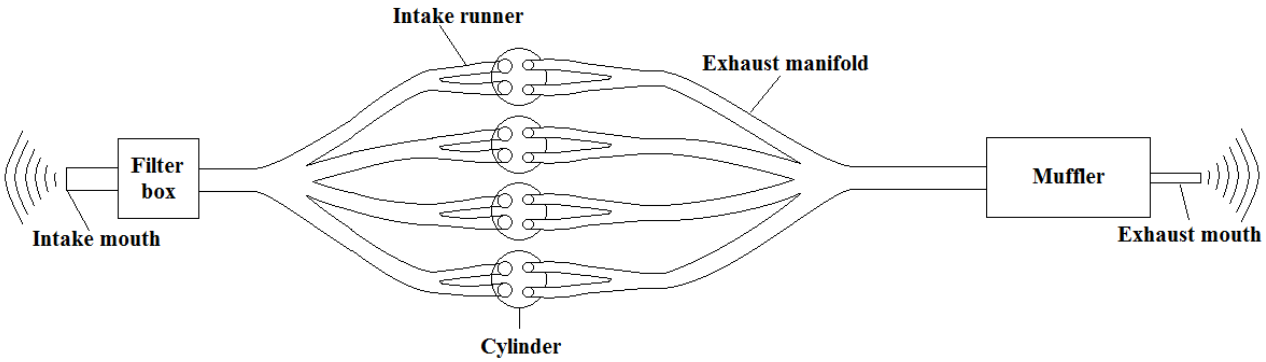


Figure 2 – Exhaust and intake noise transmission path schematization.

However, while the exhaust system is not more a primary sound source, once a good muffler has been designed, the acoustic design of the intake system of modern internal combustion engines still represents a very critical aspect. In fact, in this case, the gas-dynamic noise due to the pressure waves created at each intake process is only attenuated by the throttle (when present). In addition, the main encountered difficulty is represented by the fact that the prior task of an air induction system is to maximize the cylinders filling and not to attenuate the sound transmission. For this reason, often it happens that the best acoustic aimed design solutions are in contrast with the engine performance requirements. In fact, as it will be described in the following, most of the noise

reduction performed by traditional devices, is achieved by wave reflections based components with which pressure losses are always associated, resulting in a decrease of volumetric efficiency. This is not a desirable condition as this latter parameter strongly affects the engine power output. Moreover, the global size of such systems must satisfies as much as possible some compactness requirements within the engine bay. It follows that the acoustic design of a breathing system, in terms of being made of several acoustic filters, must take into account the above mentioned restrictions, in a way such that the best trade-off among minimizing noise emission and maximizing engine output and fuel consumption efficiency must be achieved.

In this regards, it is possible to state that the choice of the correct trade-off is usually guided by the requirements in terms of quality of the vehicle, which can be used to differentiate the brands or the models (cheapness, high comfort, sport attitude). In every case, as already mentioned, this design process is firstly defined by considering geometrical constraints, i.e. the available space for the system under investigation, whilst other constraints are represented by the unit cost, the reliability, the durability. The old design procedures were usually based on the empirical experience and background of designers, implying time consuming and very expensive prototypes building procedures. Nowadays, the design phase has been strongly improved thanks to the massive usage of computer aided numerical simulations. In fact, they allow to develop integrated, multi-physics design strategies, where conflicting requirements are simultaneously accounted during the development loop[1]. This results in a more cost effective product with a shorter “time to market”. The effectiveness of the use of CAE tools in acoustic engineering is simple to recognize as there are several effects which may affect an acoustic field such as the presence of both acoustic and structural natural modes, thermal effects, fluid flow etc.. In general, both 1D and 3D commercial CAE software are available for helping engineers to correctly design from an acoustic point of view components, such as intake and exhaust lines, in order to achieve the desired performances[2]. At the current state of art, in order to predict the response of an acoustic filter the classical 1D simulation tools are widely used because of the very good results within the low frequency range in which only plane waves can propagate. Nevertheless, the main limitation of a pure 1D approach is represented by the rigid-wall assumption which may not reproduce the actual system under real working conditions. Moreover, a one-dimensional analysis presents some additional limitations mainly due to a rather rough schematization of those systems which often present a complex geometry. Therefore, for a more detailed analysis, within the middle/high frequency range and/or when the presence of a flexible structure cannot be neglected, a 3D simulation code is the only tool truly useful for designing and optimizing more complex systems. In general, for low frequency analysis such that plane wave propagation is ensured, the two approaches give similar outcomes and therefore one-dimensional methods are to be preferred, at least in a pre-design phase, due to the simpler modelling procedure and the low computational efforts.

In general, a complete design process usually considers two phases of the component’s project. The first, which is schematized in Figure 3, represents the stand alone study of the acoustic behavior of the system, generally in terms of its acoustic attenuation performances over a specified frequency range. Such preliminary analysis represents just a qualitative study, aimed to extract the frequency dependent attenuation curve of the system in particular conditions.

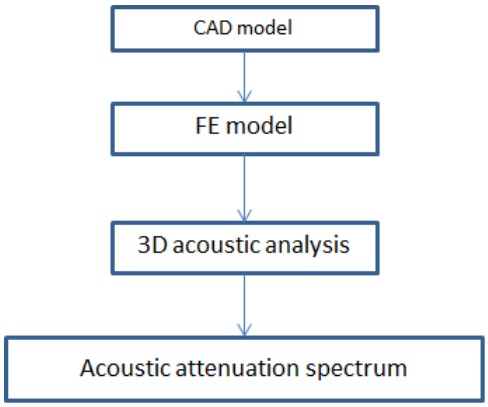


Figure 3 – Acoustic attenuation analysis process schematization.

This is done by referring to a classic acoustic performance characterization parameter such as, for example, the Transmission Loss (TL)[3]. It is worth noting that, in spite of the fact that this step does not quantify the amount of noise emitted in various real operating conditions, it is very important in order to understand how the system under investigation behaves, identifying the frequency ranges in which the acoustic attenuation is low and where to apply changes in the geometry in case of necessity. After such first step, another one is necessary, which is represented by the quantitative analysis aimed to establish how much noise is emitted and its spectral components distributions.

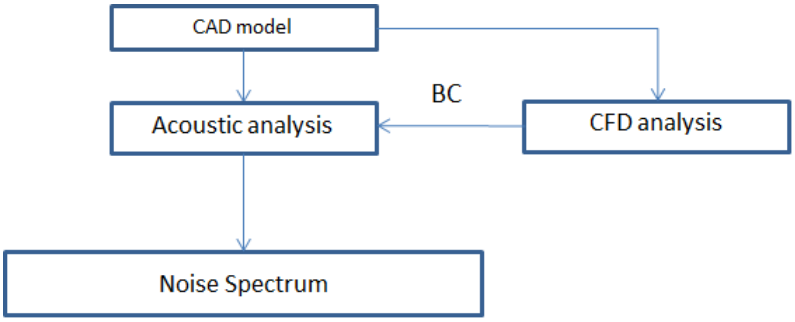


Figure 4 – Gas-dynamic noise analysis process schematization.

As it is schematized in Figure 4, the workflow takes into account also a fluid dynamic analysis because it is necessary to evaluate the pressure waves generated by the periodic charging and discharging process occurring within the engine cylinders. This process is more complex and involves the simulation of the transfer of flow energy to wave energy generating noise, which is radiated at the open terminations, and give rise to two main contributions to the overall noise emitted. In fact, from a practical point of view, the main spectral characteristics of both intake and exhaust noise are dominated by a sequence of tonal components, which are harmonically related to the engine firing frequency. Furthermore, these components are generally related to the so-called engine orders, which simply represent multiples of the crankshaft revolutions, namely

$$f_n = \frac{rpm}{60}\, n \tag{1}$$

where $n$ is the order number. Consequently, according with such nomenclature, the firing frequency[1] of a two cylinder, four stroke, internal combustion engine correspond to the first engine order. In Figure 5 a typical experimentally measured exhaust noise spectrum, for a four stroke ($\varepsilon = 2$), four cylinders spark ignition (SI) engine, running at $3750\ rpm$, is reported. Here, the first four engine orders are clearly visible within the acoustic signature.

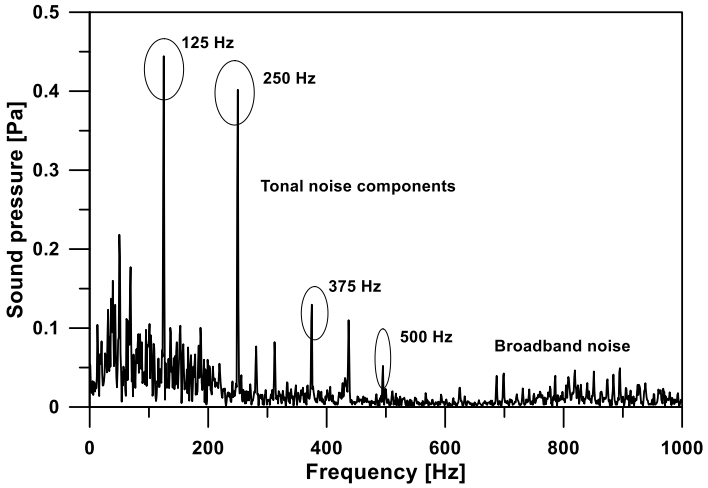


Figure 5 – Example of exhaust noise spectrum at 3750 rpm.

Besides to such tonal noise contributions, purely due to the periodic valves openings, another broadband sound must be considered which is visible at higher frequencies. This contribution is due to high velocity of the gas which generates, for example, vorticity at junction and expansion sections of elements in the transmission line, constituting an additional source of intake noise as well. In general, a comprehensive assessment of the overall noise emitted by such systems should be take into account both the above mentioned noise contributions.

Within the whole above mentioned design process, when it is found that the desired targets are not achieved, several refinement design phases have to be pursued. As matter of fact, there is no unique methodology to be followed for the acoustic optimization of a duct system such as air intake or exhaust systems. Nevertheless, the two most intuitive ways of doing that rely on two different approaches. The first relies on a target to be achieved in terms of Transmission Loss, whilst the second one is based on a target curve in terms of sound pressure level at specifics engine running points or in terms of overall sound pressure levels in various rpm conditions. By the examination of the current literature, it is evident that a lot of efforts are nowadays spent in order to improve the acoustic attenuation characteristics in terms of Transmission Loss. This is mostly done by a design ex-novo of external resonators. In this regards, however, a sensitivity analysis has to be executed for each of the new design configurations in order to ensure that the desired goals in term of acoustic properties are effectively achieved. As an example, recently Y. Han et al. [4] created and validated a Boundary Element Model of a commercial intake system, in order to execute an acoustic geometric optimization by designing both Helmholtz and quarter-wave resonators. Vishal Vaidya et al.[5] also tried to optimize the Transmission Loss of an intake system by means of one-dimensional analysis. Even in this case the acoustic optimization has relied on the design of an external resonator with the

[1] The firing frequency may be calculated as $f = \frac{z\ rpm}{60\ \varepsilon}$, being $z$ the number of cylinders and $\varepsilon$ the number of crankshaft revolutions necessary to complete an engine cycle.

final results of achieving higher TL and lower sound pressure levels. As it will be shown in chapter 8, although this may represent a quite simple choice, it is not always pursuable because of the fact that, adding external resonators, may results in a significantly increase of the size of the considered system. Such condition may be not applicable due to some compactness requirements, especially for small size engines.

More sophisticated procedures are also widespread used, which take advantage of automatic optimization loops for seeking the best design configuration, once some type of constraints are set up (e.g. geometrical, acoustical, engine performances etc.). In particular, such techniques generally rely on the use of numerical models whose geometries are modified accordingly with the information coming from the use of optimization algorithms, applied to some acoustic properties. As an example, Yeh et al. [6][7][8][9] presented an optimization method for various muffler starting configurations, using a Genetic Algorithm (GA) which is inspired on the idea of the natural biological evolution. As an example, in reference [7], the GA is applied in order to find the optimal size design of double-chamber muffler under space constraints and dealing with broadband noise. In particular, using the technique of four-pole matrix for sound transmission loss calculation, together with the GA technique, the optimization has been carried out considering maximum dimension related constraints. More recent studies have been executed by Chiu et al.[10] in order to determine the optimal shape design of a single expansion muffler with side inlet/outlet. More in detail, after an experimental validation of a Boundary Element Model of the studied system, the numerical optimizations by means of Genetic Algorithms have been applied together with three kinds of mathematic gradient method (interior penalty function method (IPFM), exterior penalty function method (EPFM) and feasible direction method (FDM)), in order to find the best design configuration which ensures the highest Transmission Loss, considering also constraint conditions. Although thanks to the use of such automatic optimization procedures there is no need to manually realize the desired modification and to investigate their impact on the acoustic properties by means of several sensitivity analyses, the main drawback is represented by the very high computational cost, especially when several targets have to be satisfied at the same time. This is generally the case when dealing with both intake and exhaust systems of internal combustion engine, for which a prescribed size must be respected together with an as high as possible acoustic performance, achieved without possibly decreasing the engine performances.

In this study, the acoustic behavior of an air induction system for a four stroke, spark ignition engine has been deeply investigated, with the aim of various Computer Aided Engineering tools, in order to refine its original shape for enhancing its acoustic properties. The main technical and mechanical characteristics of the engine are reported in Table 1. In particular, it is a downsized SI engine whose design philosophy is based on the reduction of the engine displacement, while employing a turbocharging system in order to achieve a prescribed power/torque output.

| | |
|---|---|
| Model Type | 2 cylinders, 8 valves (VVA), Turbocharged and Intercooled |
| Displacement [$cm^3$] | 875 |
| Stroke/Bore [mm] | 86/80.5 |
| Connection Rod Length [mm] | 136.85 |
| Compression Ratio | 9.9 |
| Max Brake Power [kW] | 64.6 @ 5500 rpm |
| Max Brake Torque [Nm] | 146.1 @ 2500 rpm |

Table 1 – Main technical and mechanical data of the internal combustion engine under investigation.

Thus, the aspects covered in the present thesis may be divided into two parts describing a validation and an acoustic optimization procedure respectively, for a numerical model of the system under investigation. More precisely, the validation process of a 3D Finite Element (FE) model of the air induction system is presented in the first part, in which an acoustic performance and a gas-dynamic noise analysis are discussed. As regards the acoustic performance validation procedure, in order to obtained data useful for the purpose, an experimental campaign has been carried out at the University of Florence in order to measure the acoustic attenuation characteristics in terms of Transmission Loss, by means of the impedance tube technology, in several conditions. Thanks to the very good correlation between experimental and numerical outcomes, a further validation step has been executed aimed to validate the numerical model findings when simulating also the amount of noise emitted in real working conditions. Consequently, thanks to the availability of gas-dynamic noise measurements for the studied air induction system, it has been possible to compare both experimental and numerical outcomes in terms of sound pressure levels in several engine running points. Even in this case a good correlation has been found thanks to which it has been possible to assume that the three-dimensional model is able to reproduce the acoustic response of the actual system. For this reason, a shape optimization procedure on the original device has been carried out and will be presented. Hence, the effects of several geometric changes, properly realized in order to enhance the acoustic performance related to both Transmission Loss and emitted gas-dynamic noise, are investigated. It will be shown that the presented geometric modifications may effectively enhance the acoustic performance of the original device, without decreasing the engine performances. Besides, such modifications have been designed in a way such that, if actually realized, the overall size of the original system would not be modified.

Before proceeding with the description of the main aspects related to the PhD course activity, it is very important to highlight that, as matter of fact, the in depth study of sound and vibrations is a very complicated task as, even focusing on the simplest problems, it may involve many related aspects such as structural mechanic, fluid-dynamic and acoustic. Consequently, in order to provide the necessary background for the understanding of the various topics covered in this thesis, basic definitions and other important aspects related to the physics of the investigated phenomena are briefly recalled each time when necessary, just before proceeding with the description of the analyses and corresponding outcomes. Thus, chapter 1 is devoted to the recalling of the basic equations governing the fluid flow which constitutes the very basis for the derivation of the wave equation governing acoustic phenomena, whilst chapter 2 is about the basic aspects of acoustic and sound propagation in ducts. In chapter 3, the basic concepts about the study of acoustic filters are briefly recalled together with a mention to the acoustic performance characterization parameters. Chapter 4 is devoted to an insight about how the finite element method is applied to acoustic problems. In Chapter 5 and 6 the validation procedures of the finite element model of the studied air induction system are described. Chapter 7 the theory of aerodynamic generation of sound will be recalled, making reference to the well-known aeroacoustics analogy formulated by Lighthill, together with an insight to the turbulence problem and modelling. Chapter 8 is devoted to the investigation about the effect that several geometric modifications have on the acoustic performances of the intake system. Finally, in Chapter 9 the conclusions and future developments are briefly discussed.

## Bibliography


[1] https://www.comsol.com/video/engineering-design-optimization-multiphysics-simulation.

[2] Copiello, D., Zhou, Z., and Lielens, G., "Acoustic Simulation of Vehicle Exhaust System using High Order Transfer Matrix Method Coupled with Finite Element Method," SAE Int. J. Engines 8(1):2015, doi:10.4271/2014-32-0119.

[3] M. L. Munjal, "Acoustics of Ducts and Mufflers with Application to Exhaust and Ventilation System Design", John Wiley & Sons.

[4] Y. Han, H. Zhou, M. Y. Shi, C. Jin, "Acoustic Optimization for Intake System of Commercial Bus", Applied Mechanics and Materials, Vols. 635-637, pp. 334-340, 2014.

[5] Vishal Vaidya, P.P. Hujare, "Optimization of Sound Pressure Level of Air Intake System by using GT-Power", International Journal of Emerging Science and Engineering (IJESE), ISSN: 2319–6378, Volume-2, Issue-8, June 2014.

[6] Yeh L-J, Chiu MC, Lai GJ., "Computer aided design on single expansion muffler under space constraints", In: Proceedings of the 19th National Conference on Mechanical Engineering, The Chinese Society of Mechanical Engineers, Vol. C7, pp. 625–633, 2002.

[7] Ying-Chun Chang, Long-Jyi Yeh, Min-Chie Chiu, "Design Optimization of Double-Chamber Mufflers on Constrained Venting System by GA Method", Journal of technical acoustics, 2004.

[8] Yeh L-J, Chang Y-C, Chiu M-C, "Application of genetic algorithm to the shape optimization of a constrained double chamber muffler with extended tubes", Journal of Marine Science and Technology, Vol. 12, No.3, pp. 189-199, 2004.

[9] Yeh L-J, Chang Y-C, Chiu M-C, Lai G-J., "Optimization on multi-segments muffler under space constraints", Journal of Applied Acoustics, Vol. 65, pp. 521-543, 2004.

[10] Chiu M-C, Yeh L-J, Chang Y-C, "Shape optimization of single chamber mufflers with side inlet/outlet by using boundary element method, mathematic gradient, and genetic algorithm", Tamkang Journal of Science and Engineering, Vol. 12, No.1, pp. 85-98, 2009.

# Chapter 1

# Basics of Fluid Flow

### Introduction

In general, vibro-acoustics may be defined as the branch of science which studies the generation and propagation of mechanical waves[2] in fluids and solids. Therefore, depending on the particular phenomenon to be dealt with, the subject may be very complicated as well as the theory to be studied. The purpose of this chapter is to recall some basic relationships which are the minimum mandatory for moving forward in the understanding of the topic investigated in this thesis.

## 1.1 The divergence theorem

The divergence theorem is probably one of the most important theorem in mathematics and engineering and, in general, relates the flow of a vector field through a closed surface to the behavior of the considered vector field inside the surface. Thus, considering a vector field $\boldsymbol{R} = \boldsymbol{R}(\boldsymbol{r}, t)$, the flow of $\boldsymbol{R}$ over a closed surface may be expressed as

$$\iint_S \boldsymbol{R} \cdot \boldsymbol{n}\, dS \tag{1.1}$$

where $\boldsymbol{n}$ is the outward normal from $S$. Since the goal is to find a relation for an arbitrary shaped surface, referring to Figure 1.1, let firstly consider for simplicity a closed surface enclosing a cubical volume.

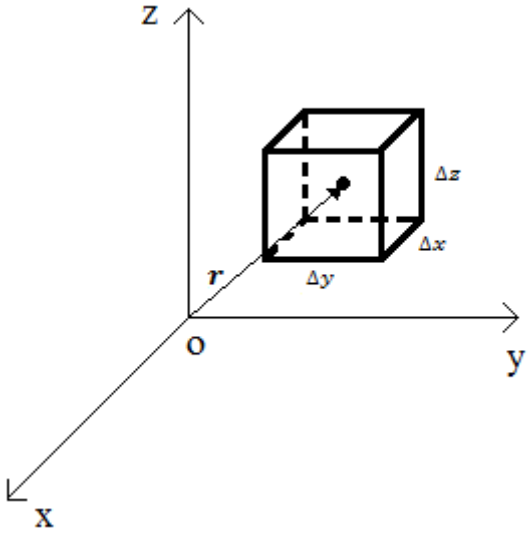


Figure 1.1 – Example of a closed surface enclosing a cubical volume.

Hence, according to eq. (1.1), the contribution to the flow of $\boldsymbol{R}$ out of $S$, in the $x$ direction, is

[2] A mechanical wave is a wave which needs a medium in order to transport energy.

$$\iint_{\Delta y \Delta z} R_1\left(x+\frac{\Delta x}{2}, y, z\right) - R_1\left(x-\frac{\Delta x}{2}, y, z\right)\, dydz = \frac{\partial R_1}{\partial x}\Delta\mathcal{V} + o(\Delta\mathcal{V}) \tag{1.2}$$

where the last term is an infinitesimal of higher order. It follows that the flow over the whole surface of the small volume may be rewritten as

$$\iint_{\Delta S} \boldsymbol{R}\cdot\boldsymbol{n}\, dS = \left(\frac{\partial R_1}{\partial x}+\frac{\partial R_2}{\partial y}+\frac{\partial R_3}{\partial z}\right)\Delta\mathcal{V} + o(\Delta\mathcal{V}) \cong (\boldsymbol{\nabla}\cdot\boldsymbol{R})\Delta\mathcal{V} \tag{1.3}$$

where the term within the brackets is the divergence of the considered vector field. Consequently, in the limit of volume being infinitesimal, it is possible to write

$$(\boldsymbol{\nabla}\cdot\boldsymbol{R}) = \lim_{\Delta\mathcal{V}\to 0}\frac{1}{\Delta\mathcal{V}}\iint_{\Delta S}\boldsymbol{R}\cdot\boldsymbol{n}\, dS \tag{1.4}$$

Now, if an arbitrary shaped volume is divided into small cubical volumes, as schematically depicted in Figure 1.2, it is possible to add the contribution of each surfaces in order to obtain

$$\sum_i^N \iint_{\Delta S_i}\boldsymbol{R}\cdot\boldsymbol{n}\, dS \cong \sum_i^N (\boldsymbol{\nabla}\cdot\boldsymbol{R})_i\Delta\mathcal{V}_i \tag{1.5}$$

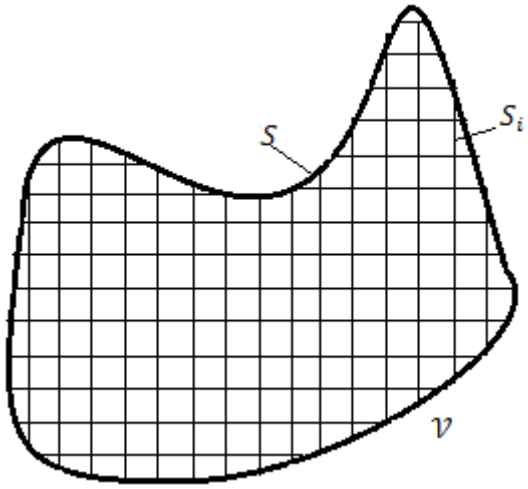


Figure 1.2 – Subdivision of an arbitrary shaped volume into a number of small cubical volumes.

Since the outer flux from a volume coincide with that entering adjacent volumes, the contributions from two coincident surfaces are the same but with opposite signs. Consequently, in the limit of $\Delta\mathcal{V}_i \to 0$ the sum of the surface integral on the left-hand side of eq. (1.5) will approach the integral over the external surface whilst the sum on the right-hand side will approach the volume integral over $\mathcal{V}$, namely

$$\iint_S \boldsymbol{R}\cdot\boldsymbol{n}\, dS = \iiint_V \boldsymbol{\nabla}\cdot\boldsymbol{R}\; d\mathcal{V} \tag{1.6}$$

which is the mathematical expression of the divergence theorem stating that the flow of a vector field over a control surface $S$ is equal to the change of $\boldsymbol{R}$ within the volume enclosed by $S$, which represents the divergence of $\boldsymbol{R}$ indeed. In such sense, the divergence of a vector field within a control volume $\mathcal{V}$ represents an indication on if the considered quantity is flowing outside or inside $\mathcal{V}$. It is easy to demonstrate that the divergence theorem may be also applied to scalar fields, by

simply multiplying both side of eq. (1.6), applied to a scalar quantity, by an arbitrary constant vector, namely

$$\iint_S \mathrm{A}\,\mathbf{a}\cdot\boldsymbol{n}\,dS = \iiint_V \nabla\cdot(\mathrm{A}\,\mathbf{a})\,d\mathcal{V} \tag{1.7}$$

or

$$\mathbf{a}\iint_S \mathrm{A}\cdot\boldsymbol{n}\,dS = \mathbf{a}\iiint_V \nabla\cdot\mathrm{A}\,d\mathcal{V} \tag{1.8}$$

where the vector may be eliminated since it is arbitrary[3].

## 1.2 Conservation equations

The conservation equations should be merely seen as just some basic relations which govern the study of whatever physical/engineering problem. Basically, when talking about conservation equations for a thermodynamic system, implicit reference is done to conservation of extensive properties like mass, momentum and energy. Such equations mathematically reproduce the most simple concept of the nature, namely that "it is impossible to get something for nothing". Before going through that, it is necessary to choose how to describe the thermodynamic system under investigation, meaning that the formulation of a conservation equations may be done once "*a position*" from which to describe the evolution of the system has been chosen. Two type of approaches may be used to describe the evolution of a system and they are called eulerian and lagrangian formulation[1]. According to the first, the thermodynamic system under investigation is defined in terms of a fixed *control volume* bounded by real or fictitious surfaces. This is schematically depicted in Figure 1.3.

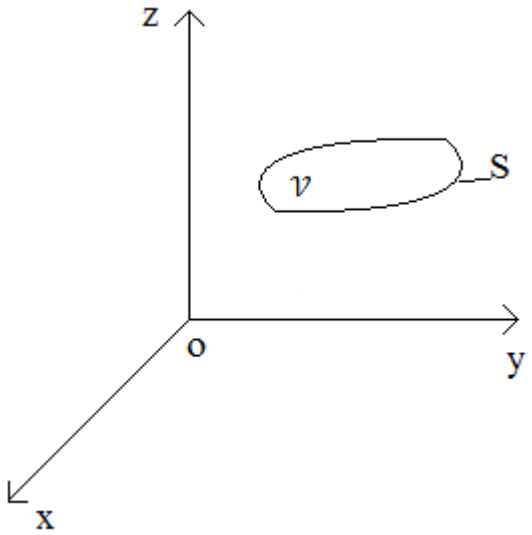


Figure 1.3 – Eulerian description of a thermodynamic system.

From a practical viewpoint, the volume of the studied system is fixed whilst the mass embedded within the it may, in general, change with respect to the flowing time. The contrary happens for the *lagrangian description* of a system, where it is assumed that the mass of the system is fixed, occupying a volume whose dimensions may change with respect to the flowing time. Therefore, in

this latter case, the system is studied in terms of the so-called control mass. This second case is schematized in Figure 1.4.

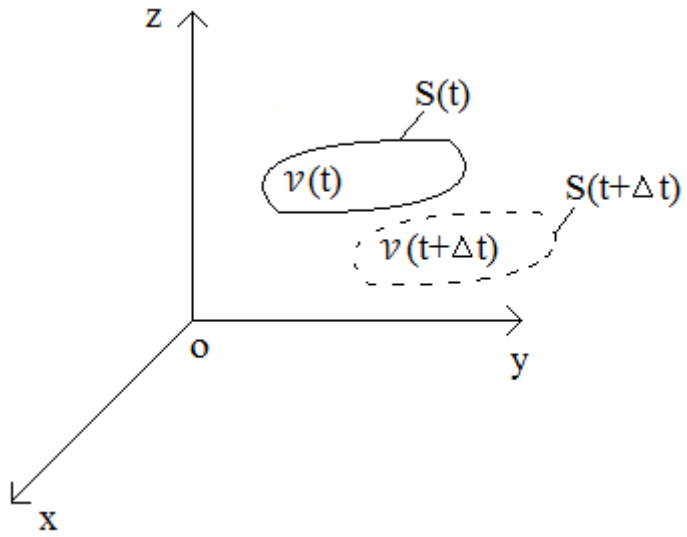


Figure 1.4 – Lagrangian description of a thermodynamic system.

Once the type of description has been chosen, the conservation equations are firstly referred to an elementary entity, in which the entire considered system may be divided, and then the relations are extended to the whole system's extension. Such elementary entity are volumes $(d\mathcal{V})$ or masses $(d\mathcal{M})$, when referring to the eulerian and lagrangian descriptions respectively. The choice of description to use for analyzing a system depends on the type of system and on the output of the analysis. For example, if the thermodynamic system consists of a fluid whose motion evolves within a rigid-wall duct, a good choice would be represented by the use of the *eulerian description*. In fact, in this case the volume occupied by the fluid system is fixed and coinciding with the interior of the duct, whilst its mass may change during the flow. As an example, in this case the control volume could coincide with the dashed line schematically depicted in Figure 1.5.

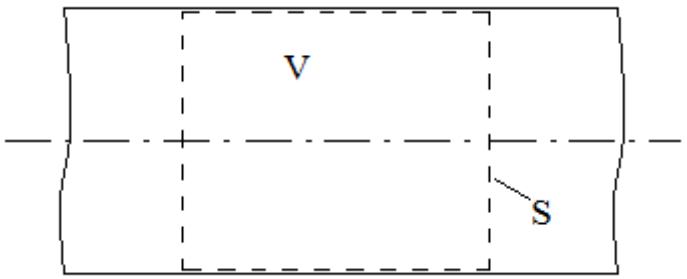


Figure 1.5 – Example of eulerian description of the motion for a fluid.

Furthermore, a classical application is represented by the case in which there are temperature gradients where one may be interested in knowing the temperature within the flow at certain fixed points within the duct (control volume), rather than the temperature of each fluid particle (which would be also practically impossible). That would be an example of eulerian study of the flow system, where the observation point is fixed at some points in space. When, on the other hand, studying structural mechanic, it may be more obvious to use a lagrangian description due to the

physic of the problem. As an example, considering the structural analysis of a table under the action of a heavy weight acting on it, the mass of the table would not change, but its volume is not fixed as a consequence of its deflection (deformation). So, in this case, the control mass would be that of the table and the final goal of the analysis would consist in evaluating the deformation of the structure.

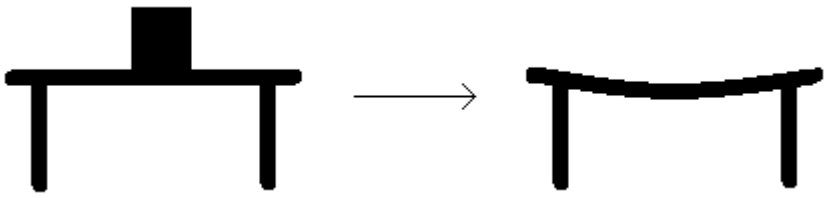

Figure 1.6 – Example of lagrangian description of deformation of a structure.

More precisely, imaging to being able to divide the table in a certain number of fixed little masses[3], the focus would be on knowing the position of each points (masses) after the application of the weight, so that the displacement of all masses constitute the deflection of the system. There are other cases in which it is obvious to choose a lagrangian approach, e.g. when studying the dynamic of a closed bottle filled with a fluid, under the action of a force; the mass trapped within the bottle is always the same because it is a closed system whilst its form may vary under the action of the externally applied forces. However, in general, when dealing with fluid flow, the difference between the two descriptions may be even more easily understood.

From what above, in order to be able to describe the flow, two descriptions may be used depending on the reference frame with respect to which the fluid is studied. In the following, it is assumed that the coordinate system, with respect to which the conservation equations are derived, is inertial[4]. Consider a continuous fluid where there are an infinity number of masses, each identifying a particle. Let's suppose that the particles the fluid consists of all remain distinct during the motion. If the position of a particle (or material point) at a certain time instant, say $t_0$, is $\boldsymbol{r}_0$ then the relation

$$\boldsymbol{r} = \boldsymbol{r}(\boldsymbol{r}_0, t) \tag{1.9}$$

identifies, for a given initial position (which means for a given particle), the motion of the particle as function of the time, as depicted in Figure 1.7.

[3] Which is what it is actually done in Finite Element structural analysis.

[4] A coordinate system is said to be inertial if a free (subjected to a zero resultant external force) and isolated (unconstrained) point is either still or moving with constant velocity.

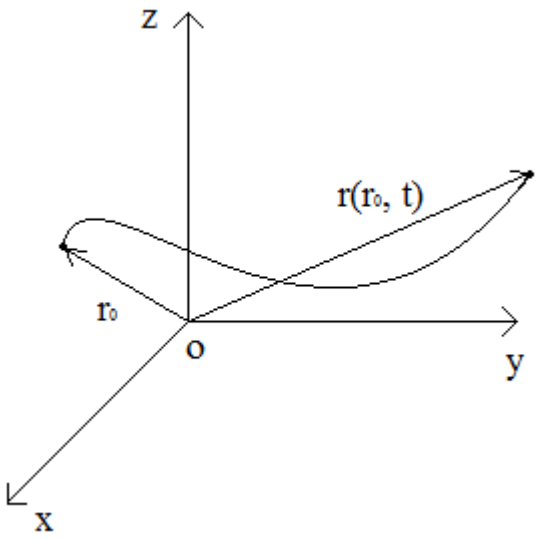


Figure 1.7 – Example of lagrangian description of the motion for a fluid.

Practically, according to this description, all the positions the particle occupies during its motion are observed starting from the initial one, namely the reference frame coincides with the center of mass of the particle. In other words, the observer follows the particle during the whole motion. As an analogy, such description of a fluid motion would be equivalent in sitting on a boat driving down a river. The description of the motion in terms of material points represents a *lagrangian description* and the coordinates $(x_0, y_0, z_0)$ of the particle are called *material* or *lagrangian coordinates* and together with the time represent the independent variables of the *lagrangian description* of the motion[5]. As an example of how to practically make such description, one could think to attach to a fluid particle a temperature sensor in order to follow the variation of the particle's temperature during its motion. However, to the aim of describing the temperature field, it would be required to describe, in this way, the temperature of all the particles of the fluid during their motion. However, as already highlighted, such lagrangian measurements are impossible to reproduce in laboratory and therefore measurements are generally made at fixed point within the flow field. This lead to the second way of studying the phenomenon. In order to understand the *eulerian description*, consider the situation in which the field has to be studied from an experimental point of view. In this case, the simplest approach consists in recording the properties of interest at specified positions in the fluid, say probe positions. For one of this fixed position, the description of the motion is given by a relation of the type

$$\boldsymbol{r}_0 = \boldsymbol{r}_0(\boldsymbol{r}, t) \tag{1.10}$$

As such, eq. (1.10) means that the motion of a particular particle (that occupying the position $\boldsymbol{r}_0$ at $t_0$) is observed when it reaches $\boldsymbol{r}$ at the time instant $t$, as it is schematized in Figure 1.8.

[5] Thus, the material coordinates $(x, y, z)$, describing the position of the particle during the motion, are dependent variable.

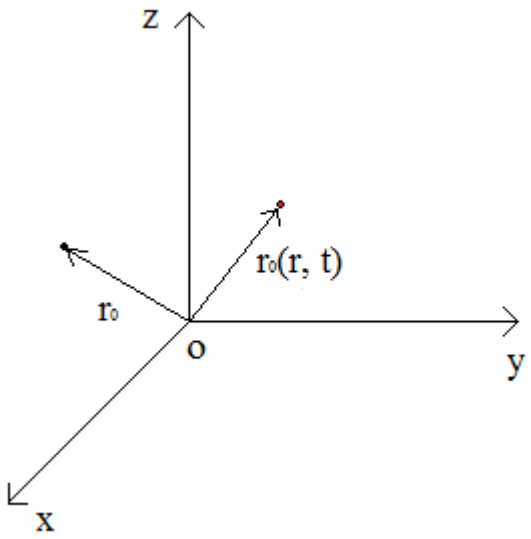


Figure 1.8 – Example of eulerian description of the motion for a fluid.

In other words, the attention of the observer (the reference frame) is fixed at a certain point in space, waiting for the fluid particles $\boldsymbol{r}_0$ to pass through it. As an analogy, such description of a fluid motion would be equivalent in sitting at a river side watching the fluid flowing. The coordinates of the observed point $(x, y, z)$ are called *spatial* or *eulerian coordinates* and together with the time represent the independent variables of the *eulerian description* of the motion[6]. From what above, it is clear that in spite of the fact that the flow field is always the same, the two descriptions are quite different. To further understand the differences, let's consider the velocity as the property of interest. In this case, the description of the field, according to both *lagrangian* and *eulerian*, is depicted in Figure 1.9.

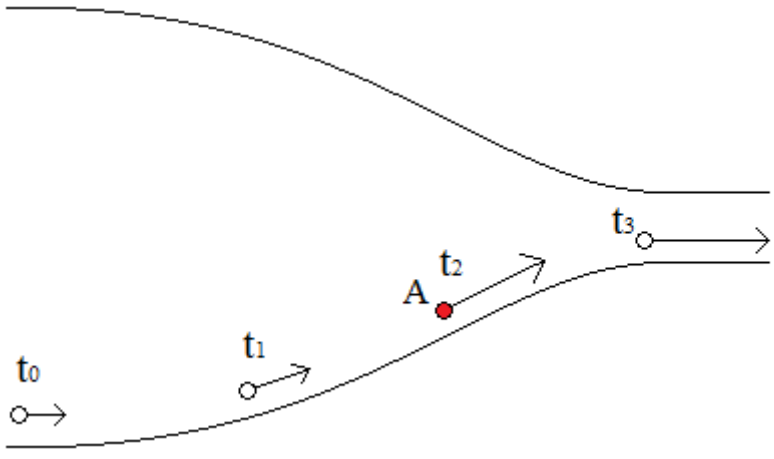


Figure 1.9 – Lagrangian and eulerian description of the velocity field in a fluid flow. The velocity is represented by a vector attached to the reference frames.

The main difference, lies in the fact that the velocity at the spatial point (red circle), does not refer to the same particle at each time instant. The two velocities coincide only at the time instant the particle (white circle) passes through point A.

[6] Thus, the eulerian coordinates $(x, y, z)$ are, together with the time, the independent variables, meaning that all the other variables are expressed as function of them.

In general, when studying the motion of a fluid, the *eulerian description* is preferred. This happens not only because it better reproduce what can be done experimentally in laboratory, but also because the balance equations are more easily formulated for a system defined in terms of control volume[2]. In fact, in this case, for a given property the balance equation may be thought as simply reproducing the way in which the system interacts with the surrounding ambient, as depicted in Figure 1.10.

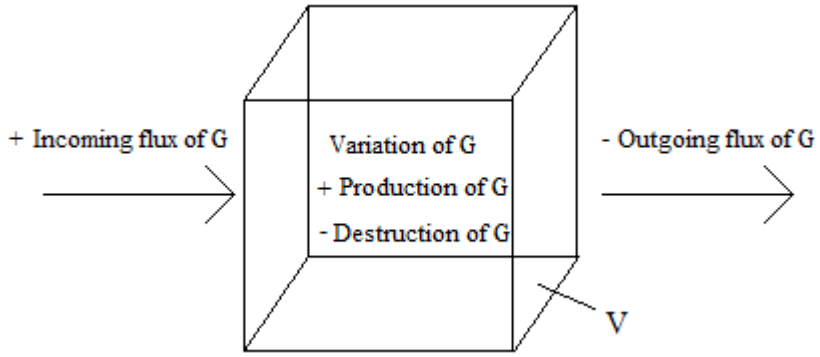


Figure 1.10 – Interactions between an eulerian system and the surrounding ambient.

Therefore, a formal balance equation for a fixed control volume simply obeys to the following simple thought

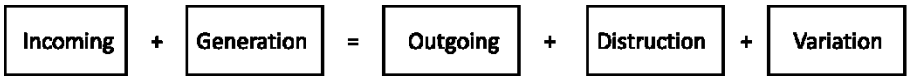


where the variation may be an accumulation or a depletion. However, most laws in nature are stated in terms of material points and so the derivation of conservation equations is more intuitive when using a *lagrangian description*, as it will be clear in the next. Therefore, it is necessary to link the two descriptions in order to be able to go from one to another. From a qualitative point of view, consider Figure 1.11 in which a fluid dynamic problem is schematized.

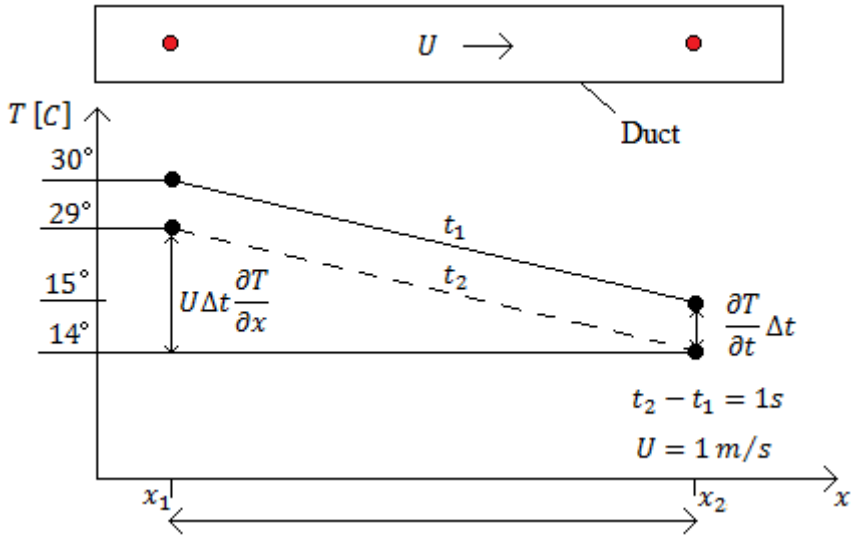


Figure 1.11 – Fluid flow in which there is the presence of both spatial gradient and temporal temperature variation.

In the above figure the two red points represent spatial coordinates. Considering both the temporal and spatial temperature variations as indicated, it is interesting to compare the decrease in the temperature according to both lagrangian and eulerian descriptions in the time interval $[t_1; t_2]$. The temperature variation experienced by a temperature sensor attached to the fluid particle during its motion would be

$$T(x_1, t_2) - T(x_1, t_1) = 16° C$$

where $x_1$ indicates that the focus is on the particle whose initial position was $x_1$. However, for a fixed observer, which is either at $x_1$ or $x_2$, the temperature variation is equal to only $1° C$. It follows that the lagrangian time variation of the temperature is equal to the eulerian one plus something else accounting for the spatial gradient of the temperature. The additional term is represented by the convective effect which affects the fluid particle during its motion, namely

$$\frac{DT}{Dt} = \frac{\partial T}{\partial t} + U\frac{\partial T}{\partial x} = 1 + 15$$

Such temperature drop is due to both a time and spatial variation of the scalar. From a more formal point of view, let's consider the description of a generic property $G$ in *lagrangian coordinates* for a particle $p$, namely

$$G = G(r_p, t) \tag{1.11}$$

Now, it is important to highlight that in a time interval $\Delta t$ a material point (and so the reference frame in the *lagrangian description*) will move forward of a certain amount, say $\Delta r = (\Delta x, \Delta y, \Delta z)$. Therefore, the variation of $G$ experienced by the observer may be expressed as Taylor expansion series, namely

$$\Delta G_p = G(r_p + \Delta r, t + \Delta t) - G(r_p, t) = \frac{\partial G}{\partial x}\Delta x + \frac{\partial G}{\partial y}\Delta y + \frac{\partial G}{\partial z}\Delta z + \frac{\partial G}{\partial t}\Delta t \tag{1.12}$$

Dividing both sides of eq. (12) by $\Delta t \to 0$, it gives the variation of $G$ from a lagrangian point of view in *eulerian coordinates*, namely

$$\frac{DG}{Dt} = \frac{\partial G}{\partial t} + \boldsymbol{V} \cdot \nabla G \tag{1.13}$$

In fact, eq. (1.13) expresses the variation of the properties $G$ experienced by the material point when moving from a spatial point $(\Delta t \to 0)$. Thus, the left-hand side of eq. (1.13) is called *time material (or lagrangian) derivative* (also known as convective time derivative) whilst the first term of the right-end side is called *time spatial (or eulerian) derivative*, both referred to a property $G$. Conceptually, the main difference lies in the convective effect that an observer, which moves with the material point, experiences during the motion.

### 1.2.1 Reynolds Transport theorem

Equation (1.13) expresses the rate of change of a generic property for an elementary entity (a generic particle) in the fluid having an infinitesimal control mass $(d\mathcal{M})$, in terms of spatial coordinates. However, in order to formulate the conservation equation, it is more useful to express the rate of change for an extensive property related to a finite control mass[1]. This is given by the

so-called transport theorem. Let's consider a control mass moving in a fluid as depicted in Figure 1.12.

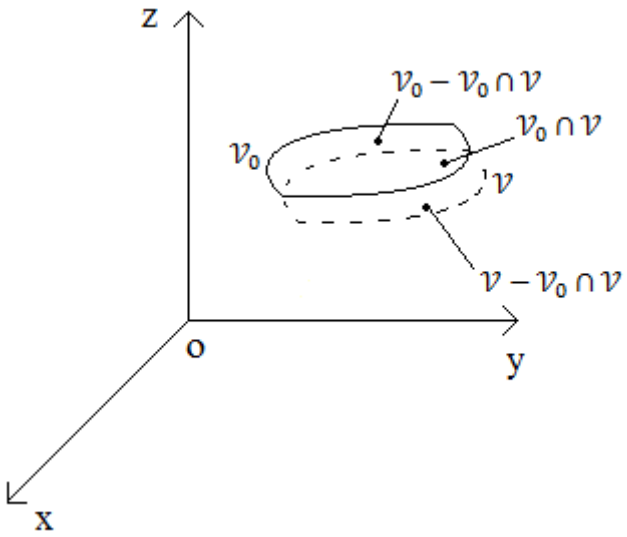


Figure 1.12 – Lagrangian description of a finite control mass.

Since a control mass has been chosen, the whole mass of the system is given by

$$\int \rho(\boldsymbol{r}, t_0) d\mathcal{V}_0 = \int \rho(\boldsymbol{r}, t) d\mathcal{V} = \mathcal{M} = cost. \tag{1.14}$$

At the same time, the generic extensive property $G$ related to such control mass is given by

$$G = \int g d\mathcal{M} \tag{1.15}$$

where $g$ stands for the specific value of the properties $G$, which depends only upon the time variable. Therefore, the variation of $G$ within the time interval $\Delta t = t - t_0$ may be expressed as

$$(\Delta G)_{\mathcal{M}} = \int_{\mathcal{V}} \rho(\boldsymbol{r}, t) g(\boldsymbol{r}, t) d\mathcal{V} - \int_{\mathcal{V}_0} \rho(\boldsymbol{r}, t_0) g(\boldsymbol{r}, t_0) d\mathcal{V}_0 = \left[\int_{\mathcal{V}} \rho g d\mathcal{V}\right]_t - \left[\int_{\mathcal{V}_0} \rho g d\mathcal{V}\right]_{t_0} = \left[\int_{\mathcal{V}_0 \cap \mathcal{V}} \rho g d\mathcal{V}\right]_t - \left[\int_{\mathcal{V}_0 \cap \mathcal{V}} \rho g d\mathcal{V}\right]_{t_0} + \left[\int_{\mathcal{V} - \mathcal{V}_0 \cap \mathcal{V}} \rho g d\mathcal{V}\right]_t - \left[\int_{\mathcal{V}_0 - \mathcal{V}_0 \cap \mathcal{V}} \rho g d\mathcal{V}\right]_{t_0} \tag{1.16}$$

By dividing eq. (1.16) by $\Delta t \to 0$, the expression for the lagrangian derivative of the property $G$ is found, namely

$$\frac{DG}{Dt} = \lim_{\Delta t \to 0} \left\{ \frac{\left[\int_{\mathcal{V}_0 \cap \mathcal{V}} \rho g d\mathcal{V}\right]_t - \left[\int_{\mathcal{V}_0 \cap \mathcal{V}} \rho g d\mathcal{V}\right]_{t_0}}{\Delta t} + \frac{\left[\int_{\mathcal{V} - \mathcal{V}_0 \cap \mathcal{V}} \rho g d\mathcal{V}\right]_t - \left[\int_{\mathcal{V}_0 - \mathcal{V}_0 \cap \mathcal{V}} \rho g d\mathcal{V}\right]_{t_0}}{\Delta t} \right\} \tag{1.17}$$

However, for $\Delta t \to 0$, $\mathcal{V}_0 \cap \mathcal{V} \to \mathcal{V} \to \mathcal{V}_0$ and the two quantities of first limit on the right-end side of eq. (1.17) are evaluated at the same point in space, so that it represents the time derivative of $G$. At the same time, according to Figure 1.13, the last two terms represent the inward (-) and outward (+) flux of $G$ from the boundary of $\mathcal{V}_0$.

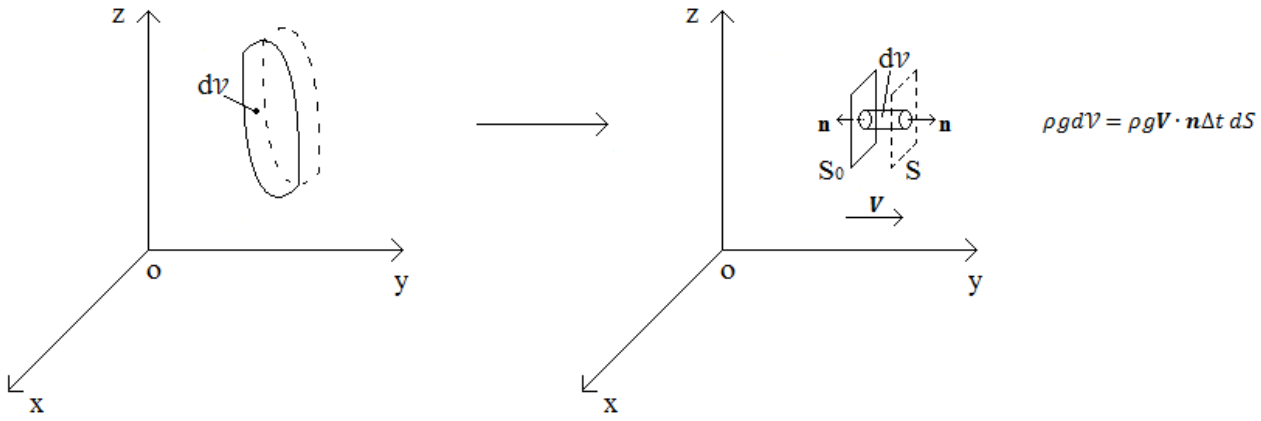


Figure 1.13 – Inward and outward flux of the generic property $G$ from the control surface $dS$.

After such considerations, the *lagrangian derivative* of a generic extensive property $G$ related to a finite control mass $\mathcal{M}$, in *eulerian coordinates*, may be expressed as

$$\frac{DG}{Dt} = \frac{\partial}{\partial t}\int_{\mathcal{V}_0} \rho g d\mathcal{V} + \int_{S_0} \rho g \boldsymbol{V} \cdot \boldsymbol{n} dS \tag{1.18}$$

which represents the Reynolds transport theorem. This latter states that the *lagrangian derivative* equals the *eulerian derivative* plus another convection term due to the motion of the control mass. Therefore, eq. (1.18) may be referred to any time instant $t$ provided that, both volume and surface integral are *eulerian*, namely those the particle effectively occupies at considered time instant. Hence the subscript $_0$ will be omitted. Making use of the divergence theorem, the *lagrangian derivative* in *eulerian coordinates* may also be expressed as

$$\frac{DG}{Dt} = \frac{\partial}{\partial t}\int_{\mathcal{V}} \rho g d\mathcal{V} + \int_{\mathcal{V}} \nabla \cdot (\rho g \boldsymbol{V}) d\mathcal{V} \tag{1.19}$$

### 1.2.2 Conservation of mass

The mass conservation law states that, considering a system defined in terms of its control mass (*lagrangian description*), in absence of source mechanism (e.g. injections) the total mass of the system is trivially constant[1]. From what has been discussed before, the mathematical representation of that may be expressed as[7]

$$\frac{D\mathcal{M}}{Dt} = \frac{D}{Dt}\int_{\mathcal{M}} d\mathcal{M} = 0 \tag{1.20}$$

For a system defined in terms of control volume (*eulerian description*), thanks to the Reynolds transport theorem, eq. (1.20) becomes

$$\frac{D\mathcal{M}}{Dt} = \frac{\partial}{\partial t}\int_{\mathcal{V}} \rho d\mathcal{V} + \int_{S} \rho \boldsymbol{V} \cdot \boldsymbol{n} dS = 0 \tag{1.21}$$

[7] $g = 1$.

which should not surprise since, given that the mass cannot be generated and destroyed, the only way to make the mass of a system change is because of convective flux across its boundaries. By means of the divergence theorem, eq. (1.21) may be rewritten as[8]

$$\int_{\mathcal{V}} \frac{\partial \rho}{\partial t} d\mathcal{V} + \int_{\mathcal{V}} \nabla \cdot (\rho \boldsymbol{V}) d\mathcal{V} = 0 \tag{1.22}$$

or

$$\frac{\partial \rho}{\partial t} + \nabla \cdot (\rho \boldsymbol{V}) = 0 \tag{1.23}$$

which represents the mass conservation law in local form. According to this latter, in absence of source terms, within an elementary control volume $d\mathcal{V}$ rate of change of mass can be achieved only by means of mass transport $(\rho \boldsymbol{V})$ from its boundaries. In fact, the divergence of the mass transport represents a measure of the amount of mass "escaping" from $d\mathcal{V}$. It follows that, a positive value of divergence implies, according to eq. (1.23), a negative rate of change of mass within $d\mathcal{V}$, namely there is a mass depletion. Vice versa, a negative value of the divergence implies a mass accumulation. Just for the sake of completeness, eq. (1.23) is generally expressed in Cartesian tensor notation as

$$\frac{\partial \rho}{\partial t} + \frac{\partial (\rho V_i)}{\partial x_i} = 0 \tag{1.24}$$

### 1.2.3 Conservation of momentum

The starting point for the momentum conservation law is represented by the Newton's law which states that, considering an inertial coordinate system, the rate of change of the momentum corresponding to a material point (particle with constant mass) equals the resultant force acting on the considered particle[1]. Mathematically this leads to

$$\boldsymbol{F} = \frac{D(\mathcal{M}\boldsymbol{V})}{Dt} \tag{1.25}$$

where $\boldsymbol{F}$ represents the total applied force. Such principle must be valid for any particles the thermodynamic system consists of. Thus, for a discrete thermodynamic system made of $n$ particles, eq. (1.25) yields

$$\sum_{i=1}^{n} \boldsymbol{F}_i = \sum_{i=1}^{n} \frac{D(\mathcal{M}_i \boldsymbol{V_i})}{Dt} = \frac{D}{Dt} \sum_{i=1}^{n} (\mathcal{M}_i \boldsymbol{V_i}) \tag{1.26}$$

The left-hand side of eq. (26) represents the resultant of both internal and external forces acting on all the particles. However, for the third law of dynamic, the internal reactions have a zero resultant. Therefore, the momentum conservation law in *lagrangian coordinates* for a continuous system is

$$\boldsymbol{F}_{est} = \frac{D}{Dt} \int_{\mathcal{M}} \boldsymbol{V} d\mathcal{M} \tag{1.27}$$

[8] Since the control volume is fixed, the order of the integral and the time derivative may be interchanges, namely $\frac{\partial}{\partial t} \int_{\mathcal{V}} \rho d\mathcal{V} = \int_{\mathcal{V}} \frac{\partial \rho}{\partial t} d\mathcal{V}$

The external forces acting on the system may be divided in body forces (acting on the elementary masses) and surface forces (acting on its surface), due to the interaction between the fluid element and the surrounding fluid. If only gravitational forces are considered as body forces, the left-hand side of eq. (1.27) may be rewritten as

$$\boldsymbol{F}_{est} = \int_{\mathcal{M}} \boldsymbol{g} d\mathcal{M} - \int_S \boldsymbol{f_n} dS \tag{1.28}$$

where $-\boldsymbol{f_n}$ stands for the force per unit area acting on the elementary surface $dS$, whose normal vector is $\boldsymbol{n}$, belonging to the whole control surface $S$, as depicted in Figure 1.14.

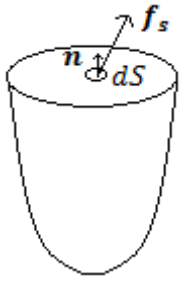


Figure 1.14 – Stress vector acting on an elementary surface $dS$.

By making use of the Reynolds transport theorem, eq. (1.27) may be expressed in *eulerian coordinates*, namely

$$\frac{\partial}{\partial t}\int_{\mathcal{V}} \rho \boldsymbol{V} d\mathcal{V} + \int_S \rho \boldsymbol{V}\boldsymbol{V} \cdot \boldsymbol{n} dS + \int_S \boldsymbol{f_s} dS = \int_{\mathcal{V}} \rho \boldsymbol{g} d\mathcal{V} \tag{1.29}$$

which is only valid for an inertial coordinate system. On the left-hand side of eq. (1.29), the first term represents the rate of change of momentum, the second term represents the convective flux of momentum and the third one represents the diffusive flux of momentum, whilst the right-hand side represents instead the generation of momentum. In order to obtain the local form of the momentum equation, it is necessary to model the stress vector $\boldsymbol{f_s}$. This latter may be identified, thanks to definition of the Cauchy stress tensor[9], as

$$-\boldsymbol{f_s} = \underline{\boldsymbol{T}} \cdot \boldsymbol{n} = \begin{bmatrix} \sigma_{xx} & \tau_{xy} & \tau_{xz} \\ \tau_{yx} & \sigma_{yy} & \tau_{yz} \\ \tau_{zx} & \tau_{zy} & \sigma_{zz} \end{bmatrix} \times \begin{Bmatrix} \alpha_x \\ \alpha_y \\ \alpha_z \end{Bmatrix} = \begin{Bmatrix} \sigma_{xx}\alpha_x + \tau_{xy}\alpha_y + \tau_{xz}\alpha_z \\ \tau_{yx}\alpha_x + \sigma_{yy}\alpha_y + \tau_{yz}\alpha_z \\ \tau_{zx}\alpha_x + \tau_{zy}\alpha_y + \sigma_{zz}\alpha_z \end{Bmatrix} \tag{1.30}$$

where $\alpha_x$, $\alpha_y$, $\alpha_z$ are the directional cosines of the normal vector $\boldsymbol{n}$, whilst $\sigma_{ij}$ and $\tau_{ij}$ represent the normal and shear forces, acting in direction $i$, per unit of area having normal $j$, respectively. In general, the Cauchy tensor may be considered as consisting of an isotropic and reversible part and another anisotropic and irreversible (or dissipative), which in Cartesian tensor form may be expressed as[10]

$$T_{ij} = \pi \delta_{ij} + s_{ij} \tag{1.31}$$

[9] It can be demonstrated that such tensor is symmetric.

[10] Isotropic means equal in all directions as it happens for the first term on the right-hand side of eq. (1.31) thanks to the presence of the Kronecker delta $\delta_{ij} = 0$ if $i \neq j$.

where the first term on the right-hand side of the above relation is the reversible part and it is conventionally equal to the average normal stresses, that is

$$\pi = \frac{\sigma_{xx}+\sigma_{yy}+\sigma_{zz}}{3} \tag{1.32}$$

Hence, the Cauchy stress tensor may be expressed in matrix form as

$$\underline{\boldsymbol{T}} = \begin{bmatrix} \pi & 0 & 0 \\ 0 & \pi & 0 \\ 0 & 0 & \pi \end{bmatrix} + \begin{bmatrix} \sigma_{xx} - \pi & \tau_{xy} & \tau_{xz} \\ \tau_{yx} & \sigma_{yy} - \pi & \tau_{yz} \\ \tau_{zx} & \tau_{zy} & \sigma_{zz} - \pi \end{bmatrix} \tag{1.33}$$

It follows that the Cauchy stress tensor is generally said to be composed of a so-called hydrostatic part (isotropic and reversible) responsible for changes in volume (as it represents an equivalent normal stress system with equal normal stresses) and a deviatoric (anisotropic and dissipative) one responsible for changes in form, trying to distort the considered element. The genesis of such nomenclature may be understood by the examination of the stresses experienced by solids and fluids, both at rest. By definition, a solid is a material which can experience shear stresses and capable of deforming only by the amount useful for reaching the equilibrium position. On the other hand, a fluid is defined as a material which cannot resist to shear stresses, continuously deforming under the action of the applied normal stresses. Consequently, the stress systems acting on an infinitesimal volume of both solid and fluid material at rest may be represented as depicted in Figure 1.15.

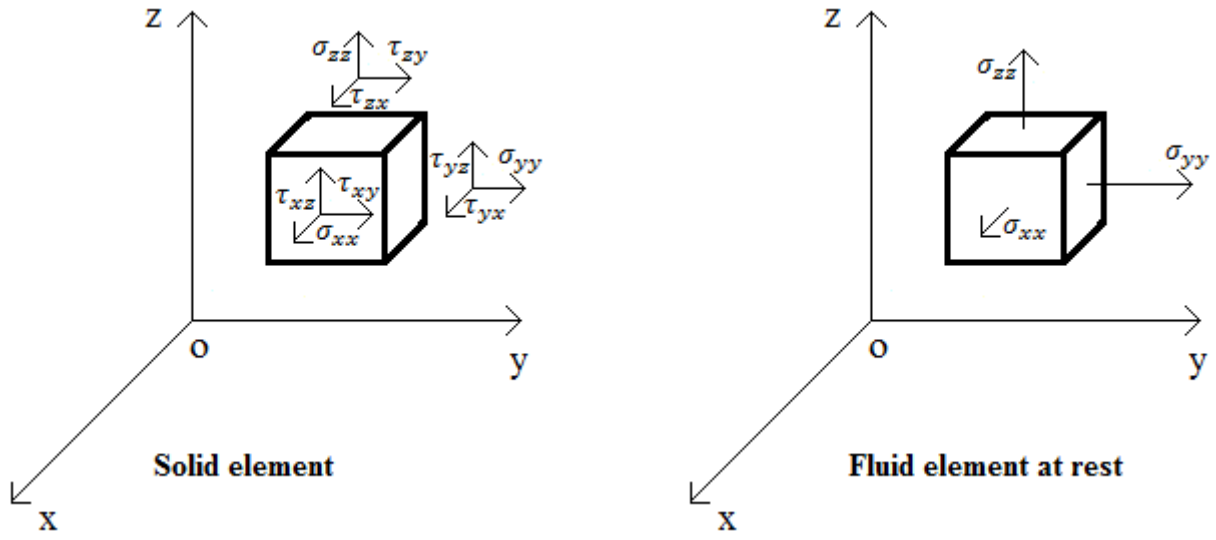


Figure 1.15 – Stress vectors acting on an elementary solid element $d\mathcal{V}$ (under the action of external forces) and on an elementary fluid element $d\mathcal{V}$.

Therefore, the stress tensor acting on a fluid element at rest is composed only be the hydrostatic part[11], whose components are linked to the pressure of the fluid. In particular, the pressure in the fluid is defined as the negative of hydrostatic stresses. However, focusing on fluid flow, both components are in general present, the first being associated with the thermodynamic pressure and the second one with the viscosity. Mathematically this leads to

[11] The only stress tensor which is experienced by a fluid at rest and therefore hydro-static.

$$\underline{\boldsymbol{T}} = -p\underline{\boldsymbol{I}} + \underline{\boldsymbol{\tau_d}} \tag{1.34}$$

where $\underline{\boldsymbol{I}}$ stands for the unity tensor. By substituting eq. (1.34) into eq. (1.30), yields to the following expression for the stress vector

$$-\boldsymbol{f_s} = -p\,\boldsymbol{n} + \underline{\boldsymbol{\tau_d}} \cdot \boldsymbol{n} \tag{1.35}$$

Therefore, the resulting momentum conservation equation in *eulerian coordinates* is

$$\frac{\partial}{\partial t}\int_{\mathcal{V}} \rho \boldsymbol{V} d\mathcal{V} + \int_S \rho \boldsymbol{V}\boldsymbol{V_n} dS + \int_S p\,\boldsymbol{n} dS - \int_S \underline{\boldsymbol{\tau_d}} \cdot \boldsymbol{n} dS = \int_{\mathcal{V}} \rho \boldsymbol{g} d\mathcal{V} \tag{1.36}$$

or[12]

$$\int_{\mathcal{V}} \frac{\partial(\rho \boldsymbol{V})}{\partial t} d\mathcal{V} + \int_{\mathcal{V}} \nabla \cdot (\rho \boldsymbol{V}\boldsymbol{V}) d\mathcal{V} + \int_{\mathcal{V}} \nabla p\, d\mathcal{V} - \int_{\mathcal{V}} \nabla \cdot \underline{\boldsymbol{\tau_d}} d\mathcal{V} = \int_{\mathcal{V}} \rho \boldsymbol{g} d\mathcal{V} \tag{1.37}$$

just because the control volume is fixed. Since this latter may be whatever, the local form of eq. (1.37) is

$$\frac{\partial(\rho \boldsymbol{V})}{\partial t} + \nabla \cdot (\rho \boldsymbol{V}\boldsymbol{V}) + \nabla p - \nabla \cdot \underline{\boldsymbol{\tau_d}} = \rho \boldsymbol{g} \tag{1.38}$$

which, in Cartesian tensor form, becomes[13]

$$\frac{\partial(\rho V_i)}{\partial t} + \frac{\partial(\rho V_i V_j)}{\partial x_j} - \frac{\partial(T_{ij})}{\partial x_j} = 0 \tag{1.39}$$

where no body forces are taken into account. Hence, the variation (accumulation or depletion) of momentum within an elementary volume $d\mathcal{V}$, may be accomplished by both convective and diffusive momentum transport. For example, intuitively a momentum accumulation in an ideal fluid (no viscous stresses) may be accomplished by a negative value of the divergence of the convective momentum transport across the boundaries of $d\mathcal{V}$, or by a negative value of the pressure gradient. It is very important to highlight at this stage that, as it is possible to appreciate from the conservation of momentum, the fluid system is intrinsically non-linear. Such circumstance, as it will be clarified later in chapter 7, is the prior cause for the existence of turbulence.

#### 1.2.3.1 Stokes' law

In order to solve the system composed by both the equation of mass and momentum, there is the need to model the deviatoric part of the stress tensor. In fact, even assuming an incompressible flow[14], there are ten unknowns (pressure, six stress components and three components of the velocity) for only four equations; the problem is said to be not closed. As it has already mentioned, the deviatoric part of the Cauchy tensor is generally associated with dissipation related with viscous effect, so that for an inviscid fluid no issues arise. When viscous effects have to be taken into account, there is the need to model $\underline{\boldsymbol{\tau_d}}$ and the most common adopted model is represented by the Newtonian fluid model, for which the relationship existing between shear stresses and velocity

[12] Making use of the divergence theorem.
[13] $f_{s,i} = -pn_i + \tau_{ij}n_j$.
[14] The variations of density are perfectly balanced so that it does not change during the flow.

gradient is linear, the constant of proportionality being the dynamic viscosity. In such sense, the Stokes' law represent the generalization of the Newton fluid model, linking the Cauchy stress tensor to the strain rate in laminar Newtonian fluid flows[1]. In order to write the general expression for the Stokes' law, it is necessary to consider the velocity vector and others two related tensors, namely

$$\boldsymbol{V} = (u, v, w)\ ; \qquad \underline{\boldsymbol{\nabla V}} = \begin{bmatrix} u_x & v_x & w_x \\ u_y & v_y & w_y \\ u_z & v_z & w_z \end{bmatrix}; \qquad \left(\underline{\boldsymbol{\nabla V}}\right)^T = \begin{bmatrix} u_x & u_y & u_z \\ v_x & v_y & v_z \\ w_x & w_y & w_z \end{bmatrix} \tag{1.40}$$

where the subscripts indicate spatial derivation. The first tensor of eq. (1.40) , which is called deformation-rate tensor, may be divided into a symmetric and antisymmetric part according to the tensor algebra[4] identities[15], namely

$$\left(\underline{\boldsymbol{\nabla V}}\right)_{sym} = \begin{bmatrix} u_x & \frac{v_x+u_y}{2} & \frac{w_x+u_z}{2} \\ \frac{u_y+v_x}{2} & v_y & \frac{w_y+v_z}{2} \\ \frac{u_z+w_x}{2} & \frac{v_z+w_y}{2} & w_z \end{bmatrix} \tag{1.41}$$

which represents the strain-rate tensor and

$$\left(\underline{\boldsymbol{\nabla V}}\right)_{antisym} = \begin{bmatrix} 0 & \frac{v_x-u_y}{2} & \frac{w_x-u_z}{2} \\ \frac{u_y-v_x}{2} & 0 & \frac{w_y-v_z}{2} \\ \frac{u_z-w_x}{2} & \frac{v_z-w_y}{2} & 0 \end{bmatrix} \tag{1.42}$$

which represents the rotation-rate tensor. By defining dilatation term $\vartheta$ as the trace[16] of $\left(\underline{\boldsymbol{\nabla V}}\right)_{sym}$ it is possible to express this latter as

$$\left(\underline{\boldsymbol{\nabla V}}\right)_{sym} = \frac{\vartheta}{3}\underline{\boldsymbol{I}} + \left(\underline{\boldsymbol{\nabla V}}\right)^0_{sym} \tag{1.43}$$

where the second term on the right-hand side indicated the version of $\left(\underline{\boldsymbol{\nabla V}}\right)_{sym}$ with zero trace, namely

$$\left(\underline{\boldsymbol{\nabla V}}\right)^0_{sym} = \begin{bmatrix} u_x - \frac{\vartheta}{3} & \frac{v_x+u_y}{2} & \frac{w_x+u_z}{2} \\ \frac{u_y+v_x}{2} & v_y - \frac{\vartheta}{3} & \frac{w_y+v_z}{2} \\ \frac{u_z+w_x}{2} & \frac{v_z+w_y}{2} & w_z - \frac{\vartheta}{3} \end{bmatrix} \tag{1.44}$$

Thus, according to the Stokes' law, the deviatoric part of the stress tensor may be expressed as

$$\underline{\boldsymbol{\tau_d}} = B(\boldsymbol{\nabla} \cdot \mathbf{V})\underline{\boldsymbol{I}} + 2\mu\left(\underline{\boldsymbol{\nabla V}}\right)^0_{sym} \tag{1.45}$$

---

[15] The generic tensor $\underline{\mathbf{A}}$ may be decomposed into symmetric and antisymmetric part thanks to the identity:
$\underline{\mathbf{A}} = \frac{1}{2}\left(\underline{\mathbf{A}} + \underline{\mathbf{A}}^T\right) + \frac{1}{2}\left(\underline{\mathbf{A}} - \underline{\mathbf{A}}^T\right)$

[16] $\vartheta = u_x + v_y + w_z = \nabla \cdot \boldsymbol{V}$ and represents the rate of change of infinitesimal volume expressed in percentage.

where $B$ and $\mu$ stands for the volume and dynamic viscosity respectively. Thus, by substituting the above relation in eq. (1.34) the expression of the Cauchy stress tensor, acting within Newtonian fluids in laminar flow, becomes

$$\underline{\boldsymbol{T}} = -p\underline{\boldsymbol{I}} + B(\boldsymbol{\nabla}\cdot\mathbf{V})\underline{\boldsymbol{I}} + 2\mu\left(\underline{\boldsymbol{\nabla V}}\right)^{0}_{sym} \tag{1.46}$$

which reveals that, for such class of fluids flow, the isotropic part corresponds to the hydrostatic stress tensor and the volume viscosity term. Obviously, according with what has been previously mentioned, when the fluid is at rest the tensor state is uniquely described by a scalar quantity which is the static pressure, as the velocity is uniformly null. Moreover, by the examination of the model expressed by eq. (1.46), it is possible to point out that, in general, the average normal stress equal

$$\pi = -p + B\vartheta \tag{1.47}$$

but it is a common choice to assume for Newtonian laminar fluid flow that the volume viscosity is negligible $(B \approx 0)$[17], so that the pressure is effectively defined as the average of the normal stresses. Anyway, for incompressible flows[18], the expression for the stress tensor in the fluid reduces to

$$\underline{\boldsymbol{T}} = -p\underline{\boldsymbol{I}} + 2\mu\left(\underline{\boldsymbol{\nabla V}}\right)_{sym} \tag{1.48}$$

or, in Cartesian tensor notation

$$T_{ij} = -p\delta_{ij} + \mu\left(\frac{\partial V_i}{\partial x_j} + \frac{\partial V_j}{\partial x_i}\right) \tag{1.49}$$

As an example, considering the very low viscosity of water, the Newtonian fluid model explains why it is so easy to slip on a water-wetted surface; due to the low value of the dynamic viscosity ($1.002 \times 10^{-3} kg/ms$ at $20°C$), it is almost incapable to resist to shear stresses when a step is made on it. This also explains why it is even more easy to slip on oil which has a lower dynamic viscosity.

Anyway, with this fluid model the problem has been closed as the deviatoric part of the Cauchy tensor is related to pressure and velocity field. When the flow is instead assumed to be turbulent, an additional turbulence model is necessary for the problem closure. Such aspect will be investigated in chapter 7.

[17] Such assumption implies that when dealing with fluids, the isotropic (or homogeneous) variation of volume does not influence the stress tensor. This is intuitively not true for elastic medium.

[18] Such definition has to not be confused with incompressible material for which the density does not vary. In fact, incompressible flow means that there are no variations of density which, thanks to the conservation of mass, implies that $\frac{\partial \rho}{\partial t} + \boldsymbol{V}\,\nabla\cdot\rho = 0$. Hence the density is not supposed to be unconditionally constant, but its variations are balanced so that it does not change.

## Bibliography


[1] G. M. Carlomagno, “Elementi di gasdinamica”, ISBN: 9788820746636.

[2] J. L. Lumley, “Eulerian and Lagrangian Descriptions in Fluid Mechanics”, reference materials for the National Committee for Fluid Mechanics Films movie series, available at http://web.mit.edu/hml/notes.html.

[3] M. Abom, “An Introduction to Flow Acoustics”, Publisher: KTH-The Royal Institute of Technology, ISBN: ISRN/KTH/AVE/N-06/04-SE.

[4] T. Astarita, “Tensor Calculus”, reference material for the course of the PhD course in Industrial Engineering (cycle XXIX), University of Naples Federico II.

# Chapter 2

# The Concept of Sound and its Propagation

**Introduction**

Noise is commonly defined as unwanted sound which is judged to be unpleasant, loud or disturbing to hearing. However, from a physic viewpoint, noise is indistinguishable from sound, as both are vibrations through a medium, such as air or water. The difference arises when the brain receives and perceives a particular sound as something pleasant or not. In the following, it will be first given an insight about some basic definition and aspects related to sound and then the basic concept related to the propagation of sound will be briefly recalled.

## 2.1 The Sound

Acoustic is defined as the branch of science which studies the sound propagation through a medium, thanks to its elastic and inertial properties. From this definition it follows that, in order to propagate, sound needs a medium and therefore a first important information is that in vacuum sound cannot propagate. Sound is generally identified as something that the human ears can detect and something we have good sensations with. Vice versa, noise is a type of sound which causes bad sensations. From an engineering point of view, sound is a little pressure disturbance around the static pressure, this latter being generally recognized as the ambient pressure ($101300\ Pa$) for most applications. As an example, when something like a thin bar is vibrating (for simplicity at one frequency), the air particles adjacent to the surface start to oscillate around their equilibrium position, as it is schematically depicted in Figure 2.1, making a pressure disturbance to propagate through the surrounding air.

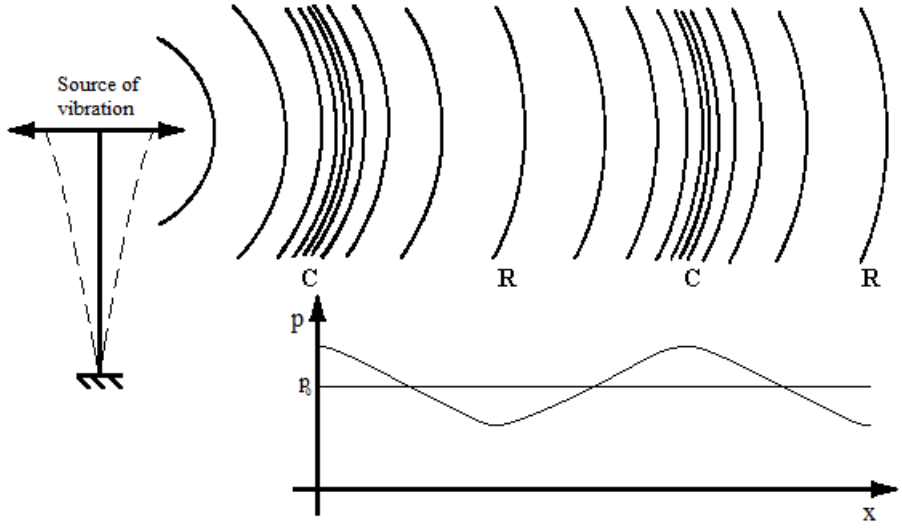


Figure 2.1 – Schematization of sound production and propagation in air due to a vibrating string, where C stands for compression and R for rarefaction.

Clearly, referring to the above figure, it is intuitively to state that the pressure variation is a function of both space and time. As it will be derived in the following, such propagation allows acoustic waves to travel at the so-called speed of sound (or phase speed), whose relation with the characteristics of the wave is

$$c = \lambda f \tag{2.1}$$

where $\lambda$ is the wavelength and $f$ is the frequency of the sound wave. Thus, it is the oscillating part of the pressure which causes human ears to detect sound and, in general, it is very little. In fact, it is worth noting that the amplitudes of such little pressure disturbance, which can be detected by human ears, belong to the range $[20\ \mu Pa; 100\ kPa]$, which means that below $20\ \mu Pa$ no sound can be heard (threshold of audible) and above $100\ kPa$ very painful sensations start to appear (threshold of pain).

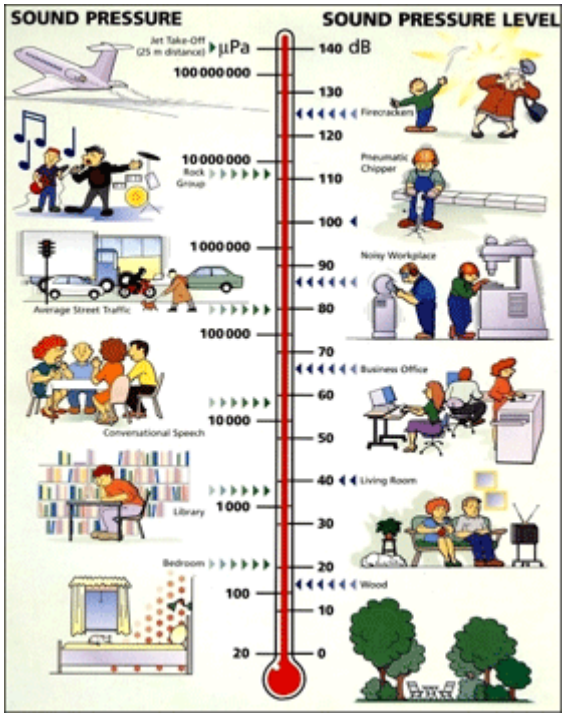


Figure 2.2 – Audible pressure disturbances.

However, it is not only the amplitude of the particle displacement around their static position which influence human perception of sound, but also the frequency. In particular, it is widespread assumed that an average healthy, young adult can hear pressure disturbance within the frequency range $[20\ Hz; 20\ kHz]$, which is generally referred as the range of audio frequencies[12]. Above the upper threshold limit there is the region of ultrasounds, whilst below the audible lower limit there is the infrasound region. Anyway, it should be clear that, because sound is related with vibration processes, no mass transport but only energy transport is related to sound propagation in a medium.

It is important to know that there are three main acoustic quantities that characterize the study a sound source and the corresponding sound field. These three quantities are the sound pressure, the sound power and the sound intensity. The sound pressure is defined as the root mean square of the variable part of the pressure at a point within a sound field, namely

$$p_s = \sqrt{\frac{1}{T}\int_0^T p_v(t)^2 dt} \qquad [Pa] \tag{2.2}$$

where $T$ represent the oscillation period. This parameter characterizes a sound field, but gives no information about the source strength. In fact, as it will be clarified more ahead, the sound pressure is only a parameter which characterize the effect of some acoustic production phenomenon in a certain ambient, but it is not something which may related to the cause of that phenomenon. In other words, considering two different acoustic domains, any particular sound source would produce two different sound fields, depending on the ambient in which it radiates. Consequently, in order to characterize a sound source, the sound power is needed, which is defined as the amount of sound energy radiated per unit of time. The sound power can be calculated by the knowledge of the sound intensity, which is defined as the flux of sound energy and may be expressed as follows

$$\overline{I_s} = p_s \bar{v} \qquad [N/m^2 s] \tag{2.3}$$

where $\bar{v}$ is the vector of the particle velocity. Since the sound intensity is representative of a vector field, it allows to perform source identification and, thanks to the Gauss theorem, to calculate the sound power of the source as

$$W_s = \iint I_s \, dS \qquad [W] \tag{2.4}$$

However, since acoustic quantities can assume values in a very wide range, as it is reported in Figure 2.2, they are commonly expressed in terms of non-dimensional quantities in the widely used Decibel scale. Therefore, instead of sound pressure, sound power and sound intensity it is generally preferred to deal with the corresponding Decibel levels defined as follows:

$$L_p = 20Log\left(\frac{p_s}{p_0}\right) \qquad [dB] \tag{2.5}$$

$$L_W = 10Log\left(\frac{W_s}{W_0}\right) \qquad [dB] \tag{2.6}$$

$$L_I = 10Log\left(\frac{I_s}{I_0}\right) \qquad [dB] \tag{2.7}$$

where $p_0 = 20\mu Pa$, $W_0 = 10^{-12} W$ and $I_0 = 10^{-12}\, W/m^2$. This three logarithmic quantities, are always used to characterized a sound source and the effect on a certain sound field.

### 2.1.1 Frequency domain study of sound

From what has been presented in the previous section, it is clear that sound is always related to oscillatory phenomena. Always, when treating such phenomena, instead of looking only at the time domain representation, it is interesting and necessary to investigate what happens in the frequency domain. As an example of such evidence, it is possible to refer to the study of the structural vibrations, in which resonant phenomena has to be extremely avoided. Besides, once again, only sound in the frequency range $[20\,Hz; 20\,kHz]$ can be detected by human ears. Moreover, the perception of sound (meaning the sensation related to a sound) is no constant with the frequency. In fact, human ears are more sensitive to high frequency sounds with respect to the low frequency sounds. This can been highlighted by looking at the so-called isophonic curves, also known as

equal-loudness[19] contour. Those curves represent a measure of sound pressure level, over the frequency spectrum, for which a listener perceives a constant loudness when exposed to a pure steady tones. In other words, they represent the way in which the sound pressure level must change with frequency, in order to make human ears to hear the same sensation of a pure tone at $1\ kHz$. Practically, these curves have been created by acquiring data on a statistical sample of normal hearing people. People were exposed, in an anechoic room (which simulate the free field sound field condition, which means with no sound reflections as it will be explained more ahead), to a pure tone at $1\ kHz$ with different amplitude in dB. At each starting amplitude at $1\ kHz$, they were asked to change the sound pressure level, as the frequency of the sound changed, in order to perceive the same acoustic sensation. The results of such experiments are depicted in Figure 2.3. Historically, this kind of research, on the topic of how the ear hears different frequencies at different levels, was firstly conducted by Fletcher and Munson in 1933[1]. In fact, equal-loudness contours are often referred to as "Fletcher-Munson" curves, but those studies have been superseded and incorporated into newer standards. The definitive curves are those defined in the international standard ISO 226:2003, which are based on a review of modern determinations made in various countries[2].

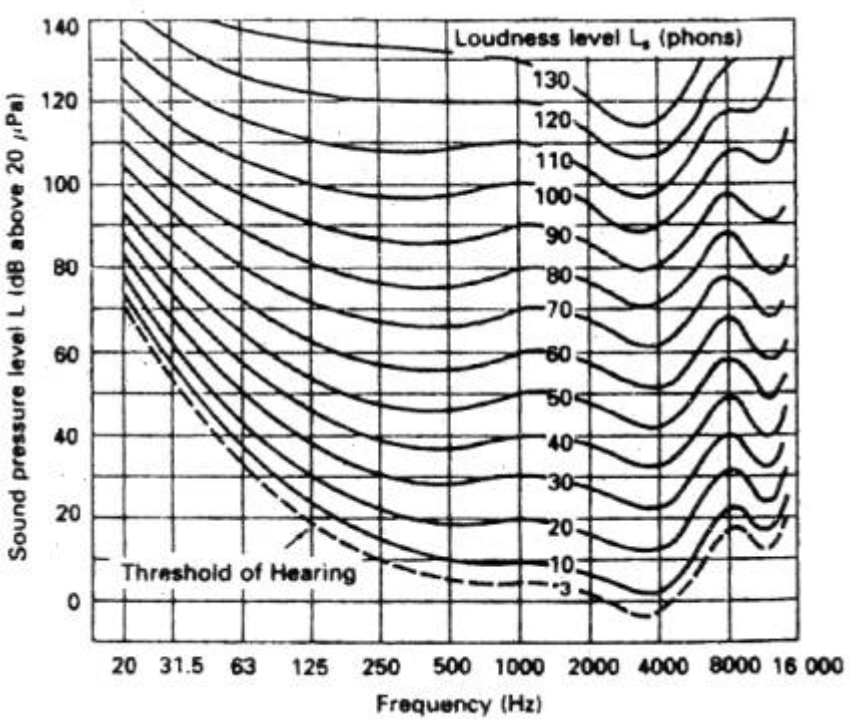


Figure 2.3 – Isophonic curves.

The acoustic sensation is measured in the so-called $phon$ unit and each values is represented by the values of the curve at $1\ kHz$. So, for example, the sensation of $50\ phon$ may be experienced by changing the sound pressure level according to the curve which reach $50\ dB$ a $1\ kHz$. By the examination of Figure 2.3, it is possible to point out that, in order to experience the same acoustic sensation, human ears need to increase “the volume” at low frequency and to decrease (or adjust)

[19] The Loudness represents an attribute of auditory sensation in terms of which sounds can be ordered on a scale extending from quiet to loud.

"the volume" at high frequency. Hence, at this point, the reader should be able to understand that, when dealing with whatever sound signal, in order to simulate the actual way in which that sound is perceived by human ears, it is necessary to "weight" (or to filter) it in the frequency domain. This is made thanks to the weighting curves, which are depicted in Figure 2.4, that are generally applied to instrument-measured sound pressure levels, in order to account for the relative loudness perceived by the human ear, as the ear itself is less sensitive to low audio frequencies.

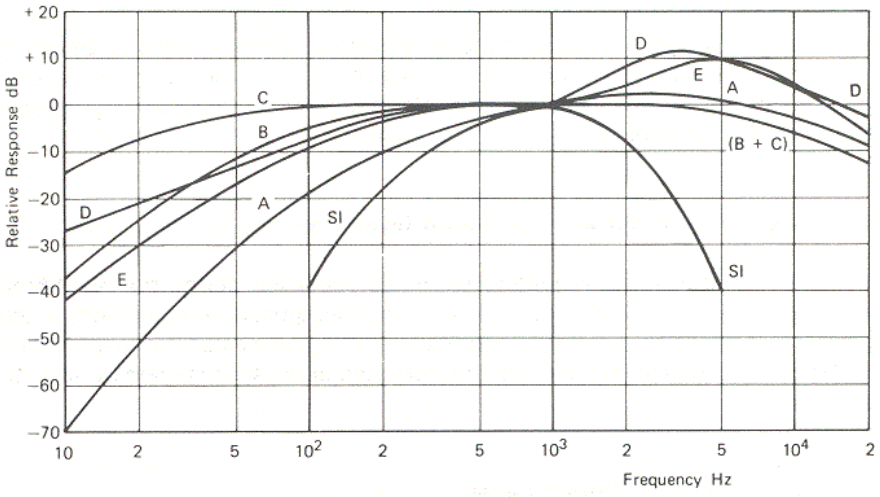


Figure 2.4 – Weighting curves for reproducing the response of human ears.

In other words, these curves describe how the sound pressure level of a sound signal must be filtered in order to reproduce how it is detected by human ears, and are defined in the International standard IEC 61672:2003 relating to the measurement of sound pressure level[3]. The most used weighting curve is the curve A, corresponding to the isophonic curve of 40 $phon$.

Generally speaking, the frequency domain study of signals is accomplished by means of the Fourier analysis, thanks to which every time-domain signals can be decomposed in a certain number of sinusoidal signals having different amplitude, phase and frequency.

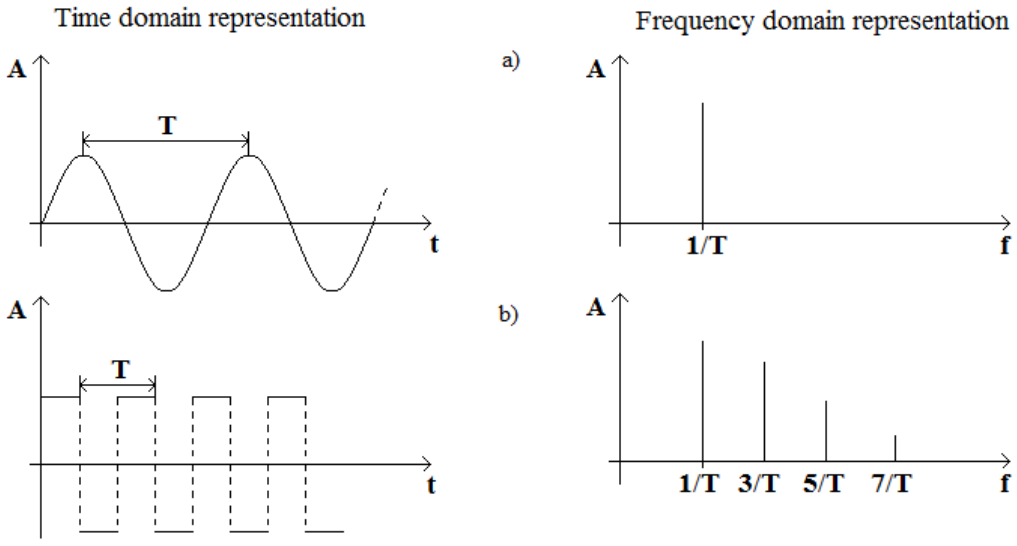


Figure 2.5 – Time vs Frequency representation of signals: a) sine wave; b) square wave.

However, many random signals, as sound may be, are composed of many frequencies, which are not harmonically related to one another, their spectrum being quite complicated to understand. Therefore, often sound representation in the frequency domain is done referring to a narrow band (or constant bandwidth), 1/8 band (octave) or 1/3 octave band (third octave), in order to make the spectrum more easily understood. The main characteristic of octave bands is that each central band is equal to half of the subsequent one. Instead, the third octave bands have a bandwidth percentage constant and equal to $23\%$ of the nominal central frequency. In table 2, all the above mentioned bands and the corresponding central band are listed.

| Nominal Central frequency Hz | Third-Octave Band Hz | Octave Band Hz | Nominal Central frequency Hz | Third-Octave Band Hz | Octave Band Hz | Nominal Central frequency Hz | Third-Octave Band Hz | Octave Band Hz |
|---|---|---|---|---|---|---|---|---|
| 1,25 | 1,12 – 1,41 | | 40 | 35,5 – 44,7 | | 1250 | 1120 - 1410 | |
| 1,6 | 1,41 – 1,78 | | 53 | 44,7 – 56,2 | | 1600 | 1410 – 1780 | |
| 2 | 1,78 – 2,24 | 1,41 – 2,82 | 63 | 56,2 – 70,8 | 44,7 – 89,1 | 2000 | 1780 – 2240 | 1410 - 2820 |
| 2,5 | 2,24 – 2,82 | | 80 | 70,8 – 89,1 | | 2500 | 2240 – 2820 | |
| 3,15 | 2,82 – 3,55 | | 100 | 89,1 – 112 | | 3150 | 2820 – 3550 | |
| 4 | 3,55 – 4,47 | 2,82 – 5,62 | 125 | 112 – 141 | 89,1 - 178 | 4000 | 3550 – 4470 | 2820 - 5620 |
| 5 | 4,47 – 5,62 | | 160 | 141 – 178 | | 5000 | 4470 – 5620 | |
| 6,3 | 5,62 – 7,08 | | 200 | 178 – 224 | | 6300 | 5620 – 7080 | |
| 8 | 7,08 – 8,91 | 5,62 – 11,2 | 250 | 224 – 282 | 178 - 355 | 8000 | 7080 – 8910 | 5620 - 11200 |
| 10 | 8,91 – 11,2 | | 315 | 282 – 355 | | 10k | 8910 – 11200 | |
| 12,5 | 11,2 – 14,1 | | 400 | 355 – 447 | | 12,5k | 11,2k – 14,1k | |
| 16 | 14,1 – 17,8 | 11,2 – 22,4 | 500 | 447 – 562 | 355 - 708 | 16k | 14,1k – 17,8k | 11,2k – 22,4k |
| 20 | 17,8 – 22,4 | | 630 | 562 – 708 | | 20k | 17,8k – 22,4k | |
| 25 | 22,4 – 28,2 | | 800 | 708 – 891 | | | | |
| 31,5 | 28,2 – 35,5 | 22,4 – 44,7 | 1000 | 891 - 1120 | 708 - 1410 | | | |

Table 2 – Third octave and octave bands.

Moreover, it is important to mention that there is typical noise, widely used in experimental activities, with a particular spectral content, which is called white noise as, in analogy with white light, it has a constant frequency spectrum when expressed as a linear function of frequency (e.g., in $Hz$). In other words, a white noise is a random noise whose spectrum is flat on a narrow band frequency scale and with a slope of $+3\ dB/octave$ on a logarithmic scale. In fact, since the width of an octave band is twice as large as the previous octave band, the level is increased by $6\ dB$ in each band.

In general, since a noise signal is characterized by a certain number of spectral characteristics whose amplitudes may significantly differ from one another, it is quite difficult to establish the strongness of signals with different spectra. So, there is the practical need to quantify the amount of noise related to a sound signal by means of a uniquely determined number. In such sense, several indicators exist which aim to quantify the amount of a noise, based on the magnitude of its spectral components. Among them, the Overall Sound Pressure Level (OSPL) is widely used to provide one unique value based on the whole frequency content of the considered signal. In order to understand how it is calculated, it is necessary to make some considerations about the energy of a signal which, in general, may be considered as representative of its magnitude. Considering continuous signals, by analogy with the electrical signals, if $x(t)$ is a voltage across a resistance of $1\ \Omega$, then the

instantaneous power dissipated by the resistor would be equal to the square of the signal amplitude, while the associated energy within a time interval would be equal to

$$E = \int_{-\infty}^{+\infty} x^2(t)dt \tag{2.8}$$

In the frequency domain the energy of a signal is expressed as function of the Fourier transform thanks to the well-known Parseval's theorem[7], namely

$$E = \int_{-\infty}^{+\infty} x^2(t)dt = \int_{-\infty}^{+\infty} |X(f)|^2 df \tag{2.9}$$

where, the square of the modulus of the Fourier transform is called energy spectral density (energy per unit of frequency bandwidth) of the signal, and represents a decomposition of the energy of the observed process as function of frequency. However, since real signals are not continuous function but discrete time series, the energy associated is not an integral anymore by a summation of the squared amplitudes. It follows that the energy associated with a discrete signal of $N$ samples, in both time and frequency domain, may be expressed as

$$E = \sum_n x^2(n\Delta t) = \frac{1}{N^2} \sum_n |X(n\Delta f)|^2 \tag{2.10}$$

where the scaling value $N^{-1}$ is due to both truncation (the discrete signal has finite length) and sampling processes[7]. Thus the energy associated with a discrete sound signal is represented by the summation over the squared amplitudes of its spectral components. It follows that, the energy of the signal represents the parameter for the overall sound pressure level calculation, namely

$$OSPL = 20Log\left(\frac{\sqrt{E}}{p_0}\right) \tag{2.11}$$

Such parameter is widespread used for comparing the intensity of different noises.

## 2.2 Sound propagation

Sound is generated thanks to various source mechanisms, the most popular of which is by means of mechanical vibrations of solid objects. Even in the simplest cases, the complete understanding of the way in which sound is generated is generally very complex. As an example, it is worth noting that if the acoustic medium is not at rest, the flow field may affect in different ways both sound generation and propagation[5][13]. Therefore, it is a common choice to study the propagation of sound separately from its generation; this is the case of the following paragraph in which no reference to source mechanism will be done. As already mentioned, sound propagates through a medium by means of waves. In fact, the corresponding governing equation of such physical phenomenon is a wave equation, which can be derived starting from two of the fundamental equations of mechanic which are the conservation of mass and momentum. In the next paragraphs, various aspect related to the propagation of sound will be discussed and the medium which allows sound to propagate will be assumed to be fluid, the reference coordinate system being, otherwise specified, rectangular.

### 2.2.1 1-D homogeneous classical wave equation

The classical wave equation is valid in an ideal (no losses) homogenous quiescent fluid, where the average quantities such as pressure $p_0$, the density $\rho_0$ etc. are supposed to be constant and the velocity field is equal to zero everywhere[4]. In such hypothesis, and considering an ideal gas as acoustic medium (like air), the thermodynamic transformation which governs the sound propagation is the adiabatic[20] isentropic expressed by the following state equation[21]

$$\frac{p}{\rho^k} = cost. \tag{2.12}$$

in which $k$ represents the specific heats ratio for the considered gas. If this transformation is depicted on the thermodynamic plane $(p, \rho)$, the results, within the ideal gas zone, is obviously a parabola, as it is shown in Figure 2.6.

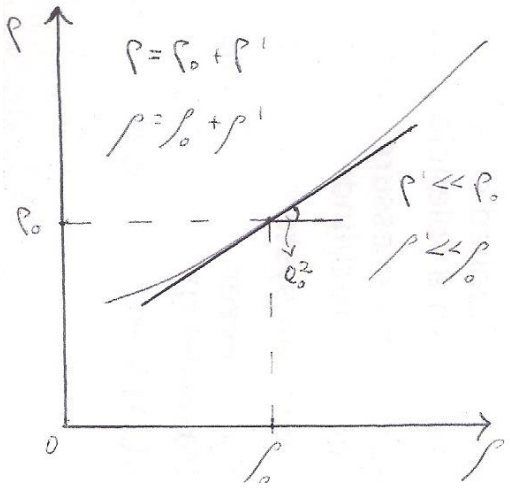

Figure 2.6 – Representation of the adiabatic isoentropic transformation on the thermodynamic plane $(p, \rho)$.

For most of the applications $p_0$ is at least equal to 1 bar (which is equal to $101300\ Pa$) and, as mentioned in the previous sections, the pressure fluctuations reach the maximum value at $100\ kP$a and the minimum at $20\mu$Pa. This means that, from a practical point of view, acoustic may be studied as a linear theory, namely linearizing the transformation in figure above. Therefore, the slope of the linearized transformation is equal to

$$\left.\frac{dp}{d\rho}\right)_{s=cost} = \frac{p-p_0}{\rho-\rho_0} = \frac{B}{\rho} \tag{2.13}$$

where $B$ is defined as the bulk modulus, which represents a measure of the resistance of the medium to an uniform compression. The left hand side of eq. (2.13) is defined as the square adiabatic speed of sound $({a_0}^2)$. This quantity, which is also called phase speed[14], may be derived directly from eq. (2.12), namely

$$d\left(\frac{p}{\rho^k}\right) = dp\rho^{-k} + p(-k\rho^{-k-1}d\rho) = 0$$

[20] If the transformation is not adiabatic the pressure fluctuations must account also for heat releases, i.e. $p' \neq \rho' a_0^2$

[21] This may be derived directly from the Gibbs equation $Tds = du + pdv$.

or

$$a_0 = \sqrt{\frac{dp}{d\rho}} = \sqrt{k\frac{p}{\rho}} = \sqrt{kRT} \tag{2.14}$$

where $R$ is the constant of the gas. So, for an ideal gas, the speed of sound only depends on the temperature of the gas. For example, at $273\,K$ the speed of sound in air is equal to $\sqrt{1{,}4 \cdot 287 \cdot 273} = 331\,m/s$.

Before proceeding with the study of sound propagation, it is necessary to highlight that differences exist, of course, between one-dimensional and three-dimensional propagation conditions. Hence, since there are common practical conditions for which one-dimensional propagation holds, it is better to firstly focus on such simpler theory. In order to obtain the 1D homogeneous classical wave equation, it is assumed that small disturbances perturb, in one direction, the fluid particles around their equilibrium state, and therefore pressure, density and particle velocity can be expressed as

$$p(x,t) = p_0 + p'(x,t) \tag{2.15}$$

$$\rho(x,t) = \rho_0 + \rho'(x,t) \tag{2.16}$$

$$u(x,t) = u'(x,t) \tag{2.17}$$

being $u$ the particle velocity component in the $x$ direction, where the subscript $_0$ indicates the average quantities. At the same time, the homogeneous conservation of mass and momentum can be rewritten in the simplified one dimensional form as

$$\frac{d\rho}{dt} + \frac{\partial}{\partial x}(\rho u) = 0 \tag{2.18}$$

$$\frac{d(\rho u)}{dt} + \frac{\partial}{\partial x}(\rho u u) + \frac{\partial p}{\partial x} = 0 \tag{2.19}$$

Thus, by substituting expressions (2.15), (2.16) and (2.17) within the two balance equations, keeping only linear terms (namely, neglecting all products of primed quantities)[22], yields the following equations

$$\begin{cases} \dfrac{d\rho'}{dt} + \dfrac{\partial}{\partial x}(\rho_0 u') = 0 & (2.20) \\ \dfrac{d(\rho_0 u')}{dt} + \dfrac{\partial p'}{\partial x} = 0 & (2.21) \end{cases}$$

Thus, substituting the expression for the density by using equation (2.13) and (2.14), and then performing[23] $\frac{d(2.16)}{dt} - \frac{\partial(2.17)}{\partial x}$, yields to the classical wave equation

$$\left[\frac{1}{a_0^2}\frac{d^2}{dt^2} - \frac{\partial^2}{\partial x^2}\right] p' = 0 \tag{2.22}$$

[22] Basically, acoustic is a linear theory because the fluctuations of any quantities represent very small variations around the mean value. In such hypothesis, the product of primed quantities (fluctuations) is negligible.

[23] Of course in 3-D it becomes $\frac{\partial(2.16)}{\partial t} - \nabla \cdot (2.17)$.

which, of course, is linear ($p'$ is power of one). Obviously, also the density satisfied the classical wave equation. However if equation (2.21) is first integrated along the spatial coordinate $x$ and then in time, it is possible to point out that

$$\rho_0 \frac{d}{dt}\left(\int_{x_0}^{x} u' dx\right) = p'(x_0, t) - p'(x, t)$$

or

$$\int_{x_0}^{x} u' dx = \varphi(x, t) - \varphi(x_0, t)$$

or

$$u' = \frac{d\varphi(x,t)}{dx} \tag{2.23}$$

which simply implies that a velocity potential exists, namely the spatial integral of the particle velocity depends only on the final and initial position. Of course the link between the pressure fluctuation and this velocity potential is expressed by equation (2.24)

$$-p' = \rho_0 \frac{d\varphi(x,t)}{dt} \tag{2.24}$$

From equation (2.24) it results that, beside pressure of density fluctuations, the dependent variable of the classical wave equation could be $u'$ or $\varphi$ as well. In general, within many numerical commercial codes which are used in acoustic, the velocity potential based version is used, namely the equation to be solved is of the form

$$\left[\frac{1}{a_0^2}\frac{d^2}{dt^2} - \frac{\partial^2}{\partial x^2}\right]\varphi = 0 \tag{2.25}$$

Such choice may be justified by the fact that, once the equation is solved for the velocity potential, it is very easy to obtain both particle velocity and acoustic pressure thanks to eq. (2.23) and (2.24).

#### 2.2.1.1 Solution of the 1-D homogeneous classical wave equation

The first thing to note about the solution of the wave equation (2.22) is that, since the theory (and so the governing equation) is linear, the superposition principle is applicable[4]. This implies that if $p_1'$ and $p_2'$ are solutions of the classical wave equation, $\alpha p_1' + \beta p_2'$, with $\alpha$ and $\beta$ constant, is also a solution. The 1-D homogeneous classical wave equation is a simplified version of the general 3D case, and its solution is the simplest one and is called plane wave solution. This latter, which was first discovered by D'Alambert[8], is represented by a sound field which, in every point, is the sum of two wave, as it is shown by the following equation (2.26)[9].

$$p'(x, t) = p'_+(t - x/a_0) + p'_-(t + x/a_0) \tag{2.26}$$

These two progressive waves propagate, with speed equal to $a_0$ and without change of shape, in the positive and negative direction. The amplitudes of the two waves have to be determined from the initial conditions and from the boundary conditions (e.g. when there are no boundaries, i.e. *free field* propagation, only forward moving wave may exist). A very simple and intuitive proof of this

combined solution can be found if it is realized that the main character of the classical wave equation is represented by the differential operator[5]

$$Ł \equiv \frac{d^2}{dt^2} - a_0^2 \frac{\partial^2}{\partial x^2} \equiv \left(\frac{d}{dt} + a_0^2 \frac{\partial}{\partial x}\right)\left(\frac{d}{dt} - a_0^2 \frac{\partial}{\partial x}\right) \tag{2.27}$$

Consequently, it is very intuitive to recognize that the forward moving wave is the solution of the first term of the wave operator, whilst the back moving wave represents the solution of its second term.

Very often, practically always, in acoustic it is assumed that the pressure disturbances are harmonic time dependent and so the sound field is given, thanks to the Fourier analysis, on a form like below

$$p'(x,t) = \Re\left(\hat{p}e^{i\omega t}\right) \tag{2.28}$$

where $\Re$ means that the real part must be considered an $\hat{p}$ is the complex valued amplitude of the wave at the angular frequency $\omega = 2\pi f$. Now if this harmonic time dependent pressure fluctuation is inserted within the classical wave equation, it yields to the one-dimensional version of the so-called Helmholtz equation, namely

$$\underbrace{\frac{d^2p'}{dt^2} = -\omega^2\hat{p}e^{i\omega t} \qquad \frac{\partial^2 p'}{\partial x^2} = \frac{\partial^2 \hat{p}}{\partial x^2}e^{i\omega t}}$$

$$\frac{d^2\hat{p}}{dx^2} + k_0^2\hat{p} = 0 \tag{2.29}$$

in which $k_0 = \frac{\omega}{a_0}$ is the so-called wave number (or propagation constant), representing the spatial frequency and, as such, it indicates how many times the waveform is repeated in one meter. Thus, the Helmholtz equation is the wave equation in the frequency domain and its solutions represents therefore monochromatic waves, or waves of some given frequency $\omega$. It is worth noting that, nowadays, methods for Fast Fourier Transform are widely available, and so conversion from time to frequency domain and vice versa are computationally very efficient. Therefore, according to many commercial codes[11], the problem of searching a solution for the wave equation is often reduced to the problem of finding the solution of the Helmholtz equation, which is an equation of lower dimensionality (3 instead of 4) than the wave equation itself. Thus, generally the Helmholtz equation is solved first, and then, thanks to the Inverse Fourier Transform, the solution to the wave equation may be obtained (if necessary).

Anyway, in analogy to eq. (2.26), the solution of the wave equation in terms of forward and backward moving waves may be rewritten as[24]

$$p'(x,t) = \widehat{p_+}e^{j\omega(t-x/a_0)} + \widehat{p_-}e^{j\omega(t+x/a_0)} = \left(\widehat{p_+}e^{-jk_0x} + \widehat{p_-}e^{jk_0x}\right)e^{j\omega t} \tag{2.30}$$

where both $\widehat{p_+}$ and $\widehat{p_-}$ are called standing wave components of $p'$ and represent the amplitudes of the waves frequency per frequency. At the same manner, since the particle velocity also satisfies the classical wave equation, it is possible to express the velocity components as

[24] $\Re$ has been omitted for clarity of the notation.

$$u'(x,t) = \left(\widehat{u_+}e^{-jk_0x} + \widehat{u_-}e^{jk_0x}\right)e^{j\omega t} \tag{2.31}$$

In order to obtain a more interesting representation for the values of the two complex valued particle velocity components, corresponding to the forward moving and back moving waves, it is necessary to substituting equations (2.30) and (2.31) within the momentum balance (2.21). In this way it is possible to write

$$j\omega\left(\widehat{u_+}e^{-jk_0x} + \widehat{u_-}e^{jk_0x}\right) = -\frac{1}{\rho_0}\left(-jk_0\widehat{p_+}e^{-jk_0x} + jk_0\widehat{p_-}e^{jk_0x}\right)$$

or

$$\left(\widehat{u_+}e^{-jk_0x} + \widehat{u_-}e^{jk_0x}\right) = \frac{1}{\rho_0 a_0}\left(\widehat{p_+}e^{-jk_0x} - \widehat{p_-}e^{jk_0x}\right)$$

Therefore, the values of the complex amplitudes are found to be equal to

$$\widehat{u_+} = \frac{\widehat{p_+}}{\rho_0 a_0} \quad , \quad \widehat{u_-} = -\frac{\widehat{p_-}}{\rho_0 a_0}$$

Therefore the particle velocity components are linked to the acoustic pressure components via the parameter $\rho_0 a_0$. More precisely, substituting these values in eq. (2.31) yields to the desired analytic expression of the particle velocity, namely

$$u'(x,t) = \frac{1}{Z_0}\left(\widehat{p_+}e^{-jk_0x} - \widehat{p_-}e^{jk_0x}\right)e^{j\omega t} \tag{2.32}$$

where $Z_0$ is defined as characteristic impedance of the medium and represents the ratio of the acoustic pressure and particle velocity of a plane progressive wave (e.g. $\widehat{p_+}/\widehat{u_+}$ which coincides with $\hat{p}/\hat{u}$ in *free field*). Since acoustic is a linear theory, the characteristic impedance of the medium at a certain field point is independent from the source creating the sound field. The concept of acoustic impedance is very important in acoustic but, nevertheless, it founds some difficulties in being correctly understood. Substantially, as it name suggests[25], it represents the acoustic resistance that a component holds to the sound transmission. In fact, it is possible to state that the acoustic pressure is responsible for the sound excitation whilst the particle velocity is responsible for the sound transmission (considering an elettro-acoustic analogy it is possible to state that the acoustic pressure corresponds to the electric voltage, whilst the particle velocity corresponds to the current). For example, the acoustic impedance is always defined as the ratio between acoustic pressure and particle velocity

$$Z = \frac{p'}{u'}$$

Therefore when Z→0 this means that no resistance is imposed to the sound transmission (as it happens for acoustic resonators) and the particle velocity is "infinitely" high, whilst when Z→∞ the particle velocity goes to zero and no sound transmission is allowed (has it happens for some material which have very high surface impedance).

[25] Impedance means something impeding the flow of energy and, in fact, may be electrical, mechanical or acoustical.

Anyway, by the examination of equation (2.32), it is possible to figure out that, if plane wave propagation holds, the magnitude of particle velocity corresponding to the two plane waves is equal to the acoustic pressure divided by the characteristic impedance of the medium. However, since the velocity is always a vector characterized by amplitude and direction, the pressure components of the two waves are considered with opposite signs. Such circumstance could be more easily understood by looking at Figure 2.7.

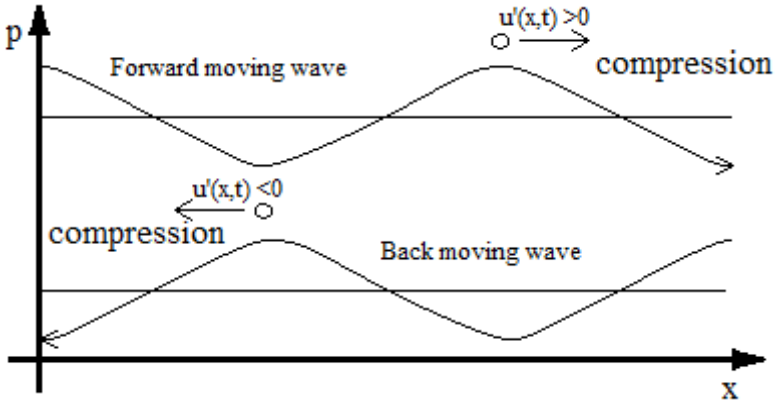


Figure 2.7 – Representation of the forward moving and back moving wave.

In fact, once the coordinate system has been fixed, considering the forward moving wave, a movement towards the positive direction implies a compression of the medium particles, whilst, considering the back moving wave, a movement towards the positive direction implies a rarefaction.

Another important thing to note is that, for the special case of sound propagation in ducts, it is possible to define both a volume velocity and mass velocity, thanks to eq. (2.33) and (2.34) respectively, and the corresponding characteristic impedances, namely

$$V = Su \quad \xrightarrow{yields} \quad Z_0 = \frac{\rho_0 a_0}{S} \tag{2.33}$$

$$v = \rho_0 S u \quad \xrightarrow{yields} \quad Z_0 = \frac{a_0}{S} = Y_0 \tag{2.34}$$

In both cases, because of the fact that the impedance involves the cross section of the duct (indicated by $S$) it takes the name of characteristic impedance of the tube[5]. However, generally speaking, when treating hot exhaust gas systems, it is more correct to refer to the acoustic mass velocity because it involves the density, and so

$$v'(x,t) = \frac{1}{Y_0}\left(\widehat{p_+}e^{-jk_0x} - \widehat{p_-}e^{jk_0x}\right)e^{j\omega t} \tag{2.35}$$

Clearly, in analogy to what has been mentioned above, considering a generic duct element, the two amplitudes $\widehat{p_+}$ and $\widehat{p_-}$ have to be determined thanks to the boundary conditions imposed by the elements which precede and follows the duct element under investigation.

### 2.2.2 Homogeneous classical wave equation and solution

One-dimensional sound propagation theory represents only a particular case of a more general situation in which the acoustic perturbations propagate differently in all directions. Consequently, in order to highlight the limitations of the plane wave theory, it is necessary to have a look at the general theory of the three-dimensional propagation in ducts[5]. For this purpose, let's consider for example the rectangular duct depicted in Figure 8.

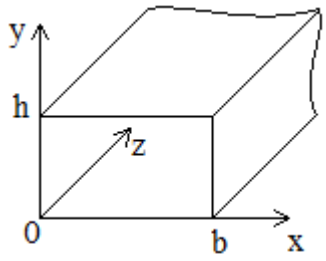


Figure 2.8 – Infinite rectangular duct representation.

Making use of the same hypothesis and following a similar derivation process, the homogenous wave equations in both domain (time and frequency) are obtained as well, namely

$$\left[\frac{1}{a_0^2}\frac{\partial^2}{\partial t^2} - \nabla^2\right]p' = 0 \tag{2.36}$$

$$\nabla^2\hat{p} + k^2\hat{p} = 0 \tag{2.37}$$

By means of the method of separation of the variable[10], the solution of eq. (2.36), which represents the acoustic pressure at any point within the domain and at any time instant, may be expressed as follows

$$p'(x,y,z,t) = \left(C_1 e^{-jk_z z} + C_2 e^{jk_z z}\right)\left(e^{-jk_x x} + C_3 e^{jk_x x}\right)\left(e^{-jk_y y} + C_4 e^{jk_y y}\right)e^{j\omega t} \tag{2.38}$$

$$k_0^2 = k_x^2 + k_y^2 + k_z^2 \tag{2.39}$$

where eq. (2.39) represents a compatibility propagation condition. As before, the values of the complex valued wave amplitudes must be determined thanks to the boundary conditions. Considering duct with infinitely rigid walls, the particle velocity has to be equal to zero at the wall and so, thanks to the momentum balance equation, the boundary conditions to be applied are:

$$\begin{cases} \dfrac{\partial p'}{\partial x} = 0 & x = 0, b \\ \dfrac{\partial p'}{\partial y} = 0 & y = 0, h \end{cases}$$

From the first two BCs, it follows that

$$C_3 = 1$$

and

$$-e^{-jk_x b} + e^{jk_x b} = 0$$

or

$$2sin(k_x b) = 0 \quad \xrightarrow{yields} \quad k_x = \frac{m\pi}{b} \qquad m = 0,1,2 \ldots$$

Similarly, from the BCs in the y direction

$$C_4 = 1$$

$$k_y = \frac{n\pi}{h} \qquad n = 0,1,2 \ldots$$

Therefore, the solution of the wave equation can be rewritten as

$$p'(x,y,z,t) = \sum_{m=0}^{\infty}\sum_{n=0}^{\infty} cos\left(\frac{m\pi x}{b}\right) cos\left(\frac{n\pi y}{h}\right)\left(C_{1(m,n)}e^{-jk_{z,(m,n)}z} + C_{2(m,n)}e^{jk_{z,(m,n)}z}\right)e^{j\omega t} \tag{2.40}$$

in which the propagation constant for the $(m,n)$ mode is given by

$$k_{z(m,n)} = \sqrt{k_0^2 - \left(\frac{m\pi}{b}\right)^2 - \left(\frac{n\pi}{h}\right)^2} \tag{2.41}$$

Hence, it follows that the acoustic pressure distribution inside the duct may be expressed as a superposition of all the natural modes of the acoustic system. In analogy to the structural vibrations[14], an acoustic mode represents a particular acoustic pressure pattern within the cross section of the considered duct, which is characteristic of the dimensions of the cavity (or acoustic domain). In fact, when solving the homogeneous wave equation, the goal is to find every possible acoustic pressure distribution which satisfy the considered particular geometry. Every modes for which $m$ and/or $n$ are not equal to zero are called higher order modes; $m$ and $n$ represent the number of nodal lines in the pressure distribution within the cross section, as shown in Figure 2.9.

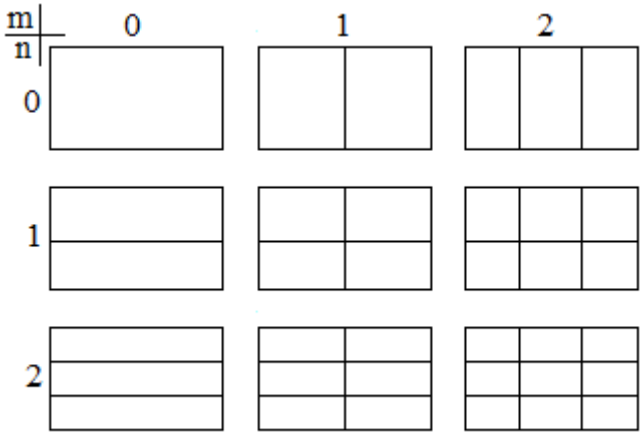


Figure 2.9 – Representation of the first 9th higher order modes in a rectangular duct.

In order to evaluate the axial particle velocity for the $(m,n)$ propagation mode, it is possible to make use of the momentum equation in the axial direction, namely

$$u'_{z,(m,n)} = \hat{u}e^{j\omega t} \quad \xrightarrow{yields} \quad \frac{\partial u'_{z,(m,n)}}{\partial t} = j\omega\hat{u}e^{j\omega t} = -\frac{\partial p'(x,y,z,t)}{\partial z}\frac{1}{\rho_0}$$

or

$$u'_{z,(m,n)} = \frac{k_{z(m,n)}}{k_0 Z_0} cos\left(\frac{m\pi x}{b}\right) cos\left(\frac{n\pi y}{h}\right)\left(C_{1(m,n)}e^{-jk_z z} - C_{2(m,n)}e^{jk_z z}\right)e^{j\omega t} \tag{2.42}$$

From what above, it follows that, for the same acoustic pressure, the amplitude of particle velocity for the $(m,n)$ propagation mode is less ($k_{z(m,n)}/k_0$ times) than the one corresponding to the plane wave solution (0,0). Now, thanks to eq. (2.42), it is possible to derive the acoustic mass velocity by the integration over the cross section of the duct:

$$v'_{z,(m,n)} = \rho_0 \iint u'_{z,(m,n)} dS = \rho_0\left(C_{1(m,n)}e^{-jk_z z} - C_{2(m,n)}e^{jk_z z}\right)e^{j\omega t}\int_0^b cos\left(\frac{m\pi x}{b}\right)dx \int_0^h cos\left(\frac{n\pi y}{h}\right)dy$$

which yields

$$v_{z,(m,n)} = 0 \quad for \;\; m \neq 0; n \neq 0$$

and

$$v'_{z,(m,n)} = \frac{bh}{a_0}\left(C_{1(m,n)}e^{-jk_0 z} - C_{2(m,n)}e^{jk_0 z}\right)e^{j\omega t} \quad for \;\; m = n = 0 \tag{2.43}$$

So, the concept of acoustic mass velocity is meaningless for higher order modes. Moreover, any particular higher order mode will propagate unattenuated within the duct only if its propagation constant is a real number, namely

$$k_0^2 - \left(\frac{m\pi}{b}\right)^2 - \left(\frac{n\pi}{h}\right)^2 > 0$$

or

$$\frac{4}{\lambda^2} - \left(\frac{m}{b}\right)^2 - \left(\frac{n}{h}\right)^2 > 0$$

or

$$\lambda < \frac{2}{\sqrt{\left(\frac{m}{b}\right)^2 + \left(\frac{n}{h}\right)^2}} \tag{2.44}$$

Therefore, if for example $b > h$, then the first higher order mode will be (1,0) and it would start propagate (or would be cut-on) if

$$\lambda > 2b \quad \text{or} \quad f > \frac{a_0}{2b}$$

Hence, summarizing, in a rectangular duct only plane waves would propagate if the frequency is small enough so that

$$\lambda < 2b \quad \text{or} \quad f < \frac{a_0}{2b} \tag{2.45}$$

where $b$ is the larger of the two cross sectional dimensions; all higher order modes, even if present, will be cut-off, namely attenuated exponentially.

Generalizing, such determination of the frequency of the problem may be also made by means of a dimensionless number called Helmholtz number which is defined as

$$He = \frac{2\pi L}{\lambda} = k_0 L \tag{2.46}$$

where $L$ is the characteristic length scale of the problem. If the Helmholtz number is much less than $\pi$, then the problem is said to be low frequency problem. Hence, by assuming $L = b$, eq. (2.45) is confirmed for $He < \pi$ (low frequency range).

### 2.2.3 3-D propagation in tubes

Probably, together with the rectangular duct, the most common shape for a duct is that of a tube, that is with a circular cross section. When a three-dimensional wave propagation phenomenon occurs within a tube, as the one which is schematically depicted in Figure 2.10, the governing wave equation is still represented by eq. (2.36). The only difference lies in the form of the Laplace operator which, if a cylindrical coordinate system is adopted[5], may be expressed as

$$\nabla^2 = \frac{\partial^2}{\partial r^2} + \frac{1}{r}\frac{\partial}{\partial r} + \frac{1}{r^2}\frac{\partial^2}{\partial \theta^2} + \frac{\partial^2}{\partial z^2} \tag{2.47}$$

where $r$, $\theta$ and $z$ are the radial, polar and axial coordinates respectively.

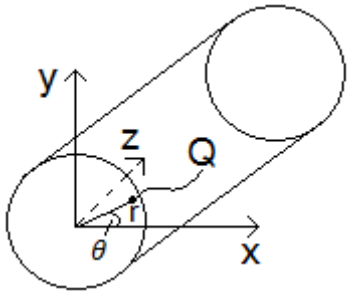


Figure 2.10 – Circular duct (or tube) representation.

By assuming a time and theta dependence of the type $e^{j\omega t}$ and $e^{jm\theta}$ respectively, and by making use of the method of separation of the variable[10], the acoustic pressure may be expressed as

$$p'(r,\theta,z,t) = \sum_m R_m(r)\left(C_1 e^{-jk_z z} + C_2 e^{jk_z z}\right) e^{j\omega t} e^{jm\theta} \tag{2.48}$$

which, once substituted into the wave equation, yields to the following Bessel equation[15] for $R(r)$

$$\frac{\partial^2 R_m(r)}{\partial r^2} + \frac{1}{r}\frac{\partial R_m}{\partial r} + \left(k_r^2 - \frac{m}{r^2}\right) R_m = 0 \tag{2.49}$$

where $k_r^2 = k_0^2 - k_z^2$. In general, the Bessel equation has a solution which is a linear combination of two functions, namely

$$R_m = A\, J_m(k_r r) + B\, N_m(k_r r) \tag{2.50}$$

where $J_m(k_r r)$ and $N_m(k_r r)$ stand for the $m^{th}$ order Bessel functions of the first and second kind respectively[6]. They are depicted in Figure 2.11, for three values of the coefficient $m$ (0,1,2) (note that $m$ is linked to the polar coordinate).

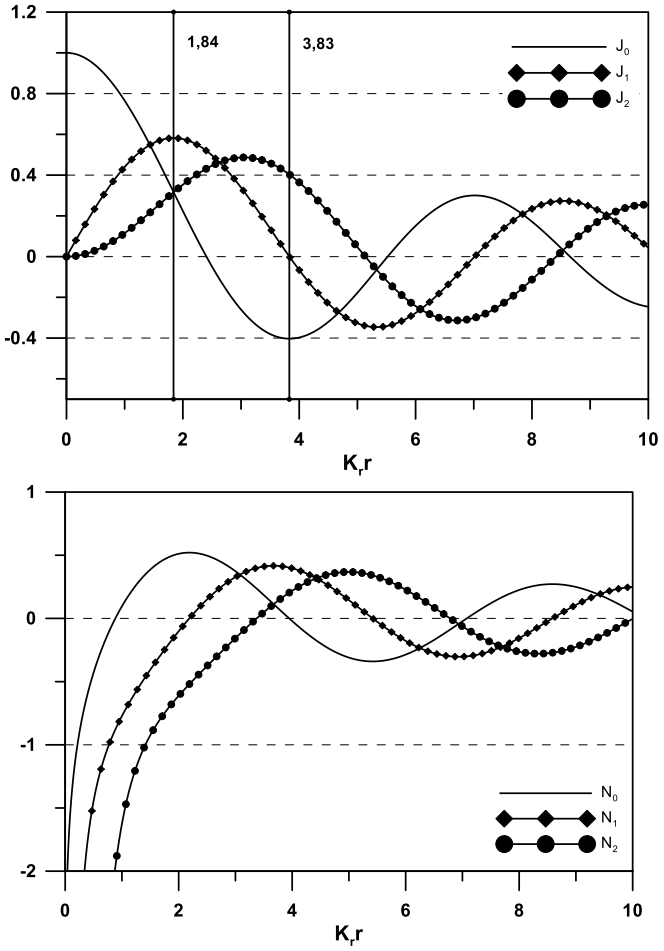


Figure 2.11 – Bessel function of the first kind a) and second kind b).

As usually, the values of the constants $A$ and $B$ should be found from the boundary conditions. The Bessel function of the second kind approaches minus infinity at the $z$ axis ($r = 0$), and, as the acoustic pressure must have a finite value everywhere, it follows that $B = 0$. Moreover, since the focus is on tubes whose wall are extremely rigid, the radial particle velocity must equal zero at the wall ($r = r_0$) which, thanks to the momentum balance equation, implies that

$$\frac{\partial R_m}{\partial r} = \frac{\partial J_m(k_r r_0)}{\partial r} = 0 \tag{2.51}$$

It follows that $k_r$ can only take values such that the first derivative of the Bessel function of the first type equals zero ($J'_m(k_r r_0) = 0$). If such $n$ values of the radial wave number are labeled as $k_{r,(m,n)}$, the acoustic pressure distribution within the tube may be expressed as

$$p'(r,\theta,z,t) = \sum_{m=0}^{\infty}\sum_{n=1}^{\infty} A\, J_m\left(k_{r,(m,n)} r\right)\left(C_{1,(m,n)} e^{-jk_{z,(m,n)}z} + C_{2,(m,n)} e^{jk_{z,(m,n)}z}\right) e^{j\omega t} e^{jm\theta} \tag{2.52}$$

where

$$k_{z,(m,n)} = \sqrt{k_0^2 - k_{r,(m,n)}^2} \tag{2.53}$$

According to the above nomenclature, the mode $(0,1)$ corresponds to a plane wave, which represents a discrepancy with respect to the nomenclature introduced for the rectangular duct. In fact, as it is possible to appreciate from Figure 2.11 a), the first zero ($n = 1$) of $J_0'$ is zero, namely $k_{r,(0,1)} = 0$, which simply implies that the propagation constant equals the plane wave number. Thus, it would be more convenient if $n$, instead of indicating the $n^{th}$ root of $J_m'$, would stand for the number of nodal circular line in the pressure distribution, representing the $n + 1^{st}$ root of $J_m'$. It follows that eq. (2.52) becomes

$$p'(r,\theta,z,t) = \sum_{m=0}^{\infty}\sum_{n=0}^{\infty} A\, J_m\left(k_{r,(m,n)}r\right)\left(C_{1,(m,n)}e^{-jk_{z,(m,n)}z} + C_{2,(m,n)}e^{jk_{z,(m,n)}z}\right)e^{j\omega t}e^{jm\theta} \tag{2.54}$$

which perfectly agrees with the nomenclature introduced for the three-dimensional wave propagation in ducts. In Figure 2.12, the first nine acoustic modes of tubes are schematically depicted, with the indication of the corresponding values of the modal constants $(m,n)$.

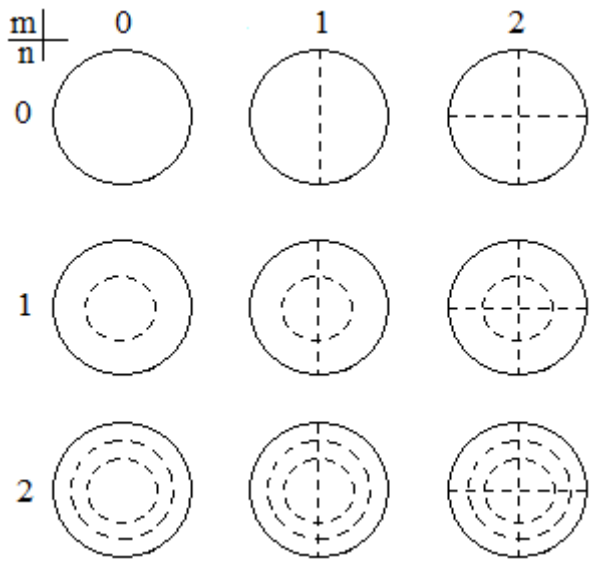


Figure 2.12 – First 9th acoustic modes propagating in tubes.

As an example, the first two higher-order modes $(0,1)$ and $(1,0)$ would propagate along the axis if the corresponding axial wave number is real, namely if $k_0 > k_{r,(0,1)}$ and $k_{r,(1,0)}$ respectively. By the examination of Figure 2.11 a), the second zero of $J_0'$ occurs at $k_{r,(0,1)}r_0 = 3{,}83$ whilst the first zero of $J_1'$ occurs at $k_{r,(1,0)}r_0 = 1{,}84$. Consequently, the condition according to which only plane waves can propagate in tubes is the following

$$k_0 r_0 < 1{,}84 \tag{2.55}$$

or

$$f < \frac{1{,}84a_0}{\pi D_0} \tag{2.56}$$

where $D_0$ stands for the diameter of the cross section. In order to evaluate the axial particle velocity for the $(m,n)$ propagating acoustic mode, it is possible to make use of the momentum equation in the axial direction, namely

$$u'_{z,(m,n)} = -\frac{\partial p'(x,y,z,t)}{\partial z}\frac{1}{j\omega\rho_0}$$

or

$$u'_{z,(m,n)} = \frac{k_{z,(m,n)}}{k_0 Z_0} J_m\left(k_{r,(m,n)}\right)\left(C_{1,(m,n)}e^{-jk_{z,(m,n)}z} - C_{2,(m,n)}e^{jk_{z,(m,n)}z}\right)e^{j\omega t}e^{jm\theta} \tag{2.57}$$

So, even in the case of wave propagation in tubes, for the same acoustic pressure, the amplitude of particle velocity for the $(m,n)$ propagation mode is less ($k_{z(m,n)}/k_0$ times) than the one corresponding to the plane wave solution $(0,0)$.

## 2.3 Sound propagation in moving media

In the above paragraphs, the propagation of sound in rigid-walled ducts, filled with a quiescent fluid, has been discussed. However, in many industrial applications, sound propagation is a phenomenon occurring within a moving medium. In general, as already mentioned, the presence of a velocity field may affect both sound generation and propagation. The effect of fluid flow on sound generation will be in depth discussed in chapter 7, where the basic concepts of the branch of physic so-called aeroacoustics will be given. In this paragraph the focus will be on the effect that a mean flow field has on the propagation of sound. The starting point of the study of such phenomenon is that, since the fluid is moving, the Lagrangian and the Eulerian description are not the same, the spatial time derivative being substituted by the material time derivative so that additional terms appears in the governing wave equation. Intuitively, if a sound wave propagates at the Laplacian speed of sound within a medium at rest, when sound propagates in a medium having mean velocity $U$ the velocity relative to a fixed frame of reference would be $U + a_0$ for the forward moving wave and $U - a_0$ for the back moving wave. Both waves are said to be convected downstream by the flow indeed, as it will be clear in the following. All the foregoing analysis do not take into account dissipative effects of the medium.

### 2.3.1 The convective wave equation and solution

In order to appreciate the differences with the case of stationary acoustic medium, let's firstly focus on the one-dimensional case. To this aim, consider for simplicity that the acoustic medium is moving with velocity $U$, constant and uniform along a duct[5]. At the same time, it is assumed that small disturbances perturb, in one direction, the fluid particles around their equilibrium state, and therefore pressure, density and particle velocity can be expressed as

$$p(x,t) = p_0 + p'(x,t) \tag{2.58}$$

$$\rho(x,t) = \rho_0 + \rho'(x,t) \tag{2.59}$$

$$u(x,t) = U + u'(x,t) \tag{2.60}$$

Thus, by substituting eq. (2.58), (2.59) and (2.60) within the equation of conservation of mass (2.18), keeping only linear terms (which means, again, neglecting all products of primed quantities), yields

$$\frac{\partial \rho'}{\partial t} + U\frac{\partial \rho'}{\partial x} + \rho_0 \frac{\partial u'}{\partial x} = 0$$

or, recalling the definition of material time derivative[26]

$$\frac{D\rho'}{Dt} + \rho_0 \frac{\partial u'}{\partial x} = 0 \tag{2.61}$$

By performing the same substitution within the momentum conservation equation (2.19), yields

$$\rho_0 \frac{\partial u'}{\partial t} + U\frac{\partial \rho'}{\partial t} + 2\rho_0 U\frac{\partial u'}{\partial x} + U^2\frac{\partial \rho'}{\partial x} + \frac{\partial p'}{\partial x} = 0 \tag{2.62}$$

or, making use of eq. (2.61)

$$\rho_0 \frac{\partial u'}{\partial t} + \rho_0 U\frac{\partial u'}{\partial x} + \frac{\partial p'}{\partial x} = 0$$

or, recalling the definition of lagrangian time derivative

$$\rho_0 \frac{Du'}{Dt} + \frac{\partial p'}{\partial x} = 0 \tag{2.63}$$

Thus, substituting the expression for the density by using equation (2.13) and (2.14), and then performing[27] $\frac{D(2.61)}{Dt} - \frac{d(2.63)}{dx}$, yields to the following convective wave equation

$$\left[\frac{D^2}{Dt^2} - a_0^2\frac{\partial^2}{\partial x^2}\right]p' = 0 \tag{2.64}$$

or

$$\frac{\partial}{\partial t}\left(\frac{\partial p'}{\partial t} + U\frac{\partial p'}{\partial x}\right) + U\frac{\partial}{\partial x}\left(\frac{\partial p'}{\partial t} + U\frac{\partial p'}{\partial x}\right) - a_0^2\frac{\partial^2 p'}{\partial x^2} = 0 \tag{2.65}$$

or

$$\frac{\partial^2 p'}{\partial t^2} + 2U\frac{\partial^2 p'}{\partial t \partial x} + (U^2 - a_0^2)\frac{\partial^2 p'}{\partial x^2} = 0 \tag{2.66}$$

By means of the method of separation of the variable[10] and assuming a time dependence of the type $e^{j\omega t}$, the solution of eq. (2.66), which represents the acoustic pressure at any point within the domain and at any time instant, may be expressed as follows

$$p'(x,t) = \widehat{p_+}e^{j\omega(t-x/a_0+U)} + \widehat{p_-}e^{j\omega(t+x/a_0-U)} = \left(\widehat{p_+}e^{-jk^+x} + \widehat{p_-}e^{jk^-x}\right)e^{j\omega t} \tag{2.67}$$

[26] It is possible to reach the same result by considering, instead of the eulerian time derivative, the lagrangian time derivative in eq. (2.20). In fact, in this latter case the convection effect of the mean flow is already accounted in the time derivative, so that there is no need to use eq. (2.60) anymore.

[27] The Lagrangian and Eulerian time derivative are not the same anymore, due to the presence of flow. The substantial derivative is now equal to $\frac{DG}{Dt} = \frac{\partial G}{\partial t} + \boldsymbol{V}\cdot\nabla G$.

The above equation is very similar to that of the stationary medium case apart from the fact that the expression for the wavenumber is changed, namely

$$k^{\pm} = \frac{k_0}{1 \pm M} \tag{2.68}$$

where $M = U/a_0$ is the Mach number. From eq. (2.68) the convective effect of the mean flow, on both the forward and backward moving wave components of the sound field, is highlighted. In fact, in case of the presence of mean flow velocity different from zero, the phase speed differs for the two standing wave components, namely

$$a_{ph} = \frac{\omega}{k^{\pm}} = a_0(1 \pm M) \tag{2.69}$$

where the plus and minus sings refer to the forward and backward moving wave respectively. Following a similar process as the one previously outlined in order to obtain an expression for the particle velocity, this latter turns out to be equal to

$$u'(x,t) = \frac{1}{Z_0}\left(\widehat{p_+}e^{-jk_0x/1+M} + \widehat{p_-}e^{jk_0x/1-M}\right)e^{j\omega t} \tag{2.70}$$

in which $Z_0$ is again the characteristic impedance of the medium and is always equal to the product of the density and the speed of sound. By defining the acoustic mass velocity as $v = \rho_0 S u$, one gets

$$v'(x,t) = \frac{1}{Y_0}\left(\widehat{p_+}e^{-jk_0x/1+M} + \widehat{p_-}e^{jk_0x/1-M}\right)e^{j\omega t} \tag{2.71}$$

where the characteristic impedance of the tube is the same as for the case of stationary medium.

As regards the analysis of a three-dimensional sound field, the solution of the 3D convected wave equation, for the rectangular duct depicted in Figure 2.8, yields to the following expression for the pressure fluctuations

$$p'(x,y,z,t) = \sum_{m=0}^{\infty}\sum_{n=0}^{\infty} cos\left(\frac{m\pi x}{b}\right) cos\left(\frac{n\pi y}{h}\right)\left(C_{1(m,n)}e^{-jk^{+}_{z,(m,n)}z} + C_{2(m,n)}e^{jk^{-}_{z,(m,n)}z}\right)e^{j\omega t} \tag{2.72}$$

where the compatibility condition is

$$k^2_{z,(m,n)} + k_x^2 + k_y^2 = \left(k_0 + Mk_{z,(m,n)}\right)^2 \tag{2.73}$$

The solution of eq. (2.73) in terms of $k_{z,(m,n)}$, yields to the following expression for the propagation constant for the $(m,n)$ acoustic mode

$$k^{\pm}_{z,(m,n)} = \frac{\mp Mk_0 + \left[k_0^2 - (1-M^2)\left(k_x^2 + k_y^2\right)\right]^{\frac{1}{2}}}{1-M^2} \tag{2.74}$$

It follows that the condition for the $(m,n)$ mode to propagate unattenuated, coinciding with the case of a real propagation constant, is found when the argument of the square root is positive, namely

$$k_0^2 - (1-M^2)\left(k_x^2 + k_y^2\right) \geq 0 \tag{2.75}$$

This, in terms of wavelength, simply implies that only plane waves will propagate if the following condition is satisfied

$$\lambda > \frac{2b}{(1-M^2)^{1/2}} \tag{2.76}$$

or, in terms of frequency

$$f < \frac{a_0}{2b}(1-M^2)^{1/2} \tag{2.77}$$

Thus, if $b > h$, the cut-off frequency of the first higher order modes $(1,0)$ is lower by a factor equal to $(1-M^2)^{1/2}$, $M$ being the mean flow Mach number, with respect to the case of a stationary medium. The expression for the particle velocity may be determined by means of the momentum conservation equation in the axial direction, substituting in it the expression of the pressure fluctuation. This process yields to the following expression

$$u'_{z,(m,n)} = \frac{1}{Z_0} cos\left(\frac{m\pi x}{b}\right) cos\left(\frac{n\pi y}{h}\right)\left(\frac{k^+_{z,(m,n)}}{k_0 - Mk^+_{z,(m,n)}} C_{1(m,n)} e^{-jk^+_{z,(m,n)}z} - \frac{k^-_{z,(m,n)}}{k_0 + Mk^+_{z,(m,n)}} C_{2(m,n)} e^{-jk^-_{z,(m,n)}z}\right) e^{j\omega t} \tag{2.78}$$

From what concerns the three-dimensional acoustic propagation in tubes with mean flow, similar expression may be derived. The important thing is that in that case the lowering effect on the cut-off frequency is practically the same as in the case of rectangular ducts. In fact, the cut-off frequency of the first high order mode would be

$$f = \frac{1{,}84a_0}{\pi D_0}(1-M^2)^{1/2} \tag{2.79}$$

below which only plane wave can propagate. However, for low Mach number flow application (say $M < 0.2$) it is assumed that the influence of the flow convection effects on the acoustic propagation is negligible.

## Bibliography


[1] Fletcher, H. and Munson, W.A. "Loudness, its definition, measurement and calculation", Journal of the Acoustic Society of America 5, 82-108 (1933).

[2] http://www.iso.org/iso/catalogue_detail.htm?csnumber=34222.

[3] https://webstore.iec.ch/publication/5708.

[4] M. Abom, “An Introduction to Flow Acoustics”, Publisher: KTH-The Royal Institute of Technology, ISBN: ISRN/KTH/AVE/N-06/04-SE.

[5] M. L. Munjal, “Acoustics of Ducts and Mufflers with Application to Exhaust and Ventilation System Design”, John Wiley & Sons.

[6] https://en.wikipedia.org/wiki/Bessel_function.

[7] K. Shin, J.K. Hammond, Foundamental of signal processing for sound and vibration engineers, © 2008, pag. 1-225.

[8] D'Alembert, (1747) "Recherches sur la courbe que forme une corde tenduë mise en vibration", Histoire de l'académie royale des sciences et belles lettres de Berlin, vol. 3, pages 214-219.

[9] F. Hautmann, “Normal Modes, Wave Motion and the Wave Equation”, Oxford University Hilary Term 2012, Printed lecture notes.

[10] J. Feldman, ” Solution of the Wave Equation by Separation of Variables”, January 21, 2007.

[11] Actran 15.1 User’s Guide,Volume 1 “Installation, Operations, Theory and Utilities”, April 2015.

[12] Leo L. Beranek, Tim J Mellow, “Acoustics: Sound Fileds and Transducers”, Academic Press, ISBN:978-0-12-391421-7.

[13] Lighthill, M. J. (1952). "On sound generated aerodynamically. I. General theory". Proceedings of the Royal Society A. 211 (1107): 564–587, doi:10.1098/rspa.1952.0060.

[14] F. Fahy, “Sound and Structural Vibration: Radiation, Transmission and Response”, Publisher Academic Press, Inc., ISBN: 0-12-247670-0.

[15] Bowman, F. Introduction to Bessel Functions. New York: Dover, 1958.

# Chapter 3

# Basics of Sound Propagation in Duct

## Introduction

As it has been already mentioned, the problem of attenuating noise is of primary concern, whose traditional solution generally relies on inserting something on the path between sound source and receiver. When the path through which sound propagates is constituted by ducts and pipes, the branch of acoustics concerned with sound propagation is called duct acoustics. Such particular theory is of practical relevance in many areas of acoustics and noise control. As an example, it is possible to refer to air-distributing systems for air-conditioning in which the challenge is represented by the attenuation of the fan noise. Also, the reduction of noise from both intake and exhaust systems of gasoline and Diesel internal combustion engines is a very important task to be accomplished, in order to respect the overall vehicle noise emissions standard. However, not always duct systems are located between source and receiver in order to attenuate noise. In particular, for sport/luxury cars, the acoustic design of such system is done so that they are properly tuned, in order to deliver the desired sound quality. In all these cases, the duct system is nothing else than a set of pipes and mufflers, this latter being classifiable as either dissipative or reflective. The basic principle of dissipative mufflers is that sound is attenuated by means of acoustic energy dissipation into heat. Such dissipation mechanism is achieved thanks to the use of absorption material. Vice versa, the sound attenuation accomplished by reflective mufflers relies on reflection of acoustic energy. More precisely, basic reflective mufflers are essentially constituted by combinations of pipes having different cross sections which causes impedance mismatch, thanks to which interference between incident and reflected acoustic waves is accomplished, resulting in a lower sound level transmitted downstream. In the following pages, the basic concepts about how reflective mufflers work will be recalled, making reference to the theory of the acoustic filters.

An acoustic filter is nothing else than an acoustic element (or generally more than just one) located between the sound source and the receiver, e.g. the atmosphere. Thus, an exhaust muffler is an acoustic filter in which, according to what has been previously highlighted, the acoustic waves are convected downstream by the moving medium, which is constituted by the exhaust gases. However, for simplicity, the acoustic filter's theory will be recalled considering a stationary medium and plane waves propagation, as the common used diameters are such that the condition expressed by eq. (2.56) is satisfied in the range of interest. Therefore, the governing equation is the classical 1-D wave equation, namely

$$\left[\frac{1}{a_0^2}\frac{d^2}{dt^2} - \frac{d^2}{dx^2}\right] p' = 0 \tag{3.1}$$

assuming $x$ as the direction of propagation. The two state variables which characterize acoustic waves and the acoustic state at each section of an acoustic filter are the acoustic pressure $p'(t)$ and particle velocity $u'(t)$. As already mentioned, these two quantities characterize the flux of acoustic energy per unit of area across a surface (real or hypothetical) which is termed acoustic intensity.

More precisely, the sound intensity related to a surface equals the time average product of sound pressure and the normal component (to the surface) of the particle velocity, namely

$$I_s = \overline{p'(t)\, u'_n(t)} \tag{3.2}$$

Therefore, the total acoustic power radiated by a sound source may be evaluated by the surface integral of the sound intensity over a real or hypothetical surface enclosing the source, that is

$$W_s = \iint I_s \, dS \tag{3.3}$$

Considering an acoustic wave, the so-called wave front is defined as the locus of points indicating the particles having the same phase. So, the total acoustic power associated with a plane wave, in a duct of cross section *S*, would be given by

$$W = S\ \overline{p' \cdot u'} = \frac{1}{\rho_0} p'_{rms} v'_{rms} \tag{3.4}$$

where *v*' is the acoustic mass velocity and is equal to $S\rho_0 u'$. Such velocity is preferred in hot gases system since, as it has been shown in the previous chapter, it allows to refer to the characteristic impedance of the tube $Y_0 = a_0/S$. If both acoustic pressure and acoustic mass velocity are assumed to vary with sinusoidal law, that is

$$p' = Pe^{j\omega t} \rightarrow\ p'_{rms} = \frac{P}{\sqrt{2}} \tag{3.5}$$

$$v' = Ve^{j\omega t} \rightarrow\ v'_{rms} = \frac{V}{\sqrt{2}} \tag{3.6}$$

then the total acoustic power associated with a plane wave inside a duct would be equal to

$$W = \frac{1}{2\rho_0}(PV)cos\vartheta \tag{3.7}$$

where $\vartheta$ is the phase difference between *P* and *V*. As every signal may be expressed in terms of its spectral components, thanks to the Fourier analysis, in the following, all formulation will refer to the frequency representation of acoustic variables. Therefore, the symbols *p* and *v* stand for the complex amplitudes of the two state variables.

## 3.1 Basic theory of acoustic filters

Generally speaking, a silencer is a very complex system in which several reactive and dissipative effects may occur, in order to lower the gas-dynamic noise (due to the exhaust valve opening) which is emitted at the end of the so-called tail pipe and radiated outside. However, it is possible to recognize a few types of elementary acoustic filters and then it is possible to focus on the study of complex mufflers as composed of such basic elements. It follows that, in the next paragraphs the fundamental aspects of such elementary elements will be reported. In doing so, each acoustic filter will be characterized by its acoustic impedance which characterizes the resistance exerted by the element to sound transmission. Such circumstance is generally presented in analogy to what happens in electric circuits theory. In fact, according to this theory, the impedance is nothing else than the resistance when dealing with alternate current circuits, which represent a complex number whose real and imaginary part are termed electric resistance and reactance respectively. The same

concepts apply to acoustic propagation theory, considering the acoustic impedance as a measure of the opposition that a system presents to the acoustic transmission, resulting from an acoustic pressure applied to the system. Consequently, as already mentioned, acoustic pressure and particle velocity are equivalent to voltage and current respectively within electric theory.

### 3.1.1 Specific acoustic impedance of an uniform tube

As it has been learned before from the solution of the classical wave equation, the acoustic pressure and the acoustic mass velocity may be expressed in terms of forward moving and back moving wave components as follows[28]

$$p'(x,t) = Ae^{-jk_0x} + Be^{jk_0x} \tag{3.8}$$

$$v'(x,t) = \frac{1}{Y_0}\left(Ae^{-jk_0x} - Be^{jk_0x}\right) \tag{3.9}$$

where the exponential time factor has been embedded within the complex amplitudes *A* and *B*. It is important to note that conventionally the characteristic impedance is denoted by $Z_0$ but, in the theory of acoustic filters, the subscripts denote the $n^{th}$ elements of the considered filter whilst $Z_0$ is called the radiation impedance of the atmosphere. Therefore, in eq. (3.9) the characteristic impedance (defined as the ratio of sound pressure and particle velocity, both associated with a *plane progressive wave*) has been indicated with $Y_0$ (actually since the acoustic mass velocity has been adopted, it indicates the characteristic impedance of the tube). It also represents the ratio between sound pressure and acoustic mass velocity in free field, where there are only forward moving wave.

However, in duct propagation problem the sound field is expressed by eq. (3.8) and so, considering a uniform tube as depicted in Figure 3.1, the specific acoustic impedance at any point in the *standing wave field* is defined as

$$\Gamma(x) = \frac{p'(x,t)}{v'(x,t)} = Y_0 \frac{Ae^{-jk_0x} + Be^{jk_0x}}{Ae^{-jk_0x} - Be^{jk_0x}} \tag{3.10}$$

and represents the equivalent impedance of the complete passive subsystem downstream of the considered point.

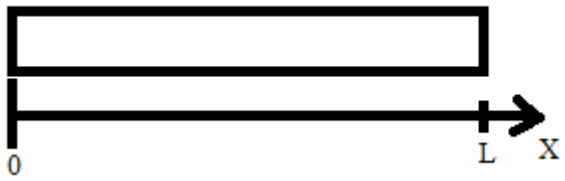


Figure 3.1 – Uniform tube schematization.

Once, the origin of the coordinate system has been chosen, at the beginning of a tube such specific acoustic impedance is equal to

[28] It is implicit that the real part has to be considered.

$$\Gamma(0) = Y_0 \frac{A+B}{A-B} \tag{3.11}$$

whilst its value at the end of the tube is

$$\Gamma(L) = Y_0 \frac{Ae^{-jk_0L} + Be^{jk_0L}}{Ae^{-jk_0L} - Be^{jk_0L}}$$

$$= Y_0 \frac{(A+B)cos(k_0L) - j(A-B)sin(k_0L)}{(A-B)cos(k_0L) - j(A+B)sin(k_0L)}$$

$$= Y_0 \frac{(A+B)/(A-B) - j\,tan(k_0L)}{1 - j(A+B)/(A-B)tan(k_0L)} \tag{3.12}$$

or

$$\Gamma(L) = \frac{\Gamma(0)\cos(k_0L) - j\,Y_0\sin(k_0L)}{\cos(k_0L) - j\,\Gamma(0)/Y_0\sin(k_0L)} \tag{3.13}$$

Of course, by simply rearranging eq. (3.13), it is possible to obtain the specific acoustic impedance at the beginning of the tube as function of that at the end

$$\Gamma(0) = \frac{\Gamma(L)\cos(k_0L) + j\,Y_0\sin(k_0L)}{\cos(k_0L) + j\Gamma(L)/Y_0\sin(k_0L)} \tag{3.14}$$

Both eq. (3.13) and (3.14) express the so called the impedance translation theorem. Hence, if the end of the tube at *x=L* is rigidly closed, that is the acoustic mass velocity equals zero, then the acoustic impedance goes to infinity and so the impedance at *x=0* may be approximated as

$$\Gamma(0)_{rigid\ end} = -jY_0\cot(k_0L) \tag{3.15}$$

Generally speaking, as it has already mentioned, an acoustic filter consists of a series of uniform duct, with different cross-sectional area, connected at the discontinuities. There, it happens that part of the incident energy is reflected, another part is dissipated (generally a very small part) whilst the remainder is transmitted downstream. Moreover, as it will be recalled later, at the junctions of area changes three-dimensional waves arise that simple one-dimensional theory cannot take into account. Thus, instead of referring to the acoustic impedance, a termination is often described in terms of its reflection coefficient, by the knowledge of which the evaluation of the reflected wave may be simply achieved. In fact, the reflection coefficient is defined as the ratio between the reflected wave and the incident wave, namely

$$R = |R|e^{j\theta} \tag{3.16}$$

where $|R|$ and $\vartheta$ are the modulus and the phase[29] of the reflection coefficient. Thus, in terms of incident and reflected wave components, the reflection coefficient at the beginning and at the end of the tube may be expressed respectively as

$$R(0) = \frac{B}{A} \tag{3.17}$$

[29] The phase information takes into account the presence of the above mentioned 3D effect which cannot be taken into account in a one-dimensional theory.

and

$$R(L) = \frac{Be^{jk_0L}}{Ae^{-jk_0L}} \tag{3.18}$$

Of course, it is easy to see, by the examination of eq. (3.10), that the relation between the acoustic impedance and the reflection coefficient at $x = 0$ are the following

$$\Gamma = Y_0 \frac{1+R}{1-R} \tag{3.19}$$

and

$$R = \frac{\Gamma - Y_0}{\Gamma + Y_0} \tag{3.20}$$

Therefore, as expected, at a rigid termination $\Gamma$ goes to infinity and so the incoming wave is completed reflected (with the same amplitude and phase)

$$R_{rigid\ end} \to 1 \tag{3.21}$$

It is important to mention the existence of another specific termination, which is often used in both experimental and numerical acoustic, and it is the so-called anechoic termination, for which no reflections are possible. More precisely, during experiments, this is a very important type of termination as it tries to reproduce the acoustic response in *free field* conditions. In fact, as it should be intuitively clear enough at this point, acoustic measurements are not as "simple" as others types of measurement. This is because, in acoustic, the general focus is on the evaluation of the effect of an acoustic source in terms of, for example, acoustic pressure. However, the acoustic field is highly dependent on the environment in which the measure is made as, at certain point in space, the resulting acoustic pressure is affected by the source emission and by reflection, diffraction, scattering effects due to the boundaries of the measurement environment and to the eventual presence of obstacles to the sound propagation. This is not the case, for example, of structural vibration measurements, during which the response of a structure is not dependent on the measurement environment. So, there is the need of performing acoustic measurements in very particular environments trying to reproduce standard conditions, as those of *free field* propagation. Consequently, in case of anechoic termination, the reflection coefficient is equal to zero and therefore the acoustic impedance equals the characteristic impedance of the tube, namely

$$\Gamma_{anechoic\ end} \to Y_0 \tag{3.22}$$

### 3.1.2 Radiation impedance

So far, the concept of impedance has been recalled and several examples have been discussed. However, apart from the characteristic impedance of the medium, characteristic impedance of the tube and the above discussed specific acoustic impedance relative to a point in the standing waves field, before considering other elemental acoustic elements, it is necessary to mention another type of impedance, namely the radiation impedance. In acoustics, radiation impedance is the impedance exerted by the surrounding medium on any vibrating solid or fluid which radiates sound. It is

generally defined as the ratio, at the interface, of the force a radiator exerts on a medium (equal and opposite to the force that the medium exerts on the radiator), to the velocity of the radiator. It is associated with the acoustic load from the surrounding medium. Consequently, when sound propagation occurs in a tube terminating within an external ambient, the radiation impedance must be taken into account before being able to estimate the corresponding sound field. In this case, it is defined as the impedance that the atmosphere imposes at the end of a tube, and, as already mentioned, it is commonly indicated by $Z_0$. It follows that, from an electro-acoustic analogy, the radiation impedance represents the final load of the equivalent electric circuit.


Figure 3.2 – Equivalent acoustic circuit representations.

The availability of a model which makes easy to quantify the radiation impedance is very important because, as already highlighted, an acoustic filter has the main task of attenuating the noise transmission between a sound source and a receiver which is generally located in the atmosphere. Consequently, the "resistance" to the sound transmission imposed by the external medium plays an important role in such sense. A situation in which it is possible to analytically determine the radiation impedance is represented by the particular case of a tube terminating in an infinite flange (or hemispherical space), as schematically depicted in Figure 3.3.

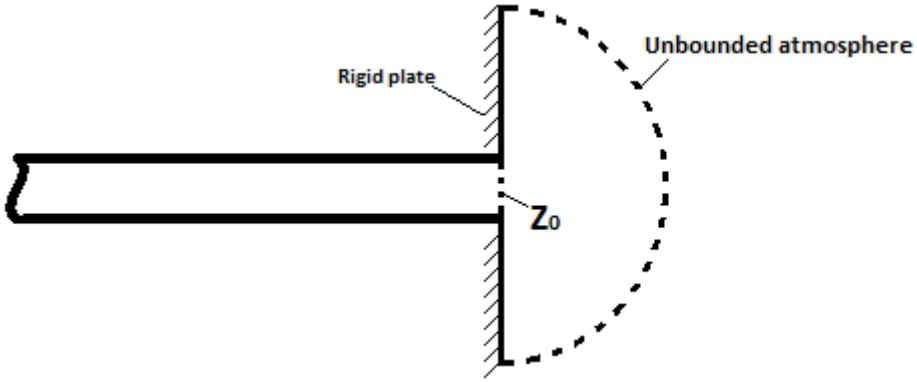


Figure 3.3 – Schematization of an end pipe terminating in an infinite flange.

The goal is to evaluate the acoustic pressure and particle velocity on the interface which is represented by the outlet mouth of the pipe and, from their ratio, the radiation impedance. Before being able of doing this, it is necessary to make use of the expression for the pressure field due to a simple source located in an unlimited medium[2]. Since it is easier to deal with velocity-potential as independent variable, let's firstly recall the wave equation in terms of velocity-potential involving simple sources[30] distribution, namely

[30] A simple source is represented by pulsating volume flow (or pulsating injection of mass).

$$\left[\frac{1}{a_0^2}\frac{\partial^2}{\partial t^2} - \nabla^2\right]\varphi = \emptyset \tag{3.23}$$

where $\emptyset$ stands for a source strength per unit of volume. The first thing to note is that, assuming the nature of the source as vanishing outside a small volume, the integration of eq. (3.23) through such a small space including the source distribution yields

$$0 - \iint \frac{\partial \varphi}{\partial n} dS = \iiint \emptyset d\mathcal{V} \tag{3.24}$$

since the wave propagation is assumed to occur outside the volume occupied by the source[31] and use has been done of the divergence theorem for the second term on the left hand side. Equation (3.24) shows how the effect of the simple source $\emptyset$ could be seen as introduction or abstraction of fluid through the boundary of $\mathcal{V}$ (such circumstance will be clarified in the chapter dealing with the aerodynamic generation of sound). For what it will be explained in chapter 7, in which an insight on the theory of aeroacoustic will be given, eq. (3.23) has a solution of the type[32]

$$\varphi = \iiint \frac{\emptyset\left(t-\frac{r}{a_0}\right)}{4\pi r} d\mathcal{V} \tag{3.25}$$

By assuming an harmonic nature for the sound source, it is possible to make use of the Fourier transform of $\emptyset\left(t - \frac{r}{a_0}\right)$, namely

$$\varphi = \iiint \frac{\emptyset\, e^{-jk_0 r}}{4\pi r} d\mathcal{V} \tag{3.26}$$

where the exponential time factor has been embedded within the complex amplitude. If the source, say $\emptyset'$, is distributed over an infinite surface splitting the unbounded acoustic medium in two parts, the new solution may be thought as particular case of eq. (3.26). In fact, it is possible to rewrite the velocity-potential as

$$\varphi = \iiint \frac{\emptyset'\, e^{-jk_0 r}}{4\pi r} dS \tag{3.27}$$

where $\emptyset' = b\emptyset$, being $b$ the thickness of the surface such that $d\mathcal{V} = bdS$. Moreover, thanks to eq.( 3.24), the velocity-potential expressed by eq. (3.27) may be rewritten in terms of normal particle velocity of fluid in contact with the infinite plane surface. In fact, since the surface is supposed to be plane, then the integral expressed by eq. (3.27) is symmetrical with respect to it, and therefore

$$\frac{\partial \varphi}{\partial n_1} = \frac{\partial \varphi}{\partial n_2} \tag{3.28}$$

being $n_1$ and $n_2$ the outward normal on both side of $S$. It follows that, by substituting eq. (3.28) within eq. (3.24), $\varphi$ may be expressed as

$$\varphi = -\frac{1}{2\pi}\iiint \frac{\partial \varphi}{\partial n}\frac{e^{-jk_0 r}}{r} dS \tag{3.29}$$

---

[31] $\frac{\partial^2}{\partial t^2}\iiint \varphi d\mathcal{V} = 0$ since $\varphi \neq 0$ outside the source region.

[32] It naturally follows from the theory of the free field Green's function.

which gives the velocity-potential field at any point, on both side of the unbounded space, whose distance from the infinite plate (in normal periodic motion) is $r$. The next step is to evaluate such velocity-potential in the special case in which the vibrating surface (the source distribution may be seen like that) is circular. More precisely, it is possible to state that if the normal particle velocity $\frac{\partial \varphi}{\partial n}$ has a constant non-zero value only on an circular area belonging to the infinite plane $S$, the force corresponding to the whole pressure variation acting on one side of the plate is given by[33]

$$\iint p' \, dS' = -\rho \iint \dot{\varphi} \, dS' = -jk_0 a_0 \rho \iint \varphi \, dS' \tag{3.30}$$

or by means of eq.(3.29)

$$\iint p' \, dS' = \frac{jk_0 a_0 \rho}{\pi} \frac{\partial \varphi}{\partial n} \sum\sum \frac{e^{-jk_0 r}}{r} dS \, dS' \tag{3.31}$$

After some complicated algebra[2], the double summation in eq. (3.31) turns out to be equal to

$$\sum\sum \frac{e^{-jkr}}{r} dS \, dS' = \frac{\pi^2}{2k_0^3} K_1(2k_0 r_0) - j \frac{\pi^2 r_0^2}{k_0} \left(1 - \frac{J_1(2k_0 r_0)}{k_0 r_0}\right) \tag{3.32}$$

where $r_0$ stands for the radius of the circular area, $J_1(2k_0 r_0)$ and $K_1(2k_0 r_0)$ are given by

$$\left(1 - \frac{J_1(2k_0 r_0)}{k_0 r_0}\right) = \frac{(k_0 r_0)^2}{1 \cdot 2} - \frac{(k_0 r_0)^4}{1 \cdot 2^2 \cdot 3} + \frac{(k_0 r_0)^6}{1 \cdot 2^2 \cdot 3^2 \cdot 4} - \frac{(k_0 r_0)^8}{1 \cdot 2^2 \cdot 3^2 \cdot 4^2 \cdot 5} + \cdots \tag{3.33}$$

and

$$K_1(2k_0 r_0) = \frac{2}{\pi} \left[ \frac{(2k_0 r_0)^3}{1^2 \cdot 3} - \frac{(2k_0 r_0)^5}{1^2 \cdot 3^2 \cdot 5} + \frac{(2k_0 r_0)^7}{1^2 \cdot 3^2 \cdot 5^2 \cdot 7} - \cdots \right] \tag{3.34}$$

Thus, the total force exerted of the circular plate is finally given by

$$\iint p' \, dS' = a_0 \rho \, \pi r_0^2 \frac{\partial \varphi}{\partial n} \left(1 - \frac{J_1(2k_0 r_0)}{k_0 r_0}\right) + j \frac{a_0 \rho \, \pi}{2k_0^2} \frac{\partial \varphi}{\partial n} K_1(2k_0 r_0) \tag{3.35}$$

From what above, an expression for the reacting force of the air, within an hemispherical space, due to the normal harmonic motion of a circular area belonging to the infinite flange has been given. By the examination of eq. (3.35), such reaction force consists of two terms: one proportional to the velocity of the circular plate and another inertial one, which is proportional to its acceleration[34].

If the circular area is assumed to be the outlet mouth of a tube, terminating in an infinite flange with particle velocity $u = \partial\varphi/\partial n$, as in Figure 3.3, then the radiation impedance at the outlet would be given by the ratio

$$Z_0 = \frac{p}{v} = Y_0 \left(1 - \frac{J_1(2k_0 r_0)}{k_0 r_0}\right) + j \frac{Y_0}{2(k_0 r_0)^2} K_1(2k_0 r_0) \tag{3.36}$$

or

$$Z_0 = R_0 + jX_0 \tag{3.37}$$

[33] If the velocity-potential is supposed to be an harmonic function of the type $\varphi = \hat{\varphi} e^{j\omega t}$, then $\dot{\varphi} = j\omega \hat{\varphi} e^{j\omega t}$.

[34] If the harmonic velocity of the plate is $\frac{\partial \varphi}{\partial n} e^{j\omega t}$, then the acceleration would be $jka_0 \frac{\partial \varphi}{\partial n} e^{j\omega t}$.

For sufficiently low frequencies such that $k_0 r_0 \ll 1$, only the first terms of eq. (3.33) and (3.34) must be taken into account and the expression of radiation impedance reduces to

$$Z_0|_{hemispherical\ space} = R_0 + jX_0 = Y_0 \left(\frac{k_0^2 r_0^2}{2}\right) + jY_0(0.85 k_0 r_0) \tag{3.38}$$

$R_0$ is termed radiation resistance and, since it is proportional to the particle velocity, it is responsible for the acoustic radiation from the tail-pipe, whilst $X_0$ is called radiation reactance and, since it is proportional to the inertia of the air, it results in a phase difference between pressure and velocity.

In case where the considered tube termination ends in an external ambient without any flange, the derivation of an analytic expression for the radiation impedance is even more complex and so not discussed for brevity' sake. Nevertheless, in such a case it may be approximated by[3]

$$Z_0|_{open\ end} = Y_0 \left(\frac{k_0^2 r_0^2}{4}\right) + jY_0(0.6133 k_0 r_0), \qquad k_0 r_0 \ll 1 \tag{3.39}$$

Rather than making consideration on such radiation impedance in order to understand how the external ambient affects the propagation of sound from a pipe, it is more intuitively to deal with the reflection coefficient. In fact, thanks to the definition of the radiation impedance, it is possible to evaluate the reflection coefficient at an open end of a tube, which is related to the specific acoustic impedance at that point by means of eq. (3.20). It follows that, by inserting eq.( 3.39) within eq.( 3.20), the reflection coefficient at an open end is found to be equal to

$$|R| e^{j\vartheta} = \frac{R_0 + jX_0 - Y_0}{R_0 + jX_0 + Y_0} = \frac{(0.25 k_0^2 r_0^2 - 1) + j(0.6133 k_0 r_0)}{(0.25 k_0^2 r_0^2 + 1) + j(0.6133 k_0 r_0)} \tag{3.40}$$

After some algebra, the modulus and phase of the reflection coefficient are given below

$$|R| = \frac{\sqrt{\left(0.0625 k_0^4 r_0^4 + 0.36 k_0^2 r_0^2 - 1\right)^2 + (1.2 k_0 r_0)^2}}{0.0625 k_0^4 r_0^4 + 0.36 k_0^2 r_0^2 + 1} \cong 1 - 0.14 k_0^2 r_0^2 \tag{3.41}$$

$$\vartheta = tan^{-1}\left(\frac{1.2 k_0 r_0}{0.0625 k_0^4 r_0^4 + 0.36 k_0^2 r_0^2 - 1}\right) \cong tan^{-1}(-1.2 k_0 r_0)$$

$$\cong \pi - tan^{-1}(1.2 k_0 r_0) \tag{3.42}$$

Therefore, at an open termination, the amplitude of the reflection coefficient is almost equal to one, whilst its phase is slightly less than π. Hence, from an engineering point of view, it is possible to point out that, at low frequencies, the incoming wave is reflected almost completely with an opposite phase, whilst only a little fraction is radiated out. This is especially true for very low frequencies, whilst at higher frequency the modulus and phase of the reflection coefficient follows ($k_0 r_0 \ll 1$) eq. (3.41) and (3.42), as it is depicted in Figure 3.4.

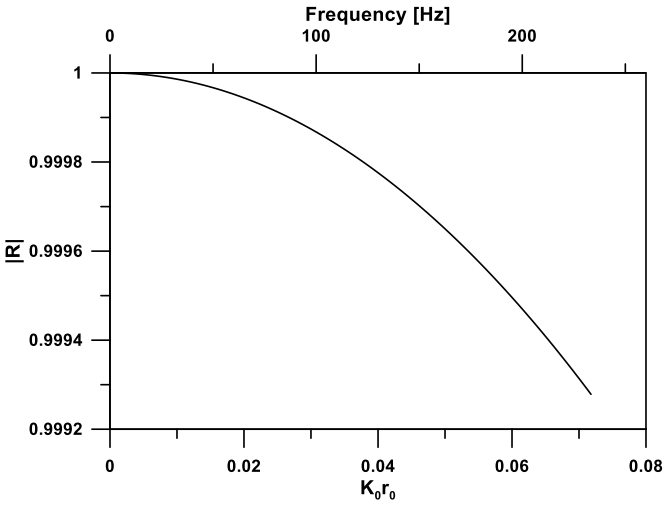


Figure 3.4 – Modulus of the reflection coefficient at an open end ($r_0 = 0.03$m).

In the following, an insight to the lumped element representation will be presented, introducing three quantities which are called lumper inertance, end correction and lumped compliance. As it will be clear more ahead, these concepts are very useful for the description of a very important acoustic element represented by the so-called Helmholtz resonator and the concentric hole-cavity resonator. Vice versa, the previously introduced concept of specific acoustic impedance is very useful for explaining and understanding the behavior of another important acoustic element which is called quarter-wavelength resonator.

### 3.1.3 A lumped inertance

The lumped element modelling approach is very useful for simplifying the task of studying acoustic elements which turn out to be acoustically compact. Such condition is satisfied when their characteristic dimension is much less than the wavelength of the problem. In this way, the spatial variation of acoustic quantities across such kind of element may be neglected, meaning that the phase is roughly constant throughout the considered lumped element. Let the focus be, for example, on a wave propagation phenomenon along an acoustically small length ($k_0 l \ll 1$), as that depicted in Figure 3.5.

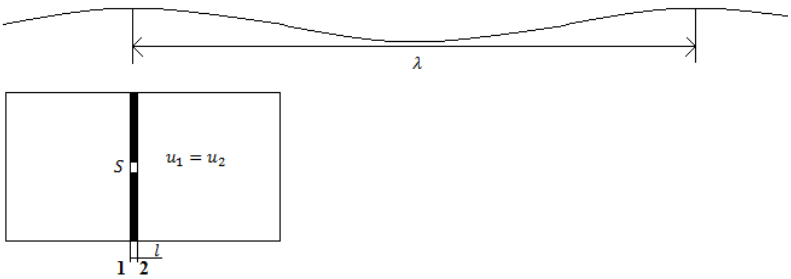


Figure 3.5 – Acoustically small tube schematization.

Since the small aperture within the plate is acoustically compact, as a consequence of an applied acoustic perturbation at one end, all the mass trapped into the tube, which is equal to $\rho_0 S l$, would be rigidly displaced by the same amount. Thus, a very little time delay will exist between the

responses of the two ends such that all the medium particles would move with the same particle velocity. Thus, by the application of the Newton' second law, it follows that

$$pS = \rho_0 Sl\frac{du}{dt} \tag{3.43}$$

But, recalling that the particle velocity varies with sinusoidal law

$$u' = ue^{j\omega t} \rightarrow \frac{du'}{dt} = uj\omega$$

the corresponding impedance equals

$$Z = \frac{p}{v} = \frac{\rho_0 lj\omega u}{\rho_0 Su}$$

or

$$Z_{lumped\ inertance} = j\omega\frac{l}{S} \tag{3.44}$$

Thanks to electro-acoustic analogies, $l/S$, which is the analogous of the lumped inductance, is called lumped inertance.

### 3.1.4 End correction

As already mentioned above, in general every time that a wave comes across a discontinuity part of the incident energy is reflected back with a phase change. This latter aspect occurs not only because of the impedance of the discontinuities, but also because of localized three-dimensional effects which arise at the discontinuities and that cannot be modeled in one-dimensional theory. These three-dimensional effects may be thought as evanescent higher-order modes. At the location where such 3D effects vanish, the plane wave propagation holds again. Therefore, in order to overcome this modelling issue, an extra length is to be added to the considered duct, in order to reproduce the phase shift corresponding to such three-dimensional effects arising at the discontinuity. Such additional length is called end correction and it is the extra length which must be added to the real length of a tube when it terminates into a different atmosphere (see Figure 3.6), having in this way an equivalent longer acoustic element.

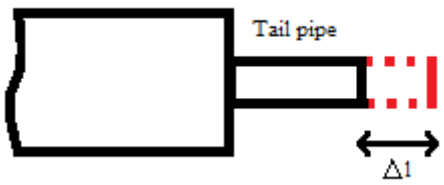


Figure 3.6 – Schematization of the concept of end correction.

As an example of application of the end correction, which may be understood at this point, if an acoustically small tube is exposed to the atmosphere, the radiation reactance can be added to the lumped inertance in order to obtain a reactance of an equivalent larger tube, namely

$$\frac{j\omega l_{hypo}}{S} = \frac{j\omega l_{real}}{S} + j\frac{a_0}{S}(0.6k_0 r_0)$$

or

$$\delta_{open\ end} = l_{hypo} - l_{real} = 0.6r_0 \tag{3.45}$$

where $\delta$ is termed end correction. It follows that, the end correction of a small hole in a plate would be twice of the length expressed by the analogous case of eq. (3.38) (that is if a small tube is exposed to a hemispherical space), namely

$$\delta_{hole} = l_{hypo} - l_{real} = 2 \cdot 0.85r_0 \tag{3.46}$$

Figure 3.7 – End correction of an hole in a plate.

Nevertheless, in general, if a small tube is acoustically long, the radiation reactance cannot be considered as end correction and so, the atmosphere and the tube must be considered as two distinct acoustic elements.

### 3.1.5 A lumped compliance

In Figure 3.8 a cavity of volume *V* with a neck of cross-sectional area *S* is shown. Considering a pressure *p'* to be applied at the neck of cross-sectional area, it is possible to assume that the volume decreases adiabatically.

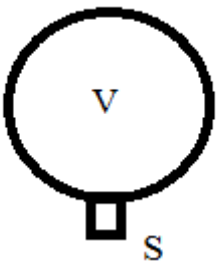


Figure 3.8 – A neck-cavity schematization.

In this hypothesis, the two versions of Gibbs's equations yield

$$TdS = dH - Vdp = 0 \rightarrow$$

$$\frac{dT}{T} = \frac{Rdp}{c_p p} \tag{3.47}$$

or

$$TdS = dU + pdV = 0 \rightarrow$$

$$\frac{dT}{T} = -\frac{RdV}{c_v V} \tag{3.48}$$

Combining Eq. (3.47) and (3.48) yields,

$$\frac{p}{p_0} + \gamma \frac{\Delta V}{V} = 0 \tag{3.49}$$

or

$$p' = \frac{\gamma p_0 \Delta V}{V} \tag{3.50}$$

where $\gamma$ is the ratio between the specific heats. However, the displacement at the neck and the corresponding volume contraction may be expressed as

$$\delta = \int u \, dt = \frac{u}{j\omega} \tag{3.51}$$

and

$$\Delta V = -S\delta = -\frac{Su}{j\omega} \tag{3.52}$$

Therefore, the expression of the impedance of a lumped compliance is

$$Z_{cavity} = \frac{p}{v} = \frac{1}{j\omega(V/a_0^2)} \tag{3.53}$$

Even in this case, by electro-acoustic analogy, $V/a_0^2$, which is the analogous of the lumped capacitance, is called lumped compliance.

### 3.1.6 Acoustic resonators

An acoustic resonator is a very common element for an acoustic filter, whose impedance goes to zero at certain frequencies not allowing acoustic transmission. From the easiest point of view, an acoustic resonator may be thought as an acoustic medium (air) within a pipe closed at one end whilst open at the other. Such mass of air may be seen as a simple mass-spring system vibrating, in more or less complete independence from the external atmosphere, at certain frequency which depends on the geometry. Actually, the inertia of the air outside the resonator has a damping effect, since the acoustic energy of the resonator is radiated (dissipated) through it. In presence of an external sound source, the air within the resonator start to vibrate, the magnitude depending on the closeness between the forcing frequency and the natural frequency of the resonator itself. In the next sections, the three main types of acoustic resonator will be described, which are quarter-wavelength, Helmholtz and concentric hole-cavity resonators.

### 3.1.6.1 Extended-tube (quarter-wave) resonator

The simplest example of extended-tube resonator is represented by an uniform tube rigidly closed[35] at one end, whilst opened at the other. Others classical examples of extended-tube resonators are schematized in figure below, where they are inserted in ducts systems. Three interfaces have been highlighted, which have been numbered by 1,2 and 3, corresponding to the inlet of the outlet tube, resonator inlet and outlet of the inlet tube respectively. From what above, each element is characterized by its own impedance and thus, according to the plane wave propagation hypothesis, this resonator would be equivalent to a branch element within an equivalent acoustic circuit, as the following boundary conditions are satisfied

$$p_1 = p_2 = p_3 \tag{3.54}$$

and

$$v_3 = v_1 + v_2 \tag{3.55}$$

where the last condition represents the continuity of the acoustic mass flux.

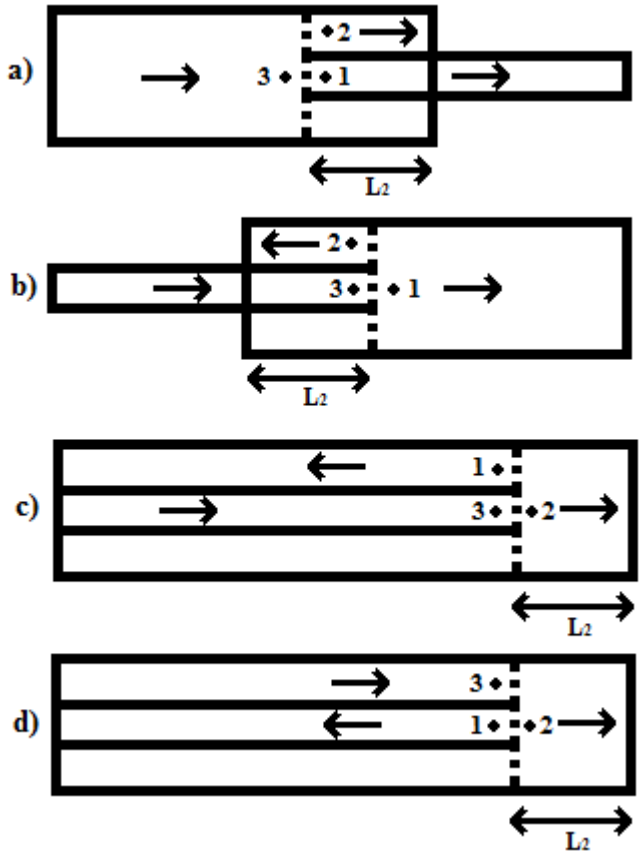


Figure 3.9 – Extended tube resonators: a) extended outlet, b) extended inlet, c) reversal expansion, d) reversal contraction.

By combining eq. (3.54) and (3.55), it is possible to obtain the relationship among the impedance of the tubes, namely

[35] Actually, infinity rigid end plates do not exist.

$$\frac{1}{\Gamma_3} = \frac{1}{\Gamma_1} + \frac{1}{Z_2}$$

where $Z_2$ is the equivalent impedance of the resonant cavity, at the junction with the other tubes, and can be expressed making use of eq. (3.14) as

$$Z_2 = \frac{p_2}{v_2} = Y_2 \frac{\Gamma(L_2)\cos(k_0 L_2) + j\, Y_2 \sin(k_0 L_2)}{Y_2 \cos(k_0 L_2) + j\Gamma(L_2)\sin(k_0 L_2)}$$

The equivalent acoustic circuit representation is depicted in Figure 3.10, where the resonator is indeed represented as a shunt element. At certain frequencies, it happens that impedance at section 2 goes to zero (which means that the cavity resonates) and the resonator will be equivalent to a short circuit. Consequently, no acoustic power is transmitted to the downstream tube 1. All the incoming power flux will be useful for resonating the closed-end cavity.

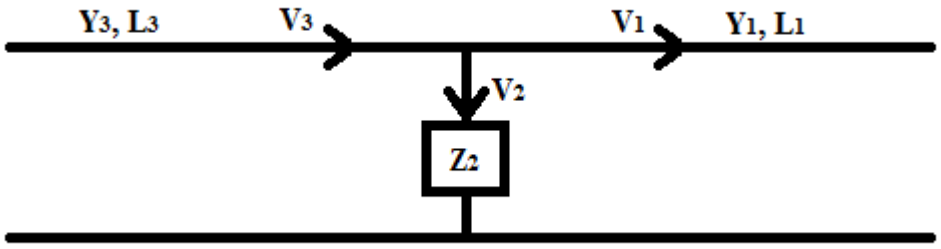


Figure 3.10 – Circuit representation of an extended tube resonator.

A common assumption is that the closed-end is perfectly rigid, that is the specific impedance $\Gamma(L_2)$ goes to infinity. Then, as it has already been shown for the uniform tube, the specific impedance at the interface 2 will be equal to

$$Z_2 = -jY_2 \cot(k_0 L_2)$$

Consequently, the resonance of the cavity would occur when $\cot(k_0 L_2)$ goes to zero, that is when the following relation is satisfied

$$k_0 L_2 = (2n+1)\frac{\pi}{2} \quad n = 0,1,2 \ldots$$

or

$$L_2 = (2n+1)\frac{\lambda}{4} \qquad n = 0,1,2 \ldots$$

This also means that, for a given length of the resonator, the resonance would occur at odd multiples of the fundamental frequency $f_r = a_0/4\, L_2$. By the examination of the last relation, it should be clear why extended-tube resonators are also called quarter-wave resonators. In order to clarify this, consider, for example, a source of continuous vibration like a piston at the inlet of a tube having a side branch terminating with a closed end. In the frequency range for which only

plane waves appear, the propagation of the disturbance generated by the source may be schematized as Figure 3.11 shows.

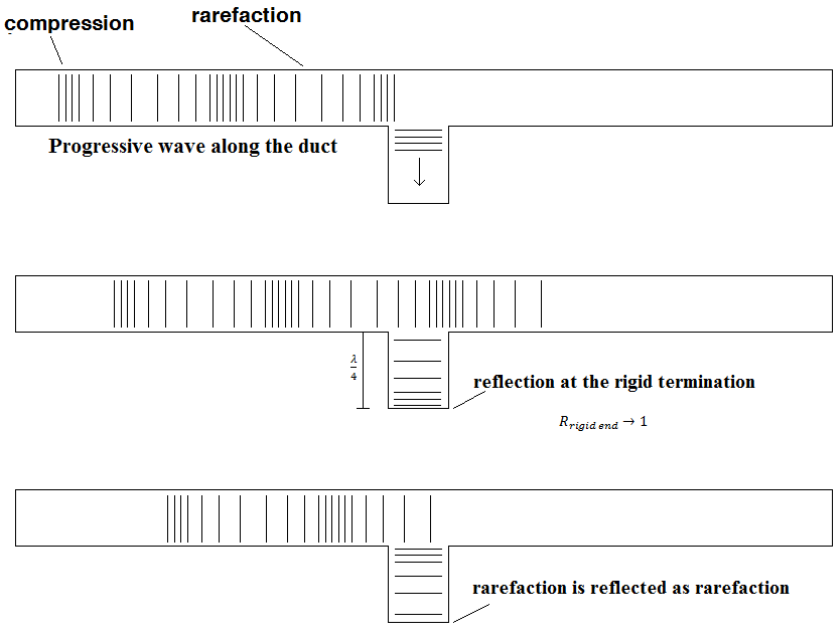


Figure 3.11 – Behavior of quarter-wave resonator.

When the source start to vibrate from the left to the right, a pressure disturbance (consider for simplicity the compression) start travelling along the tube, entering the side branch where it is reflected at the closed termination. If the length of the side tube is equal to $\lambda/4$, the peak of the reflected wave will reach back the open end when the pressure in the main duct is minimum (rarefaction) and so:

1 The sum of compression and rarefaction nullifies the pressure disturbance going downstream
2 the compression is reflected as rarefaction (in order to maintain the low pressure at the open end) and is reflected again as a rarefaction at the rigid end of the resonator.

Then, when such rarefaction reaches again the open end, the pressure in the main duct will be maxima (compression). Such process holds until the source vibrates, not allowing acoustic energy to escape after the junction. Consequently, from the coupling with the source, standing wave are set up into the main pipe with a nodal point (zero pressure fluctuations) at the open end, as the two contributions (the main wave and the reflected one into the side tube) cancel out each other. It follows that no noise will be transmitted at such frequency.

Actually it is important to mention that in real world applications, the end plate of the cavity is not rigid because the reflection coefficient is not unity (see eq. 3.19) but, in general, it may be taken close to 0,95[4]. Moreover, there is another more important thing to note, which is represented by the fact that, in reality, the acoustic length of the resonator is slightly larger than the physical length with which the resonator has been designed[6]. In fact, as it has already been mentioned, even if the frequency is low enough to ensure plane wave propagation, evanescent higher-order modes rise up at the discontinuities. At the location in which such higher-order modes vanish, the plane wave

propagation holds again. Thus, when using the above relationships, the length $L_2$ of the resonator must take into account the end correction for the evanescent modes at the junction, namely $L_2 = L_{geo} + \delta_{end\ correction}$.

### 3.1.6.2 Helmholtz resonator

Another very common type of resonator is represented by the so-called Helmholtz resonator, which owns is name to the scientist Hermann Ludwig Ferdinand von Helmholtz. An Helmholtz resonator is an acoustic element which may be schematized as consisting of a very small tube linked with a closed cavity, as schematically depicted in Figure 3.12. Here again, three interfaces have been highlighted which have been numbered by 1,2 and 3 corresponding to the inlet of the outlet tube, resonator inlet and outlet of the inlet tube respectively. The cavity is characterized by its volume whilst the small tube, which is called cavity's neck, is characterized by both its length and cross-sectional area. From the above concluding remark, in figure below the neck's end correction has been schematically depicted.

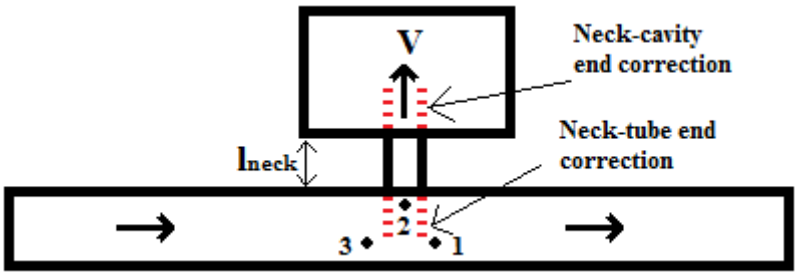


Figure 3.12 – Schematization of an Helmholtz resonator.

Even in this case, the continuity of the acoustic mass flux yields to the same condition as eq. (3.55) and, therefore, the equivalent circuit representation of an Helmholtz resonator is also a shunt element. However, such shunt element is nothing else than a series of lumped inertance and lumped compliance[36]. In other words, the total shunt impedance is the sum of both neck and cavity impedances. Hence, adding the radiation impedance at either side of the neck (in this case it is possible to assume that the neck comes out in two hemispherical spaces)

$$Z_2 = \frac{j\omega l_{hypo}}{S_{neck}} + \frac{1}{j\omega(V/a_0^2)} + 2Y_0\left(\frac{k_0^2 r_0^2}{2}\right)$$

or

$$Z_{Helmholtz} = j\left(\omega\frac{l_{hypo}}{S_{neck}} - \frac{a_0^2}{\omega V}\right) + \frac{\omega^2}{\pi a_0} \tag{3.62}$$

where the hypothetical equivalent neck's length is given by eq.( 3.46). If the radiation resistance terms are neglected, the shunt element would resonate when the corresponding impedance equals zero, namely when

[36] In the limit of the Helmholtz number being less than unity, that is $k_0 L \ll 1$ where L stands for both characteristic lengths of cavity and resonator's neck.

$$\omega = a_0 \sqrt{\frac{S_{neck}}{l_{hypo} V}} \tag{3.63}$$

By dividing eq. (3.63) by the quantity $2\pi$ an expression for the resonant frequency at which the Helmholtz resonator blocks the acoustic transmission to the downstream tube 1 is found. Actually, the acoustic propagation is almost fully blocked, being limited only by the radiation resistance terms. In fact, the acoustic mass velocity in the downstream tube 1 is linked to those in the upstream tube and resonator interface by eq. (3.55). So, the value of $v_1$ is connected also by the value of $v_2$, and this latter, when ω satisfies eq. (3.63), is only limited by the radiation resistance in eq. (3.62).

### 3.1.6.3 Concentric hole-cavity resonator

A resonator which combines all the above mentioned aspect is represented by the concentric hole-cavity resonator. In principle, it mainly consists of an annular cavity communicating with the main tube through several little holes, arranged in circle within the wall of the propagation tube. This layout is schematized in Figure 3.13.

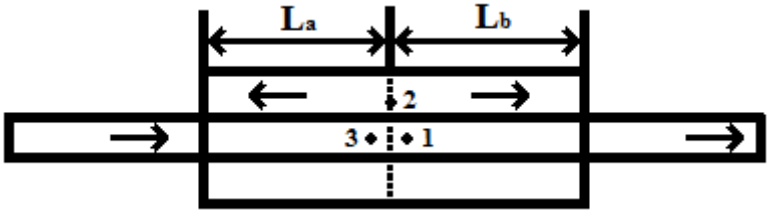


Figure 3.13 – Schematization of a concentric hole-cavity resonator.

As it happens for both the quarter-wave and the Helmholtz resonator, even in this case, within the equivalent circuit representation, such resonator is a shunt element. More precisely, by the examination of Figure 3.13, it can be noted that resonant cavity could be seen as two extended-tube resonator in parallel. Besides, all the little holes in a row, are several shunt lumped inertances too. Therefore, the expression of the impedance at the junction, if rigid end plates hypothesis holds, is

$$Z_2 = \frac{1}{n_h}\left(\frac{j\omega l_{hypo-hole}}{S_{hole}} + \frac{\omega^2}{\pi a_0}\right) + \frac{[-jY_{cav}cot(k_0 L_a)][-jY_{cav}cot(k_0 L_b)]}{-jY_{cav}cot(k_0 L_a) - jY_{cav}cot(k_0 L_b)}$$

$$= \frac{1}{n_h}\left(\frac{j\omega l_{hypo-hole}}{S_{hole}} + \frac{\omega^2}{\pi a_0}\right) - \frac{jY_{cav}}{tan(k_0 L_b) + tan(k_0 L_a)} \tag{3.64}$$

where $n_h$ is the number of holes in one circular row in the propagation tube. It can be easily seen that, in the low frequency range where $tan(k_0 L) \cong k_0 L$, eq. (3.64) reduces to eq. (3.62). Therefore, the Helmholtz resonator is only a lumped-element approximation of the concentric hole-cavity resonator. The resonant frequency of this latter turns out to be that at which the impedance due to the inertance of the holes in the circular row equals the impedance due to the compliance of the cavity, namely when

$$\frac{1}{n_h}\frac{\omega l_{hypo-hole}}{S_{hole}} = \frac{Y_{cav}}{tan(k_0 L_b) + tan(k_0 L_a)} \tag{3.65}$$

where the contribution of the radiation reactance has been neglected.

## 3.2 Acoustic filter performance parameters

From what above, it has been shown how the basic behavior of some elementary elements, constituting acoustic filters, can be represented and easily understood referring to an electro-acoustic analogy. In fact, the whole transmission path from the acoustic source to the receiver may by represented as an equivalent acoustic circuit. As an example, such equivalent circuit representation is shown in Figure 3.14. Of course, as already mentioned, the pressure disturbance replaces the voltage whilst the particle velocity replaces the electric current.

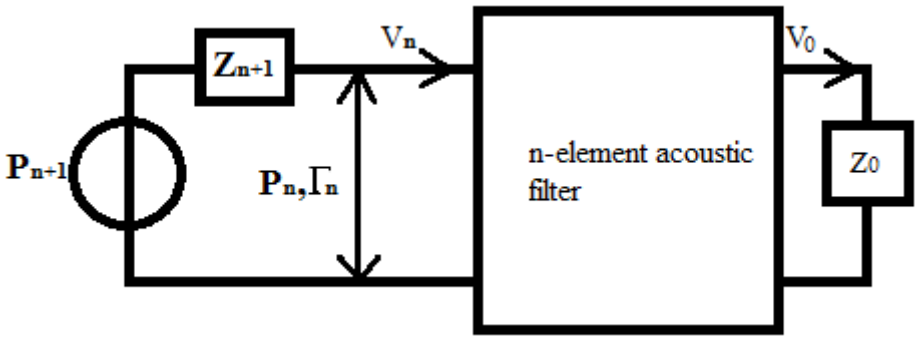


Figure 3.14 – Pressure based equivalent acoustic circuit representation.

Thus, in an equivalent acoustic circuit representation, the sound source is characterized by the fluctuating pressure $p_{n+1}$ and the source impedance $Z_{n+1}$, whilst $Z_0$ represents the load impedance of the acoustic network (radiation impedance). Then, an acoustic filter composed by $n$ elements separates the source from the load and, as it is depicted in Figure 3.14, considering a point $n$ the complete passive subsystem downstream this point can be represented by an equivalent load, characterized by an equivalent impedance $\Gamma_n$. Such equivalent impedance consists of filter impedance and radiation impedance. Therefore, following the Kirchhoff law, for a fixed source and load, the particle velocity at point *n* may be expressed as

$$v_n = \frac{p_{n+1}}{Z_{n+1} + \Gamma_n}$$

This source representation (analogous to the voltage generator convention in electric theory) is not the only possible. In fact, thanks to the Thévenin and Norton theorems[5], the voltage-pressure source representation of Figure 3.14 may be replaced by a current-velocity source representation of Figure 3.15, where the new generator provides a particle velocity to the network which is equal to

$$v_{n+1} = \frac{p_{n+1}}{Z_{n+1}}$$

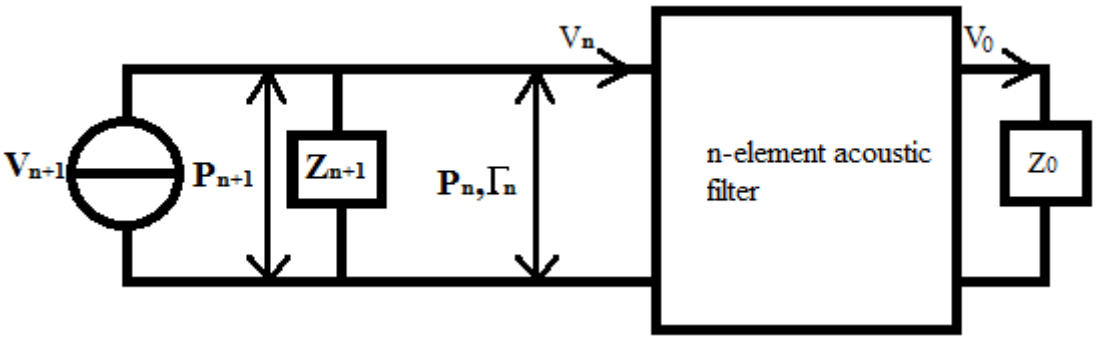


Figure 3.15 – Velocity based equivalent acoustic circuit representation.

Now, considering an internal combustion engine, the primary source of acoustic disturbances is represented by the periodic flow triggered by the inlet/exhaust valve openings. Figure 3.16 shows a schematization of the acoustic transmission path between an internal combustion engine and the atmosphere (exhaust side).

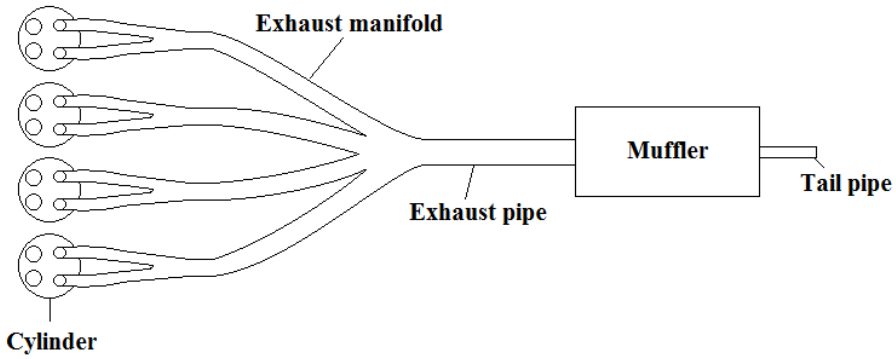


Figure 3.16 – Example of acoustic transmission path between an internal combustion engine and the atmosphere.

Immediately after the internal combustion engine, there is always a small diameter pipe (with one or more bifurcation depending on the number of cylinders) called exhaust manifold followed by a greater diameter pipe, which generally represents the proper muffler (actually, before the silencer there is always the after treatment system for the reduction of pollution emissions). Finally, the muffler is linked to the atmosphere thanks to another small diameter pipe called tail pipe. Generally, for a n-element system, the tail pipe is numbered as first whilst the exhaust pipe as the $n^{th}$. The acoustic performance characterization of an acoustic filter (or, more in general, an acoustic transmission path) is often evaluated in terms of three particular parameters which are called

- Insertion Loss (IL)
- Transmission Loss (TL)
- Noise reduction (NR)

### 3.2.1 Insertion Loss

The insertion loss is defined as the difference between the sound power level radiated by the sound source in two conditions, namely without and with an acoustic filter located in the transmission path. Mathematically this may be expressed as

$$IL = 10Log\left(\frac{W_1}{W_2}\right) \tag{3.68}$$

where the subscripts 1 and 2 stand for the without and with filter configuration respectively. Intuitively, the radiation impedances in the two cases differ and may be indicated as $Z_{0,1}$ and $Z_{0,2}$ which represent the radiation impedance without and with the acoustic filter. Thus, the equivalent acoustic circuit is depicted in Figure 3.17.

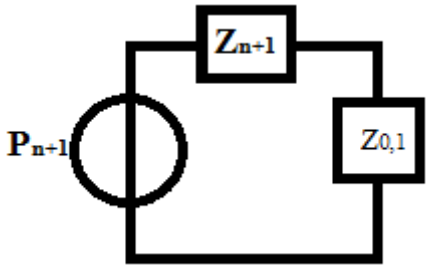


Figure 3.17– Acoustic system without filter.

By referring to an electric nomenclature, considering Figure 3.17, the power output dissipated at the radiation impedance (which means radiated to the atmosphere), is

$$W_1 = \frac{1}{2\rho_{0,1}} PVcos(\vartheta) = \frac{1}{2\rho_{0,1}} R_{0,1}V^2 = \frac{1}{2\rho_{0,1}} \left|\frac{p_{n+1}}{Z_{n+1} + Z_{0,1}}\right|^2 R_{0,1}$$

where only the radiation resistance term $R_{0,1}$ appears because it is the only responsible for the acoustic radiation. Similarly, the power output when the acoustic filter is located between the sound source and the atmosphere equals

$$W_2 = \frac{1}{2\rho_{0,1}} |V_0|^2 R_{0,2} \tag{3.70}$$

By substituting the expression of $W_1$ and $W_2$ in eq. (3.68) yields

$$IL = 10Log\left[\frac{\rho_{0,2}R_{0,1}}{\rho_{0,1}R_{0,2}} \left|\frac{p_{n+1}}{(Z_{n+1} + Z_{0,1})V_0}\right|^2\right]$$

$$= 20Log\left[\left(\frac{\rho_{0,2}R_{0,1}}{\rho_{0,1}R_{0,2}}\right)^{\frac{1}{2}} \left|\frac{Z_{n+1}}{Z_{n+1} + Z_{0,1}}\right| \left|\frac{V_{n+1}}{V_0}\right|\right]$$

Defining the velocity ratio for a passive subsystem with $r$ elements as

$$VR_r = \frac{v_r}{v_0} \qquad \text{for} \qquad v_0 \neq 0 \quad \text{and} \quad p_0 = 0$$

The expression for the insertion loss becomes

$$IL = 20Log\left[\left(\frac{\rho_{0,2}R_{0,1}}{\rho_{0,1}R_{0,2}}\right)^{\frac{1}{2}} \left|\frac{Z_{n+1}}{Z_{n+1}+Z_{0,1}}\right| |VR_{n+1}|\right] \tag{3.73}$$

Now, considering Figure 3.14, the acoustic power flux entering the filter may be expressed as

$$W_e = \frac{1}{2\rho_{0,e}}|v_n|^2 R_n = \frac{1}{2\rho_{0,e}}\left|\frac{Z_{n+1}v_{n+1}}{Z_{n+1}+\Gamma_n}\right|^2 R_n$$

whilst the acoustic power living the filter is given by eq. (3.70). If the filter is a non-dissipative one, the energy conservation requires that

$$\frac{1}{2\rho_{0,e}}|v_n|^2 R_n = \frac{1}{2\rho_{0,e}}\left|\frac{Z_{n+1}v_{n+1}}{Z_{n+1}+\Gamma_n}\right|^2 R_n = \frac{1}{2\rho_{0,2}}|v_0|^2 R_{0,2}$$

Rearranging

$$|VR_n|^2 = \left|\frac{Z_{n+1}}{Z_{n+1}+\Gamma_n}\right|^2 |VR_{n+1}|^2 = \frac{\rho_{0,e}}{\rho_{0,2}}\frac{R_{0,2}}{R_n} \cong \frac{\rho_{0,1}}{\rho_{0,2}}\frac{R_{0,2}}{R_n}$$

By obtaining the velocity ratio for the source from the above equation and substituting it in eq. (3.73), holds

$$IL = 20Log\left[\left(\frac{R_{0,1}}{R_n}\right)^{\frac{1}{2}}\left|\frac{Z_{n+1}+\Gamma_n}{Z_{n+1}+Z_{0,1}}\right|\right] \sim 10Log\left(\frac{R_{0,1}}{R_n}\right) \tag{3.77}$$

since generally (unless $Z_{n+1}$ is much less than the radiation impedance)

$$\left|\frac{Z_{n+1}+\Gamma_n}{Z_{n+1}+Z_{0,1}}\right| \sim 1$$

Therefore, the above equation turns out to be very important for understanding conceptually how non-dissipative mufflers work. In fact, as indicated by eq. (3.77), the real action of a non-dissipative muffler consists in reducing the acoustic resistance seen by the source. In fact, the acoustic resistance equals $R_{0,1}$ without muffler and $R_n$ with muffler.

### 3.2.2 Transmission Loss

Referring to Figure 3.18, the Transmission Loss is defined as the difference between sound power level incident on the muffler proper and the sound power level transmitted downstream, into an anechoic termination. As already mentioned, an anechoic termination is such that no wave reflections are allowed.

$$TL = L_{Wi} - L_{Wt}$$

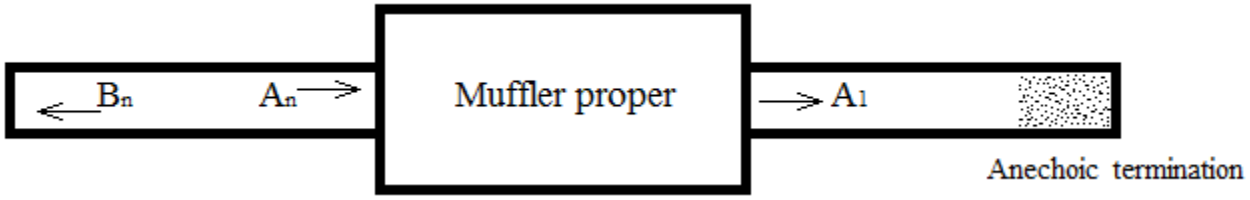


Figure 3.18 – Transmission Loss definition.

Such parameter is independent from both the source impedance and radiation impedance and so it describes the acoustic performance of the proper muffler. Thus, an analysis in terms of Transmission Loss, represent the stand-alone study of the component, without taking into account its coupling with a specific acoustic source. In terms of progressive wave components, the two sound powers may be expressed as

$$W_i = \frac{1}{2\rho_0} A_n \left(\frac{A_n}{Y_n}\right) = \frac{{A_n}^2}{2\rho_0 Y_n} \quad , \quad B_n \neq 0$$

$$W_t = \frac{1}{2\rho_0} A_1 \left(\frac{A_1}{Y_1}\right) = \frac{{A_1}^2}{2\rho_0 Y_1} \quad , \quad B_1 = 0$$

Therefore, if the exhaust pipe (representing the last part of the exhaust manifold) and the tail pipe have the same diameter (as it generally happens), the expression for the Transmission Loss is

$$TL = 20Log \left|\frac{A_n}{A_1}\right| \quad , \quad B_1 = 0 \tag{3.82}$$

The direct measurement of the TL is not as easy as its numerical calculation inasmuch the amplitude of the incident wave $A_n$ cannot be directly measured, because of the presence of the reflected wave $B_n$. Besides, perfect anechoic terminations are difficult to reproduce in laboratories. Nevertheless, the direct Transmission Loss calculation is still possible in some cases. For example, if both the exhaust and tail pipe have diameters which ensure plane waves for a wide frequency range, measurement of acoustic pressure and particle velocity may be executed so that the amplitude of the waves may be expressed as

$$A_1 = Y_1 v_1$$

$$A_n = \frac{p_n + Y_n v_n}{2}$$

Therefore eq. (3.82) becomes

$$TL = 20Log \left|\frac{p_n + Y_n v_n}{2 Y_1 v_1}\right| \tag{3.85}$$

Actually, from an experimental point of view, the Transmission Loss measurement is generally achieved in a smarter way, relying on the Transfer Matrix theory. This, as it will be explained more ahead in chapter 5, is done by making use of the so-called impedance tube technology for which it is only necessary to measure the acoustic pressure.

### 3.2.3 Noise Reduction

The Noise Reduction (which is also known as Level Difference) is defined as the difference in sound pressure level between two arbitrary points in the exhaust and tail pipe, as it is schematically depicted in Figure 3.19. Unlike the Transmission Loss, the Noise reduction makes use of the acoustic pressure and does not require an anechoic termination.

$$NR = 20Log \left|\frac{p_n}{p_1}\right|$$

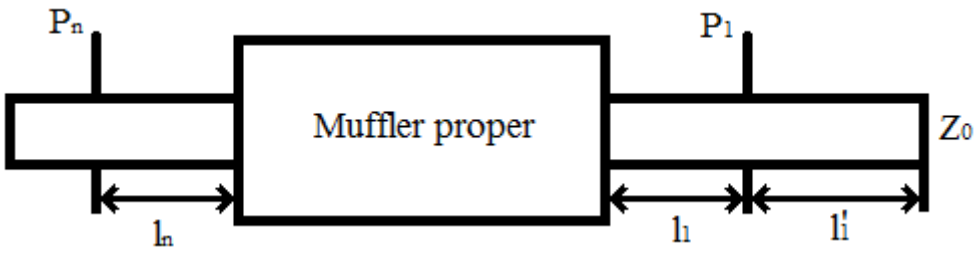


Figure 3.19 – Noise reduction definition.

Since $p_1$ may be not directly known, the Noise Reduction may be evaluated as

$$NR = 20Log\left|\frac{p_n}{p_0}\frac{p_0}{p_1}\right|$$

and the ratio $\frac{p_0}{p_1}$ may be evaluated by means of the wave components in an extra pipe of length $l_1'$. In fact

$$p_1 = A_1 + B_1$$

then

$$p_0 = A_1 e^{-jk_0 l_1'} + B_1 e^{+jk_0 l_1'}$$

$$v_0 = \frac{1}{Y_1}\left(A_1 e^{-jk_0 l_1'} - B_1 e^{+jk_0 l_1'}\right)$$

Hence

$$A_1 = \frac{p_0 + Y_1 v_0}{2} e^{+jk_0 l_1'}$$

$$B_1 = \frac{p_0 - Y_1 v_0}{2} e^{-jk_0 l_1'}$$

Therefore, after explicating the complex exponential, $p_1$ may be calculated as

$$p_1 = p_0 cos(k_0 l_1') + jY_1 v_0 sin(k_0 l_1')$$

and

$$NR = 20Log\left|\frac{p_n/p_0}{cos(k_0 l_1') + j\,Y_1/Z_0\,sin(k_0 l_1')}\right|$$

If the acoustic pressure is evaluated at the end of the tail pipe ($l_1' \to 0$), then

$$NR = 20Log\left|\frac{p_n}{p_0}\right|$$

Among the above introduced acoustic performance parameters, the Insertion Loss is the only one which truly characterizes the acoustic performance of a filter in real operating conditions, because it

represents the loss in the radiated sound power due to the insertion of the filter between the sound source and the receiver. However, its measurement may be laborious because it requires the knowledge of the source impedance $Z_{n+1}$ and radiation impedance $Z_0$. On the other hand, the Transmission Loss is independent from the sound source and it is only affected by the geometry of the filter. Nevertheless, its measurement would rely on the use of an anechoic termination, which is very difficult to experimentally reproduce, as well as specific instrumentation for the measurement of the incident wave in a standing wave acoustic field (e.g. impedance tube technology)[10]. The Noise Reduction represents instead a simple measure of the sound pressure level drop when the acoustic filter is inserted between source and atmosphere, without any boundary condition imposed at the termination of the tail pipe. It follows that the NR is the most easily adopted parameter, in order to have a first idea on the acoustic behavior of the acoustic filter.

Just as an example and in order to further clarify how a resonator works, the Transmission Loss of both a quarter-wavelength and an Helmholtz resonator have been numerically calculated for the geometries depicted in figure below. Thanks to the characteristics dimensions, which have been reported in Figure 3.20, it is easy to find that the analytical values of the resonant frequency would be equal to[37] $500$ and $451\ Hz$ for the quarter-wave and Helmholtz resonator respectively. However, for what has been previously highlighted, the resonance should not occur at such frequencies due to the end correction which makes the acoustical lengths slightly different with respect to the geometrical ones, lowering the frequency at which resonance would occur.

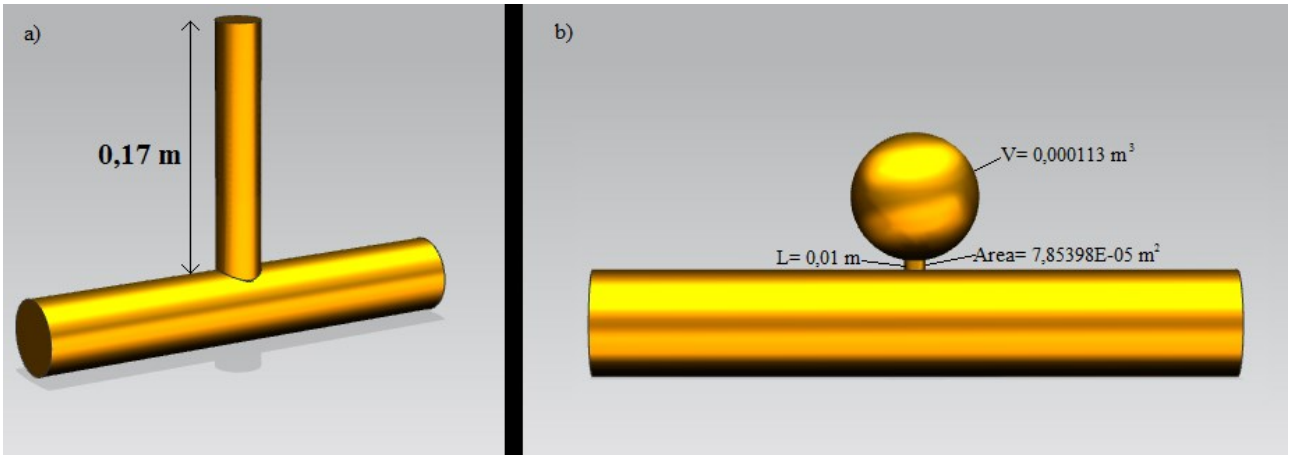


Figure 3.20 – Example of resonator geometry: a) quarter-wave and b) Helmholtz.

The corresponding results in terms of Transmission Loss are depicted in figure below. Here it is possible to appreciate the characteristic acoustic behavior of these basic resonators, together with the end correction effect. In fact, the resonances occur at slightly lower frequencies with respect to those calculated by means of eq.(3.60) and (3.63) due to a greater acoustical lengths.

[37] Considering $a_0 = 340\ m/s$.

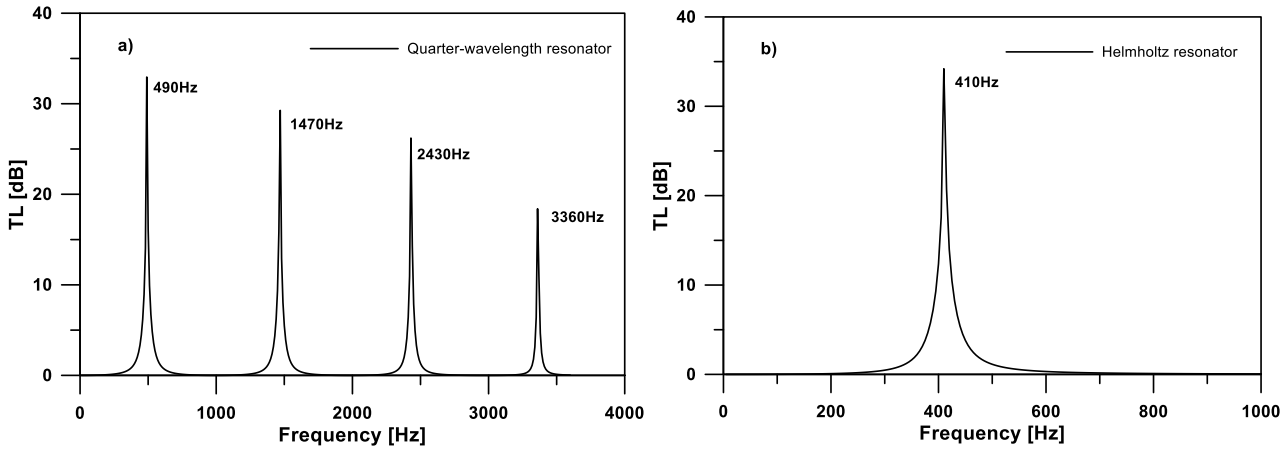


Figure 3.21 – Transmission Loss: a) quarter-wave and b) Helmholtz resonator.

Thus, it is possible to point out that the main difference in the effect produced by these two types of resonator lies in the fact that the quarter-wave resonator is characterized by several resonant frequencies in correspondence of which a decreasing high Transmission Loss peaks occur. For this reason, it is generally adopted in expansion chamber in a way such that a very widespread attenuation spectrum is achieved[6][7]. Vice versa, Helmholtz resonators, allowing very sharp TL peaks, are generally used to cancel out specific frequencies within duct systems.

### 3.2.4 Simple area discontinuities

The very basic elements of reflective silencers are represented by area discontinuities. This is because, when pressure waves travel on a transmission line, every discontinuities is thereby encountered causes a reflection to arise. The magnitude of such reflections is strongly affected by the entity of the discontinuity. Two types of simple are discontinuities exist, which are sudden expansion and sudden contraction; both are schematically reported in Figure 3.22. Here two interfaces have been highlighted and indicated with 1 and 2, representing the outlet of the inlet tube and the inlet of the outlet tube respectively.

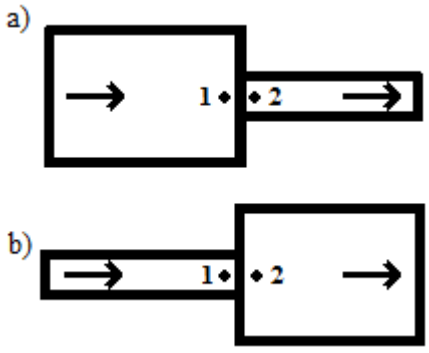


Figure 3.22 – Simple area discontinuities: a) sudden contraction, b) sudden expansion.

If the diameters of both tubes are such that plane wave propagation is ensured, the acoustic pressure and acoustic mass velocity stay uniform across the discontinuity, namely

$$p_1 = p_2$$

$$v_1 = v_2$$

It follows that also the specific impedance stays the same across the discontinuity, that is

$$\Gamma_1 = \frac{p_1}{v_1} = \frac{p_2}{v_2} = \Gamma_2$$

So, since acoustic quantities remain unchanged across a simple are discontinuity, such element is not represented at all within the equivalent acoustic circuit. However, it represents the real basis for the operation of low-pass filters. In fact, as already seen many times previously, both the acoustic pressure and the acoustic mass velocity may be expressed in terms of complex amplitudes of the two progressive wave components in the standing wave field, namely

$$A_1 + B_1 = A_2 + B_2 \tag{3.99}$$

$$\frac{A_1 - B_1}{Y_1} = \frac{A_2 - B_2}{Y_2} \tag{3.100}$$

If an anechoic termination is present, that is $B_2 = 0$, then

$$\Gamma_1 = \Gamma_2 = Y_2$$

and the reflection coefficient is given by

$$R_1 = \frac{B_1}{A_1} = \frac{\Gamma_1 - Y_1}{\Gamma_1 + Y_1} = \frac{Y_2 - Y_1}{Y_2 + Y_1} = \frac{S_1 - S_2}{S_1 + S_2} \tag{3.102}$$

So, from eq. (3.102), it is clear that for a sudden are contraction $S_1 > S_2$ ➔ $0 < R < 1$ and for a sudden expansion $S_1 > S_2$ ➔ $-1 < R < 0$. Moreover, similarly to what has been done for the Transmission Loss calculation, the incident, transmitted and reflected acoustic power may be expressed in terms of standing wave components as

$$W_i = \frac{{A_1}^2}{2\rho_0 Y_1}$$

$$W_t = \frac{{A_2}^2}{2\rho_0 Y_2} \quad , \quad B_2 = 0$$

$$W_r = \frac{{B_1}^2}{2\rho_0 Y_1}$$

The net energy flux in the upstream tube can now be written as

$$W_1 = W_i - W_r = \frac{{A_1}^2 - {B_1}^2}{2\rho_0 Y_1}$$

At the same time the power in the downstream tube may be expressed as

$$W_2 = \frac{{A_2}^2}{2\rho_0 Y_2}$$

But by combining eq. (3.99) and (3.100)[38], it can be easily seen that no loss of power happens in a sudden area change, namely

$$W_1 = W_2$$

Such components just reflect part of the incident power (related to the magnitude of the reflection coefficient) back to the source, simply creating a mismatch of the characteristic impedance of the tube ($Y_1 \neq Y_2$). As such, it is justified that they are the basic element for non-dissipative or reflective mufflers. The Transmission Loss for a sudden area change may be obtained as follows

$$TL = 10Log\left(\frac{{A_1}^2}{{A_2}^2}\frac{Y_2}{Y_1}\right)$$

$$= 10Log\left(\frac{1}{1 - R_1^2}\right)$$

$$= 10Log\left[\frac{(S_1 + S_2)}{4S_1S_2}\right]$$

## 3.3 Introduction to the study of porous materials

Previously, the basic concepts of reflective mufflers have been highlighted and it has already been mentioned that other devices exist whose acoustic attenuation characteristics do not rely on successive sound reflections thanks to impedance mismatching. The other mechanism through which sound may be attenuated is by means of energy dissipation, namely from kinetic to heat, and occurs when porous materials are present. The devices which are based on such energy conversion are generally referred as silencers rather than dissipative mufflers and they are capable of providing a wide broadband sound attenuation. This is realized thanks to the high absorption property of lining materials such as porous materials. On the contrary, at low frequencies far worse acoustic performances are achieved. This is due to the dissipation mechanism which relies on friction forces, generated among air particles in motion, which take place more efficiently at high frequency.

When referring to porous material the word "porous" refers to a material that has pores, or holes in its surface. As such, porous absorbers consist usually of thin mineral, metal or glass wool fibers (with a diameter of $2 - 30\mu m$), arranged in layers and with random fiber orientations in planes parallel to the material surface. When the sound propagates, the air is forced to pass thorough the small voids included in the material, which generates frictions converting the acoustic energy into heat. Another phenomenon which occurs is the fluid structure interaction between the vibrating particles and the material fiber, which implies kinetic energy losses of the particles.

In acoustics, the main purpose of analytic models of porous materials is being able to predict the acoustic behavior in terms of absorption coefficient. From a very simple viewpoint, when a sound wave encounters an obstacle, part of the energy it carries is reflected at the interface, part is dissipated (or absorbed) and the remainder is transmitted. This is schematically depicted in Figure 3.23.

[38] $A_2^2 = (A_1 + B_1)(A_1 - B_1) = A_1^2 - B_1^2$.

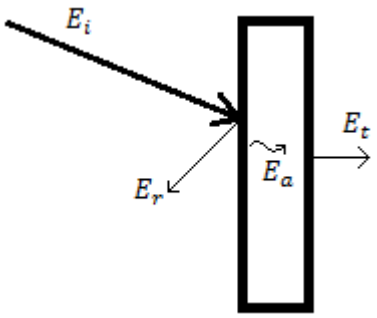


Figure 3.23- Energy balance schematization

Thus, thanks to a simple energy balance, it is possible to write

$$E_i = E_a + E_t + E_r \tag{3.110}$$

or

$$1 = \alpha + \tau + \gamma \tag{3.111}$$

where $\alpha$ , $\tau$ and $\gamma$ are the absorption, transmission and reflection coefficient respectively. The way in which fibrous materials reduce noise is by means of a high absorption coefficient, which characterizes the capacity of dissipating sound energy into heat. Such mechanism of energy conversion is achieved thanks to the air particle vibrating within the material itself.

The goodness of a model is generally measured in terms of correlation between experimental data and predicted ones. In order to understand the usefulness of very simple models, like that of Delaney and Bazley or Miki, it is important to understand how the absorption coefficient is calculated. Recalling eq.(3.10), the specific acoustic impedance at any point in a *standing wave field* is defined as

$$\Gamma(x) = \frac{p'(x,t)}{v'(x,t)} = Y_0 \frac{Ae^{-jk_0x} + Be^{jk_0x}}{Ae^{-jk_0x} - Be^{jk_0x}} \tag{3.112}$$

Considering Figure 3.24, the impedance at two points may be rewritten as

$$\Gamma(P) = \frac{p'(x_p,t)}{v'(x_p,t)} = Y_0 \frac{Ae^{-jk_0x_p} + Be^{jk_0x_p}}{Ae^{-jk_0x_p} - Be^{jk_0x_p}} \tag{3.113}$$

$$\Gamma(Q) = \frac{p'(x_q,t)}{v'(x_q,t)} = Y_0 \frac{Ae^{-jk_0x_q} + Be^{jk_0x_q}}{Ae^{-jk_0x_q} - Be^{jk_0x_q}} \tag{3.114}$$

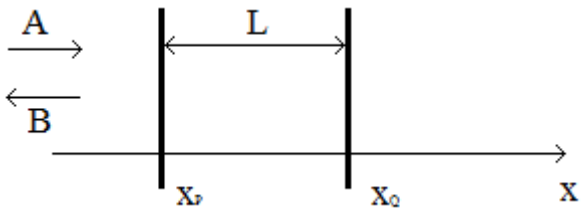


Figure 3.24 – Schematization of a standing waves field.

At the same time, thanks to its definition and the use of eq. (3.113), the reflection coefficient may be expressed as

$$R = \frac{B}{A} = \frac{\Gamma(P)-Y_0}{\Gamma(P)+Y_0} e^{-2jkx_p} \tag{3.115}$$

Now, by means of the impedance translation theorem, it is possible to express the impedance at point P as function of that at point Q, namely

$$\Gamma(P) = \frac{\Gamma(Q)\cos(k_0 L)+j\,Y_0 \sin(k_0 L)}{\cos(k_0 L)+j\Gamma(Q)/Y_0 \sin(k_0 L)} \tag{3.116}$$

Suppose that a layer of fluid 1 is bounded by a rigid termination on one side and by another fluid on the other side, as schematically depicted in Figure 3.25.

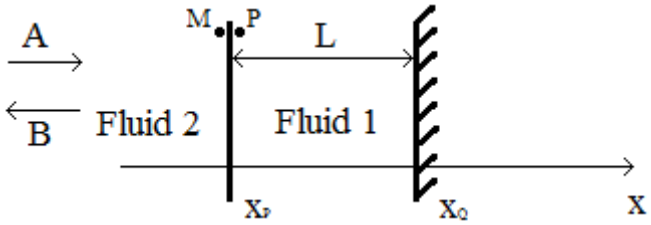


Figure 3.25- Multy-layered fluid system schematization

As it has already pointed out, since the impedance at the rigid termination goes to infinity, the impedance at Q equals

$$\Gamma(x_P)_{rigid\ end} = -jZ_{f1}\cot(k_{f1}L) \tag{3.117}$$

where $Z_{f1}$ and $k_{f1}$ are the characteristic impedance and wavenumber in fluid 1. Obviously, because of the continuity of both pressure and particle velocity at the interface between the two fluids, it follows that

$$\Gamma(P) = \Gamma(M) \tag{3.118}$$

Therefore, according to this layout, if $Z_{f1}$ and $k_{f1}$ are known, it would be possible to calculate the reflection coefficient at the interface by means of eq. (3.115). Then the absorption coefficient may be calculated as[39]

$$\alpha = 1 - |R|^2 \tag{3.119}$$

Hence, assuming a layer of porous material as an equivalent fluid, if it would be possible to know an analytic expression characterizing both the characteristic impedance and the wavenumber of such porous material it would be possible to calculate the absorption coefficient.

[39] $R$ is expressed in terms of amplitude of pressure and energy is proportional to the square of pressure.

### 3.3.1 Equivalent fluid models

Porous materials may be thought as made of an elastic frame in which closed or open cavities are embedded. With such a description, it is possible to define the total volume of the porous material as the summation of the frame volume and cavities volume, namely

$$V_T = V_C + V_F \tag{3.120}$$

Generally, the material is surrounded by air such that the cavities volume is termed air volume. Fibrous materials are often characterized by means of the so called porosity, which defines how much of the total volume is occupied by cavities. Consequently, the porosity is defined as the ratio of the cavities volume to the total volume of the porous material, namely

$$\emptyset = \frac{V_C}{V_T} \tag{3.121}$$

and it is generally very high being for most porous materials very close to unity. As it should be clear, from a sound absorption point of view, only the so called open porosity materials are of interest, since only in such mediums the air is not locked into the frame and sound waves may propagate through the cavities, causing kinetic energy to be dissipated into heat by friction during air particles motion.

Another very important parameters governing the sound absorption of porous materials is the so called flow resistivity. If a constant differential pressure is imposed across a layer of porous material having a certain degree of open porosity, then a steady flow will be induced through the material. Then, the flow resistivity is defined as the ratio of the pressure differential across a sample of porous material to the normal flow velocity through it. According to Figure 3.26, it may be expressed as

$$\sigma = \frac{(p_1 - p_2)}{vh} \tag{3.122}$$

which is generally within the range $[1000, 100000]\ Nm^{-4}s$.

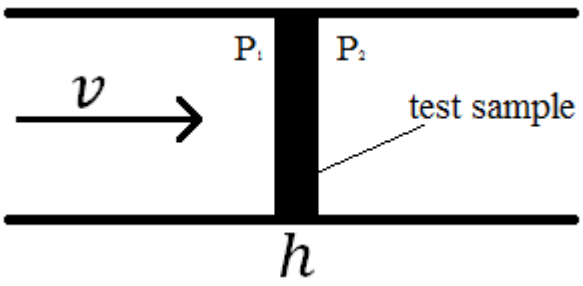


Figure 3.26- Flow resistivity measurement layout schematization

Based only on such parameter, the most utilized model for absorbent material is the semi-empirical equivalent fluid model developed by Delany and Bazley [8]. They have proposed analytical expressions for both complex wave number and characteristic impedance of porous materials. From a large number of measurements on fibrous materials with open porosities close to unity, they found the following empirical expressions in order to fit the experimental data[8]

$$\begin{cases} Z_{f,eq} = \rho_0 a_0 (1 + 0.057X^{-0.754} - j0.087X^{-0.732}) \\ k_{f,eq} = \frac{\omega}{a_0}(1 + 0.0978X^{-0.7} - j0.189X^{-0.595}) \end{cases} \tag{3.123}$$

where $X = \rho_0 f/\sigma$ and the following range of validity has been suggested

$$0.01 < X < 1.0 \tag{3.124}$$

Another analytical expression for both impedance and wavenumber has been proposed by Miki which is supposed to better match experimental data when multi layers are present[9]. The proposed corrections are reported below

$$\begin{cases} Z_{f,eq} = \rho_0 a_0 \left[1 + 5.5\left(10^3 \frac{f}{\sigma}\right)^{-0.632} - j8.43\left(10^3 \frac{f}{\sigma}\right)^{-0.632}\right] \\ k_{f,eq} = \frac{\omega}{a_0}\left[1 + 7.81\left(10^3 \frac{f}{\sigma}\right)^{-0.618} - j11.41\left(10^3 \frac{f}{\sigma}\right)^{-0.618}\right] \end{cases} \tag{3.125}$$

where $X = 10^3 f/\sigma$. The range of validity of the Miki's formulation has been suggested by the author himself as follows

$$0.01 < f/\sigma < 1.0 \tag{3.126}$$

It should not be expected that such simple expressions succeed in modelling the acoustic behavior of all the porous material. Nevertheless, thanks to the fact that only on input parameter is required, they are widely used providing reasonable values of both $Z_{f,eq}$ and $k_{f,eq}$.

## Bibliography


[1] M. L. Munjal, “Acoustics of Ducts and Mufflers with Application to Exhaust and Ventilation System Design”, John Wiley & Sons.

[2] J.W.S. Rayleigh, “The Theory of Sound”, Vol II.

[3] H. Levine, J. Schwinger, “On the Radiation of Sound from an Unflanged Circular Pipe”, Physical Review, Vol. 73, Issue 4 - February 1948, DOI: https://doi.org/10.1103/PhysRev.73.383.

[4] R. J. Alfredson, P. O. A. L. Davies, “Performance of exhaust silencer components”, Journal of Sound and Vibration, 15(2), 175-196 (1971).

[5] S. Falco, L. Verolino, “Elementi di elettrotecnica”, Liguori editore, 2003, EAN: 9788820736309.

[6] M. L. Munjal, “Recent Advances in Muffler Acoustics”, International Journal of Acoustics and Vibration, Vol. 18, No. 2, pp. 71-85,2013.

[7] E. Ramya, M. L. Munjal, “Improved tuning of the extended concentric tube resonator for wide-band transmission loss”, Noise Control Engineering Journal, Volume 62, Number 4, 1 July 2014, pp. 252-263(12).

[8] J. Allard, N. Atalla, “Propagation of Sound in Porous Media: Modelling Sound Absorbing Materials”, John Wiley & Sons, ISBN: 978-0-470-74661-5.

[9] Miki Y., Acoustical properties of porous materials - Modifications of Delany-Bazley models, J. Acoust. Soc. Jpn (E). 11(1), 1990, pp. 19-24.

[10] Bruel & Kjaer, “Transmission Loss Measurements in a Standing Wave Tube”. Techincal Review N°1 2007.

# Chapter 4

# Finite Element Method in Acoustics

## Introduction

The finite element method is probably the most useful and efficient tool which engineers have available for solving almost all real life problems[1][3]. In fact, without such a powerful method, it would not be possible to solve such problems for which an analytical solution does not exists so far. For what concerns the topic of sound related phenomena, acoustic problems span between two main categories, which are interior and exterior radiation problems. All those acoustic phenomena involving physical boundaries of the domain to be analyzed are grouped within the first category. Vice versa, when there are no boundaries and the sound field has to be evaluated in free field condition, the problem to be dealt with is an exterior acoustic problem. In principle, the traditional finite element approach may be used for solving interior acoustic problems only, since the computational domain must be of finite extension. Nevertheless, alternative formulations exist, which allows the use of FE method to solve also exterior acoustic problems, as it will be mentioned at the end of this paragraph. The basic idea is, once the equation of the physical phenomenon has been established together with the proper set of boundary conditions, to reduce the issue of finding the distribution of one or several field variables within a continuum domain, through the solution of a complicated partial different equation problem (which is in general not possible), to the issue of solving a linear system composed by a huge amount (but a finite number) of linear equations. Such a beautiful trick is made real by a discretization process of the continuum domain, which is divided in a lot of elements connected together by nodes, as depicted, for example, in Figure 4.1. The discretized domain is commonly called mesh.

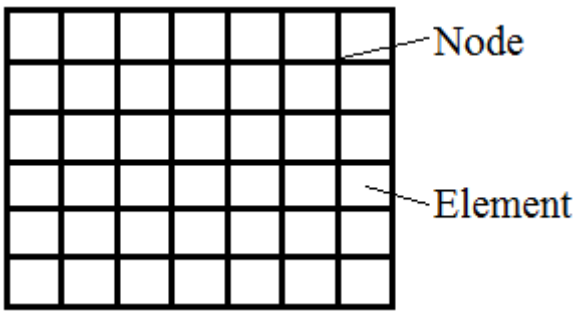


Figure 4.1 – Example of discretization of a plate.

Thus, the finite element approach relies on two fundamental steps. During the first, the original partial differential equation, governing the physic of the problem, is transformed into an equivalent integral formulation which is also known as weighted residual or variational form of the original problem. Then, the integral equation is transformed in a set of linear algebraic equations, for which numerical solution procedures are readily available, thanks to discretization of the domain and approximation of the field variable[1][2][3][4]. This latter is approximated by means of an expansion in terms of so called shape-function, which are locally defined within small subdomains

('finite elements') of the discretized domain. Such steps are mandatory for whatever FE formulation, for each physical problem, the differences laying in the governing equation to be discretize as well.

## 4.1 Problem statement

Since the focus is on acoustics, let's start from the basic governing equations. As mentioned before, sound propagation is an oscillatory phenomenon, which causes an energy propagation through a medium by means of waves. Focusing on a bounded fluid domain $\mathcal{V}$ enclosed by a closed surface $S$, in which a time-harmonic external source distribution is present, considering the air as propagation medium, the acoustic pressure distribution (if the medium is at rest) is mathematically described by the classical wave equation in which source term is kept, namely

$$\left[\frac{1}{a_0^2}\frac{d^2}{dt^2} - \nabla^2\right] p' = \dot{q} \tag{4.1}$$

where $a_0$ is the so-called phase speed of the small perturbation and $\dot{q}$ is the source term. Practically always in acoustics, the focus is on the frequency domain rather than the time domain, and so the frequency domain version of eq. (4.1) is represented by the so called Helmholtz equation, namely[40]

$$\nabla^2 p + k^2 p = -j\omega q \tag{4.2}$$

where $p$ is the complex valued amplitude of the wave at the angular frequency $\omega = 2\pi f$ and $k$ is the spatial frequency, or the wave number, which is equal to $\frac{\omega}{a_0}$. Equation (4.2) is called the *strong form* of the Partial Differential Equations (PDE) problem because of the fact that is the only one which, if solved together with the boundary conditions, would give the exact solution. In fact, in order to uniquely define the acoustic pressure field within the domain $\mathcal{V}$, one or a set of boundary conditions must be specified on the closed boundary surface. Traditionally, the most simple and commonly used boundary conditions are:

1) Imposed pressure, namely
$$p = p_b \tag{4.3}$$

2) Imposed normal velocity[41] which, making use of the momentum balance equation, may be expressed as
$$V_n = -\frac{1}{j\omega\rho_0}\frac{\partial p}{\partial n} = V_{n,b} \tag{4.4}$$

3) Imposed normal impedance, namely
$$p = Z_b V_n = Z_b \frac{j}{\omega\rho_0}\frac{\partial p}{\partial n} \tag{4.5}$$

It follows that the entire closed surface, bounding the acoustic domain, may be expressed as sum of the surfaces on which the above mentioned boundary conditions are applied, namely

$$S = S_p + S_v + S_Z \tag{4.6}$$

[40] If the time dependence of the source term is of the type $q = \hat{q}e^{j(\omega t - kx)}$ then $\dot{q} = j\omega q$.
[41] Also known as Neumann boundary condition[6].

Unfortunately, the Helmholtz equation cannot be solved as it is and there is the need of finding a more easily solvable form, which leads to an approximate solution. One available option is represented by the use of the so-called weighted residuals method, which is described in the following, and represents a very smart way to make eq. (4.2), together with the boundary conditions, more suitable for being handled (and solved) by a computer.

Inserting within the Helmholtz equation a trial unknown solution $\tilde{p}$, instead of the exact solution $p$, the right hand side would be different from zero and, more precisely, a residual would appear.

$$\nabla^2\tilde{p} + k^2\tilde{p} + j\omega q = R \neq 0 \tag{4.7}$$

Therefore, it is intuitively that, in order to find the best trial solution which approximates the exact one, the residual must tend to zero. In other words, by integrating the residual over the domain, the trial solution has to satisfy the following condition

$$\int_{\mathcal{V}}(\nabla^2\tilde{p} + k^2\tilde{p} + j\omega q)w\, d\mathcal{V} = 0 \tag{4.8}$$

or

$$\int_{\mathcal{V}} w\nabla^2\tilde{p}\, d\mathcal{V} + \int_{\mathcal{V}} wk^2\tilde{p}\, d\mathcal{V} + \int_{\mathcal{V}} wj\omega q\, d\mathcal{V} = 0 \tag{4.9}$$

where $w$ is an arbitrary weighting function and it is the analogue of the virtual displacement used in the virtual work principle[1]. Since the volume integral in eq. (4.9) is extended to the whole domain, it is referred as *global form* useful for finding the approximate solution $\tilde{p}$. The first integrant in eq. (4.9) may be rewritten as

$$w\nabla^2\tilde{p} = \nabla(w\nabla\tilde{p}) - \nabla w\nabla\tilde{p} \tag{4.10}$$

so that the *global form* may be rewritten as

$$\int_{\mathcal{V}} \nabla(w\nabla\tilde{p})\, d\mathcal{V} - \int_{\mathcal{V}} \nabla w\nabla\tilde{p}\, d\mathcal{V} + \int_{\mathcal{V}} wk^2\tilde{p}\, d\mathcal{V} + \int_{\mathcal{V}} wj\omega q\, d\mathcal{V} = 0 \tag{4.11}$$

However, making use of the divergence theorem yields

$$\int_S w\frac{\partial\tilde{p}}{\partial n}\, dS - \int_{\mathcal{V}} \nabla w\nabla\tilde{p}\, d\mathcal{V} + \int_{\mathcal{V}} wk^2\tilde{p}\, d\mathcal{V} + \int_{\mathcal{V}} wj\omega q\, d\mathcal{V} = 0 \tag{4.12}$$

or rearranging for the approximate unknown function $\tilde{p}$

$$\int_{\mathcal{V}} \nabla w\nabla\tilde{p}\, d\mathcal{V} - \int_{\mathcal{V}} wk^2\tilde{p}\, d\mathcal{V} = \int_{\mathcal{V}} wj\omega q\, d\mathcal{V} + \int_S w\frac{\partial\tilde{p}}{\partial n}\, dS \tag{4.13}$$

or, making use of the momentum balance equation,

$$\int_{\mathcal{V}} \nabla w\nabla\tilde{p}\, d\mathcal{V} - \int_{\mathcal{V}} wk^2\tilde{p}\, d\mathcal{V} = \int_{\mathcal{V}} wj\omega q\, d\mathcal{V} - \int_S wj\omega\rho_0 V_n\, dS \tag{4.14}$$

Equation (4.14) represents the so called *weak formulation* of the PDE problem because of the fact that, once solved, it gives an approximated solution. At this point, it is necessary to define the "form" of the trial and weighting function, in order to be able to solve the above derived *weak form*.

## 4.2 Galerkin procedure

The above described procedure is part of the finite element process named *method of the weighted residuals* (also known as Galerkin method[1][2][3]). As it has already mentioned, in the finite element approach, the fluid domain $\mathcal{V}$ is discretized into a number of small subdomains $\mathcal{V}_e$ (finite elements) and a number of nodes which are defined at some particular locations in each element[42]. The approximation of the field variable (acoustic pressure) in each finite element, which is the trial solution $\tilde{p}$, is expressed as a weighted summation, namely

$$p^e(x,y,z) \approx \tilde{p}^e(x,y,z) = \sum_i^n N_i^e(x,y,z)\, a_i \tag{4.15}$$

which represents a linear combination of the $N_i$ field functions, known as shape or interpolation functions, prescribed in terms of independent coordinates $(x,y,z)$ and $a_i$ are the weights of the summation. The shape functions are chosen so that they equal unity at the location of the node they correspond to, namely

$$N_i^e(x_i,y_i,z_i) = 1 \tag{4.16}$$

while

$$N_i^e(x_j,y_j,z_j) = 0 \tag{4.17}$$

In this way, the weighting coefficients $a_i$ represents the approximated acoustic pressures nodal values, that is

$$\tilde{p}_i^e = N_1^e(x_1,y_1,z_1)\, a_i + 0\, a_i + \cdots + 0\, a_n \tag{4.18}$$

It follows that the trial solution $\tilde{p}$, within each element of the discretization, may be expressed as

$$\tilde{p}^e = \sum_i^n N_i^e(x,y,z)\, \tilde{p}_i \tag{4.19}$$

$\tilde{p}_i$ being the unknown nodal values. As an example, in Figure 4.2 the shape functions of three nodes corresponding to two linear elements are shown.

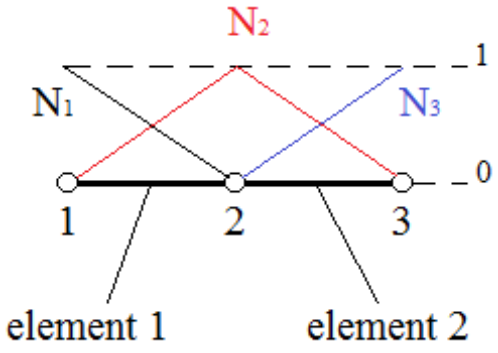


Figure 4.2 – Example of linear shape functions for two linear elements.

[42] Generally, the nodes are defined at each corner point of the finite element they belong.

Besides the definition of such local shape function $N_i^e$, it is very useful to define a global shape function $N_I$ with the same constraint as the $N_i^e$.[43] Consequently, the global pressure expansion may be expressed as

$$\tilde{p}(x,y,z) = \sum_{i=I}^{n_T} N_i(x,y,z)\,\tilde{p}_i = [N]\{\tilde{p}\} \tag{4.20}$$

where $n_T$ stands for the total number of nodes within the finite element discretization, $[N]$ is a $(1\,x\,n_T)$ global shape function vector and $\{\tilde{p}\}$ is a $(n_T\,x\,1)$ of approximated unknown nodal pressures vector. The difference between local and global shape function is schematically depicted in Figure 4.3, for a two-dimensional grid made of several rectangular elements.

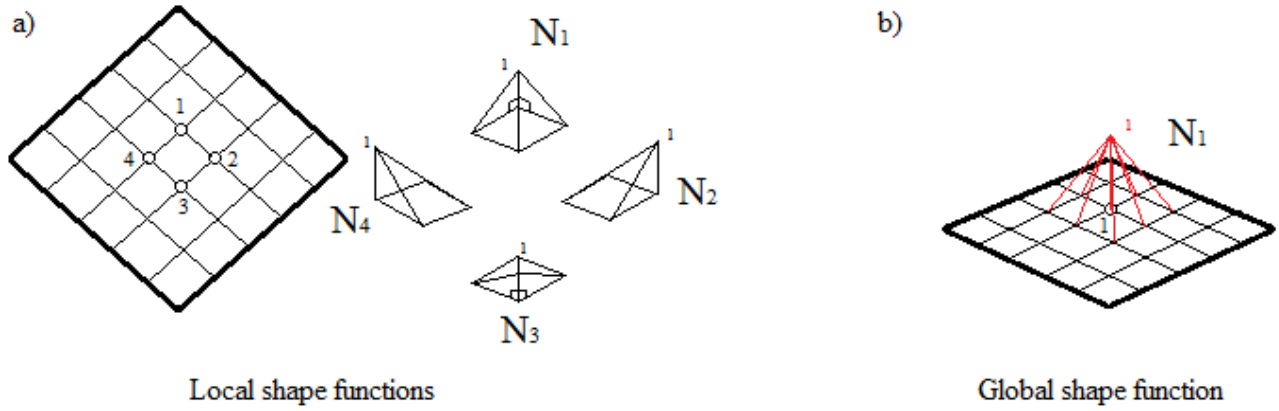


Figure 4.3 – Shape function definitions: a) local and b) global.

At the same time, the acoustic pressure gradient approximation may be expressed as

$$\nabla\tilde{p}(x,y,z) = \begin{bmatrix} \partial\tilde{p}/\partial x \\ \partial\tilde{p}/\partial y \\ \partial\tilde{p}/\partial z \end{bmatrix} = [\partial][N]\{\tilde{p}\} = [B]\{\tilde{p}\} \tag{4.21}$$

where $[\partial]$ is a $(3\,x\,1)$ gradient operator vector and $[B]$ is a $(3\,x\,n_T)$ matrix of the gradient components of the global shape functions.

From what concern the definition of the arbitrary weighting function, according to the Galerkin procedure, the same expansion is assumed, namely

$$w(x,y,z) = \sum_{i=I}^{n_T} N_i(x,y,z)\,w_i = [N]\{w\} \tag{4.22}$$

and

$$\nabla w(x,y,z) = \begin{bmatrix} \partial w/\partial x \\ \partial w/\partial y \\ \partial w/\partial z \end{bmatrix} = [\partial][N]\{w\} = [B]\{w\} \tag{4.23}$$

Thus, by inserting the above introduced expansion in terms of shape functions within the weak formulation, yields to the following integral equation

[43] $N_I(x_I,y_I,z_I) = 1$ and $N_I(x_J,y_J,z_J) = 0$.

$$\int_{\mathcal{V}}([B]\{w\})^T([B]\{\tilde{p}\})\,d\mathcal{V} - \int_{\mathcal{V}}([N]\{w\})^T k^2([N]\{\tilde{p}\})\,d\mathcal{V} = \int_{\mathcal{V}}([N]\{w\})^T j\omega q\,d\mathcal{V} - \int_S([N]\{w\})^T j\omega\rho_0 V_n\,dS \quad (4.24)$$

which, as it will be shown in the following, enables the definition of acoustic stiffness, mass and damping matrices, together with an acoustic excitation vector.

Acoustic stiffness matrix

The first integral within eq. (4.24) may be rewritten as

$$\int_{\mathcal{V}}([B]\{w\})^T([B]\{\tilde{p}\})\,d\mathcal{V} = \{w\}^T \int_{\mathcal{V}}[B]^T[B]\,d\mathcal{V}\ \{\tilde{p}\} = \{w\}^T[K]\,\{\tilde{p}\} \quad (4.25)$$

where the $(n_T\ x\ n_T)$ square matrix $[K]$ is termed, by analogy with structural mechanic[7], acoustic stiffness matrix. The generic $ij$ element of such matrix has the following expression

$$K_{ij} = \int_{\mathcal{V}}\left(\frac{\partial N_i}{\partial x}\frac{\partial N_j}{\partial x} + \frac{\partial N_i}{\partial y}\frac{\partial N_j}{\partial y} + \frac{\partial N_i}{\partial z}\frac{\partial N_j}{\partial z}\right)\,d\mathcal{V} \quad (4.26)$$

Obviously, thanks to the way in which the shape functions have been defined (see Figure 4.3), $N_i$ and $N_j$ are non-zero only for the elements to which node $i$ and $j$ belong. It follows that the global integral expressed by eq. (4.26) may be calculated as summation of integrals over the elements to which both node $i$ and $j$ belong (so that both $N_i$ and $N_j$ are non-zero), namely

$$K_{ij} = \sum_{e=1}^{p_{ij}} \int_{\mathcal{V}_e}\left(\frac{\partial N_i^e}{\partial x}\frac{\partial N_j^e}{\partial x} + \frac{\partial N_i^e}{\partial y}\frac{\partial N_j^e}{\partial y} + \frac{\partial N_i^e}{\partial z}\frac{\partial N_j^e}{\partial z}\right)\,d\mathcal{V} = \sum_{e=1}^{p_{ij}} K_{ij}^e \quad (4.27)$$

where $p_{ij}$ is the number of elements to which both node $i$ and $j$ belong and $K_{ij}^e$ is the element acoustic stiffness matrix. According to the general calculation procedure, the stiffness matrix for each element is firstly calculated and then each element of the global stiffness matrix is calculated thanks to eq. (4.27). Considering that each node $i$ share elements with only few adjacent nodes $j$ the global acoustic stiffness matrix turns out to be sparse populated. Besides, if the elements numbering is done in a proper way within the finite element discretization, the few populated elements of the matrix $[K]$ are arranged around the diagonal.

Acoustic mass matrix

To the aim of rewriting eq. (4.24) in a more convenient form, the second integral may be rewritten as

$$\int_{\mathcal{V}}([N]\{w\})^T k^2([N]\{\tilde{p}\})\,d\mathcal{V} = \omega^2\{w\}^T \int_{\mathcal{V}}\frac{1}{a_0^2}[N]^T[N]\,d\mathcal{V}\,\{\tilde{p}\} = \omega^2\{w\}^T[M]\,\{\tilde{p}\} \quad (4.28)$$

where the $(n_T\ x\ n_T)$ square matrix $[M]$ is termed, by analogy with structural mechanic[7], acoustic mass matrix and its generic $ij$ element has the following expression

$$M_{ij} = \int_{\mathcal{V}}\frac{1}{a_0^2}\left(N_i N_j\right)\,d\mathcal{V} = \sum_{e=1}^{p_{ij}}\int_{\mathcal{V}_e}\frac{1}{a_0^2}\left(N_i^e N_j^e\right)\,d\mathcal{V} = \sum_{e=1}^{p_{ij}} M_{ij}^e \quad (4.29)$$

So, by the examination of the above expression, it is easy to find out that, even in this case, the acoustic mass matrix turns out to be sparse populated since the shape functions $N_i^e$ and $N_j^e$ are

contemporarily non-zero only for few elements to which both the generic nodes $i$ and $j$ belong. Even in this case, the acoustic mass matrix for each element is firstly calculated and then the global mass matrix is assembled by the calculation of each element thanks to eq. (4.29).

Acoustic excitation vector

The first integral on the right-hand side of eq. (4.24) may be expressed as

$$\int_{\mathcal{V}}([N]\{w\})^T j\omega q \, d\mathcal{V} = \{w\}^T \int_{\mathcal{V}}[N]^T j\omega q \, d\mathcal{V} = \{w\}^T\{Q\} \tag{4.30}$$

where $\{Q\}$ is a $(n_T \; x \; 1)$ vector defining the strength of eventual acoustic source located at some node of the finite element discretization. For this reason, $\{Q\}$ is also called acoustic excitation vector.

Boundary conditions

As it has been previously introduced, in order to uniquely define the acoustic pressure field within the domain $\mathcal{V}$, one or a set of boundary conditions must be specified on the closed bounding surface. To this scope, the second integral on the right-hand side of eq. (4.24) is very useful, as it is intuitively clear by considering the fact that it is the only surface integral in the whole expression. In fact, considering that the surface enclosing the acoustic domain $\mathcal{V}$ may be divided into the surfaces on which different boundary condition are applied (see eq. (4.6)), the surface integral in eq. (4.14) may be expressed as

$$-\int_S wj\omega\rho_0 V_n \, dS = -\int_{S_p} wj\omega\rho_0 V \cdot n \, dS - \int_{S_v} wj\omega\rho_0 V_n \, dS - \int_{S_Z} wj\omega\rho_0 A \, \tilde{p} \, dS \tag{4.31}$$

where $A$ is called acoustic admittance, representing the inverse of the acoustic impedance. Making use of eq. (4.22), the first surface integral may be rewritten as

$$-\int_{S_p} wj\omega\rho_0 V \cdot n \, dS = \{w\}^T \left(-\int_{S_p}[N]^T j\omega\rho_0 V \cdot n \, dS\right) = \{w\}^T\{P\} \tag{4.32}$$

where $\{P\}$ is called input pressure vector, defining the pressure boundary condition in each node where it is defined.

As regards the normal velocity boundary condition, by substituting the expansion in terms of shape function for weighting function, the second integral becomes

$$-\int_{S_v} wj\omega\rho_0 V_n \, dS = \{w\}^T \left(-\int_{S_v}[N]^T j\omega\rho_0 V_n \, dS\right) = \{w\}^T\{V_n\} \tag{4.33}$$

where $\{V_n\}$ is a $(n_T \; x \; 1)$ vector, also known as input velocity vector, defining the nodes at which the imposed Neumann boundary condition is applied. Therefore, the generic imposed nodal normal velocity may be expressed as

$$V_{ni} = -\int_{S_v} N_i j\omega\rho_0 V_n \, dS \tag{4.34}$$

The value of a global shape function $N_i$ at the boundary surface is non-zero only for those nodes that are located on the boundary surface $S_v$. Besides, within the finite element discretization, $S_v$ is

the sum of only some elements surfaces. Consequently, the calculation of the generic component of the input velocity vector is accomplished thanks to the following expression

$$V_{ni} = \sum_{e=1}^{p_i} \sum_{S_v^e=1}^{n_i} - \int_{S_v^e} N_i^e j\omega\rho_0 V_n \, dS \tag{4.35}$$

where $p_i$ is the number of elements which share node $i$ whilst $n_i$ is the number of surfaces on the boundary $S_v$, belonging to one element, sharing node $i$.

In a similar way, the third integral on the right-hand side of eq. (4.31) may be expressed as

$$-\int_{S_Z} wj\omega\rho_0 A \, \tilde{p} \, dS = -j\omega\{w\}^T \left(\int_{S_Z} [N]^T [N] \rho_0 A \, dS\right) \{\tilde{p}\} = -j\omega\{w\}^T [C] \{\tilde{p}\} \tag{4.36}$$

where the matrix indicated by $[C]$ is a $(n_T \, x \, n_T)$ matrix which is called acoustic damping matrix. The generic $ij$ element of such matrix has the following expression

$$C_{ij} = \int_{S_Z} \rho_0 A \left(N_i N_j\right) dS \tag{4.37}$$

However, the boundary surface $S_Z$ is, after the finite element discretization, equal to the sum of some elements surfaces, so that the generic element of the element acoustic damping matrix may be expressed in the following form

$$C_{ij} = \sum_{S_v^e=1}^{n_i} \int_{S_v^e} \rho_0 A \left(N_i^e N_j^e\right) dS \tag{4.38}$$

from which it is possible to point out that, as per the definition of shape function, $N_i$ and $N_j$ are contemporarily non-zero (and so $C_{ij}$) only if node $i$ and node $j$ are located on at least one common element face that is part of the boundary surface $S_Z$. This results in a matrix $[C]$ which is also sparse populated.

After introducing the above mentioned matrices and vectors, the way in which the finite element model is assembled and solved, for the wanted approximated solution, may be more easily understood. In fact, by substituting expressions (4.25), (4.28), (4.30), (4.32), (4.33) and (4.36) into Eq. (4.24), the weak form of the weighted residual formulation of the Helmholtz equation, including the boundary conditions (4.4) and (4.5), becomes

$$\{w\}^T [K] \{\tilde{p}\} - \omega^2 \{w\}^T [M] \{\tilde{p}\} + j\omega\{w\}^T [C] \{\tilde{p}\} = \{w\}^T \{Q\} + \{w\}^T \{P\} + \{w\}^T \{V_n\}$$

or

$$([K] \; - \omega^2 [M] \; + j\omega[C])\{\tilde{p}\} = \{Q\} + \{P\} + \{V_n\} \tag{4.40}$$

as the weighted residuals formulation must hold for any weighted function. Thus, a set of $n_T$ linear equations in the $n_T$ nodal acoustic pressure unknowns $\tilde{p}_i$ is obtained. These latter are commonly denoted by degrees of freedom of the Finite Element model.

Actually, the imposed pressure boundary condition, which is represented by the vector $\{P\}$ within the above equation, is not applied making use of eq. (4.32). In fact, the application of such type of boundary condition is usually done by directly assigning the imposed pressure value at each node located on the boundary surface $S_p$. When this is done, the system of eq. (4.40) becomes

overdetermined, meaning that the number of equations is greater than the number of unknowns. When this assignment is done for the $n_p$ nodes on the boundary surface, only $n_T - n_p$ approximated acoustic pressure values are still unknown. Consequently, in order to have again a well-determined set of equations, the equations related to the nodes on which the pressure is assigned must be eliminated. Then, by moving on the right-hand side the terms involving the imposed pressure values within the equations where they appear, the assembled finite element model becomes

$$([K]_R - \omega^2[M]_R + j\omega[C]_R)\{\tilde{p}\}_R = \{F_a\}_R \tag{4.41}$$

where the subscript $R$ indicates that the number of equations has been reduced. In fact, the acoustic stiffness, mass and damping matrices are now $(n_R\ x\ n_R)$ matrices for which $n_R = n_T - n_p$, whilst $\{F_a\}_R$ is the new $(n_R\ x\ 1)$ acoustic force vector, grouping the first and the third "reduced" vector on the right hand side of eq. (4.40).

From what above, it is possible to identify the various steps in which the Finite Element Method is composed, as it is schematically depicted in figure below.

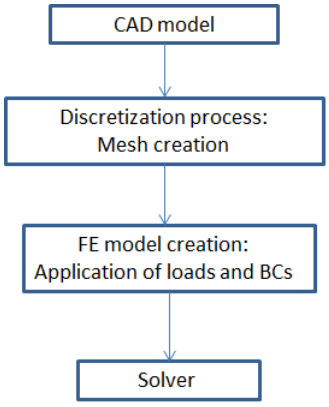


Figure 4.4 – The main phases of the Finite Element Method.

The starting point is of course represented by the availability of the CAD (Computer Aided Design) model of the acoustic domain under investigation. Then, such originally supposed continuous system has to be discretized into a finite number of elements constituting the acoustic mesh. This latter, together with the loads and boundary conditions represents the Finite Element Model to be assembled[44] and solved. In general, nowadays various CAE software are available for solving engineering problems with FE approach and all of them consist in two parts which are a graphic user interface and a dedicated solver. The pre /post processing interface is used to create the discretization and for the application of the boundary conditions and loads, whilst the assembling procedure of the various matrices and the solution of eq. (4.41) is accomplished by the solver. Once the solution has been found for each of the nodes the mesh consists of, it is possible to view the results in the graphic interface.

[44] The assembling procedure is generally devoted to the evaluation of the acoustic mass, stiffness and damping matrices.

## 4.3 Convergence of the model

From what has been showed before, the problem of solving the complicated partial differential equation problem expressed by eq. (4.2) and the related boundary conditions (4.3), (4.4) and (4.5) has been transformed into the problem of solving the system of linear equations (4.41), with unknowns represented by the acoustic pressure at some discrete point within the computational domain $\mathcal{V}$. However, the convergence of the approximate solution to the exact one is ensured considering some constraints, which are related to both the "form" of the shape functions expansion and the geometric discretization[4]. This leads to the definition of two types of errors when using the finite element method, which are defined as approximation and discretization error.

From what concerns the approximation error, this is due to the fact that the exact solution of the Helmholtz equation is an approximated one, as it is explicitly expressed by eq. (4.15). Since the spatial functions in such expansion are represented by the shape functions, the approximation error is related to the way in which they are defined. Generally, the shape functions are polynomial functions as they are very easy to differentiate and integrate. Thus, the convergence of the approximated solution is ensured if two conditions are satisfied which are:

- *Completeness*, meaning that, being $m$ the highest derivative order in the weak formulation (4.14) of the trial and weighting functions, the element shape functions must represent at least all polynomial terms of order $\leq m$, otherwise the formulation cannot hold. A set of shape functions that satisfies this condition is called m-complete.
- *Compatibility*, meaning that the element shape function must be chosen so that the integrals are always finite. To achieve this, the first order derivative of the shape function of the acoustic element must exist and the approximate acoustic pressure must be continuous between interconnected elements.

Thus, from the above convergence conditions, a polynomial shape functions for an acoustic finite element discretization must be such that, the functions are complete up to at least the first order derivative and that the whole pressure expansion is continuous between elements. Therefore, a very common choice is represented by linear rectangular for two-dimensional problems and linear tetrahedral elements for three-dimensional problems.


Figure 4.5 – Linear rectangular and linear tetrahedral elements.

As an example, the element shape function for linear rectangular elements are defined as

$$N_i^e = \frac{1}{4}(1 + \eta_i\eta)(1 + \xi_i\xi) \qquad i = 1,2,3,4 \tag{4.42}$$

where the two local coordinates $(\eta, \xi)$ are depicted in Figure 4.5. As it is possible to appreciate by the above expression, such polynomial shape function perfectly agrees with the first constraint represented by the fact that $N_i^e$ must equal unity at node $i$ and zero at the others nodes. Also it is

easy to find out that the pressure expansion is continuous between elements. In fact, the pressure approximation along the boundary $\eta = 1$ and $-1 \leq \xi \leq 1$ may be expressed as[45]

$$\tilde{p} = \frac{\tilde{p}_1 + \tilde{p}_2}{2} + \left(\frac{\tilde{p}_1 - \tilde{p}_2}{2}\right)\xi \tag{4.43}$$

which is uniquely defined by the nodal pressure at node 1 and 2. The same thing happens for the adjacent element which ensure the continuity of the pressure expansion across the inter-element boundary.

As regards the discretization error, it is necessary to point out that, for most real-life acoustic problems, the computational domain $\mathcal{V}$ may have a very complex, arbitrary, geometrical shape, which cannot be discretized exactly into a set of simple geometrical entities, such as rectangular and tetrahedral elements. In these cases, the finite element discretization induces not only an approximation error, due to the shape function expansion, but also a discretization one due to the more or less poor geometrical description of the actual geometry. In other words, the discretization error is due to the fact that the finite element discretization may not fit the exact geometry. This is schematically depicted in Figure 4.6.

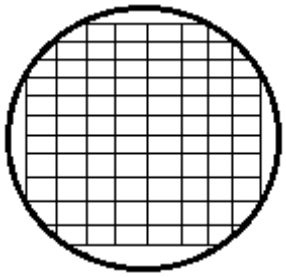

Figure 4.6 – Example of poor description of circular geometry using rectangular elements.

Thus, in order to lower as much as possible the discretization error, there is the need to use more complex elementary entities. Such very important circumstance leads to the concept of parametric mapping, which "simply" allows the use of distorted version of ideal elements, allowing the better handling of complex geometries. More precisely, the starting point is represented by the "ideal" element shape, corresponding to the so-called parent element (e.g. rectangular in two-dimensional symmetry). By distorting such a parent element, together with its local element coordinate system, a new element is created together with its local curvilinear coordinate system, as schematically indicated in Figure 4.7. Note that, thanks to the simple geometry of the parent rectangular element, the edges of the distorted elements are characterized by constant values of the curvilinear local coordinate system.

[45] $\tilde{p} = \frac{1}{4}[(\tilde{p}_1 + \tilde{p}_2 + \tilde{p}_3 + \tilde{p}_4) + (\tilde{p}_1 + \tilde{p}_2 - \tilde{p}_3 - \tilde{p}_4)\eta + (\tilde{p}_1 - \tilde{p}_2 - \tilde{p}_3 + \tilde{p}_4)\xi + (\tilde{p}_1 - \tilde{p}_2 + \tilde{p}_3 - \tilde{p}_4)\,\eta\xi\,]$.

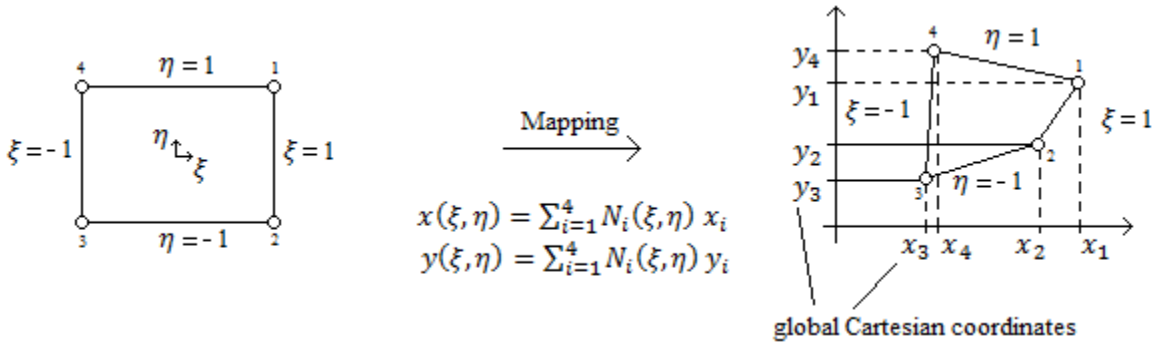


Figure 4.7 – Schematization of the element distortion procedure.

The relationship between the global Cartesian and the local curvilinear coordinates, for each point in the distorted element domain, is described in terms of shape functions expansion, namely

$$\begin{cases} x(\xi,\eta) = \sum_{i=1}^{4} N_i(\xi,\eta)\, x_i \\ y(\xi,\eta) = \sum_{i=1}^{4} N_i(\xi,\eta)\, y_i \end{cases} \tag{4.44}$$

Considering the corners of the distorted element, in a similar way to what happens for the expansion of the acoustic pressure approximation, in this case the shape function for a node is defined to be equal unity at the node and zero at the others. In this way, the global coordinates of each point of the distorted element are expressed as weighted summation of such "geometric" shape function, the global coordinates of the corners being the weights. The case in which the same shape functions, describing the approximate acoustic pressure, are used for describing the change of geometrical coordinates is common and the corresponding elements are denoted as isoparametric acoustic elements. By means of relations of the type (4.44) it is possible to express the integration functions of eq. (4.14) in local coordinates, simplifying the integration limits which are constant $(-1 \leq \xi, \eta \leq 1)$ due to the very simple geometry of the parent element. Besides, according to the rules of partial differentiation, the spatial derivatives with respect to the local element co-ordinates $\xi$ and $\eta$ may be expressed in terms of those with respect to the global Cartesian coordinates, namely

$$\begin{Bmatrix} \frac{\partial N_i^e}{\partial \xi} \\ \frac{\partial N_i^e}{\partial \eta} \end{Bmatrix} = \begin{bmatrix} \frac{\partial x}{\partial \xi} & \frac{\partial y}{\partial \xi} \\ \frac{\partial x}{\partial \eta} & \frac{\partial y}{\partial \eta} \end{bmatrix} \begin{Bmatrix} \frac{\partial N_i^e}{\partial x} \\ \frac{\partial N_i^e}{\partial y} \end{Bmatrix} = [J(\xi,\eta)] \begin{Bmatrix} \frac{\partial N_i^e}{\partial x} \\ \frac{\partial N_i^e}{\partial y} \end{Bmatrix} \tag{4.45}$$

where the matrix $[J]$ is the Jacobian of the coordinates transformation. Hence, thanks to relations such as (4.44) and (4.45), the calculation of the integrals for the distorted elements in the FE model may be accomplished in the element local coordinates, which makes the procedure simpler. The above description holds also for three-dimensional discretizations and, as an example, the distorted element acoustic stiffness matrix may be calculated as

$$[K^e] = \int_{\mathcal{V}_e} ([\partial][N])^T ([\partial][N])\, dxdydz = \int_{\mathcal{V}_e} ([\partial][N])^T ([\partial][N])\, |J| d\xi d\eta d\psi \tag{4.46}$$

where $|J|$ is the determinant of the Jacobian and the integration limits on the right-hand side reduce to three integration in the range $[-1; 1]$ in the three local variables $\xi$, $\eta$ and $\psi$.

As already pointed out, practically always in real engineering problems, the geometries to deal with may be quite complex and cannot be discretized as constituted by simple or ideal element type so that the distortion process has to be accomplished. Intuitively, from what has been described above, the discretization error is highly dependent on the quality of the acoustic mesh, meaning how much the elements of the discretization differ from their ideal shape. In this framework, some geometrical checks have to been verified on the element quality and, of course, a lot of mesh quality parameters have been, during the years, defined. Just as an insight, one of them is the Jacobian which, as per its definition, measures how much the element is distorted. In other words, the determinant of the Jacobian indicates the local stretching of an element whose excessive extent must be avoided, in order to not lead to wrong matrices calculation.

Another important aspect which has to be taken into account, when solving acoustic problems by means of finite element approach, is that, as acoustic is a wave propagation phenomenon, the spatial variation of acoustic pressure is mainly affected by the distribution of sources and the considered frequency. This latter circumstance derives, of course, by the fact that the acoustic wavelength is related with the considered frequency via the speed of sound. Considering a low order polynomial function used as shape functions, it can only faithfully reproduce very little spatial variations. This is schematically indicated in Figure 4.8, where a linear shape function has been considered.

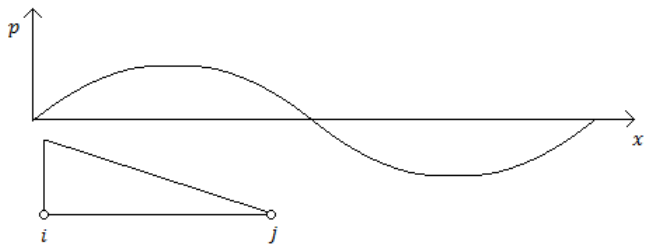


Figure 4.8 – 1D element linear interpolation versus sinusoidal spatial variation.

It follows that a large amount of elements is required in order to well approximate the oscillatory response within the computational domain, particularly at a high frequency. In this framework, a very common guideline states that, in order to achieve a suitable level of accuracy, the mesh should be fine enough so that at least 6 elements per acoustic wavelength are ensured. As a consequence, the element size to be used in an acoustic FE analysis should be choose based on the highest frequency to be examined, no matter if a coarser resolution would be sufficient at low frequencies.

## 4.4 Modelling exterior acoustic problems

In the introduction to the practical implementation of the finite element method in acoustics, it has been explicitly considered that the computational domain $\mathcal{V}$ is bounded by an external surface $S$. Intuitively, it must be like that because the computational effort may be only spent to solve a finite number of degrees of freedom. In other words, the finite element method could not be used to solve unbounded acoustic problems, where the computational domain has an infinite extent. Nevertheless, there exist several modelling approaches which allow the use of the FE method to solve exterior acoustic problems. Basically, the finite element discretization has to be modified and divided in several acoustic domains.

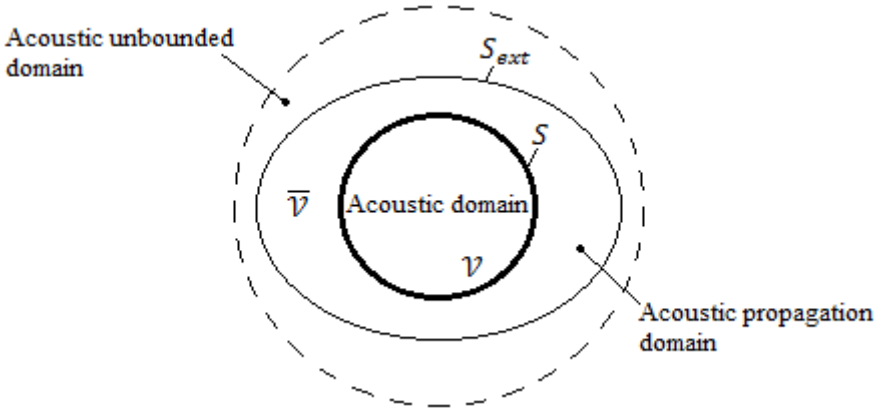


Figure 4.9 – Schematization of the finite element discretization for solving exterior acoustic problem.

As schematically indicated by Figure 4.9, considering the boundary surface $S$ of the original interior problem, a fictitious surface $S_{ext}$ is created, increasing the extent of the mesh. Then, the computational domain consists of three domains identified as the original bounded domain $\mathcal{V}$, one discretized part of the unbounded space enclosed between $S$ and $S_{ext}$ $(\bar{\mathcal{V}})$ and another part of the unbounded space which spread out toward the infinity. Hence, the model is assembled in a way such that a non-reflecting boundary condition is ensured at the physical limit of the domain, which coincides with the surface $S_{ext}$, and somehow the propagation in the real, not discretized, unbounded space must be handled.

At the surface $S_{ext}$, the so-called Sommerfeld radiation boundary condition is generally imposed[6]. This is the simplest non-reflecting boundary condition modelling the free (without reflections) propagation of acoustic waves towards the infinity and, mathematically, it arises from the sound field of a monopole source in free field conditions, when the distance from the source is great. In fact, considering the sound field produced by a simple monopole source in free field, the pressure gradient in the radial direction, at large distance from the source, may be expressed as[46]

$$\frac{\partial p}{\partial r} = -jkp \tag{4.47}$$

Among the various approaches which may be used to approximate such radiation condition the most simple is certain represented by the imposition of the characteristic impedance of the medium as impedance condition on the surface $S_{ext}$. This would lay to an acoustic pressure-particle velocity relation of the type

$$p(\boldsymbol{r}) = Z_0 v(\boldsymbol{r}) = \rho_0 a_0 \, v(\boldsymbol{r}) \qquad , \qquad \boldsymbol{r} \in S_{ext} \tag{4.48}$$

The main drawback of this simple implementation is that, in order to be valid, the fictitious surface $S_{ext}$ must be located far away from the boundary $S$, in order to approximate free plane wave propagation. This may result in a very large computational domain, to which high computational efforts corresponds.

More sophisticated approaches rely on the use of the so-called infinite elements (IE). These latter allow to model the sound field in unbounded domains, insuring a free-field condition. They are

[46] As it is derived in chapter 7, the frequency domain expression of the monopole field is $p(\omega, \boldsymbol{r}) = \frac{p}{4\pi r} e^{j(\omega t - kr)}$.

defined starting from the surface $S_{ext}$, which is generally referred as the finite-infinite interface, extending toward the infinity.

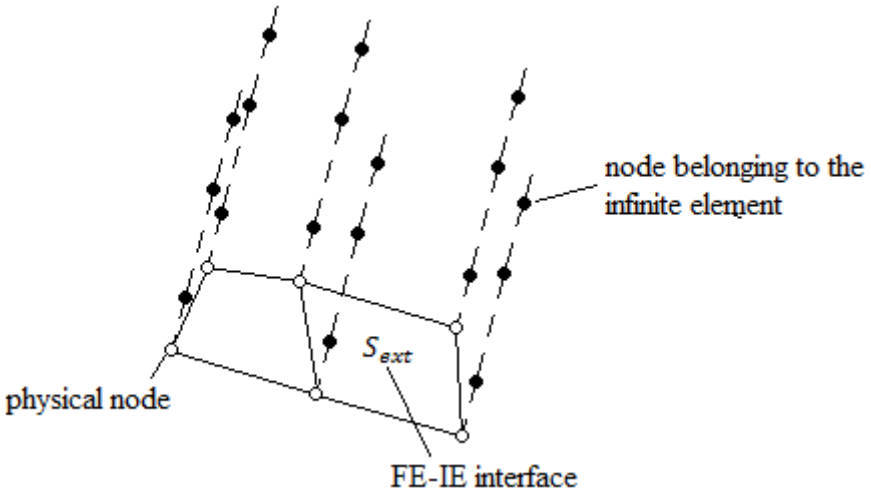


Figure 4.10 – Schematization of the infinite element discretization.

The sound field within the exterior domain is approximated thanks to a multipole expansion of the sound field on the finite-infinite interface[5]. Thanks to such modelling approach, the size of the computational domain may be significantly smaller with respect to the whole exterior domain to be modelled, depending on the position of the fictitious surface defining the finite-infinite interface.

## Bibliography


[1] O. C. Zienkiewicz, R. L. Taylor, "Finite Element Method: Volume 1", 5th Edition, Publisher Butterworth-Heinemann, ISBN 07-50-650-49-4.

[2] P. Nithiarasu, "Finite Element Method", notes from lectures given during the Post Graduate Educational Program, 14-18 July 2014.

[3] G. Sandberg, R. Ohayon, "Computational Aspects of Structural Acoustics and Vibration", Publisher Springer-Verlag Wien, ISBN 978-3-211-89651-8.

[4] W. Desmet, D. Vandepitte, "Finite Element Method in Acoustics", in ISAAC13-International Seminar on Applied Acoustics, Leuven, 2002, ISBN 90-73802-73-3.

[5] Actran 15.1 User's Guide,Volume 1 "Installation, Operations, Theory and Utilities", April 2015.

[6] Fine Acoustics Theoretical Manual, Release 5.2.3, July 2014.

[7] J. Kim Vandiver, "Modal Analysis: Orthogonality, Mass Stiffness, Damping Matrix", MIT course, 2.003SC Engineering Dynamics, Fall 2011.

# Chapter 5

# Acoustic Performance Analysis

## Introduction

In the present chapter the acoustic performance analyses of the intake system under investigation are described. These analyses have been aimed to predict the noise attenuation characteristics in terms of Transmission Loss. Thus, the outcomes of both experiments and simulations will be compared in order to achieve a first validation step of the modelling procedure for the studied system. The results which will be shown below partly refer to the following journal article:

*Siano, D., Ferrara, G., Lenzi, G., D'Agostino, D. et al., "Experimental and Numerical Comparison of the Acoustic Performance of the Air Filter Box of a SI-ICE," SAE International Journal of Engines 8(5):2015, doi:10.4271/2015-24-2527.*

As it has been mentioned in the introduction, the object of the present thesis is represented by the numerical modelling of an intake system for a commercial spark ignition engine. In particular, this chapter is dedicated to the description of the acoustic performance analysis of the studied system.

As it has been already mentioned in chapter 3, the most common used parameter for characterizing the acoustic attenuation properties of a system is the so called Transmission Loss. It is calculated according to eq. (3.79) and represents the sound power attenuation which is achieved within a transmission path, thanks to an acoustic filter located between sound source and receiver, considering an anechoic filter's termination. This common choice directly follows from the fact that such parameter only depends upon system's geometry and material (this latter dependence being particularly true when accounting for structural participation). Besides, as it will be clear from the next sections, it is very simple to measure thanks to the well-known Transfer Matrix theory and by means of the impedance tube method.

The knowledge of the Transmission Loss of a system, by means of either measurements or calculations, is indeed a very important step during the design or optimization phases. As matter of fact, many real systems have a very complex geometry and therefore they cannot be thought as an elementary acoustic filter, as those briefly examined in chapter 3. A prelaminar Transmission Loss study reveals which part of the studied geometry is responsible for high acoustic attenuation, e.g. a resonator, and, in general more important, which part has to be modified because of high acoustic transparency.

In this chapter, the results coming from the Transmission Loss assessment of the system under investigation will be presented. In particular, the analysis schematized as flowchart in Figure 5.1 will be discussed. Both simulations and experiments have been executed in no-flow conditions, which means without taking into account the convective effect of a mean velocity field on the acoustic wave propagation, according to what has been mentioned at the end of chapter 2.

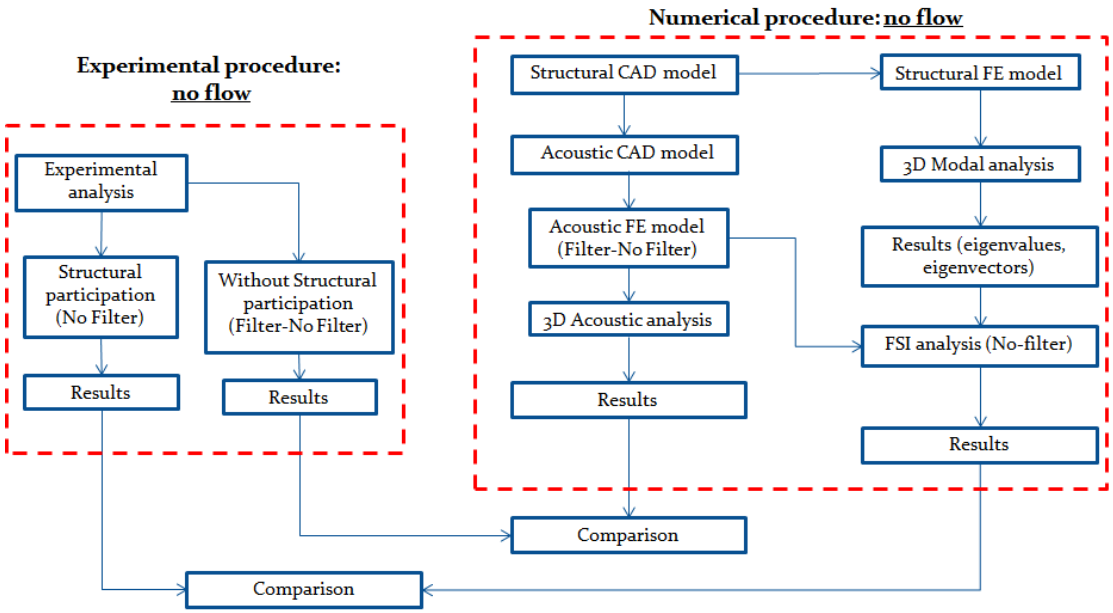


Figure 5.1 - Flow chart schematization of the Transmission Loss analyses.

Firstly, the experimental analysis and related background theory are briefly described together with the corresponding results. Here, two main analyses have been carried out: the first considering the structure of the system as infinitely rigid and the second accounting for the structural participation. Besides, in the first configuration, the influence of the presence of the air filter on the sound attenuation characteristic is also assessed. Then, following the layout of the above figure, the numerical analyses and related results will be described, starting from the availability of the structural CAD model which is mandatory for the finite element model creation. Finally, from the discussion of the comparison between experimental and numerical data in terms of Transmission Loss, the first step in the validation procedure of the numerical model is successfully achieved.

Before proceeding with the description of the above mentioned activities, an acknowledgement has to be done to the Research Group "*Reciprocating Engines and Advanced Systems for Energy*", of the University of Florence, and in particular to Prof. Giovanni Ferrara, PhD Giulio Lenzi and the PhD student Andrea Fioravanti, for the efforts which have been spent during the experimental Transmission Loss analyses which will be briefly described in this chapter.

## 5.1 Transfer Matrix Method

Generally speaking, duct elements have only two openings with enough small diameters which allow the plane wave propagation to be satisfied within a wide frequency range (see eq. (2.45) and (2.56)). Systems like that may be thought as acoustic two ports systems[1][2], as schematically depicted in Figure 5.2.

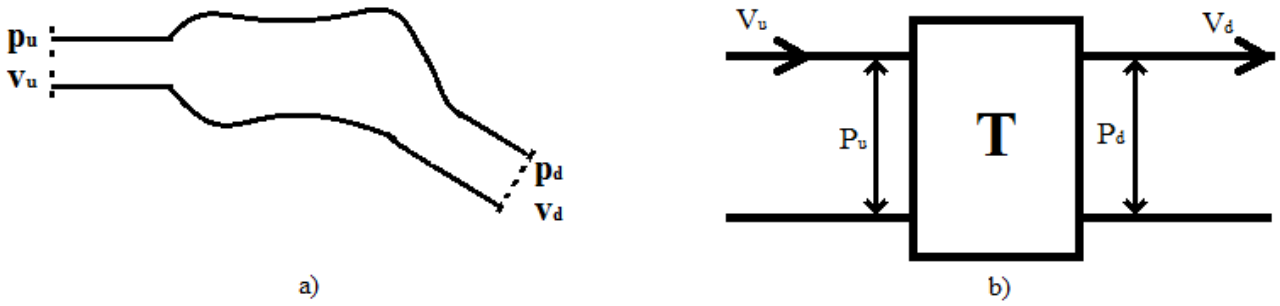


Figure 5.2 – a) acoustic system schematization and b) equivalent circuit representation.

In this framework, the so-called Transfer Matrix is the matrix which links the state variables at the upstream position of a filter and those at the downstream position. Considering an element of an acoustic filter and adopting the acoustic pressure and the acoustic mass velocity as state variables, the following matrix expression holds

$$\begin{bmatrix} p_u \\ v_u \end{bmatrix} = \begin{bmatrix} A_{11} & A_{12} \\ A_{21} & A_{22} \end{bmatrix} \begin{bmatrix} p_d \\ v_d \end{bmatrix} \tag{5.1}$$

where $[p_u; v_u]$ and $[p_d; v_d]$ are the state vectors at the upstream and downstream position respectively, whilst the parameters of the square matrix appearing on the right-hand side are called four pole parameters. From eq. (5.1), it is easy to point out that the so-called four-pole parameters can be expressed mathematically, as following

$$A_{11} = \left.\frac{p_u}{p_d}\right)_{v_d=0} \tag{5.2}$$

$$A_{12} = \left.\frac{p_u}{v_d}\right)_{p_d=0} \tag{5.3}$$

$$A_{21} = \left.\frac{v_u}{p_d}\right)_{v_d=0} \tag{5.4}$$

$$A_{22} = \left.\frac{v_u}{v_d}\right)_{p_d=0} \tag{5.5}$$

Therefore, each of the four-pole parameters represent a physical situation, e.g. $A_{11}$ represents the theoretical case in which the downstream position is rigidly fixed (infinite specific acoustic impedance) whilst $A_{12}$ represents the theoretical case of a totally free downstream (zero specific acoustic impedance). From the knowledge of the transfer matrix of an acoustic element, it is possible to calculate for example the acoustic intensity (or the acoustic power when the inlet and outlet section have different area), hence the transmission loss. The above expressions of the four-pole parameters allow the numerical evaluation of each by means of finite element models of complex geometries, when an exact solution is not available[3][4]. From what has been introduced in the chapter 3, all the basic elements of a straight-through low-pass filter may be represented by one of the three types of element depicted in Figure 5.3.

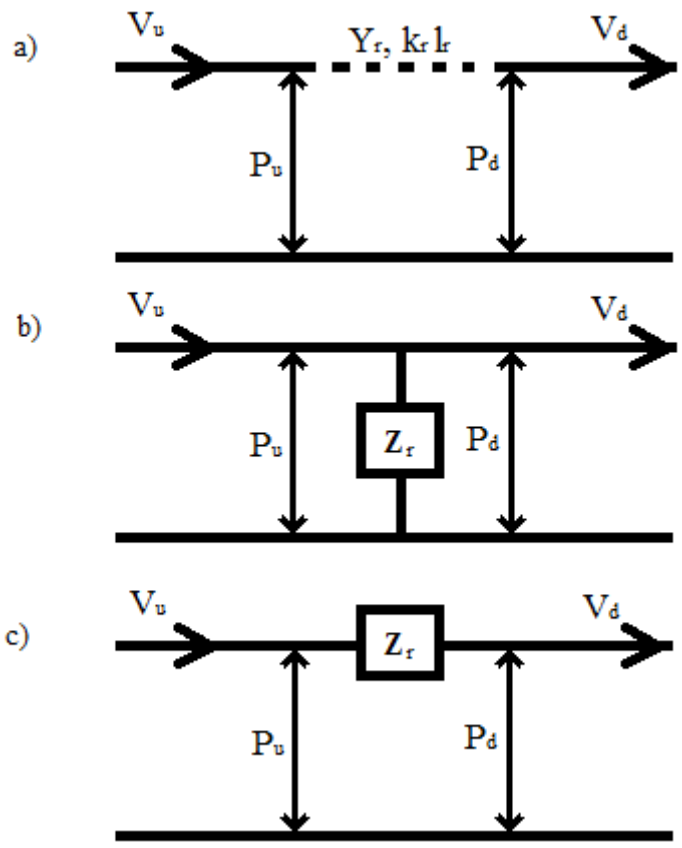


Figure 5.3 – Basic element equivalent representation: a) distributed element, b) shunt lumped element, c) in-line lumped element.

Thanks to the transfer matrix relation, it is possible to uniquely represent one of these elements by means of its Transfer Matrix. For example, by using the standing wave relations, the Transfer Matrix for the uniform tube may be evaluated. In fact, for the upstream position the standing wave relations yield

$$p_u = A_u + B_u \tag{5.6}$$

$$v_u = \frac{(A_u - B_u)}{Y_u} \tag{5.7}$$

and for the downstream position

$$p_d = A_u e^{-jk_0 l_u} + B_u e^{+jk_0 l_u}$$

$$= (A_u + B_u)cos(k_0 l_u) - j(A_u - B_u)sin(k_0 l_u)$$

$$= p_u cos(k_0 l_u) - jY_u v_u sin(k_0 l_u) \tag{5.8}$$

$$v_d = \frac{1}{Y_u}\left(A_u e^{-jk_0 l_u} - B_u e^{+jk_0 l_u}\right)$$

$$= \frac{(A_u - B_u)}{Y_u} cos(k_0 l_u) - j\frac{(A_u + B_u)}{Y_u} sin(k_0 l_u)$$

$$= v_u cos(k_0 l_u) - j\frac{p_u}{Y_u} sin(k_0 l_u) \tag{5.9}$$

$l_u$ being the length of the uniform tube. In this way, the downstream state vector may be expressed in a matrix form, namely

$$\begin{bmatrix} p_d \\ v_d \end{bmatrix} = \begin{bmatrix} cos(k_0 l_u) & -jY_u sin(k_0 l_u) \\ -\frac{j}{Y_u} sin(k_0 l_u) & cos(k_0 l_u) \end{bmatrix} \begin{bmatrix} p_u \\ v_u \end{bmatrix} \tag{5.10}$$

or, by inverting the above matrix relation

$$\begin{bmatrix} p_u \\ v_u \end{bmatrix} = \begin{bmatrix} cos(k_0 l_u) & jY_u sin(k_0 l_u) \\ \frac{j}{Y_u} sin(k_0 l_u) & cos(k_0 l_u) \end{bmatrix} \begin{bmatrix} p_d \\ v_d \end{bmatrix} \tag{5.11}$$

For the in-line lumped element of Figure 5.3 c), it is possible to write for the upstream and downstream position

$$p_u - p_d = Z_u v_u \tag{5.12}$$

$$v_u = v_d \tag{5.11}$$

and therefore the desired matrix form is

$$\begin{bmatrix} p_u \\ v_u \end{bmatrix} = \begin{bmatrix} 1 & Z_u \\ 0 & 1 \end{bmatrix} \begin{bmatrix} p_d \\ v_d \end{bmatrix} \tag{5.13}$$

Similarly, for the shunt lumped element of Figure 5.3 b), it is possible to write for the upstream and downstream position

$$p_u = p_d \tag{5.14}$$

$$v_u = \frac{p_u}{Z_u} + v_d \tag{5.15}$$

and therefore the desired matrix form is

$$\begin{bmatrix} p_u \\ v_u \end{bmatrix} = \begin{bmatrix} 1 & 0 \\ 1/Z_u & 1 \end{bmatrix} \begin{bmatrix} p_d \\ v_d \end{bmatrix} \tag{5.16}$$

For what concerns the sudden area changes, because, as it has been demonstrated in the chapter 3, all the state variables remain unchanged across the discontinuity, the transfer matrix is the unity matrix[1].

However, these are just simple examples and in general, an acoustic filter composed of *n* elements is represented by the equivalent acoustic circuit depicted in Figure 3.15. The transfer matrix representation still holds for the whole filter and the matrix relation may be expresses as

$$\begin{bmatrix} p_{n+1} \\ v_{n+1} \end{bmatrix} = [T_{n+1}][T_n] \dots [T_1] \begin{bmatrix} p_0 \\ v_0 \end{bmatrix} \tag{5.17}$$

where the state vector at the termination may be rewritten, considering Figure 5.3 (c, as

$$\begin{bmatrix} p_0 \\ v_0 \end{bmatrix} = \begin{bmatrix} 1 & Z_0 \\ 0 & 1 \end{bmatrix} \begin{bmatrix} 0 \\ v_0 \end{bmatrix} \tag{5.18}$$

while the $[T_{n+1}]$ matrix is the analogous of eq. (5.16).

As already mentioned, the Transmission Loss of an acoustic filter may also be evaluated thanks to the knowledge of its the overall transfer matrix. In fact, considering Figure 3.18, the Transfer Matrix relation between the upstream and downstream position is[47]

$$\begin{bmatrix} p_n \\ v_n \end{bmatrix} = \begin{bmatrix} T_{11} & T_{12} \\ T_{21} & T_{22} \end{bmatrix} \begin{bmatrix} p_1 \\ v_1 \end{bmatrix} \tag{5.19}$$

and, once again, recalling the standing wave relations

$$p_n = A_n + B_n \tag{5.20}$$

$$v_n = \frac{(A_n - B_n)}{Y_n} \tag{5.21}$$

$$p_1 = A_1 \quad , \quad B_1 = 0$$

$$v_1 = \frac{A_1}{Y_1} \tag{5.22}$$

Therefore

$$A_n = \frac{p_n + Y_n v_n}{2}$$

$$= \frac{\left[\left(T_{11}A_1 + T_{12}\frac{A_1}{Y_1}\right) + Y_n\left(T_{21}A_1 + T_{22}\frac{A_1}{Y_1}\right)\right]}{2} \tag{5.23}$$

Hence the expression for the Transmission Loss reduces to[1]

$$TL = 20Log\left\{\left(\frac{Y_1}{Y_n}\right)^{\frac{1}{2}} \frac{\left[T_{11} + \frac{T_{12}}{Y_1} + Y_n\left(T_{21} + \frac{T_{22}}{Y_1}\right)\right]}{2}\right\} \tag{5.24}$$

where the same diameter is sometime supposed for both the inlet and outlet pipe. The above expression is the basis of the probably most used experimental technique for the Transmission Loss measurement, through the use of the so-called Kundt's tube, which is briefly described in the following.

### 5.1.1 Experimental evaluation of the TL: the impedance tube technology

The impedance tube technology, which makes use of the so-called standing wave tube, is a particular experimental technique, thanks to which it is possible to measure the Transmission Loss and other acoustical quantities of materials (and more in general acoustic filters) placed inside it[10][1]. The measurement layout is depicted in Figure 5.4.

[47] The four pole parameters have been labelled with $T$, in order to not be confused with the amplitude of the forward moving wave in the standing wave field.

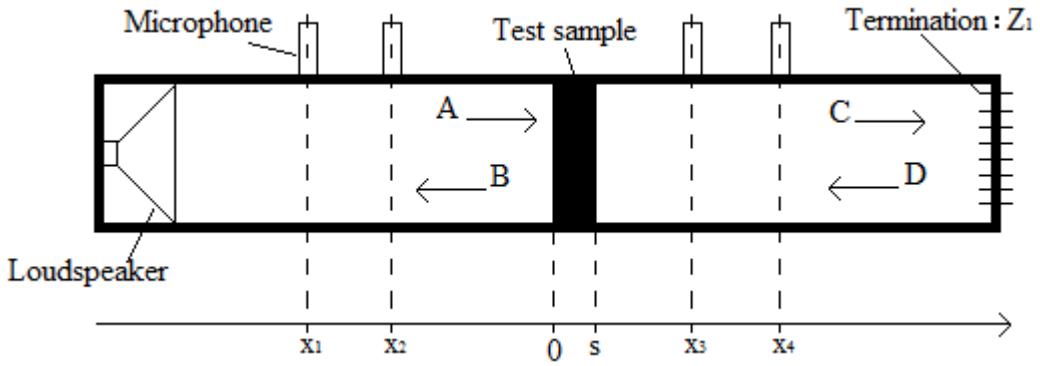


Figure 5.4 – Schematization of the measurement layout related to the standing wave tube.

As schematically described in the above figure, on the left-hand side of the tube, a loudspeaker is placed which generate the sound field whilst, in the middle of the tube the test sample is placed. At the end of the tube there is a rigid or another type of termination, depending on what is the goal of the measure. Besides, two couples of microphones are wall-placed at opposite locations with respect to the test sample. This wall-location represents the main limitation of such instrument. In fact, because of that, the measurements are valid only in the plane wave region for which the sound pressure is uniform with respect to the cross section of the tube. So, the highest frequency of the analysis depends on the diameter on the tube whilst, the lowest frequency depends upon the sound source. In order to understand how the measurements are made, it is necessary to recall that, from the solution of the classical wave equation, the sound field at any point upstream and downstream the test sample may be expressed in terms of forward and back moving waves as

$$p'_u(x,t) = Ae^{-jk_0x} + Be^{jk_0x} \tag{5.25}$$

$$p'_d(x,t) = Ce^{-jk_0x} + De^{jk_0x} \tag{5.26}$$

where the exponential time factor has been embedded within the complex amplitudes *A*, *B, C* and *D.* Thus, the four sound pressures, which are measured at the four microphone locations, may be expressed as

$$p'_1(x_1,t) = Ae^{-jk_0x_1} + Be^{jk_0x_1} \tag{5.27}$$

$$p'_2(x_2,t) = Ae^{-jk_0x_2} + Be^{jk_0x_2} \tag{5.28}$$

$$p'_3(x_3,t) = Ce^{-jk_0x_3} + De^{jk_0x_3} \tag{5.29}$$

$$p'_4(x_4,t) = Ce^{-jk_0x_4} + De^{jk_0x_4} \tag{5.30}$$

Therefore, after some algebra, it is possible to express the four constants in terms of the measured sound pressures as follows

$$A = \frac{j(p'_1e^{jk_0x_2} - p'_2e^{jk_0x_1})}{2sin[k(x_1 - x_2)]} \tag{5.31}$$

$$B = \frac{j(p'_2e^{-jk_0x_1} - p'_1e^{-jk_0x_2})}{2sin[k(x_1 - x_2)]} \tag{5.32}$$

$$C = \frac{j\left(p_3' e^{jk_0 x_4} - p_4' e^{jk_0 x_3}\right)}{2sin[k(x_3 - x_4)]} \tag{5.33}$$

$$D = \frac{j\left(p_4' e^{-jk_0 x_3} - p_3' e^{-jk_0 x_4}\right)}{2sin[k(x_3 - x_4)]} \tag{5.34}$$

Once the complex coefficients have been calculated, they could be used to determine directly the Transmission Loss based on eq. (3.82), providing that $D = 0$ (namely $Z_1$ is such that the termination is anechoic). However, experimentally it is not possible to realize a perfect anechoic termination, so that even small reflections may alter the ratio $A/C$. Therefore, the more correct way to proceed is to calculate the TL based on the knowledge of Transfer Matrix of the test sample, which is its intrinsic characteristic and not of the measurement environment. When the Transfer Matrix is known, it is possible to calculate the TL, whatever the termination of the tube is, following the procedure described below.

#### 5.1.1.1 Transfer Matrix formulation: the two-load method

The complex coefficients *A*, *B*, *C* and *D* may be calculated once the sound pressures at the four microphone locations are measured, as shown by eq. (5.31) to (5.34). This allows the possibility of measure also the sound pressure and the particle velocity at the two faces of the test sample, as shown by Figure 5.4. In fact, these may be expressed in terms of standing wave components as

$$p'(0,t) = A + B \tag{5.35}$$

$$u'(0,t) = \frac{A - B}{\rho_0 c} \tag{5.36}$$

$$p'(s,t) = Ce^{-jk_0 s} + De^{jk_0 s} \tag{5.37}$$

$$u'(s,t) = \frac{Ce^{-jk_0 s} - De^{jk_0 s}}{\rho_0 c} \tag{5.38}$$

where $\rho_0 c$ is the characteristic impedance of the air inside the standing wave tube. Of course, as already explained above, these four quantities are linked together by the Transfer Matrix of the test sample by the well-known matrix relation

$$\begin{bmatrix} p \\ u \end{bmatrix}_{x=0} = \begin{bmatrix} T_{11} & T_{12} \\ T_{21} & T_{22} \end{bmatrix} \begin{bmatrix} p \\ u \end{bmatrix}_{x=s} \tag{5.39}$$

where reference has been done again to Figure 5.4. However, in order to calculate the four pole parameters, the only measurement of the sound pressure at the four microphone locations is not sufficient. In fact, eq. (5.39) represents a system of two linear equations in the four unknowns $T_{11}$, $T_{12}, T_{21}$ and $T_{22}$. Thus, the other two equations, necessary to solve the system (5.39), may be found by making another measurement with another impedance terminating the measurement tube. In this way, after the two measurements, the four-pole parameters may be expressed, after some simple algebra, as

$$\begin{bmatrix} T_{11} & T_{12} \\ T_{21} & T_{22} \end{bmatrix} = \frac{1}{G} \begin{bmatrix} (p_1|_{x=0}\, u_2|_{x=s} - p_2|_{x=0}\, u_1|_{x=s}) & (p_2|_{x=0}\, p_1|_{x=s} - p_1|_{x=0}\, p_2|_{x=s}) \\ (u_1|_{x=0}\, u_2|_{x=s} - u_2|_{x=0}\, u_1|_{x=s}) & (p_1|_{x=s}\, u_2|_{x=0} - p_2|_{x=s}\, u_1|_{x=0}) \end{bmatrix} \tag{5.40}$$

where

$$G = p_1|_{x=s}\, u_2|_{x=s} \; - \; p_2|_{x=s}\, u_1|_{x=s} \tag{5.41}$$

In the above equations, $p_i|_{x=j}$ and $u_i|_{x=j}$ represents sound pressure and particle velocity during the experiment $i$ at location $j$. Once the elements of the Transfer Matrix are known, considering an anechoic termination, the Transmission Loss of the test sample may be found by using the following expression

$$TL = 20Log\left\{\frac{\left[T_{11}+\frac{T_{12}}{\rho_0 c}+\rho_0 c\left(T_{21}+\frac{T_{22}}{\rho_0 c}\right)\right]}{2e^{jk_0 s}}\right\} \tag{5.42}$$

In the following paragraph, the experimental Transmission Loss analyses, which have relied on the use of the above described Transfer Matrix method, will be described.

## 5.2 Experimental procedure

As already mentioned before, the system under investigation is an intake system of a commercial VVA internal combustion engine, and it is reported in Figure 5.5, where it is within the laboratory at the Istituto Motori-CNR of Naples.

Figure 5.5 - Intake system of the considered internal combustion engine at the Istituto Motori-CNR.

The experimental tests have relied on the above described transfer matrix theory and on the use of the standing wave tube. More precisely, at the University of Florence an acoustic custom test rig for Transmission Loss analysis has been realized. Such test rig is designed with two measurement sections, upstream and downstream the system under investigation, as it is depicted in Figure 5.6. Each section is made up of a straight duct, having length and diameter equal to 0.700 $m$ and 0.04 $m$ respectively. Along the duct, four microphones are placed at specific relative distance between each other. At the inlet of the first measurement section, an acoustic source, constituted of four speakers (Monacor ® SPH-135C), generates an acoustic pressure field at the minimum frequency of 40 $Hz$, this lower limit being imposed by the adopted speakers. As regards the upper limit for which plane wave propagation is ensured, it depends from the geometry of the duct and its first cut-off frequency, as it has been previously highlighted in chapter 2. So, according to eq. (2.56) the upper limit is

$$f_{cut-off} = \frac{1{,}84\, a_0}{\pi\, D_0} \cong 4978\ Hz \tag{5.43}$$

It is important to highlight that the main necessity for plane wave propagation is due to the fact that the acoustic measurements are made at the duct wall. The intensity of incident wave on the test case

has been set to $120\,dB$ using a wave form generator (Agilent ® 33210A) and an amplifier (Monacor ® PA180). Downstream to the second measurement section, an acoustic termination, designed following the ISO 5136:2003[10] guidelines, sets the acoustic boundary condition. Using the multi microphones technique[7], it is possible to evaluate the incident and reflect wave on each port of the intake system. The wave decomposition algorithm makes use the pressure signals measured by the four wall-mounted microphones (GRAS ¼"), at each measurement section. For sake of brevity, a deep description of the test rig and of its software is omitted, since it may be found in reference[6].

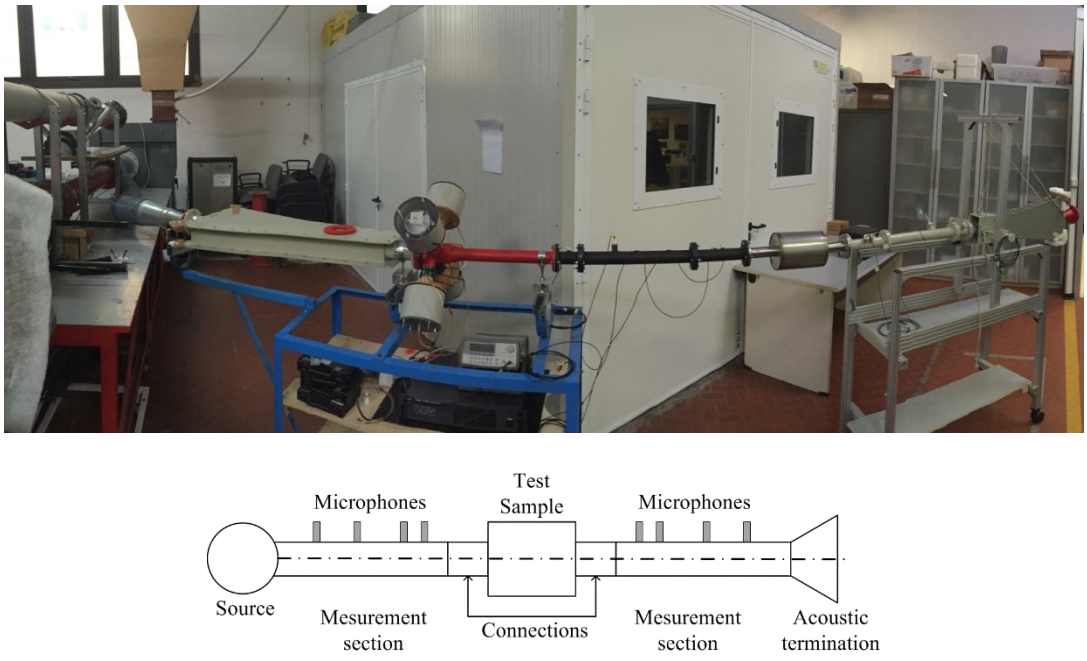


Figure 5.6 - Custom test bench (top) for Transmission Loss analysis and its schematization (down).

Before proceeding with the description of the experimental outcomes, it is necessary to highlight the complexity of the air induction system assembling procedure on the test rig. In fact, as it is highlighted in Figure 5.7, both the outlet and inlet duct have not a straight constant cross section shape, but both are complex curved and with a variable diameter. Then, considering that the inlet and outlet diameters are different with respect to those of the measurement sections of the test rig, it has been necessary to make two short custom connections which are visible in the figures below. Such additional ducts are made of steel and have been located inside the modified inlet and outlet duct, as it is highlighted in red within the above mentioned figure.

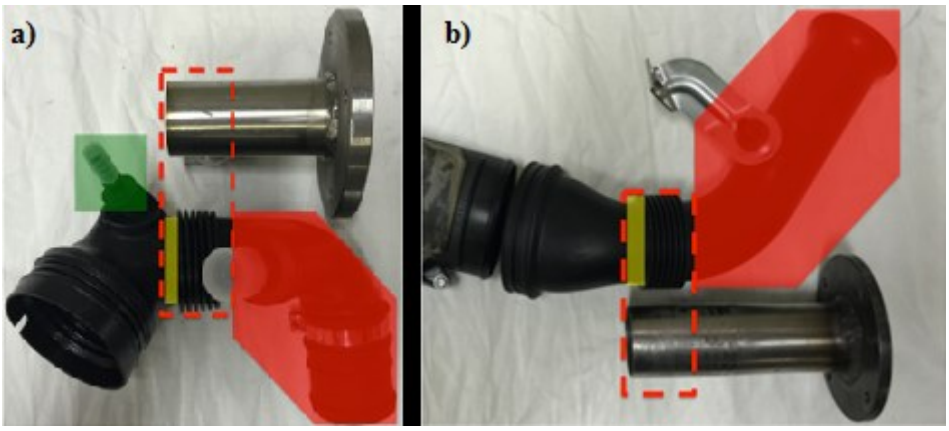


Figure 5.7 - Outlet tube (engine side) a) and inlet tube (ambient side) b) of the air induction system.

The experimental tests allow the evaluation of the TL of the whole system under investigation. More in detail, the acoustic properties of the intake have been evaluated between the inlet section and the outlet section both highlighted in yellow in Figure 5.7.

Thus, the Transmission Loss analysis has been carried out within the range $[40;\ 2000]\ Hz$ with a frequency step equal to $20\ Hz$. All the tests are performed at ambient condition without mean flow, as reported in table 3.

| | | |
|---|---|---|
| Ambient Temperature | [K] | 288 |
| Ambient Pressure | [Pa] | 101000 |
| Relative Humidity | [-] | 50% |

Table 3- operating conditions during the Transmission Loss experiments.

Basically, the acoustic performance of the test case has been investigated in three conditions. The first two tests have been executed with and without the presence of the air filter respectively. The third analysis has been made in order to assess the influence of the structure flexibility on the Transmission Loss. In this regards, in order to not enable acoustic induced structural vibrations, the system has been made infinitely rigid by putting it in a box fully filled with sand, as depicted in Figure 5.8.

Figure 5.8 - The intake system is placed in a box filled with sand in order to ensure no structural vibration.

In fact, with this particular experimental layout the structure of the system should not be allowed to vibrate under the action of the acoustic field inside it. In Figure 5.9, the effects on the TL profile of the structural participation are depicted. Here, the black line refers to the rigid wall configuration, while the red one refers to the flexible wall configuration.

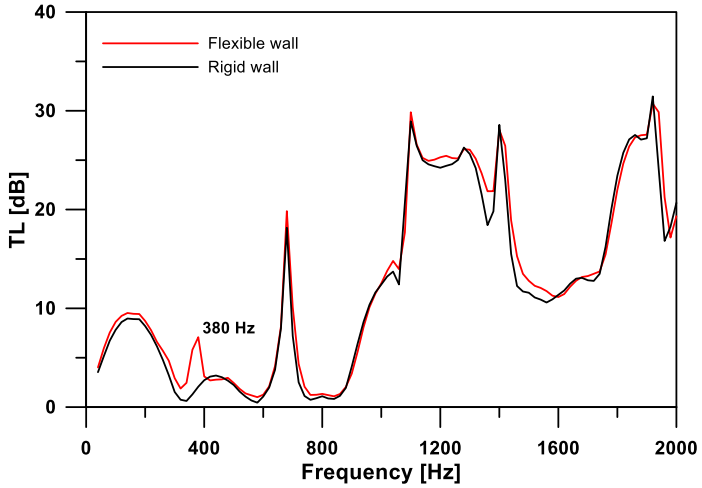


Figure 5.9 - Experimental Transmission Loss comparison, with and without structural participation.

The first comment which has to be done is that the Transmission Loss of the intake system has a quite smooth profile except for the presence of some peaks. However, it is impossible to understand why the TL profile appears in such a trend as that depicted above, meaning that it is not possible to know, for example, if a peak is due to a cavity mode or a resonator. Such information may only be available with the aim of a numerical model, as it will be shown in the next section. Secondly, from the comparison of the two tests the effect of the structural participation on the acoustic attenuation characteristic is evident. More precisely, the fluid-structure interaction seems to take place only in correspondence of the peak of the TL at 380 $Hz$, while at the other frequencies it does not have a substantial effect. However, it is important to highlight that even if an experimental analysis of this type is able to reveal any particular difference in the Transmission Loss profile due to structural modes, it is impossible to point out which of the structural resonances is responsible for that peak in the TL profile.

As regards the third experiment, the air filter inside the intake system is reported in Figure 5.10. As it is possible to appreciate in figure below, it is a rectangular shaped geometry made of a support (orange) and the air filter itself. This latter consists of several paper sheets arranged in a way such that 94 plies are present along the longest dimension.

Figure 5.10 – Air filter inside the air induction system.

The Transmission Loss assessment test has been executed without taking into account the structural participation, obviously in the same way of the no-filter condition (see Figure 5.8), and the results are depicted in Figure 5.11. Here the red curve refers to the presence of the air filter during the experiment, whilst the black one refers to the no-filter condition.

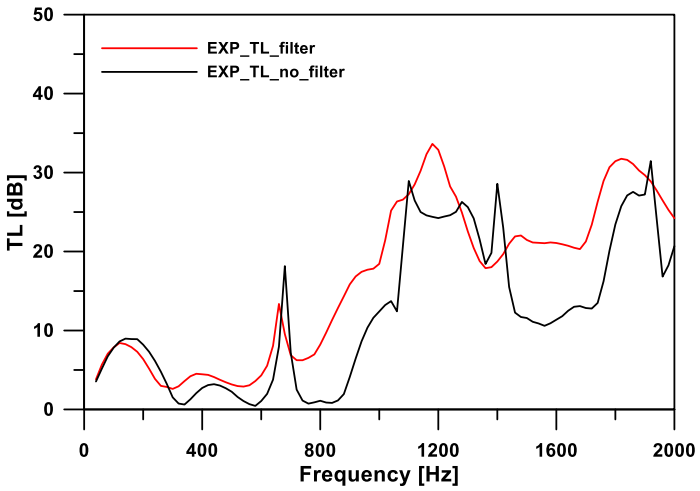


Figure 5.11 – Experimental Transmission Loss comparison, with and without the air filter inside the system.

As it is possible to point out from the comparison within the above picture, the maximum benefit on the Transmission Loss is achieved at high frequencies. This is not surprising because of the sound attenuation mechanism the air filter relies on. In fact, such further component is made of porous material which has an high absorption coefficient whose effect is due to the dissipation of acoustic

energy into heat. The higher the frequency the higher the friction effect between air particles within the porous material. Another effect to appreciate, due to the sound attenuation achieved when the filter is located inside the air induction system, is the smoothening effect achieved by the presence of the filter.

## 5.3 Numerical procedure

In this section, the numerical analyses will be in depth discussed. In particular, the procedures aimed to the finite elements model creation, and the corresponding results are presented, following the schematization on the right-hand side of the flow chart depicted in Figure 5.1.

### 5.3.1 CAD preparation and FE models creation

In general, and as Figure 5.1 suggests, the starting point of whatever numerical analysis is represented by the availability of the CAD model of the system under investigation, since it is a mandatory crucial information for the preparation of the finite element discretization. In Figure 5.12, the structural CAD model corresponding to the studied system (see Figure 5.5) is reported. Here, it is possible to recognize both the original inlet and the outlet sections with their original dimensions, together with the components the system consists of.

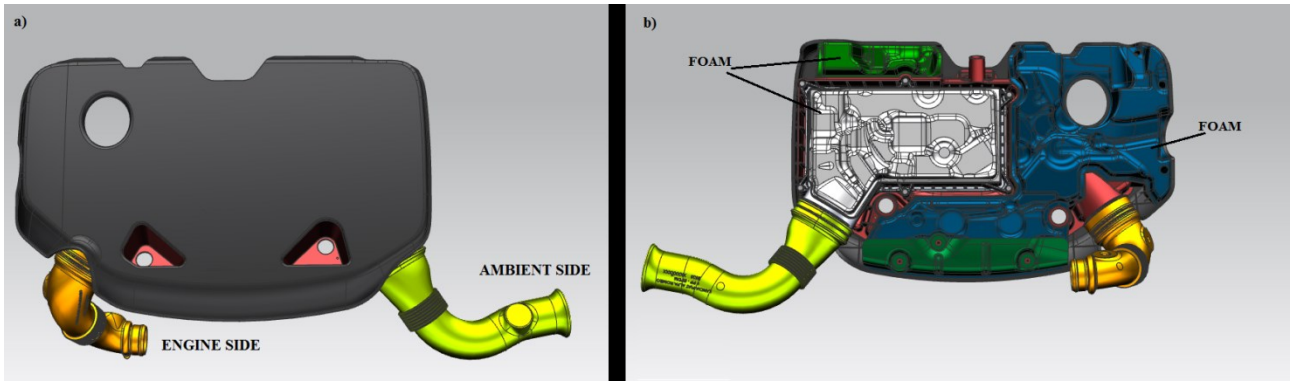


Figure 5.12 - Structural CAD model of the studied system: a) top and b) down view.

In particular, by the examination of the above figures, it is evident that the global system is composed by five subsystems: inlet (yellow), filter box (white), airbox (red), outlet (orange), cover (black). Moreover, as it is possible to appreciate be the examination of Figure 5.5 b), behind the original device some foam material (green, white and blue reported in Figure 5.12 b)) is attached, which is likely useful in order to damp the mechanical vibrations transmitted by the engine head and to prevent extremely high heating of the intake system. In fact, excessive heating of the intake system must be avoided as the higher the temperature of the air the lower the volumetric efficiency of the engine. In figure below, a particular view of the air induction system is shown, in which it is possible to appreciate the CAD model of the air filter.

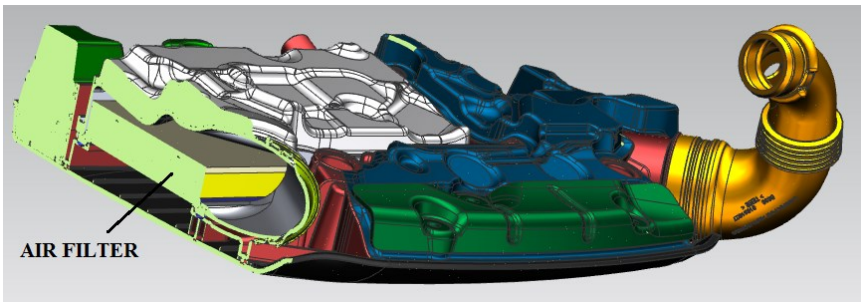


Figure 5.13 - Structural CAD model of the studied system: a) top and b) down view.

As it has been already mentioned, it consists of a paper sheet arranged in a way such that several plies are formed in the direction orthogonal to the flow propagation within the filter box. Additional views are reported in figure below.

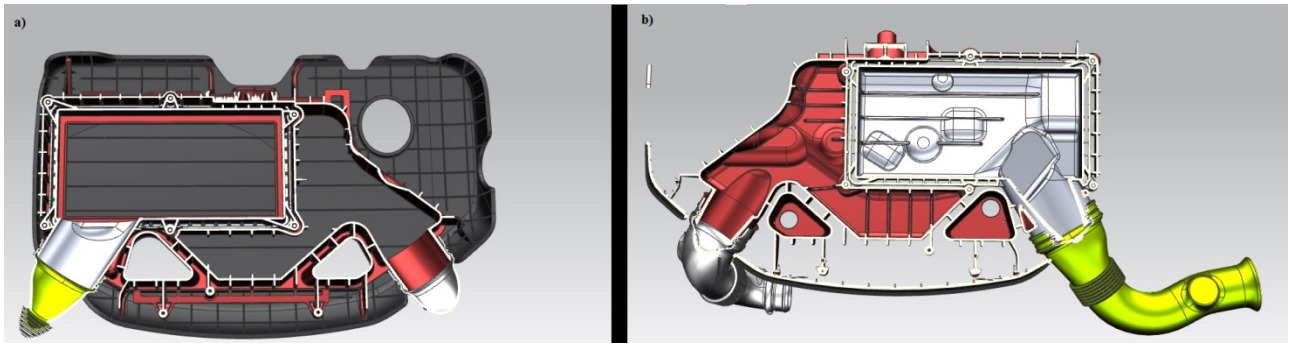


Figure 5.14 - Detailed view of the structural CAD model of the studied system: a) down and b) top.

As it is possible to appreciate from Figure 5.14, the assembly is quite complex as there are a lot of geometrical details. In particular, considering the detailed view of the filter box depicted in Figure 5.15, there are a plenty of small features which need to be removed in order to proceed with the creation of the finite element mesh. As matter of fact, most of the times, the preparation of the CAD model for FE simulations represents a complex, time consuming task but necessary for the sake of successful ending of the simulation.

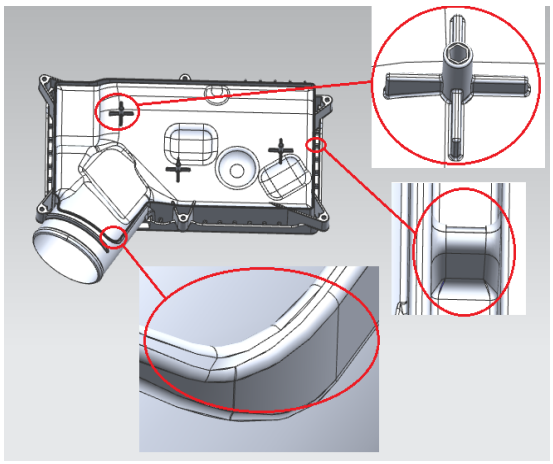

Figure 5.15 - Example of small surfaces which are present on the CAD representation of the filter box.

In fact, a CAD representation is often composed of a large number of small faces, some of which may be narrow (also called slivers) or short edges that are much smaller than the desired FE

element size (to be set up for following mesh generation). Consequently, these faces and edges represent only topological information which in principle are redundant for the meshing process. Such inconsistencies often cause either poorly-shaped elements and zones in which the mesh is locally over-densified. As consequence, these inconsistencies not only slow down the solver (because of a useless, large amount of elements) but also produce poor or erroneous simulation results, generally because of failing in the geometry checks of the solver, for some highly distorted element. For these reasons, the first step on the way of the finite element creation has been represented by the elimination of all such geometrical features that do not influence the acoustic response of the whole system, but only the computational time and, in some cases, the goodness of the results.

Once the structural CAD model has been cleaned, it has been necessary to reproduce the acoustic interior domain represented by the air volume embedded inside the structure. The results of this further step is represented by the additional acoustic CAD model depicted in Figure 5.16.

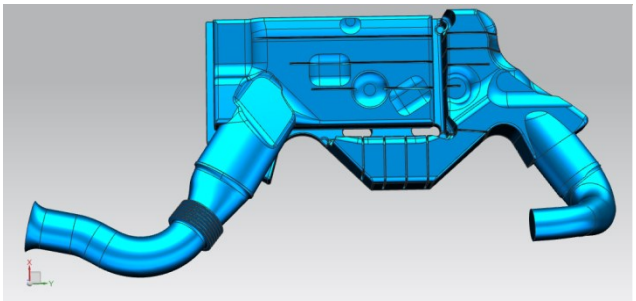

Figure 5.16 - Original acoustic CAD model.

However, before proceeding with the finite element model creation, both inlet and outlet tubes have been modified in order to reproduce the experimental layout. These modification, applied on both structural and acoustic CAD model, are depicted in Figure 5.17.

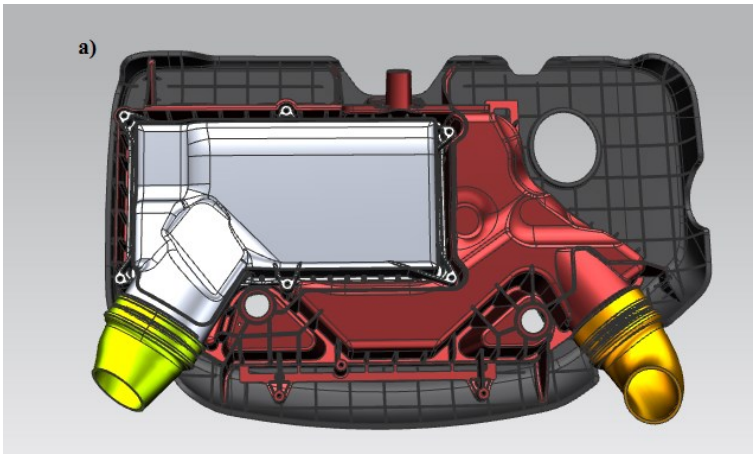

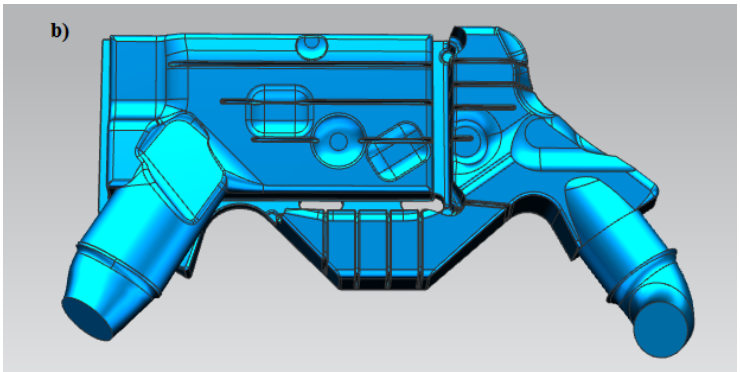


Figure 5.17 - Modified structural CAD model a) and the corresponding acoustic one b).

A brief summary about the building-up procedures for the numerical model is below reported, with regards to three different FE analyses which have been conducted by using the commercial software Actran release 15.1, powered by Free Field Technology. More precisely, in order to reproduce the experimental Transmission Loss assessment, the following models have been created:

- Rigid wall assumption without the presence of the air intake filter
- Rigid wall assumption with the presence of the air intake filter
- Flexible wall assumption without the presence of the air intake filter

#### 5.3.1.1 Numeric purely acoustic models

Once the CAD model of the acoustic domain has been realized, the discretization process takes place. In particular, the mesh generation phase has relied on the use of a commercial software. As already mentioned above, finite element codes, which are used for solving acoustic problems, generally solve the frequency domain version of the wave equation. In this regards, for acoustic FE analyses, according to the rule of thumb mentioned in chapter 4, it is generally recommended that the maximum element size does not exceed the lowest wavelength (highest frequency) of interest divided by six, namely

$$E_{size} = \frac{\lambda}{6} \tag{5.44}$$

Such need is required by the fact that otherwise there would be a poor spatial resolution for obtaining reliable results at the maximum frequency of interest. This is schematically depicted in Figure 5.18, where two types of finite element discretizations have been schematized in 2D symmetry.

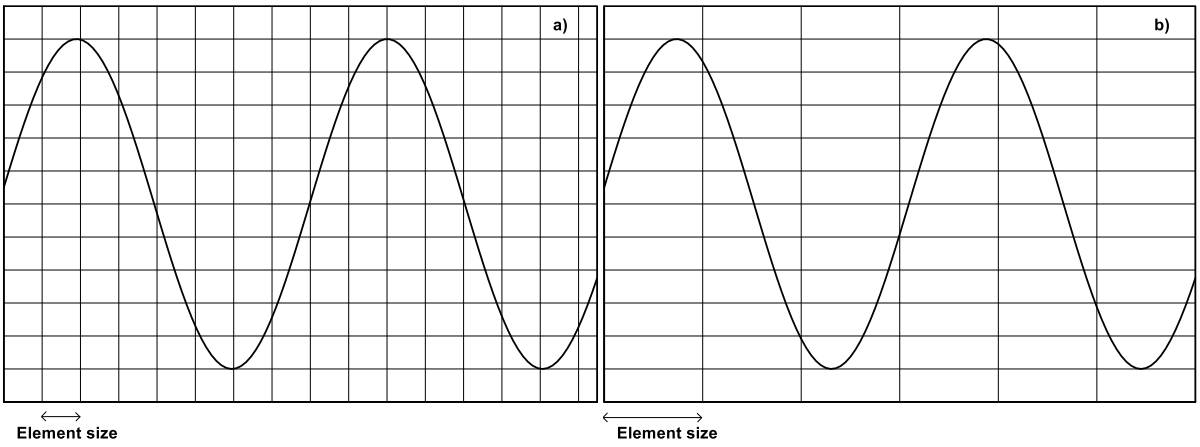


Figure 5.18 - Schematization of a) fine and b) coarse finite element model discretization.

More precisely, discretization ensuring almost 8 elements per wavelength and almost 3 elements per wavelength are shown in Figure 5.18 a) and b) respectively. Thus, as it is possible to appreciate by the examination of the above figures, considering a fixed frequency, the higher the element size the lower the accuracy in catching the wave propagation in the horizontal direction. Following such fundamental guideline, the cavity mesh has been created and it is reported in Figure 5.19.

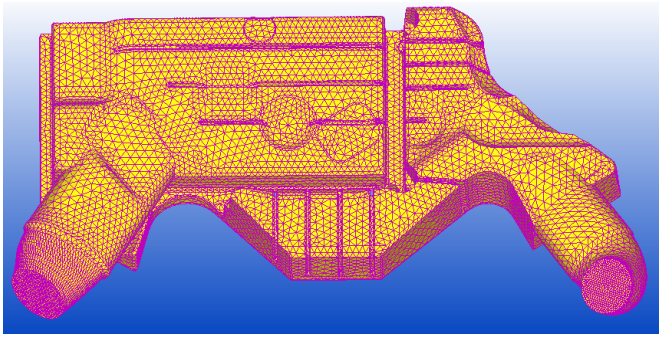

Figure 5.19 - Acoustic mesh of the modified acoustic CAD model.

It is constituted by 84286 nodes and 51844 of solid elements (Tetra 10-noded), allowing acoustic analyses until $5000\,Hz$ considering a spatial resolution of six points per wavelength. From a modelling point of view, in order to simulate the presence of an arbitrary acoustic source at the outlet section, a white noise signal, represented by a constant unit amplitude of sound pressure, has been imposed, whilst a non-reflecting boundary condition has been imposed at the inlet section. More precisely, among the available boundary conditions for simulating incident pressure fields, in order to be able to evaluate the Transmission Loss, a semi-infinite duct has been used in which unit amplitude (equally spread in the frequency domain) plane waves propagating towards the system has been imposed (waves eventually travelling in the opposite direction are damped)[5]. In this way the computed power entering the system is only due to the contribution of the imposed wave. Such modelling procedure is schematized in figure below.

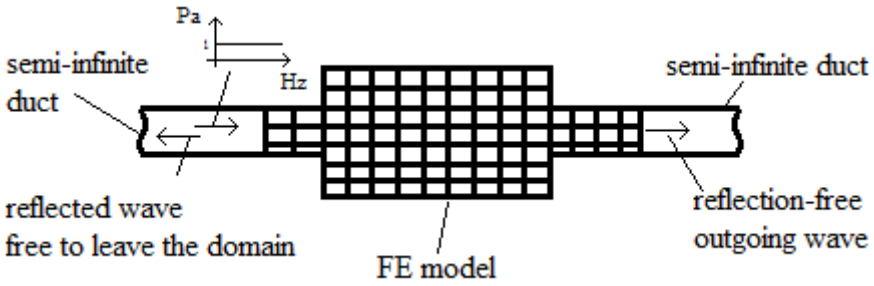


Fig. 5.20 - Schematization of the imposed boundary conditions for Transmission Loss.

The node at which such boundary conditions have been applied are depicted in red (acoustic source) and green (anechoic termination) in Figure 5.21.

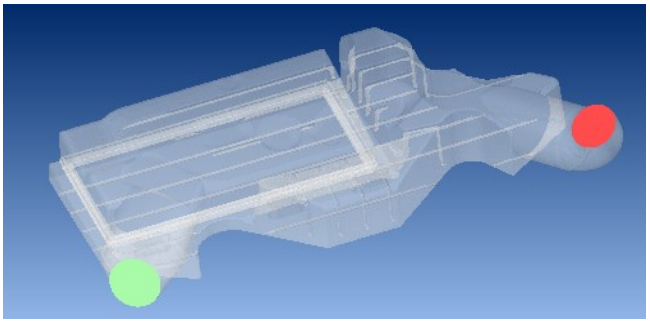

Fig. 5.21 - Boundary condition for the purely acoustic model.

Besides, this simulation does not take into account the structural-acoustic coupling, meaning that the structure is supposed to be infinitely rigid. From a practical point of view, this means that the particle velocity, and so (thanks to the momentum balance) the normal pressure gradient, at the wall is zero. Thus, apart from the above mentioned boundary conditions, the further following condition has been implicitly imposed

$$\left(\frac{\partial p}{\partial n}\right)_{wall} = 0 \tag{5.45}$$

which is known as Neumann BC[3]. The numerical analysis has been carried out within the range $[20;\ 2000]\,Hz$ with a frequency step equal to $20\,Hz$. The corresponding output in terms of Transmission Loss is depicted in Figure 5.22.

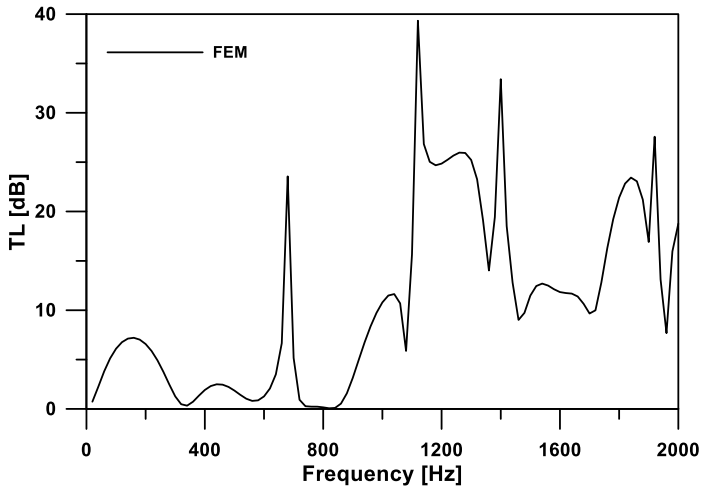


Figure 5.22 - Transmission Loss results in rigid wall configuration.

As it is possible to appreciate from Figure 5.22, the Transmission Loss is quite smooth apart from the presence of some sharp peaks at distinct frequency location. As it has been already pointed out, for very complex geometries as the air induction system, such trend cannot be explained with an experimental analysis. Such circumstance highlights the importance of building up and validating a 3D finite element model, like the one descried above, by means of which it is quite easy to identify why the system acoustically acts the way it is depicted above. In particular, a detailed explanation of the TL trend depicted in Figure 5.22 will be given in chapter 8.

Almost the same model has been realized when accounting for the presence of the air filter, except from the need of modelling the sound propagation through porous media. The air intake filter is represented by a series of paper sheets arranged as indicated by Figure 5.23 a). It is effectively a porous medium with strongly anisotropic characteristics.

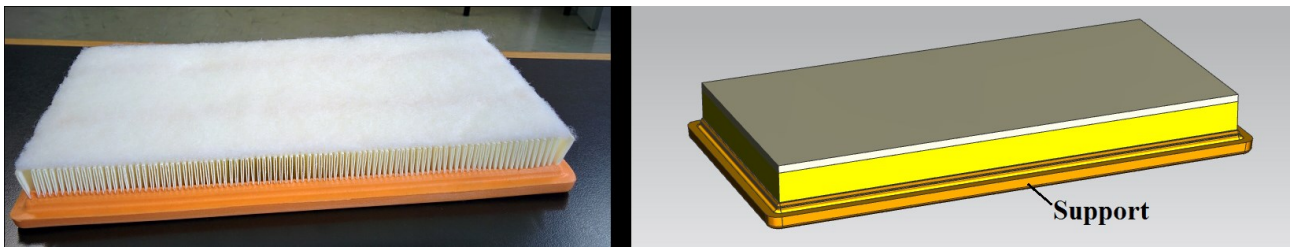


Fig. 5.23 - Air intake filter a) and corresponding CAD model b).

As depicted within the above figure, the filter is placed inside the system with a gummy-like support which has been not modelled in this thesis, on the assumption that its influence on sound propagation is negligible. Thus, from the merely finite element discretization point of view, the further step is represented by the splitting of the acoustic volume according with the propagation in the various acoustic domains. In particular, in this case the propagation of sound takes place in a fluid domain and in a porous medium, as depicted in Figure 5.24.

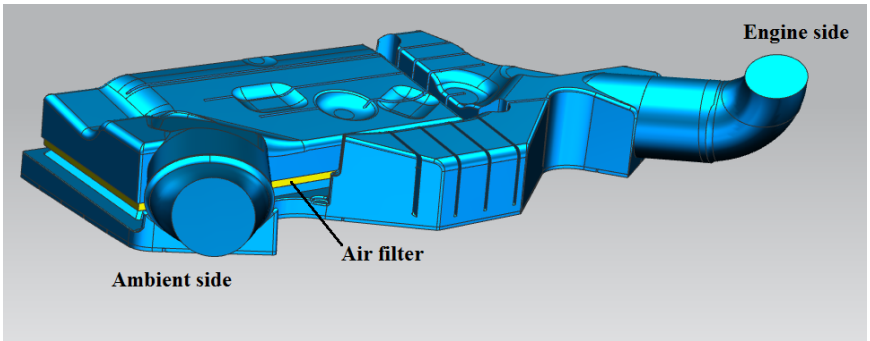


Fig. 5.24 – Acoustic CAD model accounting for the presence of the air filter.

From a numerical point of view, a further complication exists which is represented by the necessity of modelling the sound propagation through such a new medium. A lot of work has been done during the recent history on the way of acoustically modelling porous materials. The available models are divided into micro-models and fluid equivalent models. To the first category belong all that models, e.g. Biot, Allard-Johnson etc.[15], which need as input parameters some characteristics of the pore itself like, tortuosity, viscous and thermal lengths etc.. However, due to the unavailability of such information corresponding to the air filter, the Delaney-Bazley model has been used. In fact, as it has been briefly explained at the end of chapter 3, it only needs one input parameter, namely the flow resistivity, to model the sound propagation considering the filter as an equivalent fluid system (and isotropic as such). The corresponding Actran model with the imposed boundary conditions is depicted in Figure 5.25. The acoustic mesh consists of 54440 elements (Tetra 10-noded) and 93882 nodes, allowing acoustic analyses until 5000 $Hz$, considering a spatial resolution of six points per wavelength.

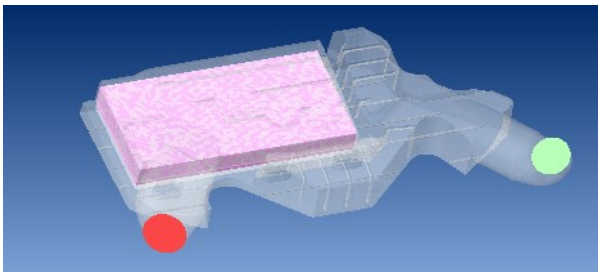

Fig. 5.25 - Boundary condition for the purely acoustic model with the air filter modelled.

Again, in the above picture, the elements on which the non-reflecting boundary condition has been applied are depicted in green whilst those simulating the presence of a sound source are depicted in red; the elements on which the Delaney-Bazley model has been used are depicted in purple. Unfortunately, no flow resistivity measurements have been done so that various analyses have been executed by changing the value of the flow resistivity in the porous region, in order to find the best match with the experimental data. In table 4, the tested values are reported with the corresponding suggested range of validity, according to eq. (3.126).

| Flow Resistivity $[Ns/m^4]$ | Suggested range of validity $[Hz]$ |
|---|---|
| 1000 | $[10; 1000]$ |
| 2000 | $[20; 2000]$ |
| 3500 | $[35; 3000]$ |

Table 4 - input parameter for the Delaney-Bazley model.

However, even in this case, to the aim of comparing both experimental and numerical outputs, the numerical analysis has been carried out within the range $[20;\ 2000]\ Hz$, with a frequency step equal to $20\ Hz$. The outcomes in terms of Transmission Loss are below depicted in Figure 5.26, for the three flow resistivity values of above table.

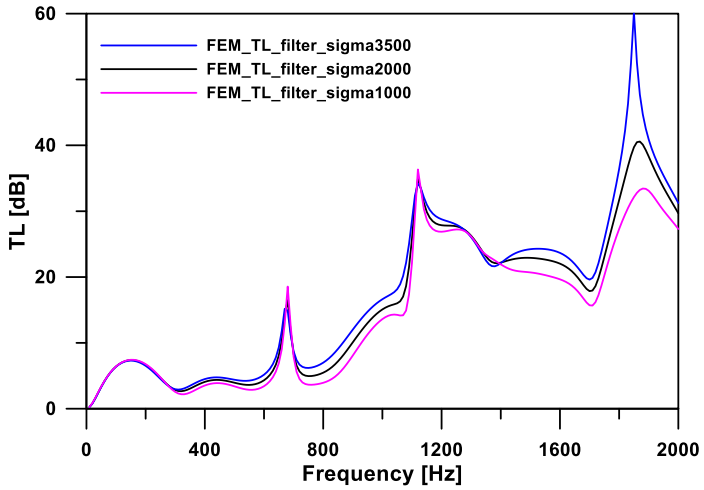


Fig. 5.26 - Transmission Loss results in rigid wall configuration and with the air filter modelled.

Thanks to the comparison of Figure 5.26, it is confirmed the fact that the higher the flow resistivity, imposed in the porous region, the higher the sound attenuation which is achieved by the whole system[11]. The final comparison of experimental and numerical data for model validation purpose, is reported at the end of this chapter.

### 5.3.1.2 Numeric structural-acoustic model

Although a rigid-wall analysis is able to correctly give some important information about the acoustic behavior of the system under investigation, sometimes the presence of a flexible structure may play an important role in determining the acoustic response as well. Considering for example a flexible structure filled with an acoustic medium in which acoustic waves propagate, it might happen that the acoustic field turns out to be as a not negligible load on the solid boundaries, possibly resulting in quite strong structural vibrations. This happens especially when the spectral components of the acoustic phenomenon excite the natural frequencies of the structure. Similarly, if an acoustic fluid is in contact with a vibrating thin-walled structure, the vibrations of the wall may significantly modify the sound field inside and outside the system. Thus, when it is necessary to take into account the coupling between acoustic medium and surrounding structure, a Fluid-Structure Interaction (FSI) Analysis must be performed and the whole system must be analyzed as a coupled structural-acoustic problem[14][13][14]. For Fluid-Structure Interaction problems related to an arbitrarily shaped structure, a numerical solution technique must be used. Typically, in a coupled acoustic-structural analysis, two different FE models are needed, one for each subsystem such as the acoustic domain and structural one. It follows that the further step, with respect to the analysis described in the previous section, has been represented by the modal analysis of the intake system's envelope, aimed to extract the dynamic characteristics of the structure such as natural frequencies and corresponding mode shapes. From an algebraic point of view, once the FE model has been assembled specifying material properties and constraint conditions (as per experimental

layout), the modal analysis for slightly damped structure is carried out by solving the set of equations representing the free vibrations of the system[16][7]

$$[M]\{\ddot{X}\}+[K]\{X\}=\{0\} \tag{5.46}$$

where [M] is the assembled mass matrix and [K] is the assembled stiffness matrix of the system. This is equivalent to solve the following eigenvalue problem

$$([K]-\omega^2[M])\{\Phi\}=\{0\} \tag{5.47}$$

which allows to first extract the eigenvalues $\omega$ (natural frequencies) and then the eigenvectors $\Phi$ (natural modes). Such information represents an additional boundary condition in order to perform a fluid-structure interaction analysis, as it is schematically indicated by the flow chart of Figure 5.27.

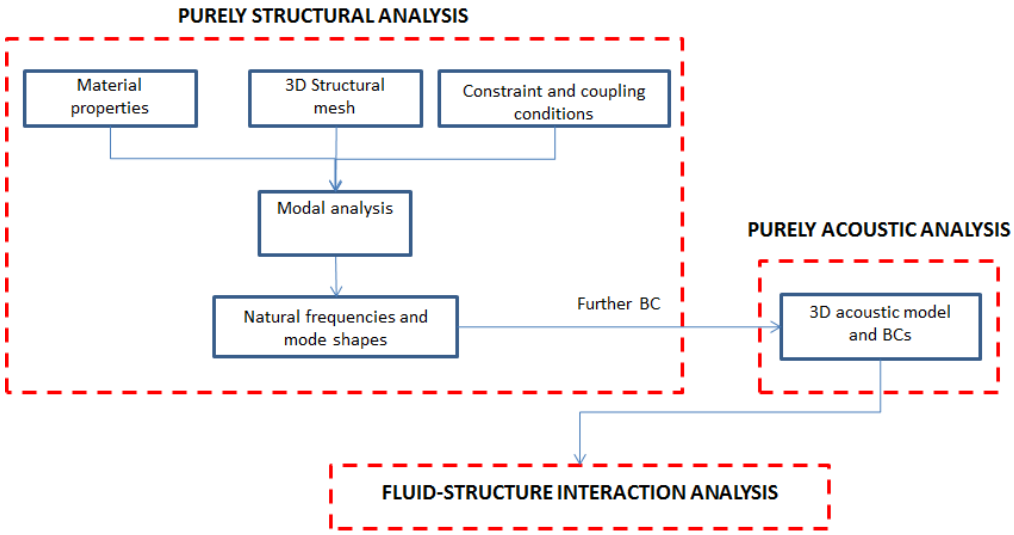


Figure 5.27 - Flow chart schematization of fluid-structure interaction analysis.

Consequently, the same procedure, useful for the purely acoustic finite element model creation, has been used to build up the structural model. In this case however, the correct element size has to be chosen on the basis of consideration about the nature of waves propagating in solid structures. These are transverse shear and bending waves for which different speeds of propagation (and so wavelength) have to be considered. More precisely, considering the wave propagation speeds in bars, they may be expressed as[14]

$$a_s = \sqrt{\frac{E}{2\rho(1+\nu)}} \tag{5.48}$$

$$a_b = \sqrt{\omega}\left(\frac{EI}{m}\right)^{1/4} \tag{5.49}$$

where $E$ is the young modulus, $I$ is the moment of inertia of the cross section with respect to the neutral axis of the considered solid, $\rho$ is the mass density, $\nu$ is the Poisson coefficient and $m$ is the mass per unit of length of the solid (e.g. a bar). It is easy to see that the smaller between the two speeds of propagation is that related to flexural waves and consequently, by the examination of eq. (2.1), the shorter wavelength is the flexural one. It follows that this latter must be taken into account

when calculating the element size for the structural mesh. This latter is depicted in figure below, being constituted by about 1080337 nodes and of 584722 elements (CTETRA-10), considering a spatial resolution of eight elements per wavelength. Here, the various components such as inlet, filter box, airbox, cover and outlet have been indicated in blue, grey, red, green and yellow respectively.

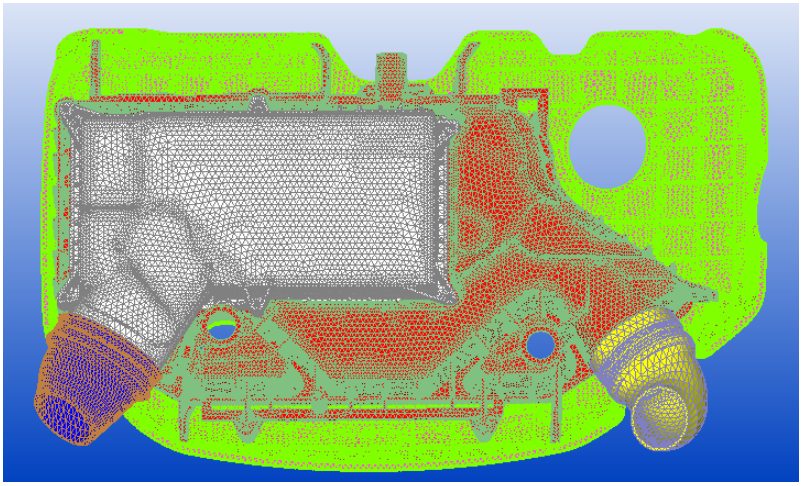

Figure 5.28 - Structural mesh of all the components the intake system is made of.

Then, as already mentioned, the preliminary step in the preparation of the coupled structural-acoustic model is represented by the structural modal analysis of the assembly. Such intermediate analysis has been performed with the help of dedicated software used for structural FE analyses. Here, as schematically depicted in the flow chart of Figure 5.27, the boundary conditions are essentially represented by material properties, constraint conditions and, as the system under investigation is made of several parts, coupling conditions among each components.

| Young Modulus $[GPa]$ | Poisson ratio | Density $[Kg/m^3]$ |
|---|---|---|
| 1,5E+9 | 0,43 | 900 |

Table 5 - Material properties for the structural model.

Hence, the model has been realize by using a glass-fibre reinforced polyamide material[48] (see table 5 for the properties) with the proper fixed constraints, in order to reproduce the same experimental layout, as it is possible to appreciate from the figure below.

[48] Nylon PA 6.6.

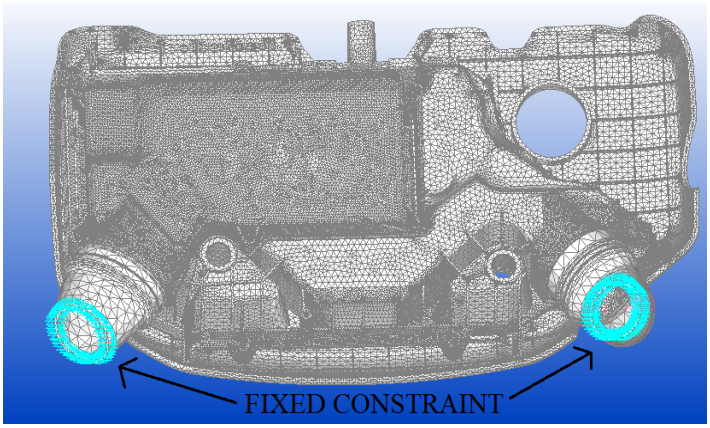


Fig. 5.29 - Constraint conditions for the structural model.

The structural modal analysis has been conducted in the range $[0; 4000]$ Hz[49], in order to account for the influence of modes outside the range of interest[14][14], and 768 normal modes have been found. However, most of them affect local areas of the cover, rather than the actual structure bounding the fluid system. As an example, consider the displacement of the system corresponding to the natural modes depicted in Figure 5.30. Here, within the color map, the purple indicates no motion, whilst the red indicates high amplitudes.

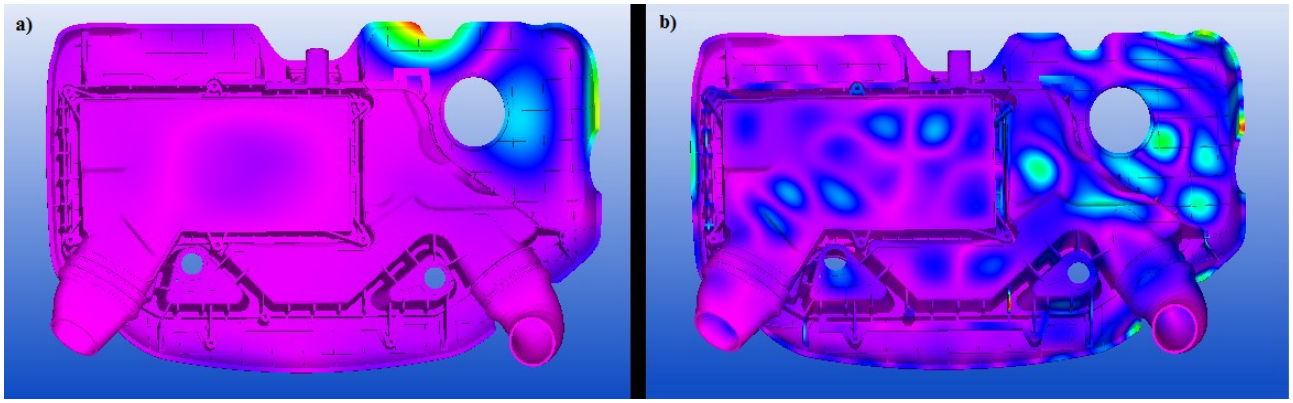


Figure 5.30 – Structural natural modes at 287 Hz a) and 1894 Hz b).

Consequently, it is expected that the flexibility of the structure should not significantly influence the acoustic behavior of the system under investigation. Once the results of the purely structural model, in terms of natural frequencies and corresponding mode shapes, are available, it is possible to feed such information as additional boundary condition for the coupled model, which is depicted in Figure 5.31.

[49] A rule of thumb states that, in order to capture the dynamic behavior of a system within a certain frequency range, all the natural modes having natural frequency below twice the maximum frequency of interest must be considered[13].

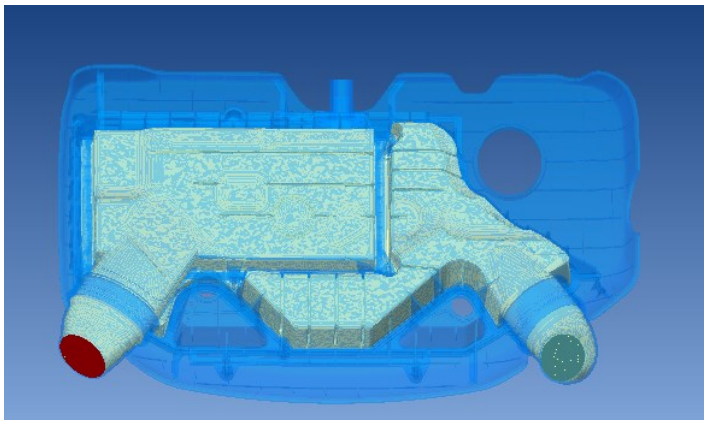

Figure 5.31 - Boundary condition for the coupled structural-acoustic model.

More precisely, in the above picture, the elements on which both the non-reflecting and sound source boundary condition have been applied are again depicted in green and red respectively, whilst the acoustic and structural elements have been indicated in yellow and blue respectively. Even in this case, the Transmission Loss analysis has been carried out within the range $[20;\ 2000]\ Hz$, with a frequency step equal to $20\ Hz$. The corresponding results are depicted in Figure 5.32, where a comparison with the rigid wall analysis (without the air filter) has been made. Here, the black and red line refer to rigid and flexible structure configuration respectively.

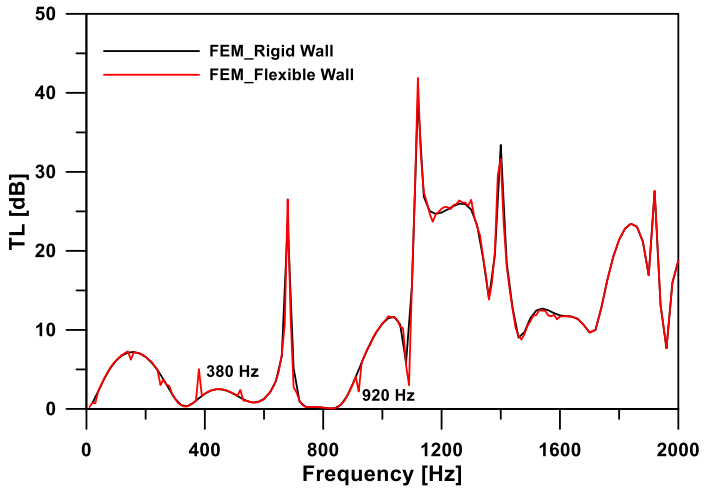


Figure 5.32 - Comparison of the Transmission Loss analysis in both rigid and flexible wall configuration.

As it is possible to appreciate by the examination of the above figure, the Transmission Loss profile remains almost unchanged when accounting for the flexibility of the intake system' structure. The only difference between the two curves relies in the two peaks occurring at 380 and 920 $Hz$. This is probably due to the presence of two structural modes at such frequencies which are reported in figure below.

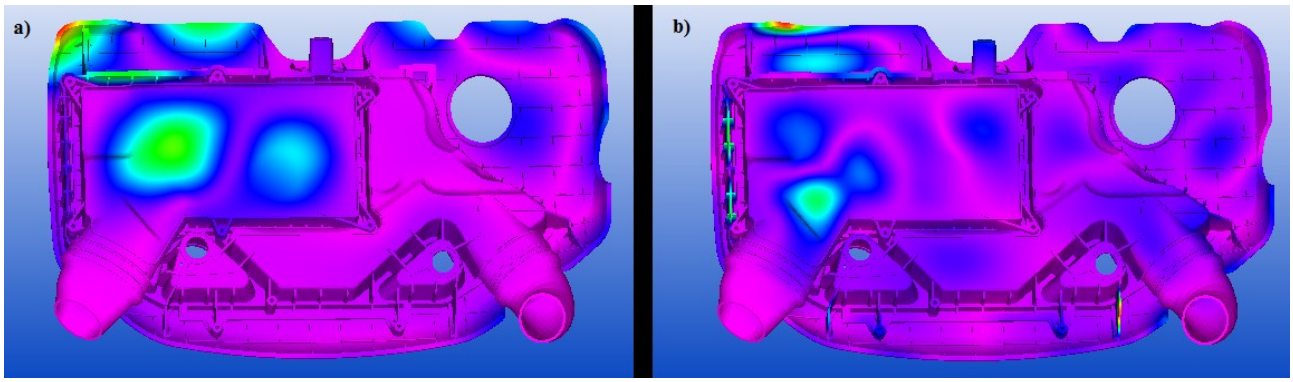


Figure 5.33 – Structural natural modes at 380 Hz a) and 920 Hz b).

Although it is possible to conclude that, in this particular case, the structure does not affect the acoustic response of the system, the possibility of identifying structural modes causing deviation from the rigid wall assumption represents a very important information available thanks to numerical simulations. In fact, with the aim of only experimental Transmission Loss analysis, it would have not been possible to identify the structural modes affecting the response of the system at the two above mentioned frequencies.

## 5.4 Experimental vs Numerical comparison: model validation

Once data from both experimental and numerical analyses have been produced, it has been possible to proceed with various comparisons in order to establish the goodness of the above described Finite Element models. In general, the model validation phase is very crucial within an optimization procedure. In fact, once the FE model has been validated, it is reasonable to assume that the effect of whatever change, which is realized on the model, would be the same if such change is actually realized on the real system. On this idea, in this study a first model validation phase in terms of Transmission Loss has been made. The first comparison is reported in Figure 5.34, where the outputs of the rigid wall configurations, in no filter condition, are reported. More precisely, the red and the black curves stand for the experimental and numerical outcomes respectively.

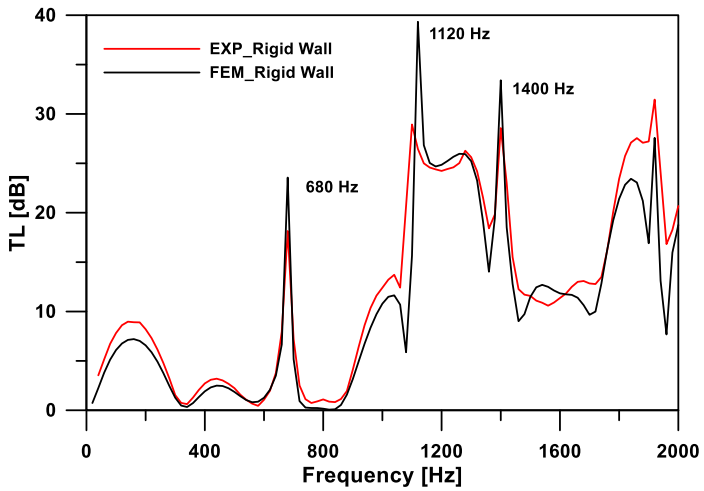


Fig. 5.34 - Experimental vs Numerical comparison in rigid wall configuration.

As it is possible to appreciate from the above figure, a very good comparison has been found between the two Transmission Loss trends. In particular, the numerical solution seems to

underestimates the experimental result, except in correspondence of the first three peaks located at 680 $Hz$, 1120$Hz$ and 1400 $Hz$, where the black curve overestimates the red one. However, thanks to the global satisfactory agreement, it is possible to explain, for example, the presence of this three peaks. In fact, at the end of the FE simulation, when the acoustic pressure has been evaluated at each mesh point, it is quite easy to know what the pressure distribution inside the system looks like, at each resolved frequency. As an example, in Figure 5.35 the acoustic pressure distribution at 680 $Hz$ is depicted.

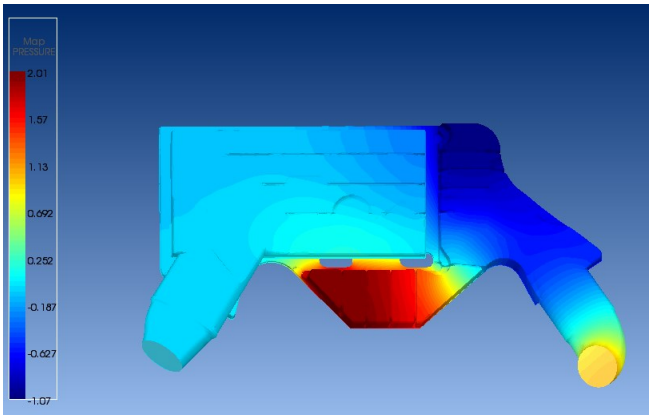


Figure 3.35 - Pressure distribution at 680 Hz.

The important thing that the above figure reveals is that the peak of sound attenuation achieved by the intake system at 680 $Hz$ is due to the cavity highlighted in red which, evidently, acts as an Helmholtz resonator. The same kind of explanation holds for the peak located at 1120 $Hz$, for which the pressure distribution is depicted in Figure 5.36. Here the resonant cavity is highlighted in blue.

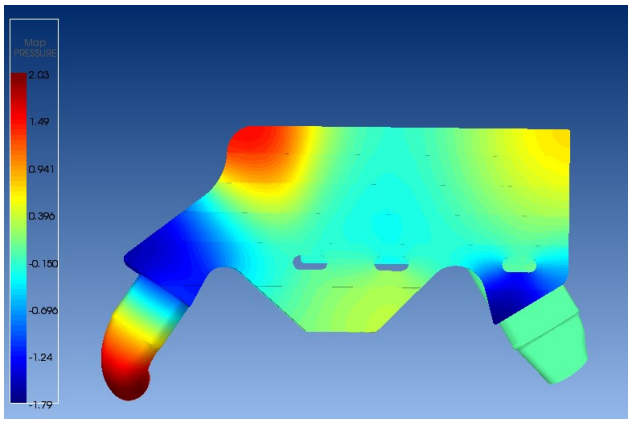


Fig. 5.36 - Pressure distribution at 1120 Hz.

Moreover, as it is possible to appreciate by the examination of Figure 5.34, the above mentioned peak occurs slightly shifted with respect to the corresponding peak in the experimental curve. This is probably due to a small difference in the volume of the cavity, between the CAD model and the actual one, which changes the resonant frequency. Another and more complicated explanation holds for the high value of the Transmission Loss reached at 1400 $Hz$. Such behavior could be probably explained from the examination of the acoustic modes of the system. In fact, it is well known that, as it happens for the structural modal theory, thanks to the modal expansion theorem each pressure

distribution inside the system may be represented as a weighted summation of all the acoustic modes. As an example, the general expression of the sound field in a duct is obtained by the superposition of the modes as expressed by eq. (5.50)[2]

$$p'(x,t) = \sum_n \left[ \hat{p}_n^+ \psi_n e^{-jk_{1,n}x_1} + \hat{p}_n^- \psi_n e^{+jk_{1,n}x_1} \right] e^{j\omega t} \tag{5.50}$$

where $\hat{p}_n^{\pm}$ are complex valued amplitudes, $x_1$ is the direction of propagation, $k_{1,n}$ is the wave number in the direction of propagation and $\psi_n$ is the n$^{th}$ natural mode. Consequently, in this case it has been necessary to perform a modal analysis of the acoustic volume, in order to evaluate its resonant frequencies and the corresponding mode shapes. The modal analysis has been executed until 1600 $Hz$ and the resonant frequencies are summarized in Table 6.

| Mode number | Resonant frequency [Hz] |
|---|---|
| 1 | 300 |
| 2 | 510 |
| 3 | 652 |
| 4 | 715 |
| 5 | 859 |
| 6 | 1079 |
| 7 | 1101 |
| 8 | 1348 |
| 9 | 1393 |
| 10 | 1425 |
| 11 | 1551 |

Table 6- First 11 natural frequency of the acoustic cavity depicted in Figure 5.18.

With these information available, it has been found that the ninth acoustic mode, occurring at 1393 $Hz$, is responsible for the peak in sound attenuation at 1400 $Hz$. To the aim of strengthen such evidence, the pressure distribution at 1400 $Hz$ and that corresponding to the above mentioned acoustic mode are depicted in Figure 5.37.

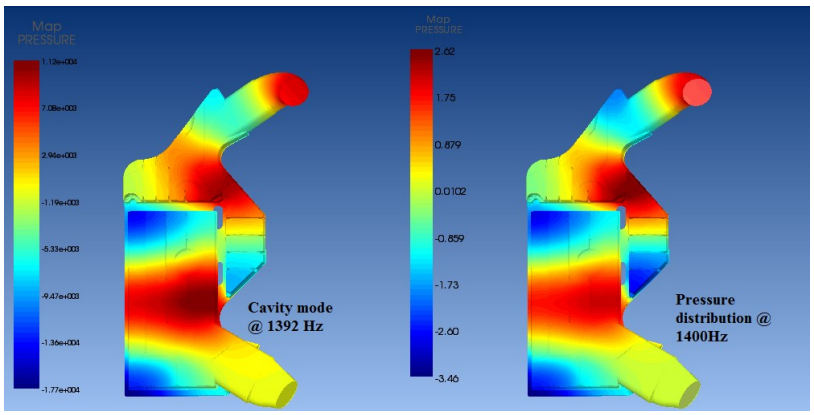


Figure 5.37 - Acoustic pressure distribution a) acoustic mode at 1393 Hz; (b) system response at 1400 Hz.

By the examination of the above figure it is clear that the acoustic response of the system is dominated by the presence of the cavity mode. Such brief analysis highlights, once again, the

importance of a finite element model which perfectly represents the actual system. A more detailed analysis of the acoustic behavior of the intake system will be given in chapter 8.

As regards the comparison in flexible wall condition, both the experimental and numerical outcomes are reported in Figure 5.38, where the same color legend of Figure 5.34 has been used.

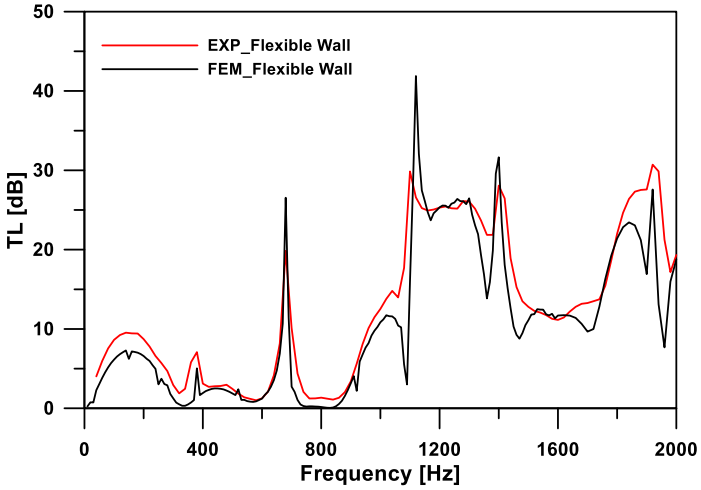


Figure 5.38 - Experimental vs Numerical comparison in flexible wall configuration.

Even in this case, the comparison between numerical and experimental data is globally very good and quite accurate, meaning that the numerical modelling of the acoustic-structural coupling well approximates the real behavior of the whole real system. As already discussed above, the peak at 380 $Hz$ represents the effect of the structural participation as well as the peak located at 920 $Hz$, both mainly involving the filter box area. However, as it follows by the examination of both Figure 5.10 and 5.32, it can be state that the structural model is very stiff and it, in any way, does not substantially alter the acoustic behavior of the system itself.

In Figure 5.39, the last comparison in rigid wall configuration with the presence of the air filter inside the system is reported. Here, the red and black curve represents, again, the experimental and numerical outcomes respectively.

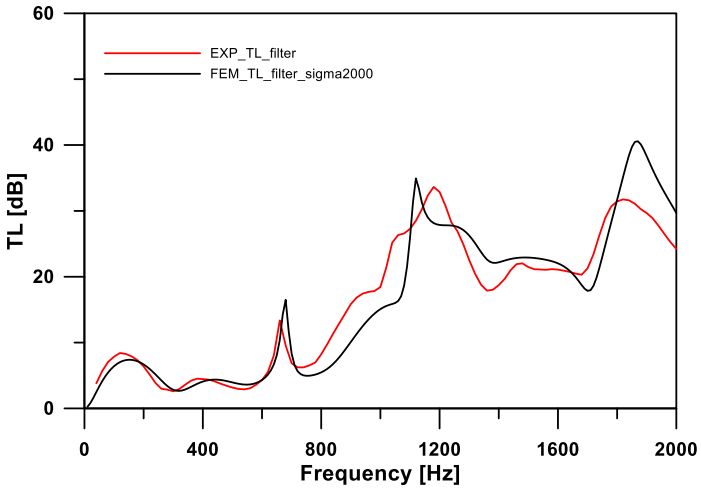


Figure 5.39 - Experimental vs Numerical comparison in rigid wall configuration with the presence of the air filter.

As already mentioned, the Delaney-Bazley law has been used to model the sound propagation through the porous medium constituting the air filter. Among the values of flow resistivity reported in table 2, the second one has proved to better match the experimental results. In fact, by the examination of Figure 5.39, a good agreement is found between the two curves. More precisely, a very good quantitative agreement is found at low frequencies (say until $800\,Hz$), whilst a good trend agreement is found at higher frequencies. Such circumstance is not surprising, as the main effect of the acoustic absorption takes place at high frequencies and the simplest model available has been used, due to lack of information regarding the characteristics of the pores within the paper sheet. Nevertheless, it must be highlighted that the quality of the comparison may be certainly enhanced once a more sophisticated porous model is used for simulating the air filter.

In conclusion to this chapter, a very good agreement has been found between experimental and numerical results, for all the investigated conditions. Such circumstance allows to consider the finite element model of the air induction system as well representing the acoustic behavior, in terms of Transmission Loss, of the actual geometry. However, this represents just a preliminary step for building up a trustworthy numerical model. In fact, what has been discussed in this chapter is just the acoustic characterization study of the stand-alone system. Therefore, further analyses have been conducted in order to confirm such good findings when modelling the noise emitted in real working conditions, namely when the system is coupled with the engine and the other components. However, before proceeding in such further validation process, it has to be taken into account that the system has proved to be quite rigid, at least in the investigated constraint conditions (see Figure 5.29). Consequently, according to the rigid behavior of the structural sub-system which has been observed in the TL analysis and considering the fact that, as it is shown in figure below, the system is even more constrained when located on the engine block, in the subsequent analyses the structure has been assumed as infinitely rigid.

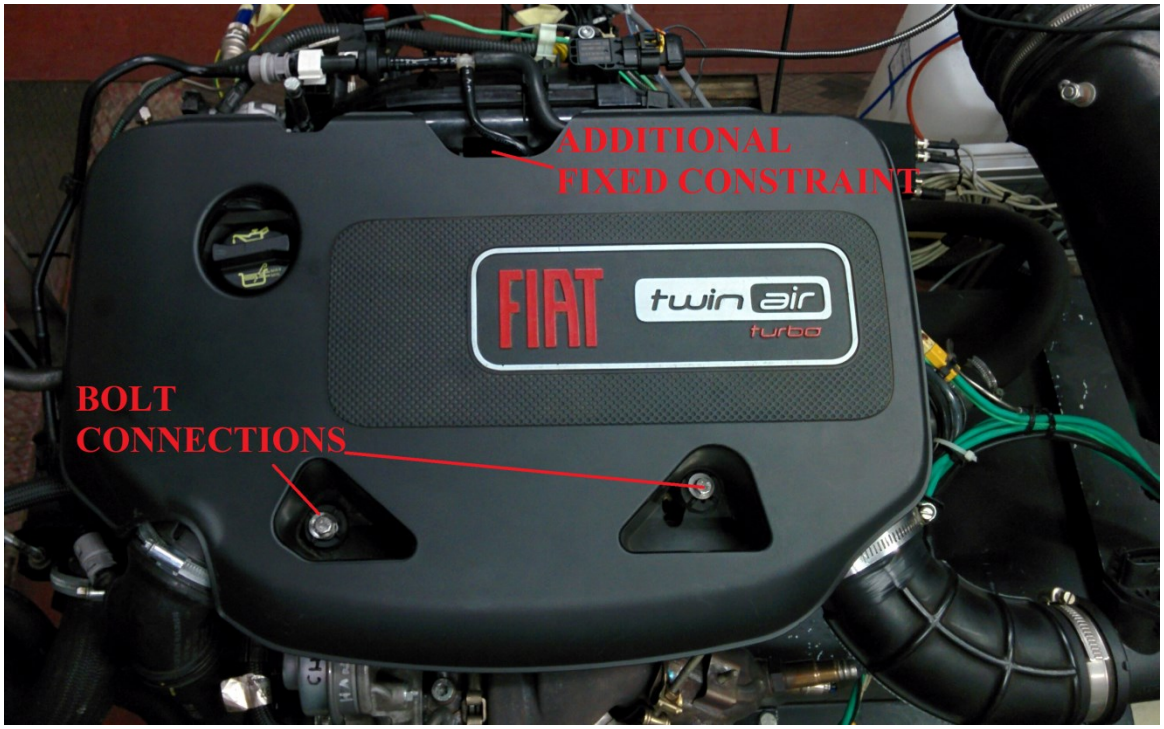


Figure 5.40 – constraint conditions of the air induction system when located on the engine block.

Therefore, further analyses have been conducted taking into account only the propagation of sound in the acoustic domain by means of the purely acoustic model, thus sensibly decreasing the computational time efforts.

## Bibliography


[1] M. L. Munjal, “Acoustics of Ducts and Mufflers with Application to Exhaust and Ventilation System Design”, John Wiley & Sons.

[2] M. Abom, “An Introduction to Flow Acoustics”, Publisher: KTH-The Royal Institute of Technology, ISBN: ISRN/KTH/AVE/N-06/04-SE.

[3] Fine Acoustics Theoretical Manual, Release 5.2.3, July 2014.

[4] O. C. Zienkiewicz, R. L. Taylor, “Finite Element Method: Volume 1”, 5th Edition, Publisher Butterworth-Heinemann, ISBN 07-50-650-49-4.

[5] Bruel & Kjaer, “Transmission Loss Measurements in a Standing Wave Tube”. Techincal Review N°1 2007.

[6] Ferrara G., Ferrari L., Vichi G., Lenzi G. et al., “Acoustic Characterization of Automotive Mufflers - Part I: Test Rig Design and Evaluation of Acoustic Properties,” SAE Technical Paper 2012-01-0800, 2012, doi:10.4271/2012-01-0800.

[7] Ih J. G. and Jang S. H., “On the multiple microphone method for measuring in-duct acoustic properties in the presence of mean flow,” Journal of Acoustic Society of America, vol. 103, no. 3, pp. 1520-1526, 1998.

[8] Heuwinkel C., Enghardt L. and Röhle I., “Experimental Investigation of the Acoustic Damping of Perforated Liners With Bias Flow,” in 13th AIAA/CEAS Aeroacoustic Conference, Rome, 2007.

[9] Heuwinkel C., Enghardt L., Röhle, I., Muhlbauer B., Noll B., Aigner M. and Busse S., “Comparison of experimental and numerical results concerning the dumping of perforated liners with bias flow,” in ASME Turbo Expo 2008: Power for Land, Sea, and Air, Berlin, 2008.

[10] ISO 5136:2003 Acoustics - Determination of sound power radiated into a duct by fans and other air-moving devices - In- duct method.

[11] Mostafa Asadi, Abdolreza Ohadi, Reza Keshavarz, “Effect of non-acoustic properties on the sound absorption of polyurethane foams”, Journal of Theoretical and Applied Vibration and Acoustics 1(2) pp. 122-132 (2015).

[12] F. Fahy, “Sound and Structural Vibration: Radiation, Transmission and Response”, Publisher Academic Press, Inc., ISBN: 0-12-247670-0.

[13] G. Sandberg, R. Ohayon, “Computational Aspects of Structural Acoustics and Vibration”, Publisher Springer-Verlag Wien, ISBN 978-3-211-89651-8.

[14] W. Desmet, D. Vandepitte, “Finite Element Method in Acoustics”, in ISAAC13-International Seminar on Applied Acoustics, Leuven, 2002, ISBN 90-73802-73-3.

[15] J. Allard, N. Atalla, “Propagation of Sound in Porous Media: Modelling Sound Absorbing Materials”, John Wiley & Sons, ISBN: 978-0-470-74661-5.

[16] Anil K. Chopra, “Modal Analysis of Linear Dynamic Systems: Physical Interpretation”, Journal of Structural Engineering, Vol. 122, Issue 5 (May 1996).

[17] J. Kim Vandiver, “Modal Analysis: Orthogonality, Mass Stiffness, Damping Matrix”, MIT course, 2.003SC Engineering Dynamics, Fall 2011.

[18] Actran 15.1 User’s Guide,Volume 1 “Installation, Operations, Theory and Utilities”, April 2015.

# Chapter 6

# Gas-dynamic Noise Analysis

## Introduction

In the present chapter the 1D CFD (Computational Fluid Dynamic) and 3D acoustic analyses of the intake system under investigation are described. These analyses are aimed to predict the gas-dynamic noise emissions, in terms of sound pressure level at the intake mouth, in various engine running points. Such predicted spectra are then compared with the available experimental data, in order to achieve the second validation step for the created FE model.

In the previous chapter, a comprehensive analysis of the acoustic attenuation characteristics of the system under investigation has been in depth presented, describing the creation of a 3D FE model which has been validated comparing both experimental and numerical data in terms of Transmission Loss. However, as it has been already outlined, a Transmission Loss analysis represents just the stand-alone study of the system, which makes available only a qualitative indication about its acoustic frequency response. In fact, no information about noise emissions when it is coupled with the engine are available at the end of the calculation/measurement procedure. Thus, in order to quantify the amount of noise which is emitted in various real operating conditions, a more complicated modelling procedure is needed. However, before proceeding with the description of the procedure aimed to simulate the gas-dynamic noise of the breathing system under investigation, a few comments must be done.

As already mentioned in the introduction of this thesis, the gas-dynamic noise radiated by the intake mouth of a breathing system of an internal combustion engine represents a prominent noise source, at least in low vehicle speed condition. In particular, for the studied system, the only sound attenuation of acoustic waves created at the IVO crank angle positions is achieved by both the throttle and the compressor of the turbocharger group. Moreover, in general, from a modelling point of view, in order to simulate the gas-dynamic noise emitted by both intake and exhaust systems it is important to separate each contribution to the overall emission.

Intuitively, the main source of sound is represented by the pulsating mass flow triggered by the periodic valves opening. However, duct systems connected to an internal combustion engine, e.g. intake and exhaust, host sound propagation in flow condition. This former circumstance, apart from introducing a convection effect on sound waves, as it has been briefly mentioned in chapter 2, allows an additional sound source mechanism to exist. Consequently, it is possible to state that there are two main sources of noise associated with the operation of breathing system of an internal combustion engine, for which noise propagates and, at the same time is generated within the connected duct systems. Hence, the first sound source is represented by the pressure waves, generated by the periodic valves opening, which travel downstream, reaching the external ambient in correspondence of the outlet mouth. Such contribution may be generally called as engine pulses. The second contribution is represented by the turbulence induced noise which is generated inside

the system during the fluid flow[50]. In fact, aerodynamic processes associated with the periodic flow through the valves, together with vortex generation at junction of sudden section changes, constitute an additional source of intake and exhaust noise as well. Such contribution constitutes the so called flow noise.

Nowadays, 1D and 3D fluid-dynamic simulation codes represent very useful tools for the design and optimization phase of systems such as intake and exhaust. In fact, they are commonly used to predict the gas-dynamic noise emissions in various operating conditions[1]. However, for the object of this thesis, a pure 1D approach would present some limitations due to a rather rough schematization of the intake system which, as already highlighted, presents a very complex geometry. Nevertheless, a 1D schematization of the intake system and the whole engine, can be successfully employed to get a first estimation of acoustic performance and boundary conditions for the 3D models.

On the other hand, a purely 3D CFD approach represents a powerful tool, suitable to investigate the flow field developed within complex geometries, allowing for a more or less accurate prediction of the emitted noise (even if some intrinsic limitations exist which will be mentioned in chapter 8). Anyway, problems arise from the setting up of the correct acoustic boundary conditions, which differ from the classical fluid dynamic ones. Consequently, a complete analysis which takes into account the two previous mentioned noise contributions would involve a coupled 1D-3D CFD and 3D acoustic modelling procedure, as it is schematically depicted in Figure 6.1.

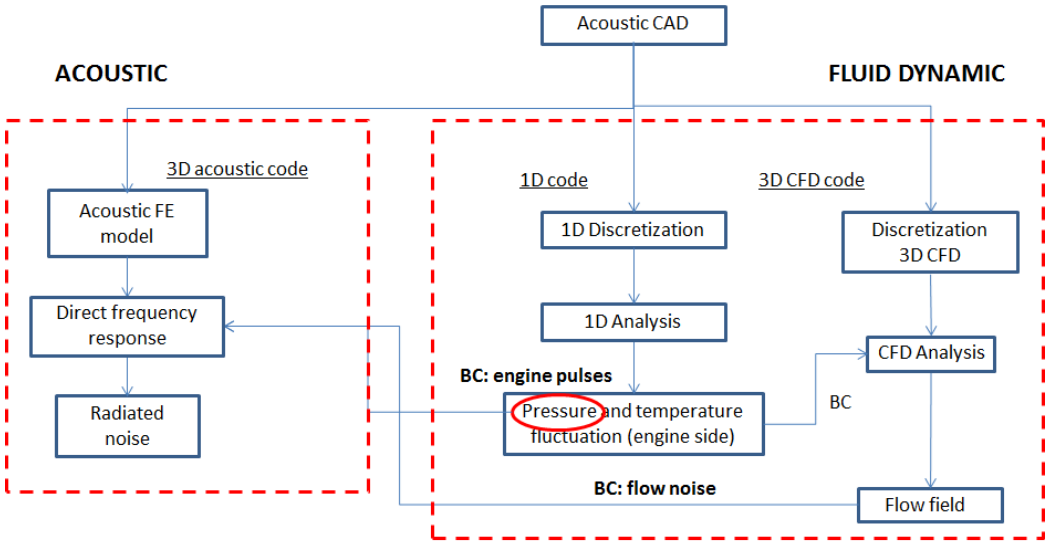


Figure 6.1 – Flow chart of hybrid procedure useful for the gas-dynamic noise analysis.

According to the flow chart above, the output of the 1D analysis is used as boundary condition for modelling the first kind of noise source within the acoustic model (engine pulses). At the same time, such boundary conditions in terms of pressure and temperature fluctuations are used to feed the 3D CFD solver in order to compute the flow field inside the system. This latter represent the additional boundary condition in order to model the flow noise contribution[51] within the purely acoustic model, where the additional proper boundary conditions are easily to set up. In this way, a very

[50] The details of the theory behind the aerodynamic generation of sound are given in chapter 7.
[51] See chapter 7 for the details.

accurate estimation of the sound emission may be made. However, due to the lack of information about the air filter modelling parameters for a 3D CFD simulation, in this chapter the flow noise contribution has not been modelled. In fact, it would be erroneous to feed the acoustic model, which takes into account the presence of the air filter in order to fit the experimental layout, with CFD data coming from a simulation which does not take into account it. Nevertheless, the study of the importance of the flow noise contribution to the overall noise emitted by the intake system is reminded to the last but one chapter of this thesis.

In this chapter, a simpler modelling procedure is described and the results coming from the gas-dynamic noise analysis of the system under investigation will be presented. In particular, the procedures schematized as flowchart in Figure 6.2 will be discussed.

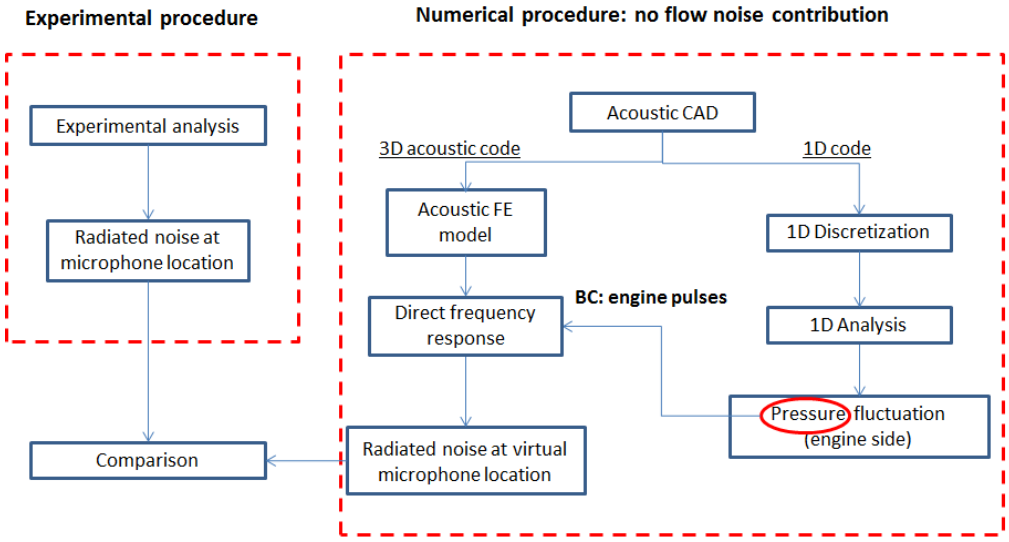


Figure 6.2 – Flow chart of the gas-dynamic noise analysis.

Initially, an experimental campaign, useful for obtaining data for the validation of the 3D acoustic model, will be briefly described. Then, following the schematization of the above figure, the 1D analysis is in depth discussed, highlighting its intrinsic limitations by comparing the outcomes in terms of sound pressure level with the experimental findings. Finally, the 3D acoustic model will be briefly described and the results will be presented in comparison with the experimental ones, in order to confirm the goodness of the model, in analogy to what has been found in the previous chapter.

## 6.1 Experimental analysis

The experimental activity has relied on a comprehensive characterization of the engine behavior in terms of radiated noise, being carried out at different operating conditions. Thus, a proper experimental campaign has been performed, in each tested engine point, to measure the gas-dynamic noise at the intake mouth of the air induction system under investigation. In particular, a schematization of the experimental layout is reported in Figure 6.3. According to the standard ISO (e.g. ISO 15619:2013), measurements have been carried out by using a microphone placed at 1 cm far away from the intake mouth. Thus, the gas-dynamic noise measurements have taken place

during an engine run-up test at full load, by varying the engine speed from $1500\,rpm$ to $5500\,rpm$, according to the engine speeds reported in table 7.

| Engine rpm | Engine rpm |
|---|---|
| 1500 | 3600 |
| 1800 | 4000 |
| 2100 | 4400 |
| 2500 | 4800 |
| 2700 | 5100 |
| 3000 | 5500 |
| 3300 | |

Table 7 – engine rpm tested point.

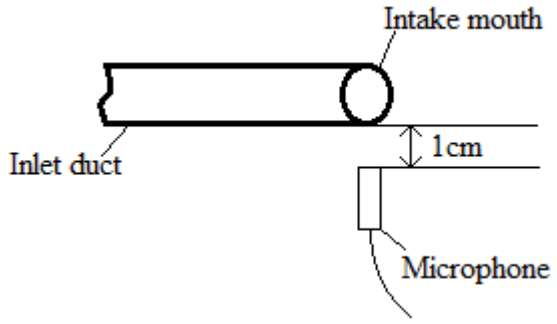


Figure 6.3 - Schematization of the experimental layout.

The microphone signal has been acquired by a multichannel system synchronized with the rotational speed, in order to perform a tracking acoustic analysis. The raw acoustic output is represented by the time domain acoustic pressure signal expressed in $[Pa]$. In a post-processing phase, such data have been then expressed within the frequency domain by performing a discrete Fourier transform in force of the well-known Fast Fourier Transform algorithm. Thus, the sound pressure levels spectra, consisting of only the first fifteen engine orders (defined according to eq. (1)), have been made available in A-weighted $dB$ scale. As an example of available data for subsequent comparisons, the sound pressure level at $3000\,rpm$ WOT (Wide Open Throttle) is shown in Figure 6.4, in $dBA$ scale.

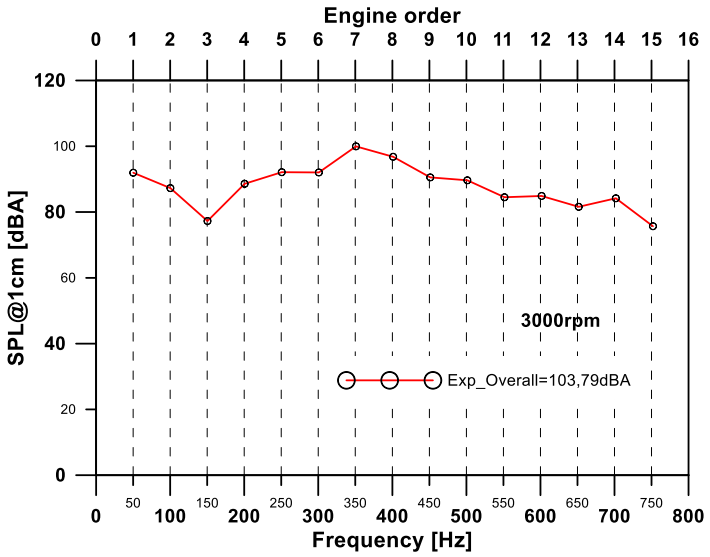


Figure 6.4 - Example of data available from the experimental campaign.

At the same time, the A-weighted overall sound pressure levels in each of the tested engine condition has been calculated, based on the available information about the first fifteen engine orders. Such additional information is reported in Figure 6.5.

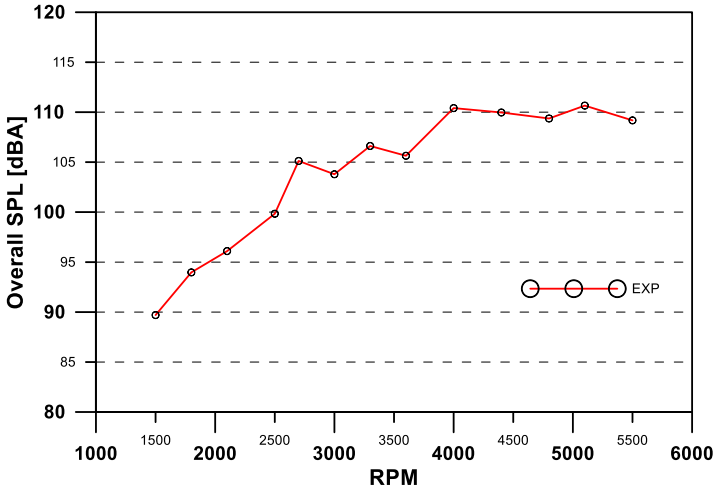


Figure 6.5 - Experimental overall levels expressed in dBA scale.

In the following, such experimental data will be used for the further validation of the 3D acoustic model. In particular, they will be firstly used in comparison with the output of a simple one-dimensional analysis, in order to highlights the limitation of such simplified approach. Then, the goodness of the three-dimensional acoustic model will be discussed, based on the correlation between experiments and simulations.

## 6.2 Numerical analysis

### 6.2.1 One-dimensional analysis

The numerical analyses following a pure 1D approach have been performed according with the flow chart schematization of Figure 6.2. The available 1D engine model has been previously developed within the commercial GT-Power™ software, powered by Gamma Technologies[2]. Such code is

based on a one-dimensional description of flow inside the intake and the exhaust pipes[52], solving the mass, momentum and energy equations. At the same time, the gas mixture inside each cylinder is indeed treated as a zero-dimensional thermodynamic system, in which all thermo-fluid dynamic variables are uniformly distributed. Hence, the virtual engine is constituted by a network of 0D and 1D components.

For what concerns the modelling of the VVA (Variable Valve Actuator) system, an 'user routine' has been specified, according to the engine control parameters and operating conditions. A database of predefined lift profiles is preliminary computed for different engine speeds, starting from $1000\,rpm$ up to $6000\,rpm$, with step of $500\,rpm$. The valve profiles have been previously derived by a valve actuation system model developed thanks to the commercial software Amesim™[3], as a function of various parameters, such as the cam profile, inertial data (valve mass, etc.), spring preload, engine speed, electro-valve opening and closure angles etc..

As regards the modelling of both combustion process and turbulence, this is achieved by means of sub-models which have been introduced in GT-power environment as 'user routines'. In particular, the fractal combustion model[4][5] has been employed. This latter is a phenomenological model sensing both combustion system geometry (head and piston shape, spark plug position, etc.) and operating variables such as engine speed, spark advance, air-to-fuel ratio, valve phasing, etc. Regarding the turbulence modelling, it is described by a proper sub-model accounting for turbulence "production" during the intake stroke[5][6] and its subsequent "destruction". In this way, it is possible to take into account variations in burning speed related to different engine operating conditions. In previous works, the goodness of such 1D model has been investigated. More precisely, by means of a comparison between numerical and available experimental data, the model has been validated at full load condition, showing a very good correlation with the experimental findings[7]. It follows that, it is possible to accurately predict the main overall engine performance and the in-cylinder pressure cycles. However, from an acoustic point of view, it is very important to have a one-dimensional schematization of the intake system as much as possible refined. In fact, as depicted in Figure 6.2, the main excitation to the 3D acoustic model is directly derived by the pressure fluctuations just before the compressor inlet, which are quite sensitive to the 1D schematization of the breathing system.

A typical air induction system is made of a central body with a cross dimension which is significantly larger than both the inlet and outlet tubes, with a more or less complex three-dimensional shape. Besides, in order to prevent unwanted particle such as dust to enter the engine, the air box also typically contains an air filter (or cleaner), which is generally constituted by a crooked piece of paper. Thus, as many times mentioned above, the entire assembly has a significant effect on engine performance, as it directly affects the pressure drop and so the volumetric efficiency, but also on the emitted sound since it represents the direct transmission path to the external ambient. Consequently, its modeling procedure represents a crucial step to perform, if realizable results are desired. Nevertheless, depending on the simulation target, two options are available. For models that will not be used to capture intake acoustic behavior, it is appropriate to use a relatively simple representation of the air box[2], whilst when it is important to simulate the intake noise emissions, it is necessary to perform a more detailed description in the air box model.

[52] The pipes are connected together by so-called orifices, which are 0D elements.

Therefore, to the aim of obtaining an as much as possible suitable one-dimensional representation of the intake system, the useful tool GEM 3D has been used. In this software environment the starting point for the model preparation is represented by the imported CAD model. Thanks to such utility, the CAD model has been firstly divided into parts, depicted in Figure 6.6, which could better represent one dimensional flow components such as straight and bent pipe, flow split etc.. As an example, by the examination of the figure below, it is possible to appreciate that the filter box has been divided in three parts which are depicted in blue, green and brown.

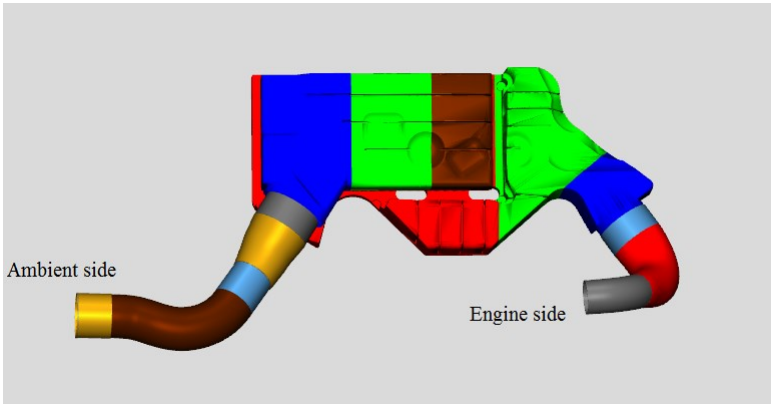


Figure 6.6 - CAD preparation for the 1D schematization process.

Once the 3D model preparation has been completed, it has been possible to carry out the corresponding 1D discretization process. As already mentioned, this latter is constituted by one-dimensional elements for modelling pipes which are used to model flow through tubes, with either constant or tapered cross section, and by zero-dimensional elements which are used for joining different physical components together. These connections, also known as orifices, are nothing else than interfaces (or planes) at which only momentum equation is solved to compute the mass flow and velocity[2]. An orifice can be also used to specify a flow restriction by setting the orifice diameter to be smaller than the diameter of the two mating components.

The result of the discretization process is depicted in Figure 6.7, where the system is made of 14 one-dimensional flow components and three zero-dimensional ones in order to model the air filter. Here it is possible to recognize the entire intake system within the dashed red rectangle and other components such as the external ambient and the engine (not displayed for protecting the innocent).

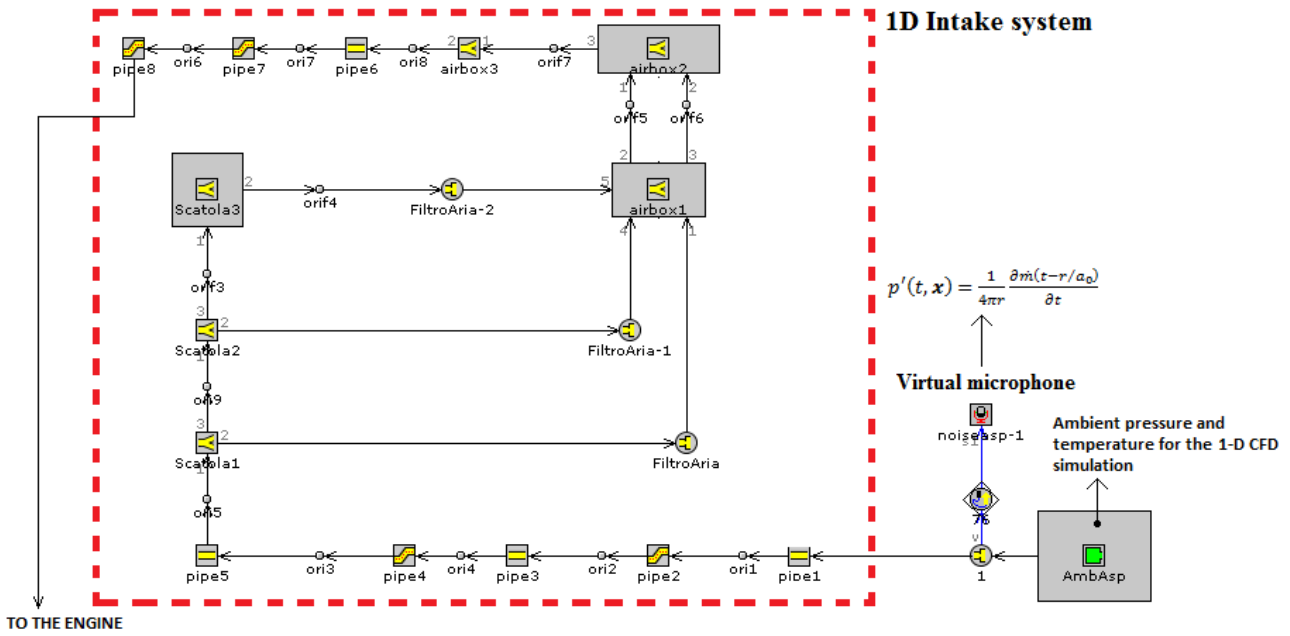


Figure 6.7 – One-dimensional schematization of the intake system.

It must be noted that the pressure drop across the air filter is usually small corresponding to the expansion/contraction related pressure losses and therefore the filter is generally not modelled. However, after carrying out a sensitivity analysis, in order to assess the influence of the presence of the air filter within the one-dimensional schematization on the acoustic simulation capabilities, it has been decided to model such element as schematized in the figure above. Besides, it is also possible to recognize the presence of a virtual microphone useful to compute the overall sound pressure level at 1 cm far away from the intake mouth, according to the experimental layout of Figure 6.3. This object allows to compute the acoustic pressure fluctuations at the experimental microphone location by treating the intake orifice as a simple pulsating monopole. More precisely, the gas-dynamic noise is calculated starting from the results of the unsteady 1D CFD simulation, where the computational domain ends at the intake mouth (ambient side). Obviously, since one dimensional symmetry has been assumed, no turbulence is modelled and the noise at the virtual microphone location involves only the engine pulses contribution on the overall sound emission and it is calculated based on the assumption that the sound field is a pure monopole field, following an inverse-square law for the sound intensity. In particular, the 1-D code makes use of the free field Green's function[53], assuming the intake mouth (ambient side) as monopole source term, namely according to eq. (6.1)

$$p'(t,\boldsymbol{r}) = \frac{\rho A}{4\pi \boldsymbol{r}}\frac{\partial u(t-r/a_0)}{\partial t} \tag{6.1}$$

where $\rho$ is density of the free field medium, $A$ is cross sectional area of the orifice, $u$ is the velocity of the gas and $\boldsymbol{r}$ stands for the distance from the intake mouth. Hence, it merely calculates the time derivative of mass out flow from the pipe, starting from the velocity at the boundary, according to the schematization of Figure 6.8.

[53] The detailed theory is reported in chapter 7.

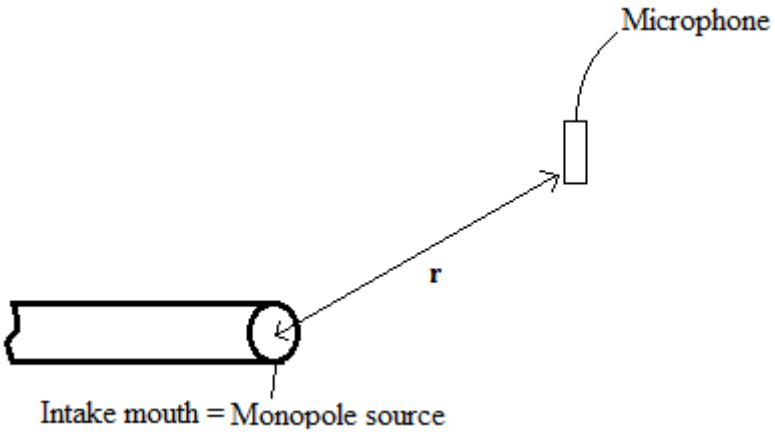


Figure 6.8 – Schematization of the virtual microphone location during the one-dimensional analysis.

The sound pressure levels, calculated in each of the experimentally tested conditions, are reported in the figures below, where the red curves represent the experimental trend whilst the blue ones stand for the 1D simulation output. Obviously, in agreement with the available experimental data, only the first fifteen engine orders have been plotted for the blue curve.

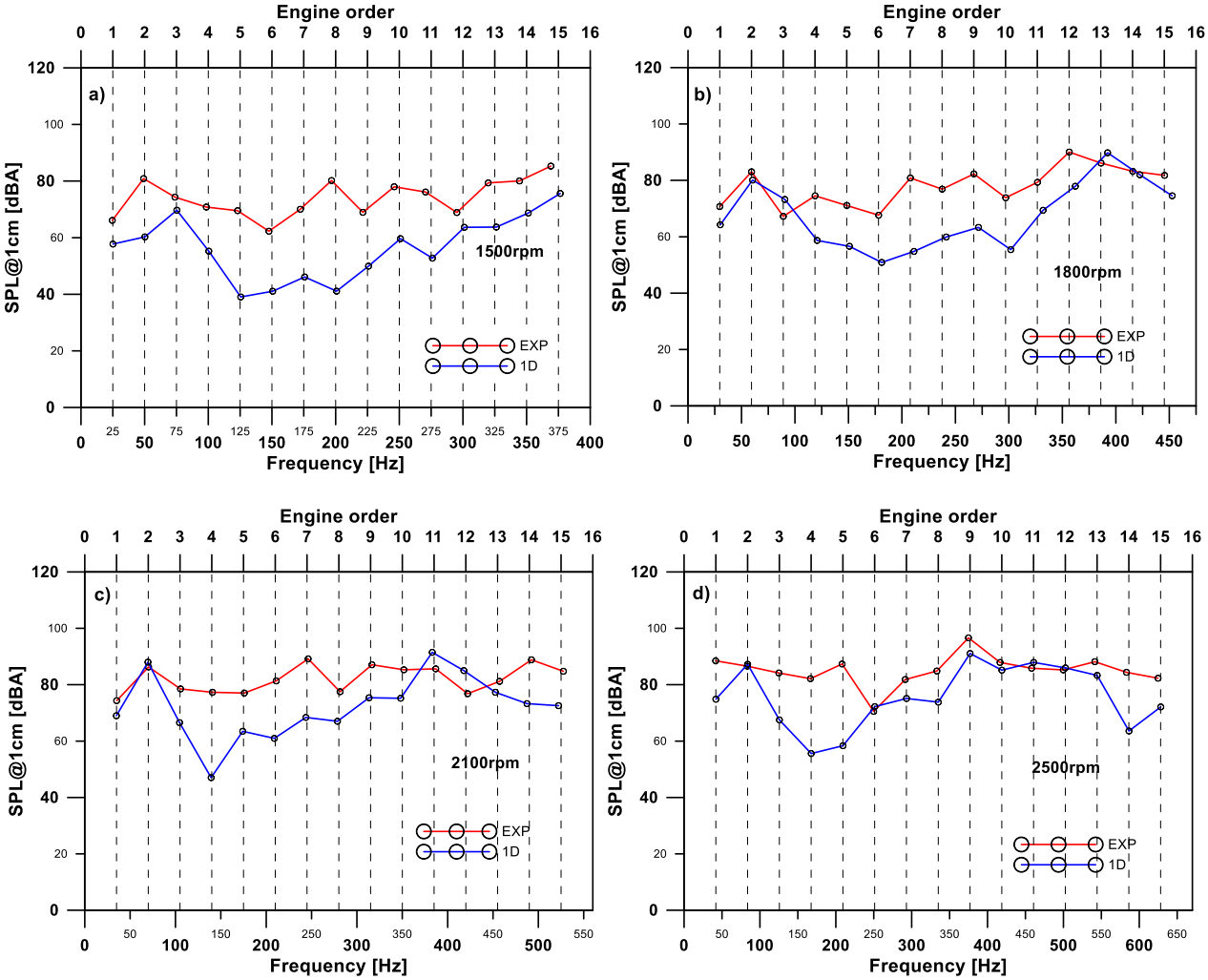

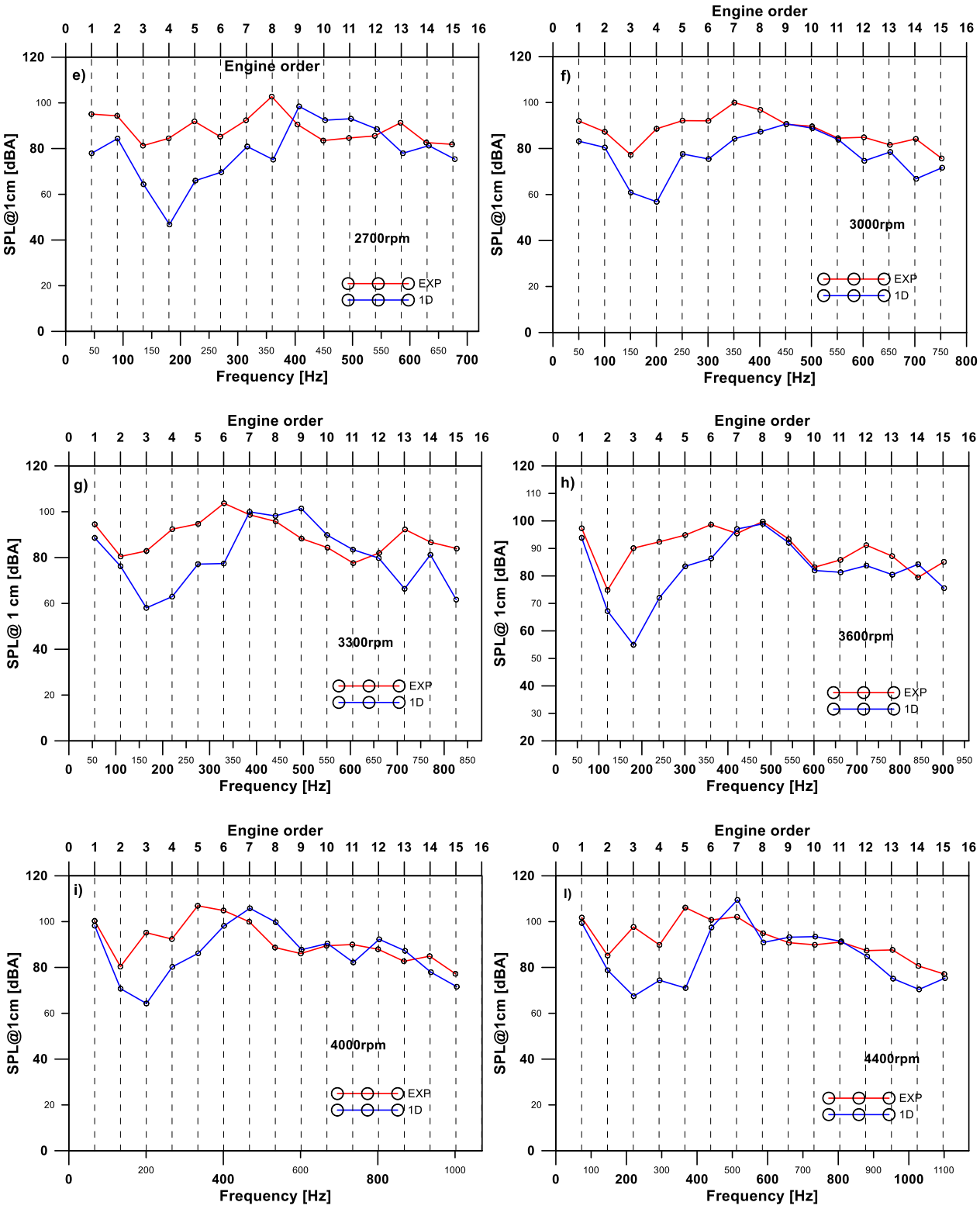
e)
Engine order
SPL@1cm [dBA]
2700rpm
EXP
1D
Frequency [Hz]
f)
Engine order
SPL@1cm [dBA]
3000rpm
EXP
1D
Frequency [Hz]
g)
Engine order
SPL@ 1 cm [dBA]
3300rpm
EXP
1D
Frequency [Hz]
h)
Engine order
SPL@ 1cm [dBA]
3600rpm
EXP
1D
Frequency [Hz]
i)
Engine order
SPL@1cm [dBA]
4000rpm
EXP
1D
Frequency [Hz]
l)
Engine order
SPL@1cm [dBA]
4400rpm
EXP
1D
Frequency [Hz]

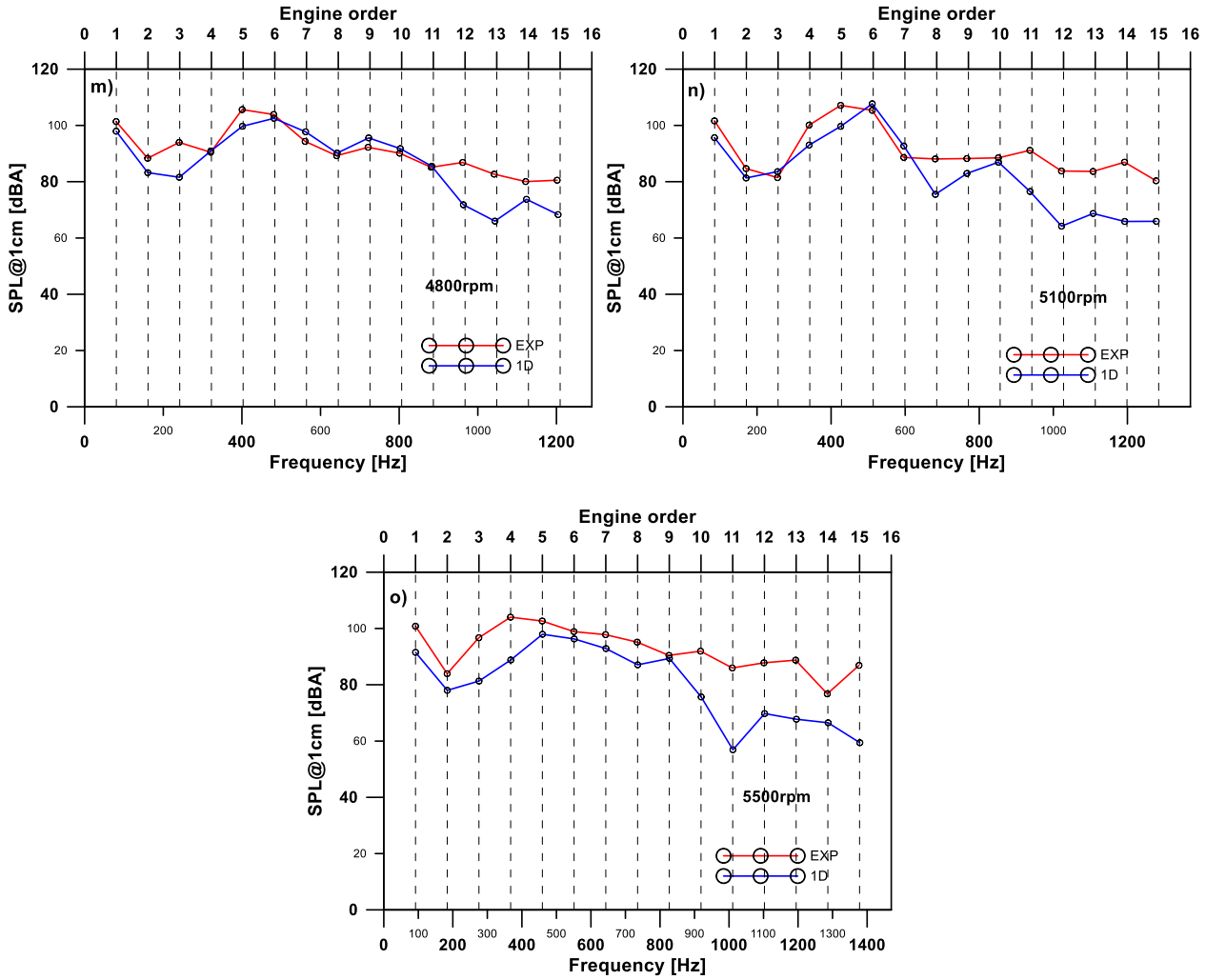


Figure 6.9 - Experimental/1D numerical sound pressure level comparison at 1 cm from the intake mouth: a) 1500rpm, b) 1800rpm, c) 2100rpm, d) 2500 rpm, e) 2700 rpm, f) 3000 rpm, g) 3300 rpm, h) 3600rpm, i) 4000 rpm, l)4400rpm, m) 4800rpm, n) 5100 rpm, o) 5500rpm.

As it is possible to appreciate from the above figures, a quite satisfactory correlation has been found between measured and simulated sound pressure levels, considering the limitation of the pure a one-dimensional approach. Moreover, there are conditions in which the overall degree of match between the two set of data under comparison is higher than the others. As an example, it is useful to focus on the experimental/numerical comparison corresponding to the 3300 and 3600 $rpm$ where the first 15 engine order occur within the same frequency range. By the examination of Figure 6.9 g) and h) it is possible to point out that the comparison at 3600 $rpm$ is quite better than that at 3300 $rpm$, suggesting that the one-dimensional solver is not able to correctly reproduce the pressure fluctuations, occurring at the outlet mouth of the intake system under investigation (engine side), with the same accuracy in each condition. This is probably due to the tuning of the VVA system "user routine", which is not able to reproduce the valve lift profile with the same accuracy in each $rpm$ condition.

It is also important to note that, for each simulation, there are frequency ranges in which the numerical output underestimates the experimental results and other zones in which the match is more accurate. In particular, the main disagreement between the two set of results has been found

within the range $[200; 400]$ $Hz$ where the 1D outcomes of each analysis suffer of a global underestimation of the SPL. Vice versa, within the range $[400; 600]$ $Hz$ there is a very good correlation between both the experimental and numerical findings. This may be due to intrinsic limitations of the 1D approach corresponding to the difficulties which are encountered when schematizing a complex three-dimensional geometry as one-dimensional. In order to strengthen this, in Figure 6.10 the experimental/numerical comparison in terms of Transmission Loss has been reported in the range $[40; 700]$ $Hz$. Here the red line refers to the experimental TL whilst the black one to the 1D results.

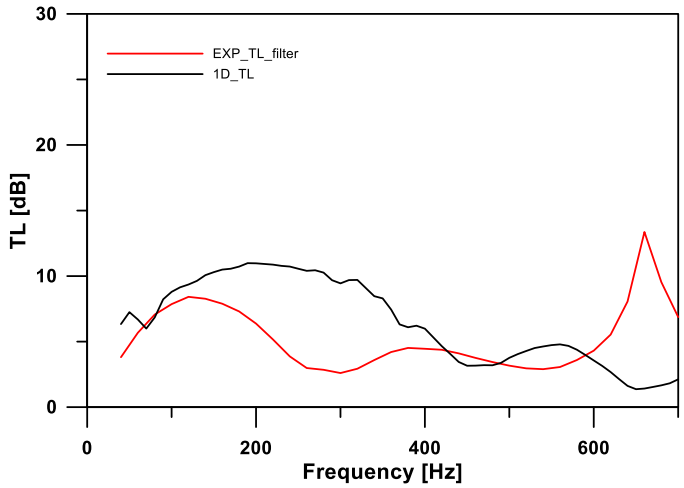


Figure 6.10 - Experimental vs 1D numerical Transmission Loss results.

As it is possible to appreciate by the examination of Figure 6.10, the one-dimensional code clearly overestimates the noise attenuation characteristic until 400 $Hz$. Such circumstance clarifies why the sound pressure level calculated with the aim of the 1D solver is always lower than the actual result below 400 $Hz$. On the other hand, the Transmission Loss curves are very close at higher frequency (until 600 $Hz$), explaining why the comparison within experimental and numerical data is always very good within the range $[400; 600]$ $Hz$.

In conclusion, from the above discussed comparisons it is possible to point out that the limitations in acoustic-response modelling of the pure 1D analysis are mainly due to the rough schematization of complex geometries, as that of the air induction system under investigation, together with the modelling issues of the VVA system. Such limitation affects both the estimation of the pressure fluctuation at the outlet of the system (engine side) and its propagation towards the external ambient. Another important aspect to consider is represented by the acoustic limited modelling capabilities of the air filter which of course affect the sound propagation too. Consequently, in order to obtain a more accurate results, the use of a 3D acoustic code is mandatory. In the following, the three-dimensional acoustic analysis and the corresponding results will be deeply discussed.

### 6.2.2 Three-dimensional acoustic analysis

The three-dimensional analyses have been carried out in order to estimate the gas-dynamic noise of the air induction system in its original configuration, with the target of achieving a better match with the experimental findings with respect to the above described one-dimensional analysis. Even in this case, the analyses have been conducted by using the commercial software Actran release

15.1, powered by Free Field Technology. Several 3D simulations have been performed at full load operation and for the entire engine speed range. However, it is worth noting that the model building-up procedure has been slightly different with respect to the Transmission Loss analysis described in the previous chapter. More precisely, apart from the fact that both inlet and outlet tubes have not been modified according to Figure 5.17, another drawing feature has been added, as it is represented in Figure 6.11.

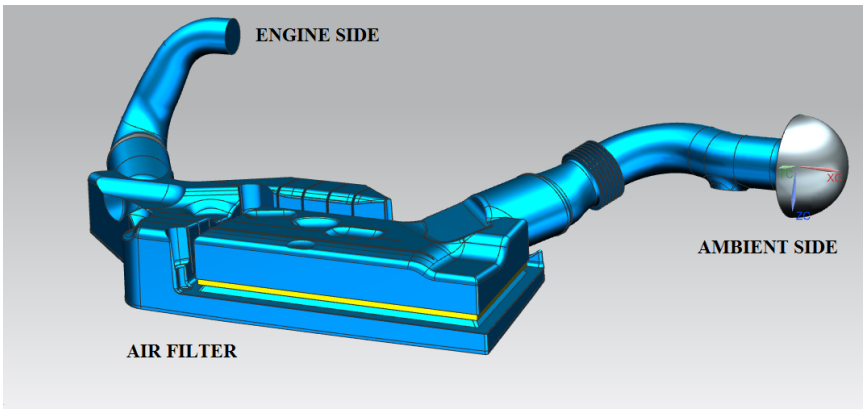


Figure 6.11 - CAD model of the intake system useful for subsequent for the gas-dynamic noise analysis.

Such new feature, which is represented by half a sphere colored in grey within the above figure, is located at the inlet mouth and it is necessary in order to simulate the sound propagation in free field conditions. Thus, the application of a non-reflecting boundary condition automatically means that the reflection coefficient at the intake mouth is not equal to zero. In other words, there is no anechoic termination anymore, which simply implies that the impedance at the inlet section equals the radiation impedance, which has been mentioned in chapter 3. The acoustic mesh corresponding to the CAD model depicted in Figure 6.11, is reported below. Here, it is possible to recognize that four different meshes have been actually created.

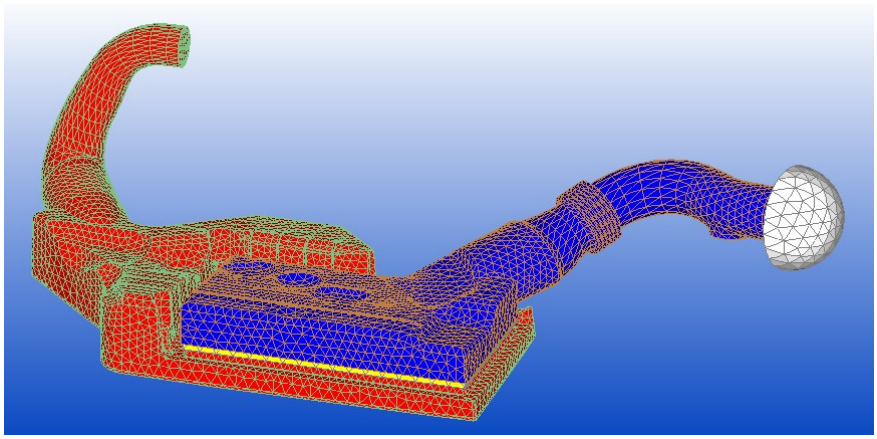

Figure 6.12 - Acoustic mesh for the gas-dynamic noise analysis.

In particular, the intake system itself has been divided in two parts, namely those before and after the air filter (the element of which are depicted in yellow) which have been depicted in red and blue respectively, in addition to the elements depicted in white which are necessary for simulating the free field propagation condition. The whole mesh consists of 49544 elements (TETRA 10-noded) and 86414 nodes allowing acoustic analysis until 2800 $Hz$, considering a spatial resolution of six

elements per wavelength. From a modelling point of view, in order to simulate the presence of the engine as acoustic source at the inlet section (engine side), the output of the 1D simulation has been used. In particular, as Actran directly solves the Helmholtz equation[5], the spectrum of the pressure profile, derived from the 1D model in the section located just upstream the turbocharger compressor, has been used as a boundary condition (engine pulses) within the acoustic model, in the same way as per the Transmission Loss analysis, that is by means of the semi-infinite duct. More precisely, recalling that for sound propagation in ducts the sound field may be decomposed in forward and backward moving waves, both pressure and velocity information, available from the 1D simulation in a section just before the compressor, has been used to calculate the incident pressure wave into the intake system. Thus, the excitation for the three-dimensional acoustic model has been calculated as

$$A = \frac{p+Z_0 u}{2} \tag{6.2}$$

being $Z_0$ the characteristic impedance of the medium. However, since such excitation has been imposed by means of a semi-infinite duct, the acoustic influence of the upstream system (engine and turbocharger group) has been only partly modelled. In fact, as explained in the previous chapter, when modelling a semi-infinite duct the eventually reflected wave from the intake system is damped whilst, in reality, it is actually reflected back by the complete system located upstream. In other words, the main excitation in terms of incident pressure wave (eq. (6.2)) represents the equivalent sound source (engine pulses), whilst the information about the source impedance is absent. At the same time, a non-reflecting boundary condition has been imposed on the 2D shell of the half sphere depicted in white in Figure 6.12, by means of an infinite element approach[5], as briefly mentioned at the end of chapter 4. The elements at which such boundary conditions have been applied are depicted in red (acoustic source) and light blue (non-reflecting condition) in figure below.

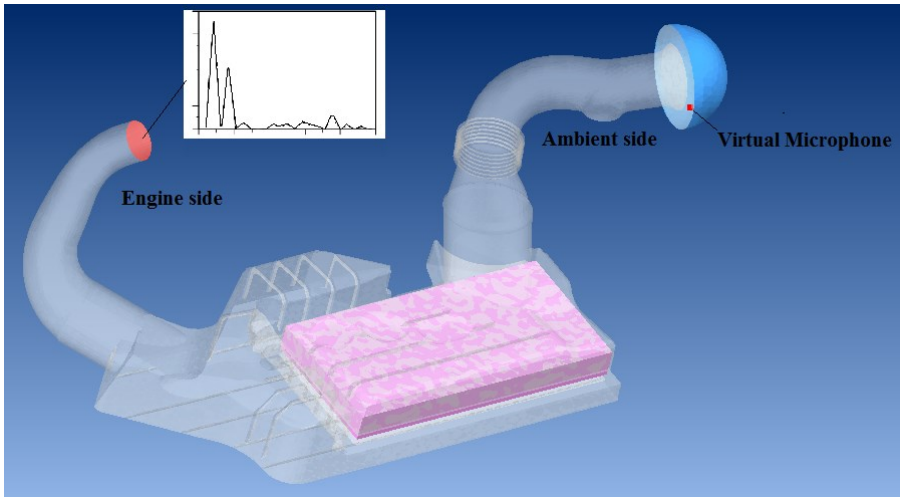


Figure 6.13 - Actran model and corresponding boundary conditions.

Obviously, even in this case the air filter has been modelled as a porous medium, namely as an equivalent fluid by means of the Delaney-Bazley formulation[8], specifying a flow resistivity equal to 2000 $[Ns/m^4]$. In analogy with the model for the Transmission Loss analysis, described in the previous chapter, the elements on which the Delaney-Bazley model has been used are depicted in

purple. Besides, a virtual microphone has been placed at 1 $cm$ away from the inlet mouth according to the experimental layout schematized in Figure 6.3. The location of such microphone within the acoustic model is highlighted by a red point in Figure 6.13. It follows that, in each simulation, the output of the acoustic analysis is represented by the gas-dynamic noise emitted in terms of sound pressure level spectrum and the corresponding overall level at such virtual microphone location. At the same time the frequency step has been changed in a way such that it is equal to half the firing frequency, namely half the first engine order, in the particular engine speed condition. Finally, the sound pressure levels calculated in each of the experimentally tested conditions are reported in the figures below. Here, the red curves represent the experimental trend whilst the blue ones stand for the 3D simulation output, for which only the first fifteen engine orders have been reported.

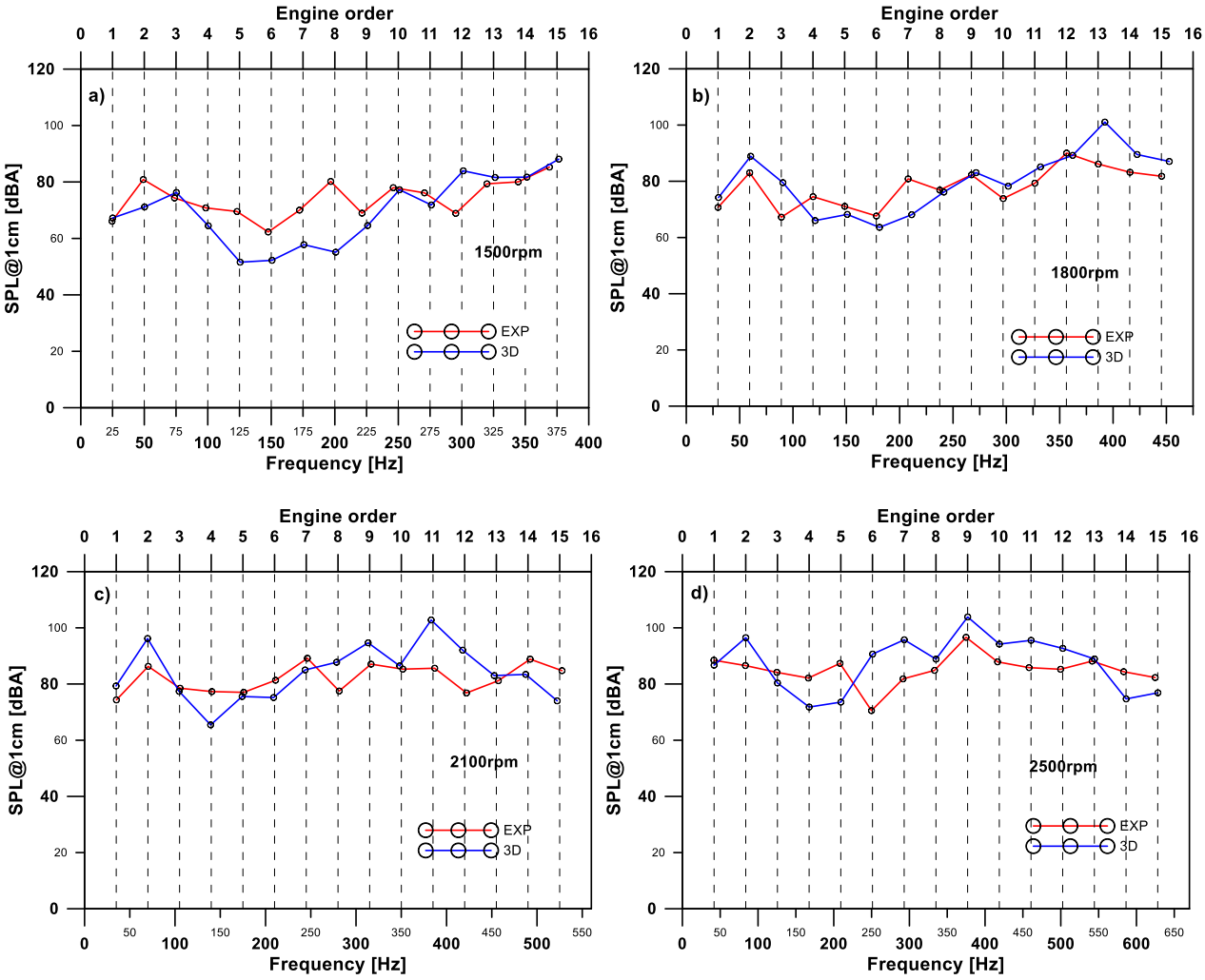

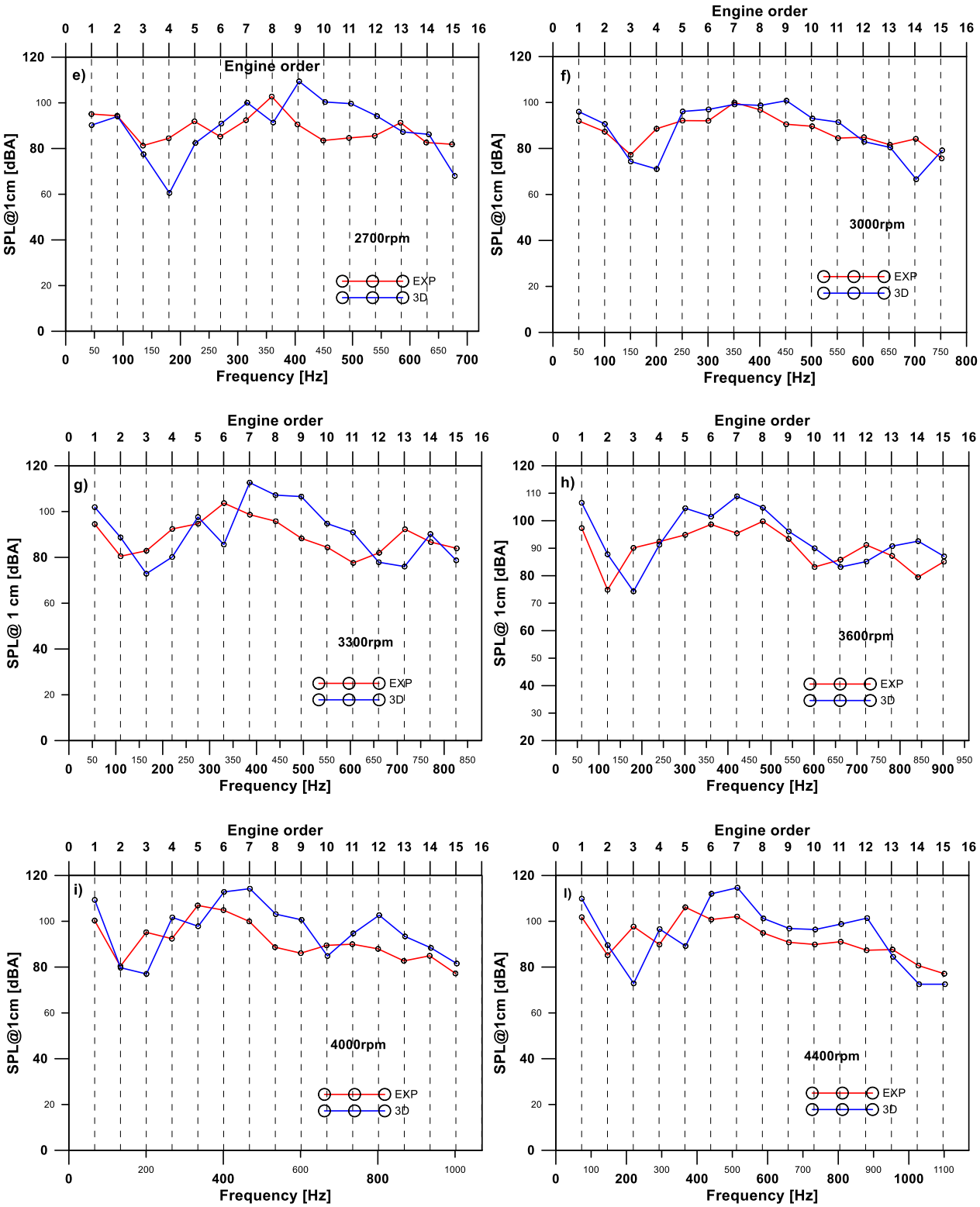
e)
Engine order
SPL@1cm [dBA]
Frequency [Hz]
2700rpm
EXP
3D
f)
Engine order
SPL@1cm [dBA]
Frequency [Hz]
3000rpm
EXP
3D
g)
Engine order
SPL@ 1 cm [dBA]
Frequency [Hz]
3300rpm
EXP
3D
h)
Engine order
SPL@ 1cm [dBA]
Frequency [Hz]
3600rpm
EXP
3D
i)
Engine order
SPL@1cm [dBA]
Frequency [Hz]
4000rpm
EXP
3D
l)
Engine order
SPL@1cm [dBA]
Frequency [Hz]
4400rpm
EXP
3D

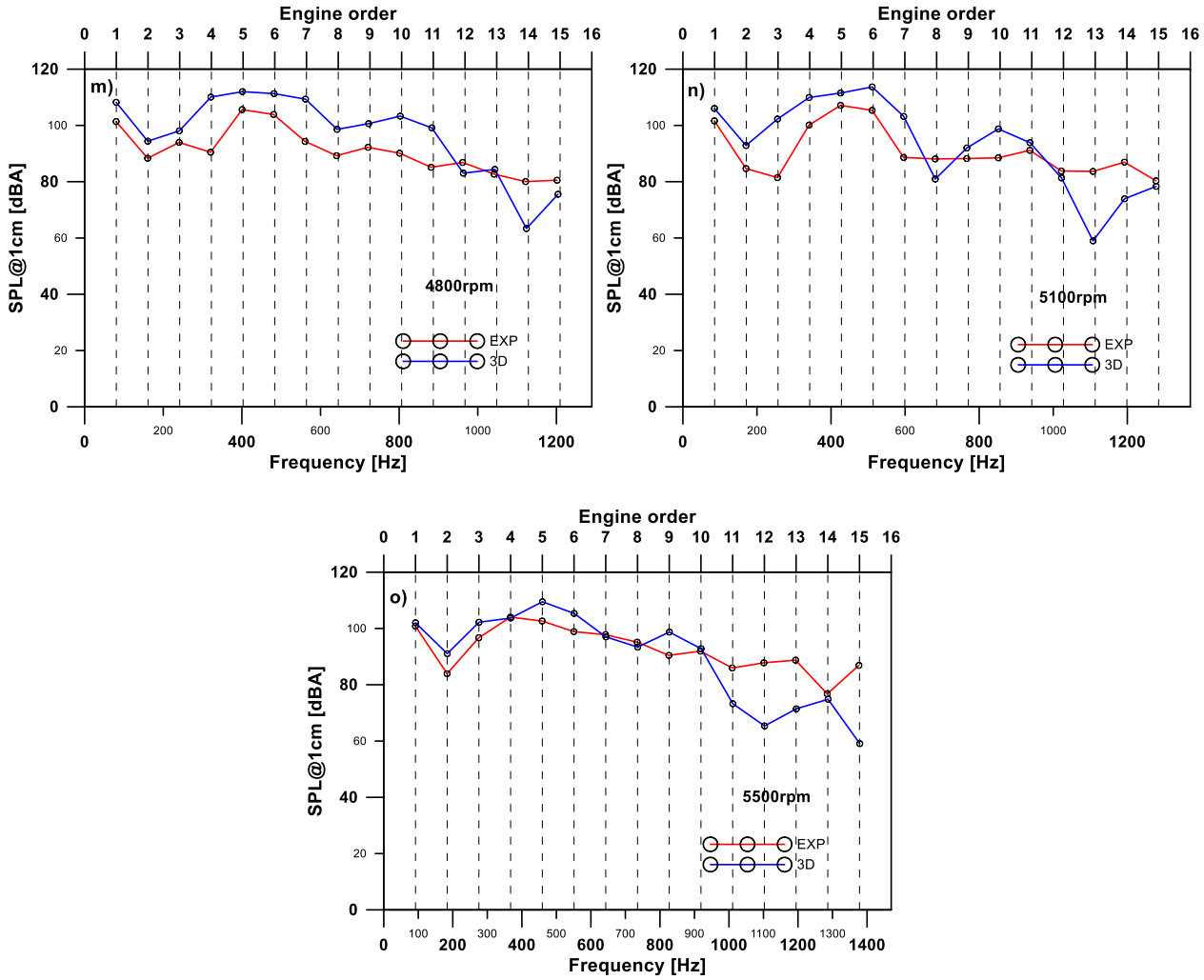


Figure 6.14 - Experimental/3D numerical sound pressure level comparison at 1 cm from the intake mouth: a) 1500rpm, b) 1800rpm, c) 2100rpm, d) 2500 rpm, e) 2700 rpm, f) 3000 rpm, g) 3300 rpm, h) 3600rpm, i) 4000 rpm, l) 4400rpm, m) 4800rpm, n) 5100 rpm, o) 5500rpm.

By the examination of the above figures, it is possible to point out that a substantial good agreement has been found between the two set of data, with a particularly good match which is achieved at low/medium engine speeds. Such circumstance is even more evident if the error percentage between the two set of data is calculated in each investigated conditions. For each engine speed, this latter has been calculated as an average among the errors corresponding to each engine order, namely

$$(e)_{rpm} = \frac{\sum_{i=1}^{15} e_i}{15} \tag{6.3}$$

where $e_i$ stands for the relative error corresponding to the $i^{th}$ engine order. The error index defined by eq. (6.3) is reported as bar chart in Figure 6.15.

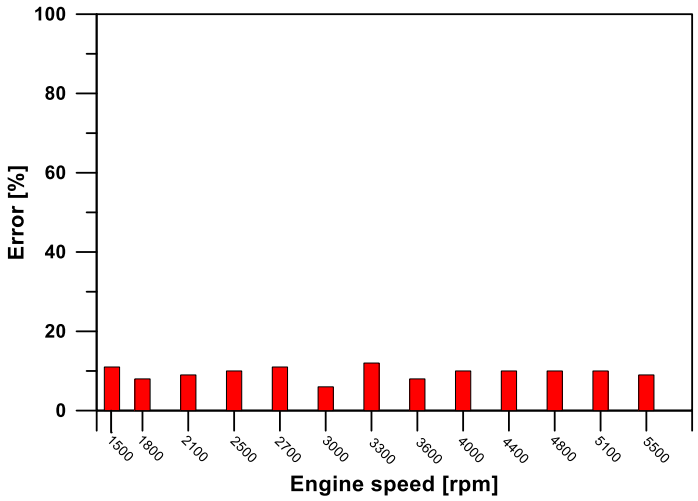


Figure 6.15 - Error between experimental and numerical sound pressure levels in the investigated engine conditions.

As it is possible to appreciate by the examination of the above figure, the error between experiments and simulations is never above 11%, reaching the minimum values within the low/medium engine rpm range. However, some relevant errors are present whose likely nature need to be more in depth discussed. First of all, it is important to separate the nature of the errors from those due to the one-dimensional modelling issue and those imputable to the 3D acoustic model's inaccuracies.

As regards the limit due to inaccuracies in the 1D analysis, it is important to highlight that the only thing which changes from one 3D simulation to another is represented by the noise source, namely the frequency spectrum of the data coming from the 1D flow simulation. Therefore, by the examination of Figure 6.14, this implies that the one-dimensional model is able to accurately estimate the pressure fluctuations on the engine side of the intake system only in some conditions[54]. As an example, when comparing the results depicted in both Figure 6.14 f) and g), it is clear that the input given when modelling the $3000\ rpm$ condition is more accurate that the other. Consequently, it is appropriate to state that the erroneous evaluation of the pressure fluctuations engine side is the primary cause of the error between three-dimensional simulations and experiments. Besides, with a closer look at Figure 6.14, it is possible to appreciate that there is a systematic error in the noise prediction capabilities of the numerical model, corresponding to an overestimation of the sound pressure level within the range $[400; 600]\ Hz$. Such overestimation occurs in all the simulated engine conditions and its effect is even more evident when comparing the overall sound pressure levels, which are depicted in the figure below, where the same color legend of Figure 6.14 has been used.

[54] Due to the already mentioned limited capabilities of the "user routine" modelling the VVA system.

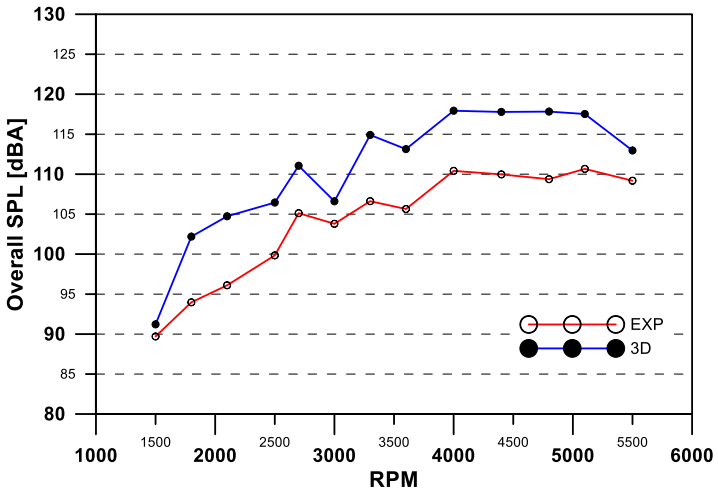


Figure 6.16 - Experimental/3D numerical comparison of the overall sound pressure levels.

Even in this case, the numerical overall in the above figure has been calculated, on the basis of the sound pressure levels corresponding to the first fifteen engine orders, by means of eq. (2.11). By the examination of the Figure 6.16, the existence of a very good qualitatively agreement is confirmed, even if amplitude shifts are present as expected. This may be partly due to the standard "map-based" description of compressor behavior within the one-dimensional schematization of the engine. In fact, according to such 1D approach, the compressor has been represented within the engine map by a volume-less interface where the steady-state compressor map data are involved[8]. The compressor map is obtained from steady-state flow tests and therefore it does not account for the attenuation exerted by the compressor itself on the pressure waves coming from the engine. In other words, this modelling approach does not allow to take into account the internal geometry of the compressor and its noise attenuation characteristics[11]. It follows that the compressor related 1D modeling inaccuracies also affect the three-dimensional results. Such effect is not present within the one-dimensional simulation output since in that case the overestimation of the noise attenuation characteristic represents a prominent effect (see the Transmission Loss comparison of Figure 6.10).

As regards the limit due to inaccuracies in the 3D modelling procedure, the primary limitation is certain due to the difficulties in modelling the air filter. In fact, as it has already mentioned in the previous chapter, due to the lack of information about micro parameters, such as viscous and thermal lengths, it has been necessary to use the simplest model for sound propagation in porous medium, namely the Delaney-Bazley model. This is just a very simple model which assumes the air filter as an equivalent fluid, in which isotropy is assumed. However, as it is possible to appreciate from Figure 5.23 a), the way in which the paper sheets are arranged makes the air filter strongly anisotropic, with the characteristic parameters varying along the three directions. Moreover, since for the air filter no measurements of flow resistivity have been available, the used value of 2000 $[Ns/m^4]$ has been chosen, as uniformly distributed, based on a sensitive analysis for determining the best match in term of Transmission Loss with the available experimental data.

Another important aspect which has not been taken into account is the flow induced noise within the air intake system. In fact, due to lack of information about the three-dimensional CFD modelling of the air filter, the presence of turbulence induced additional acoustic sources has not been taken into account within the 3D acoustic model. However, a properly set up CFD simulation

would probably improve the correlation between experiments and simulations, especially at relatively high frequencies where the flow noise is expected to be prominent. Last but not the least, the acoustic influence of the entire upstream system (engine, turbocharger group etc.) has been modelled only in terms of incident pressure wave within the air induction system, without modelling the acoustic impedance which represents an additional lack of information. In spite of all the above mentioned modelling difficulties, the overall comparison between experimental and three-dimensional results has certainly being improved.

At this point, it is important to highlight an important aspect which explains one more aspect about the importance of an accurate three-dimensional model. Many times above it has been stated that the Transmission Loss fully characterizes the acoustic attenuation properties of the stand-alone component. This is essentially due to the assumption on which it is defined, namely the anechoic termination. However, when the intake system is working in real conditions, the termination represented by the intake mouth does not end in an anechoic way, as the system radiates noise in the external ambient. This latter represents a further acoustic load (see Figure 3.2) characterized by the so called radiation impedance and the corresponding reflection coefficient. This latter, as it has been recalled in chapter 3, for the ideal case of an unflanged pipe has a unit amplitude decreasing as the frequency increases[12]. Consequently, the sound attenuation characteristic at low frequencies are in general strongly influenced by the energy reflection imposed by the external ambient, and are very different by those in agreement with a Transmission Loss analysis. Such circumstance is depicted in Figure 6.17, where two power ratios are showed as function of the dimensionless parameter $kr_0$. Both curves have been calculated making use of the TL formula, namely

$$TL = 10Log\left(\frac{W_{in}}{W_{rad}}\right) \tag{4.4}$$

where $W_{rad}$ stands for radiated power. In case of Transmission Loss analysis (black curve), it represents the power radiated into an anechoic termination (that is the power radiated by the elements depicted in green in Figure 5.21). Vice versa, when the system radiates in external atmosphere (red curve) $W_{rad}$ is the power radiated at the non-reflecting boundary conditions (the elements depicted in blue in Figure 6.13).

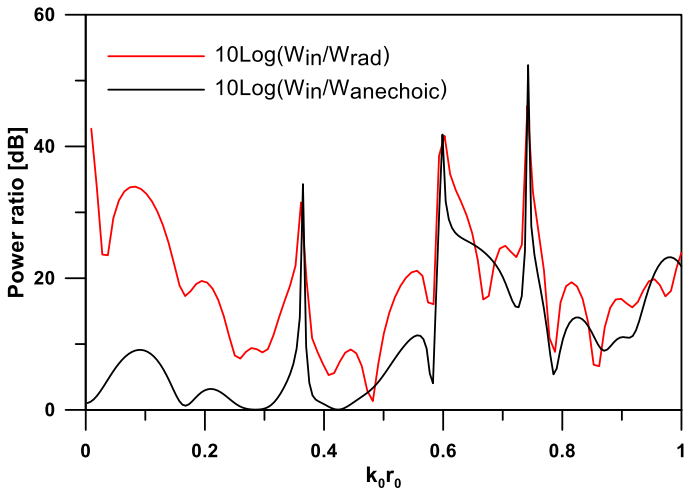


Figure 6.17 - Sound power ratio comparison.

As it is possible to appreciate from the above figure, the presence of the non-anechoic termination, when the intake system radiates in the atmosphere, deeply modify the sound attenuation, especially at low frequencies. In particular, the sound attenuation is higher with respect to that foresees with a simple Transmission Loss analysis. Consequently, it is justified that the TL only represents a qualitative indication about the sound attenuation characteristics of a system, which may considerably differ in actual working conditions.

In conclusion of this chapter, it is important to highlight that, once the experimental\numerical comparison in terms of gas-dynamic noise emissions has also given a quite satisfactory agreement, the 3D model may be considered as fully validated. Furthermore, a reliable virtual air induction system is available on which the effect of several geometric changes may be investigated, without the needs of creating expensive prototypes. To this aim, chapter 8 is devoted to the optimization of the acoustic performances of the studied system. Firstly, several geometric changes, realized in order to enhance the Transmission Loss, will be presented. Then, a gas-dynamic noise analysis will be presented and discussed, in order to assess the impact of the modifications on the noise level emissions in various engine conditions. In this regards, both engine pulses and flow noise contributions have been taken into account. So, in order to be able to understand how the turbulence induced noise has been modeled, in the next chapter an insight to the theory of the aerodynamic generation of sound will be reported.

## Bibliography


[1] Bozza, F., Gimelli, A., Piazzesi, R., Fortunato, F. et al., "The Prediction of the Performance and Gasdynamic Noise Emitted by a Medium-Size Spark-Ignition Engine by Means of 1D and 3D Analyses," SAE Technical Paper 2007-01-0380, 2007, doi:10.4271/2007-01-0380.

[2] GT-Power V.7.2, User's Manual, Gamma Technology Inc., 2011.

[3] Amesim V.4.2, User's Manual, Imagine S.A., 2004.

[4] Bozza, F., Gimelli, A., Siano, D., Torella, E. et al., "A Quasi-Dimensional Three-Zone Model for Performance and Combustion Noise Evaluation of a Twin-Spark High-EGR Engine," SAE Technical Paper 2004-01-0619, 2004, doi:10.4271/2004-01-0619.

[5] Bozza, F., Siano, D., and Torella, E., "Cycle-by-Cycle Analysis, Knock Modeling and Spark-Advance Setting of a "Downsized" Spark-Ignition Turbocharged Engine," SAE Int. J. Engines 2(2):381-389, 2010, doi:10.4271/2009-24-0020.

[6] Bozza, F., Fontana, G., Galloni, E., and Torella, E., "3D-1D Analyses of the Turbulent Flow Field, Burning Speed and Knock Occurrence in a Turbocharged SI Engine," SAE Technical Paper 2007-24-0029, 2007, doi:10.4271/2007-24-0029.

[7] De Bellis, V., Bozza, F., Siano, D., and Gimelli, A., "Fuel Consumption Optimization and Noise Reduction in a Spark-Ignition Turbocharged VVA Engine," SAE Int. J. Engines 6(2):1262-1274, 2013, doi:10.4271/2013-01-1625.

[8] Siano, D., Teodosio, L., De Bellis, V., and Bozza, F., "Analysis and Design of an Intake Filter Box for a Downsized VVA Engine," SAE Technical Paper 2014-01-1693, 2014, doi:10.4271/2014-01-1693.

[9] Actran 15.1 User's Guide,Volume 1 "Installation, Operations, Theory and Utilities", April 2015.

[10] J. Allard, N. Atalla, "Propagation of Sound in Porous Media: Modelling Sound Absorbing Materials", John Wiley & Sons, ISBN: 978-0-470-74661-5.

[11] Rämmal, H., Åbom, M., Tiikoja, H., and Bodén, H., "Experimental Facility for the Complete Determination of Sound Transmission in Turbochargers," SAE Technical Paper 2010-01-1424, 2010, doi:10.4271/2010-01-1424.

[12] J.W.S. Rayleigh, "The Theory of Sound", Vol II.

# Chapter 7

# Aerodynamic Generation of Sound

## Introduction

In chapter 2 and 3, a quite deep glance at the propagation and transmission of sound in bounded atmospheres, such as tubes and ducts, has been given with focus on both one-dimensional and three-dimensional cases. Also, an insight about the effect of a mean flow field on sound propagation has been done. Practically, no mention about the way in which sound is generated has been made. Thus, this chapter mainly deals with the generation and propagation of sound in unbounded fluids. In fact, intuitively, the generation of sound may be due to two primary mechanisms which lead to definition of structure borne and airborne sound[55]. The first mechanism generates sound because of vibrating solid boundaries in the acoustic medium, which causes, due to continuity of the velocity at the solid-acoustic interface, acoustic fluctuations at some point in space. Historically, the structure borne noise has been the only method of sound generation under deep investigation, until the rise of jet propulsion aircraft during the second half of the XX century. In fact, after world war II, jet engine, first only used for military purposes, began to be used for commercial aircraft. However, although such propulsion mechanism generates a more powerful trust for a given weight, the noise emission is much more intense. The need to reduce jet noise, stimulated James Lighthill to study the problem of aerodynamic generation of sound[13][2], which laid to the foundation of the field of research which today is called aeroacoustics, representing the branch of acoustics which studies how (and how much) kinetic energy of a flow is converted into acoustic energy. The basic idea of Lighthill's theory (published in 1951) is "just" to formulate a mathematical description for the airborne noise in order to model what every person experiences daily. Air induced sound is not only associated with periodic phenomena, as charging and discharging the cylinder of an internal combustion engine. For instance, a steady stream of air can produce sound, as it happens when using a flute. As matter of fact, sound is just a pressure fluctuation around an average value. Such evidence gives rise to two questions[3]:

1) How do more or less intense pressure fluctuations arise as a steady jet emerges into the atmosphere?
2) Which fraction of the energy is radiated away as sound?

The answer to the first question lies in two words which are "flow instability", which may generate an unstable vortex layer between the core jet and the external atmosphere[4]. A schematic representation of the grow rate of the vortices, as they travel downstream, versus the frequency is depicted in Figure 7.1.

[55] Sometimes, in the automotive sector, reference is generally made to airborne noise, as the noise contribution which propagates in air path as orifices of the passenger cabin.

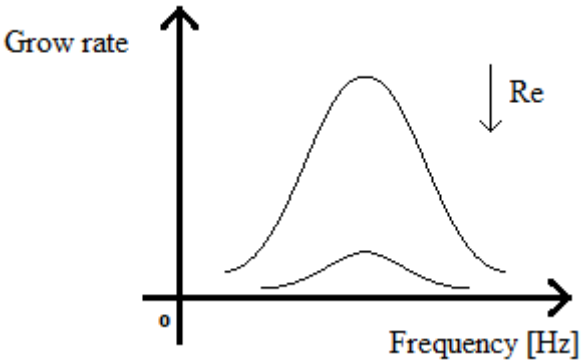


Figure 7.1 – Schematization of the grow rate within the vortex layer as function of frequency.

So, at some frequencies, the pressure disturbances quickly become very big. At high Reynolds number, disturbances in a wide range of frequency grow very fast, interacting with one another, making a so called turbulent jet. However, as the velocity of the jet decreases, the viscous forces start to become predominant and the grow rate decreases accordingly, so that only a small frequency range vortex grow as they travel downstream. Consequently, at low Reynolds numbers, the disturbances which appear are quite regular and do not radiate away as sound. Such evidence leads to the answer of the second question, that is, apart from the pressure fluctuations which successfully radiate away as sound, there are other pressure fluctuations (actually more intense) which balance the local fluid accelerations near the jet outside. These latter do not propagate at all and therefore they are called *pseudo-sound* (only *pseudo* because they do not propagate as sound). A very simple example of such phenomenon may be highlighted when a person is blowing, as schematically depicted in Figure 7.2.

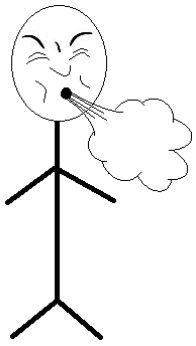

Figure 7.2 – Schematization of a blowing person.

Near the orifice (the mouth) human ears can detect a kind of noise but, far away no audible sound may be detected. As it will be clear in the following, far away from the orifice, this happens because the sound intensity decays following an inverse-square low. However, before being able to understand such behavior of sound generated aerodynamically, it is necessary to make some backward steps in order to recall some basic definitions and relationships.

In chapter 2 it has been shown the solution of the classical wave equation within a rectangular coordinate system. However, another important case refers to the situation in which a spherical coordinate system is used. Assuming a pure spherical symmetry, that is neglecting both polar and azimuthal dependence, the Laplace operator may be rewritten as

$$\nabla^2 = \frac{1}{r^2}\frac{\partial}{\partial r}\left(r^2\frac{\partial}{\partial r}\right) \tag{7.1}$$

If eq. (7.1) is inserted in the one dimensional homogeneous classical wave equation (2.22), the following expression is obtained[56].

$$\frac{1}{a_0^2}\frac{\partial^2(rp')}{\partial t^2} - \frac{\partial^2(rp')}{\partial r^2} = 0 \tag{7.2}$$

Therefore, in analogy with the plane wave solution in rectangular coordinates (see eq. (2.26)), the spherical sound field may be expressed as

$$p'(r,t) = \frac{1}{r}\left[p'_+(t - r/a_0) + p'_-(t + r/a_0)\right] \tag{7.3}$$

which leads, again, to the superposition of two waves, one travelling out from the origin and one travelling through the origin. As it is possible to appreciate from eq. (7.3), both the amplitudes of the two waves go to infinity as the radial position approaches the origin ($r \to 0$), namely a singularity exists. Such singularity may be due to a sound source located at the origin, as it will be described soon. The conservation of momentum in the radial dimension allows to derive the expression for the particle velocity, namely

$$\rho_0\frac{du'}{dt} = -\frac{dp'}{dr} \tag{7.4}$$

$$\rho_0\frac{du'}{dt} = +\frac{1}{r^2}p'_+(t - r/a_0) + \frac{1}{a_0 r}\frac{\partial p'_+(t-r/a_0)}{\partial t} + \frac{1}{r^2}p'_-(t + r/a_0) - \frac{1}{a_0 r}\frac{\partial p'_-(t+r/a_0)}{\partial t} \tag{7.5}$$

After an integration with respect to time, it is possible to express the final result in terms of particle velocity as

$$u'(r,t) = \frac{1}{\rho_0 a_0 r}p'_+(t - r/a_0) - \frac{1}{\rho_0 a_0 r}p'_-(t + r/a_0) + \frac{1}{\rho_0 r^2}P_- + \frac{1}{\rho_0 r^2}P_+ \tag{7.6}$$

where $P_\pm = \int p'_\pm(t \mp r/a_0)\,dt$ and represent the so called *near field* terms (and are related to *pseudo-sound*) as they do not contribute to the acoustic radiation far from the source because pressure and velocity are out of phase (the particle velocity being out of phase of $-\pi/2$ due to the time integral of the acoustic pressure)[5]. Besides, as it is possible to appreciate by the examination of eq. (7.6), the first two terms are in phase with the acoustic pressure and so they are called *far field* terms, as they contribute to the acoustic power radiation away from the source. These aspects will be examined more ahead in the next sections, because it is of primary importance to study the elementary sound generation mechanisms.

## 7.1 The inhomogeneous wave equation and the Green's function

If the source terms are considered within the mass and momentum conservation equations, the following inhomogeneous wave equation is obtained[5]

$$\frac{1}{a_0^2}\frac{\partial^2 p'}{\partial t^2} - \nabla^2 p' = s(\boldsymbol{x}, t) \tag{7.7}$$

[56] Note that $\frac{1}{r^2}\frac{\partial}{\partial r}\left(r^2\frac{\partial p'}{\partial r}\right) = \frac{1}{r}\frac{\partial^2(rp')}{\partial r^2}$

where $s(\boldsymbol{x},t)$ represents the source contribution at point $\boldsymbol{x}$ and time instant $t$. As it will be shown, the source terms involved at the right-hand side of the above equation may be related to unsteady injection of mass and/or fluctuating external force field acting of the fluid. Before being able to understand how such general source terms are related to a turbulent flow field, it is necessary to proceed step by step by studying the simplest possible source, namely a point source which is mathematically defined by means of the delta-function, namely

$$\iiint \delta(\boldsymbol{x}-\boldsymbol{x}_0)dV = \begin{cases} 1\ for\ \boldsymbol{x}_0 \in \mathcal{V} \\ 0\ for\ \boldsymbol{x}_0 \notin \mathcal{V} \end{cases} \tag{7.8}$$

where 3-D symmetry has been assumed and $\boldsymbol{x}_0$ represents the location of the point source. The study of the solution of the classical wave equation with a point source excitation, which is called Green's function, is very important as it represents the basis for more complex solutions. Since, in general, the focus is on the frequency domain study of sound, it will be assumed that the Green's function $\hat{G}$ is related to an harmonic point source (with unit amplitude), in a 3-D infinite space, as acoustic excitation. Therefore, such Green's function must satisfy the wave equation in both time and frequency domain, namely

$$\begin{cases} \frac{1}{a_0^2}\frac{\partial^2 G}{\partial t^2} - \nabla^2 G = \delta(t)\delta(\boldsymbol{x}-\boldsymbol{x}_0) \\ \nabla^2 \hat{G} + k^2 \hat{G} = -\delta(\boldsymbol{x}-\boldsymbol{x}_0) \end{cases} \tag{7.9}$$

A point source defined by the delta function, as it happens in eq. (7.9), is called *monopole source* and the corresponding sound field is called *monopole field*. Since a 3-D unbounded space is considered, the Green's function must exhibit a spherical symmetry, namely the sound field depend only on the radial distance from the source and should be equal to the superposition of two waves. However, the wave travelling from infinity towards the source has no physical meaning as, again, *free field* radiation is supposed. Consequently, in analogy to eq. (7.3), the frequency domain representation of the Green's function may be expressed as

$$\hat{G}(\omega,\boldsymbol{x},\boldsymbol{x}_0) = \frac{\hat{G}_+ e^{-jkr}}{r} \tag{7.10}$$

where the time dependence $\left(e^{j\omega t}\right)$ has been omitted for simplicity, $\hat{G}_+$ is the amplitude and $r$ is the distance from the monopole source located at $\boldsymbol{x}_0$, namely $r = |\boldsymbol{x}-\boldsymbol{x}_0|$. In order to find $\hat{G}_+$, it is important to note that eq. (7.10) must satisfy both eq. $(7.9)_2$ and (7.8). Besides, since eq. (7.10) satisfies the wave equation everywhere except at $\boldsymbol{x}_0$, where a singularity exists, a spherical integration small volume centered at $\boldsymbol{x}_0$ is chosen, as depicted in Figure 7.3.

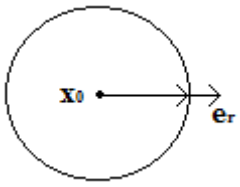


Figure 7.3 – Integration volume useful for calculate the amplitude of the Green's function.

Thus, from what above it follows that

$$\iiint \left(\nabla^2 \hat{G} + k^2 \hat{G}\right) d\mathcal{V} = -1 \tag{7.11}$$

By applying the divergence theorem to the first term in eq. (11) yields

$$\iint \nabla \hat{G} \cdot e_r dS + \iiint k^2 \hat{G} d\mathcal{V} = -1 \tag{7.12}$$

where $e_r$ is the unit vector representing the normal to the infinitesimal surface $dS$ in the radial direction. Of course, $\nabla \hat{G} \cdot e_r = \partial \hat{G} / \partial r$ and so, in the limit as $r \to 0$, eq. (7.12) yields to the following expression[57] for $\hat{G}_+$.

$$4\pi \hat{G}_+ = 1 \tag{7.13}$$

Therefore, the free 3-D field harmonic Green's function is given by

$$\hat{G}(\omega, \boldsymbol{x}, \boldsymbol{x}_0) = \frac{e^{-jkr}}{4\pi r} \tag{7.14}$$

where again the time dependence $\left(e^{j\omega t}\right)$ has been omitted for simplicity of the notation. Thus, in order to obtain an expression for the Green's function in the time domain, the inverse Fourier transform of eq. (7.14) must be taken, leading to the following inhomogeneous wave equation

$$\left[\frac{1}{a_0^2}\frac{\partial^2}{\partial t^2} - \nabla^2\right] G = \delta(t)\delta(\boldsymbol{x} - \boldsymbol{x}_0) \tag{7.15}$$

where the solution is of the form

$$G(t, \boldsymbol{x}, \boldsymbol{x}_0) = \frac{\delta(t - r/a_0)}{4\pi r} \tag{7.16}$$

which correspond to an acoustic pulse propagating towards infinity after a sudden volume change at $\boldsymbol{x} = \boldsymbol{x}_0$ occurring at $t = 0$; for $t < 0$ the fluid is at rest. In fact, the right end side of eq. (7.15) represents a point source located at $\boldsymbol{x}_0$ which pulses at $t = 0$. It is very important noting that the pressure fluctuation reaching point $\boldsymbol{x}$ at time $t$ is due to the ray of sound emitted at $\boldsymbol{x}_0$ and time instant $t - r/a_0$, as it is confirmed by the form of eq. (7.16).

More in general, there may be a distribution of sources $s(\boldsymbol{x}, t)$ and also boundaries to taken into account when solving the wave equation for the corresponding sound field. In this cases, the Green's function is still very useful for obtaining an integral expression for the sound field corresponding to more general situations. The starting point is the frequency domain representation of the physical situations, namely

$$\begin{cases} (\nabla^2 + k^2)\hat{p}(\omega, \boldsymbol{x}) = -\hat{s}(\omega, \boldsymbol{x}) \\ (\nabla^2 + k^2)\hat{G}(\omega, \boldsymbol{x}, \boldsymbol{y}) = -\delta(\boldsymbol{x} - \boldsymbol{y}) \end{cases} \tag{7.17}$$

where $\boldsymbol{y}$ represents the location of the point source $\delta(\boldsymbol{x} - \boldsymbol{y})$ and $\boldsymbol{x}$ stands for a generic sound field point. Equation $(7.17)_1$ represents the general situation in which there is a distribution of sources, whilst eq. $(7.17)_2$ represents the situation in which only a point source is present and for which the

[57] By definition of solid angle, it follows that $dS = d\Omega\, r^2$ whilst $d\mathcal{V} = 4\pi r^2 dr$. Thus, $\iint \nabla \hat{G} \cdot e_r dS + \iiint k^2 \hat{G} d\mathcal{V} = -4\pi \hat{G}_+ e^{-jkr}(1 + jkr) + 4\pi \hat{G}_+ k^2 \left[-\frac{re^{-jkr}}{jk} + \frac{1}{(jk)^2}(e^{-jkr} - 1)\right]$

solution (in a 3-D unbounded space) is represented by the Green's function expressed by eq. (7.14), or equivalently by eq. (7.16) in the time domain. Consider the general three-dimensional space depicted in Figure 7.4, in which a volume $\mathcal{V}$ is bounded by an external and internal surfaces, $S^e$ and $S^i$.

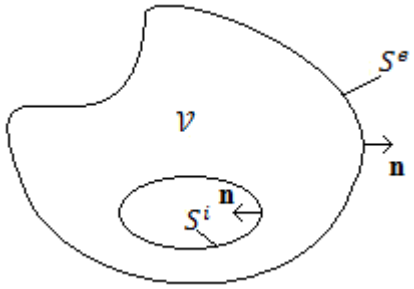


Figure 7.4 – Schematization of a generic 3-D space.

By multiplying eq. $(7.17)_1$ by $\hat{G}(\omega, \boldsymbol{x}, \boldsymbol{y})$ and eq. $(17)_2$ by $\hat{p}(\omega, \boldsymbol{x})$ and then performing $(7.17)_1$-$(7.17)_2$, yields

$$\hat{G}\nabla_x^2\hat{p} - \hat{p}\nabla_x^2\hat{G} = \hat{p}(\boldsymbol{x})\delta(\boldsymbol{x}-\boldsymbol{y}) - \hat{s}\hat{G} \tag{7.18}$$

where the subscript $x$ denotes a derivation with respect to $\boldsymbol{x}$, and the frequency dependence has been suppressed for clarity of the notation. By integrating eq. (7.18) over the volume depicted in Figure 4 yields[58]

$$\iiint \left(\hat{G}\nabla_x^2\hat{p} - \hat{p}\nabla_x^2\hat{G}\right) dV_x = \hat{p}(\boldsymbol{y}) - \iiint \hat{s}\hat{G}\, d\mathcal{V}_x \tag{7.19}$$

At the same time, by applying the divergence theorem to the volume integrals of the left hand side of the above equation yields

$$\iint \left(\hat{G}\nabla_x\hat{p} - \hat{p}\nabla_x\hat{G}\right)\cdot \boldsymbol{n}\, dS_x^e + \iint \left(\hat{G}\nabla_x\hat{p} - \hat{p}\nabla_x\hat{G}\right)\cdot \boldsymbol{n}\, dS_x^i = \hat{p}(\boldsymbol{y}) - \iiint \hat{s}\hat{G}\, d\mathcal{V}_x \tag{7.20}$$

In general, $S^i$ is chosen so that it coincides with solid body boundaries (if present) and if the domain is not externally bounded $S^e$ may be moved to infinity. In this latter case, for $r \to \infty$ the contribution of the first surface integral goes to zero (as $\hat{G}$ does), normally referring to this condition as *Summerfeld radiation* (non-reflecting boundary condition)[6]. After this hypothesis, by interchanging $\boldsymbol{x}$ and $\boldsymbol{y}$ for convenience (they are just space coordinates) and by introducing the outward normal of $S^i$ ($\boldsymbol{n} = -\boldsymbol{n}_{out}$), pointing within the fluid domain, the expression for the sound field takes the form of the so-called Kirchhoff-Helmholtz equation[59], namely

$$\hat{p}(\boldsymbol{x}) = \iint \left(\hat{p}(\boldsymbol{y})\nabla_y\hat{G}(\boldsymbol{y},\boldsymbol{x}) - \hat{G}(\boldsymbol{y},\boldsymbol{x})\nabla_y\hat{p}(\boldsymbol{y})\right)\cdot \boldsymbol{n}_{out}\, dS_y^i + \iiint \hat{s}(\boldsymbol{y})\hat{G}(\boldsymbol{y},\boldsymbol{x})\, d\mathcal{V}_y \tag{7.21}$$

where $\boldsymbol{x}$ refers to a field coordinate whilst $\boldsymbol{y}$ refers to the source coordinate. In addition, if the Green's function is exact, namely it satisfies the boundary condition on $S^i$[5], then the surface

[58] Where use has been done of the integration rule for the delta function: $\iiint f(\boldsymbol{x})\delta(\boldsymbol{x}-\boldsymbol{x}_0)\, d\mathcal{V} = f(\boldsymbol{x}_0)$.

[59] The Kirchhoff-Helmholtz equation is one of the most important in acoustic, not only because it represents the basic relation for the theory of sound propagation but also for numerical solution methods like the Boundary Element Method.

integral in eq. (7.21) gives no contribution and the final expression of the sound field is given by the following relation

$$\hat{p}(\boldsymbol{x}) = \iiint \hat{s}(\boldsymbol{y})\hat{G}(\boldsymbol{y},\boldsymbol{x})\, d\mathcal{V}_y \tag{7.22}$$

which expresses the sound field of a generic distribution of source as superposition of point source solutions or *monopole fields*, as schematized in Figure 7.5.

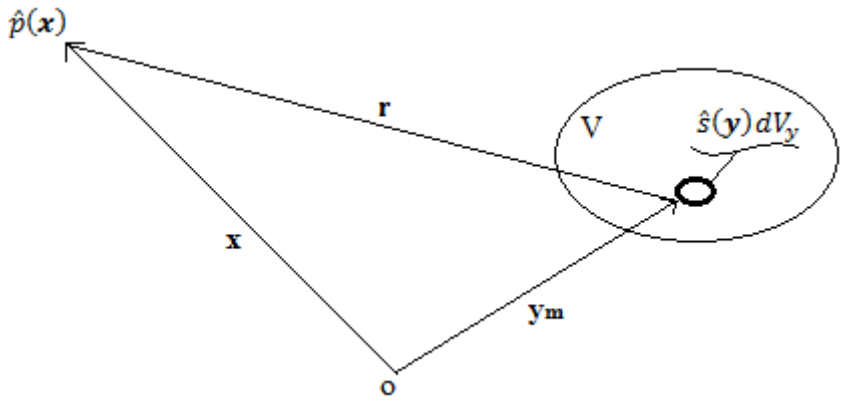


Figure 7.5 – Superposition of monopole contributions to build up the total sound field due to a source distribution.

Equation (7.22) is very important and generally valid, however the analytic (and so exact) expression of the Green's function is known only for few cases, e.g. the free field case. Therefore, if eq. (7.14) is inserted in eq. (7.22) the frequency domain representation of pressure field resulting from a source distribution in a free field without solid boundary is obtained, namely

$$\hat{p}(\omega,\boldsymbol{x}) = \iiint \frac{\hat{s}(\omega,\boldsymbol{y})\, e^{-jkr}}{4\pi r}\, d\mathcal{V}_y \tag{7.23}$$

where $r$ represents the distance from the single monopole source, i.e. $r = |\boldsymbol{x} - \boldsymbol{y}|$. Obviously, the time domain representation of the sound field expressed by eq. (7.23) is simply

$$p'(\boldsymbol{x},\mathrm{t}) = \iiint \frac{s(\boldsymbol{y},t_e)}{4\pi r}\, d\mathcal{V}_y \tag{7.24}$$

where $t_e = t - r/a_0$ and it is called *emission time*. As it is possible to appreciate from eq. (7.24), it is the time instant at which the sound wave, reaching point $\boldsymbol{x}$ at $t$, was emitted. In fact, the time lag $r/a_0$ represents the time taken for sound wave to travel a distance $r$ at the sound speed $a_0$.

## 7.2 Multipole expansion of sound fields

From what above, it has been shown that the sound field due to a whatever complicated source distribution may be seen, thanks to the Green's function, as a superposition of *monopole fields*. However, another simplification is possible, especially useful when, within the source terms of the inhomogeneous wave equation (7.7), some spatial derivatives appear. It will be shown that particular arrangement of monopole sources may be thought as equivalent to others characteristic sound sources thanks to the concept of multipole expansion of a sound field. However, before introducing the concept of multipole expansion, one further observation about the nature of the solution of the wave equation is necessary. From what it has been described at the beginning of the

previous paragraph, the Green's function, expressed by eq. (7.14), satisfies the Helmholtz equation for all points except at the origin of the disturbance, namely

$$\nabla^2 \hat{G} + k^2 \hat{G} = 0 \qquad , \; r \neq 0 \tag{7.25}$$

By applying a spatial derivative to eq. (7.25), it follows that

$$(\nabla^2 + k^2)\frac{\partial \hat{G}}{\partial x_i} = 0 \qquad , \; r \neq 0 \tag{7.26}$$

where it has been possible to exchange the order between the wave operator Ł and the differential operator since Ł has a constant coefficient and $\hat{G}$ is also sufficiently regular for $r \neq 0$[5]. From eq. (7.26), it is possible to point out that $\partial \hat{G}/\partial x_i$ is also a possible solution for the free space wave equation. Thus, by means of spatial derivatives, it is possible to generate a whole family of new solutions for the wave equation. These solutions are called multipoles and may be expressed as

$$\hat{G}_n = \frac{\partial^n}{\partial x_1^i \partial x_2^l \partial x_3^k}\left(\frac{e^{-jkr}}{4\pi r}\right) \tag{7.27}$$

where $n = i + l + k$ and $\hat{G}_n$ is called multipole of order $2^n$. As it will be clear in the next paragraph, when dealing with the Lighthill's theory for the aeroacoustic generation of sound, the multipole expansion is very useful for better understanding the nature of aerodynamic sources. Anyway, the first three multipoles are the monopole ($n = 0$), which corresponds to solutions of the type of eq. (7.24), *dipole* ($n = 1$) and *quadrupole* ($n = 2$). The order of the multipole is the number of elementary sources (*monopoles*) needed to generate the sound field $\hat{G}_n$. For example, let focus on the physical situation described in Figure 7.6. Here, by examining the source term $\left(\partial \hat{S}/\partial x_i\right)$ in the wave equation, the nature of the sound source is such that the corresponding sound field is a *dipole field* (refer to Figure 7.6 (a ).

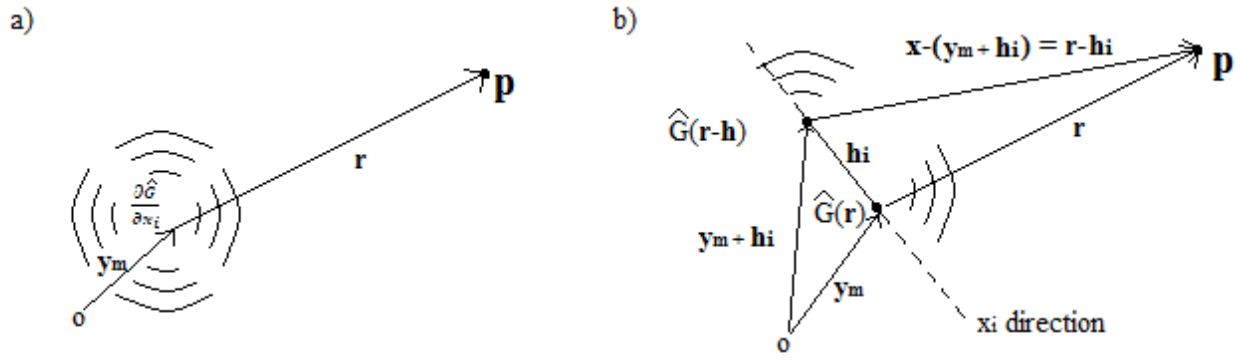


Figure 7.6 – Dipole sound field a) and associated multipole expansion b).

From what above, the *dipole field* is of the form

$$\hat{D} = \frac{\partial}{\partial x_i}\left(\frac{e^{-jkr}}{4\pi r}\right) = \frac{\partial \hat{G}}{\partial x_i} \tag{7.28}$$

However, a general function at a particular point in space may be expressed by means of its Taylor expansion series, namely

$$f(x+x_0) = f(x) + \frac{df(x)}{dx}(\Delta x) + \frac{1}{2!}\frac{d^2f(x)}{dx^2}(\Delta x)^2 + \cdots + \frac{1}{n!}\frac{d^nf(x)}{dx^n}(\Delta x)^n + o(\Delta x)^n \tag{7.29}$$

which is an exact formulation for $\Delta x \to 0$. Hence, the right end side of eq. (7.28) may be rewritten as

$$\frac{\partial \hat{G}}{\partial x_i} = \frac{\hat{G}(r) - \hat{G}(r-h)}{h} \tag{7.30}$$

namely, the dipole field $\hat{D}$ is obtained by the superposition of two equal monopole fields, $\hat{G}(r)$ and $\hat{G}(r-h)$ (in antiphase as suggested by the minus sign), spaced one another by a small quantity $h$. Moreover, thanks to the Taylor expansion series, it is possible to express a whatever complicated sound field generated by a set of monopole around the origin (see eq. (7.23)), as superposition of multipoles. As it will be clear in the next paragraphs, at low frequency, which means for low values of the Helmholtz number (compact source region), the first non-zero term will dominate the sound field and the radiated power.

Thanks to eq. (7.23), the frequency domain representation of a sound field corresponding to the contribution of one single monopole *m* may be expressed as

$$\hat{p}_m(\omega, \boldsymbol{x}) = \frac{\hat{s}_m(\omega, \boldsymbol{y_m})\, e^{-jkr_m}}{r_m} \tag{7.31}$$

where again the time factor $e^{j\omega t}$ has been omitted for clarity of the notation, whilst the $4\pi$ factor has been embedded in the source amplitude $\hat{s}_m$ and $r_m = |\boldsymbol{x} - \boldsymbol{y_m}|$ stand for the distance vector between point $\boldsymbol{x}$ and the position of the *monopole source*. As already seen, the total sound field is obtained by the superposition of all the source contributions, namely

$$\hat{p}(\omega, \boldsymbol{x}) = \sum_m \frac{\hat{s}_m(\omega, \boldsymbol{y_m})\, e^{-jkr_m}}{r_m} \tag{7.32}$$

Hence, by applying the "3-D" version of eq. (7.29) with $\boldsymbol{x_0} = -\boldsymbol{y_m}$ and $f(x) = \frac{e^{-jkx}}{x}$, yields

$$\hat{p}(\omega, \boldsymbol{x}) = \sum_m \hat{s}_m(\omega, \boldsymbol{y_m}) \left[1 - (\boldsymbol{y_m}\nabla_x) + \frac{1}{2!}(\boldsymbol{y_m}\nabla_x)^2 + \cdots + \frac{(-1)^n}{n!}(\boldsymbol{y_m}\nabla_x)^n + o(\boldsymbol{y_m})^n\right]\frac{e^{-jkx}}{x} \tag{7.33}$$

where $x = |\boldsymbol{x}|$. Eq. (7.33) is exact for a compact source for which the variation of the *emission time* may be neglected[60], being $r \cong |\boldsymbol{x}|$. The same procedure may be applied to the time domain representation of a sound field, by imposing $f(x) = \frac{s_m(\boldsymbol{y_m}, t_e)}{4\pi x}$, resulting in

$$p'(\boldsymbol{x}, \mathrm{t}) = \sum_m \left\{1 - \boldsymbol{y_m}\nabla_x + \cdots + \frac{(-1)^n}{n!}(\boldsymbol{y_m}\nabla_x)^{\boldsymbol{n}} + o(\boldsymbol{y_m})^n\right\}\frac{s_m(\boldsymbol{y_m}, t_e)}{4\pi x} \tag{7.34}$$

However, focusing on the frequency domain may results in a simpler analysis, because the derivatives are applied to the exponential factor. So, by introducing the Cartesian tensor notation

[60] A source region is said to be compact when its characteristic dimension *L* is much smaller than the wavelength, which simply implies that $He = kL \ll 1$. For a point $r$ within the sound field, the emission time is responsible for the phase shift given by $e^{j(\omega t - kr)}$. Such phase shift $kr = k(x - L)$, coincides with $kx$ for a compact source.

and changing the order of the summations yields to the desired expansion of the total sound field in terms of multipoles, namely

$$\hat{p}(\omega, \boldsymbol{x}) = \left[\hat{S} - \widehat{D}_i \frac{\partial}{\partial x_i} + \hat{Q}_{ik} \frac{\partial^2}{\partial x_i \partial x_k} + \cdots\right] \frac{e^{-jkx}}{x} \tag{7.35}$$

where the versors of the i-th and k-th directions have been suppressed for clarity of the notation, whilst $\widehat{M}$, $\widehat{D}_i$ and $\hat{Q}_{ik}$ stand for

$$\widehat{M} = \sum_m \hat{s}_m(\omega, \boldsymbol{y_m}) \tag{7.36}$$

$$\widehat{D}_i = \sum_m \hat{s}_m(\omega, \boldsymbol{y_m})\, \boldsymbol{y_{mi}} \tag{7.37}$$

$$\hat{Q}_{ik} = \frac{1}{2}\sum_m \hat{s}_m(\omega, \boldsymbol{y_m})\, \boldsymbol{y_{mi} y_{mk}} \tag{7.38}$$

In general, only the first three multipoles are important in sound field characterization and the results of the summations in eq. (7.36), (7.37) and (7.38) are called source strength. Thanks to the multipole expansion, the sound field due to a whatever complicated simple sources arrangement may be seen as made up by the superposition of fields due to *monopole*, *dipole* and *quadrupole*. This is schematically depicted in Figure 7.7.

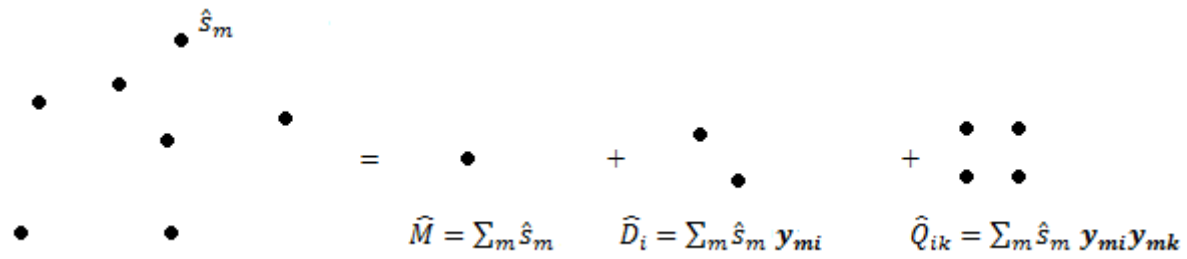


Figure 7.7 – Multipole expansion of sound field.

Another important consequence of eq. (7.24) is that, for source terms involving spatial derivatives of order $n$, it is possible to rewrite the resulting sound field as superposition of multipole of order $2^n$. In fact, by performing a spatial derivative on the wave equation, yields

$$\frac{\partial^n}{\partial x_1^i \partial x_2^l \partial x_3^k}\left[\frac{1}{a_0^2}\frac{\partial^2}{\partial t^2} - \nabla^2\right] p' = \frac{\partial^n s(\boldsymbol{x},t)}{\partial x_1^i \partial x_2^j \partial x_3^k} \tag{7.39}$$

where $p'$ satisfies eq. $(7.17)_1$. If $p'$ is assumed sufficiently regular, the order between the spatial derivative and the wave operator may be interchanged, giving

$$p'_n(\boldsymbol{x}, \mathrm{t}) = \iiint \frac{\partial^n}{\partial x_1^i \partial x_2^j \partial x_3^k}\left[\frac{s(\boldsymbol{y}, t_e)}{4\pi r}\right] dV_y \tag{7.40}$$

where $p'_n(\boldsymbol{x}, \mathrm{t})$ stands for the total multipole field of order $2^n$. Equation (7.40) represents the free field solution of the inhomogeneous wave equation as superposition of multipoles instead of monopoles. This is a very convenient form of rewriting the sound field due to aeroacoustics sources, as it will be clear later.

Before going through the theory of how sound is generated aerodynamically, it is important to characterize the *monopole*, *dipole* and *quadrupole* sound field. Firstly, in order to be able to understand the basic differences among these particular sound fields, it is advisable to get comfortable with the concepts of *near* and *far field*. Such subdivision is very useful when approaching to sound propagation problems because, as it will be clear in the following, only the *far field* term is responsible for the acoustic power radiation. The transition from *near field* and *far field* is regulated by a dimensionless number, namely

$$\begin{cases} kr \gg 1 \rightarrow farfield \\ kr \ll 1 \rightarrow nearfield \end{cases} \tag{7.41}$$

which means that, conventionally, for distances from the source greater than the wavelength the sound field is called radiation field and for distances smaller than the wavelength it is called *near field*. The reason why radiated sound is much less than the *pseudo-sound* should be clear after the understanding of the characteristic *monopole*, *dipole* and *quadrupole* sound field.

### 7.2.1 Monopole source

As already mentioned above, the type of source that generates a sound field of the form of eq. (7.16) is called *monopole source* and the corresponding sound field is called *monopole field*. As the Green's function suggests, the *free field* monopole field corresponds to an inverse square low of sound intensity at all distances from the source. This is because for spherical waves, as it happens for plane waves, the sound intensity is proportional to the square of the pressure disturbance (the constant of proportionality being the inverse of the characteristic impedance of the medium). An example of such mechanism of sound generation in fluid is represented by unsteady injection of mass[3]. When such source is located at the origin, the resulting sound field is a pure *monopole field* as depicted in Figure 7.8.

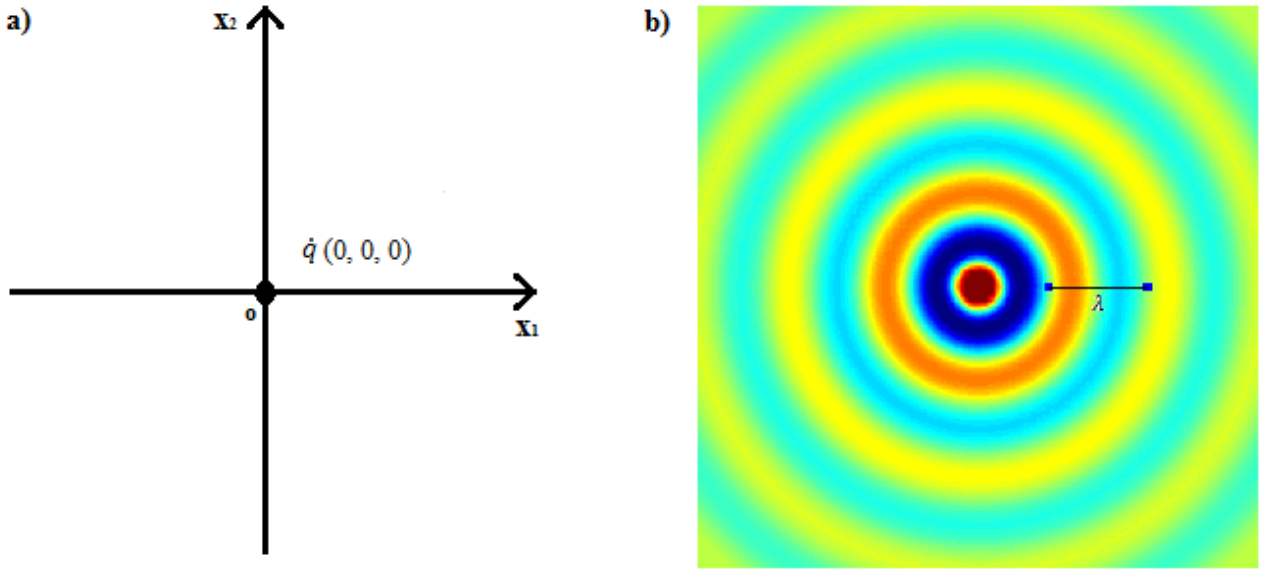


Figure 7.8 - Point source placed at the origin a) and corresponding sound field at 500Hz b).

The color map of Figure 7.8 b) indicates the intensity of the pressure fluctuations in the sound field. More precisely the red and blue color indicates compression and rarefaction respectively. A classic example of unsteady mass injection process is a radially oscillating sphere (fluid or solid). Of course, the produced sound is independent of the density of the sphere, but depends only upon the unsteady mass (and so volume produced and the density) produced in the surrounding medium. For example, any foreign body in a fluid whose volume pulsates, acts as a sound source and the mass outflow from the body is

$$\dot{m} = \rho_0 \dot{V} \tag{7.42}$$

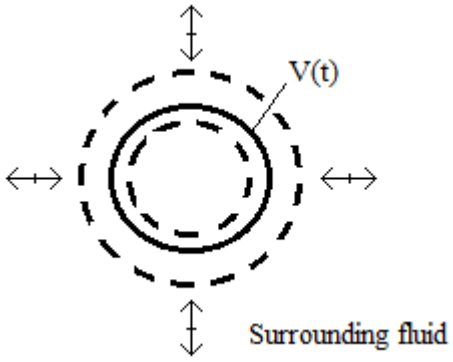


Figure 7.9 – Isotropic volume pulsation of a foreign body within a fluid.

Actually, it is intuitive to find out that only the rate of change of the mass outflow produces sound[61] and, thanks to eq. (7.34), the pressure fluctuations in a three-dimensional infinite space are given by

$$p'_M(t, \boldsymbol{x}) = \frac{1}{4\pi x} \frac{\partial \dot{m}(t - x/a_0)}{\partial t} \tag{7.43}$$

that is a pure *monopole field*, since both the dipole and quadrupole terms are zero (the source is located at the origin and so $y_m = 0$). As possible to point out from eq. (7.43), the pressure fluctuation at a generic point $x$ faithfully follows those of the source except for the *emission time* necessary to reach that point. The rate of change of the mass injection $\dot{q}(t) = \partial \dot{m} / \partial t$ is called source strength, indicated as $S_0$ in Figure 7.8. Of course, as eq. (7.43) suggests, a *monopole source* is omnidirectional, as it is possible to appreciate from the directivity plot in Figure 7.10.

[61] It is the only term appearing in the inhomogeneous wave equation when mass injection is considered in the conservation of mass.

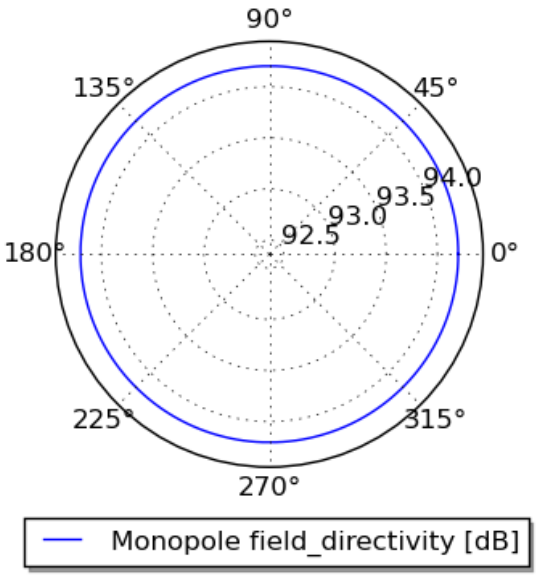


Figure 7.10 – Directivity plot at 10 Hz of a *monopole source* having a unit amplitude. The line refer to a $1m$ of radius from the source.

Another very important thing which characterizes a simple source is that the sound field cannot be divided in *near field* and *far field*. This is because the expression of the sound field do not change as the non-dimensional number $kx$ changes (see eq. (7.44)). Therefore, the sound power radiated by a monopole source may be calculated thanks to the pressure fluctuations expressed by eq. (7.43). However, in order to highlight the frequency dependence of the radiated power, let's use the frequency domain representation of the sound field, namely

$$\hat{p}(\omega, \boldsymbol{x}) = j\frac{1}{4\pi x}\omega\hat{q}e^{j(\omega t - kx)} \tag{7.44}$$

where the time dependence of the mass injection has be assumed of the type $q(\omega) = \hat{q}e^{j(\omega t - kx)}$. Hence the power radiated may be expressed as

$$W_{monopole} = \frac{|p|^2}{\rho a_0}S = \frac{\hat{q}^2}{4\pi\rho a_0}\omega^2 \cong k^2 \tag{7.45}$$

which means that, for a given source strength (rate of change of mass flow), the radiated power varies as the square of the wavenumber. This is a very important aspect which has to be taken into account when comparing the low frequency sound radiation of other type of sources.

One important example of *monopole source* modelling is represented by the openings of both intake and exhaust systems in internal combustion engines. The volume flow injected into the surrounding medium, may be calculated thanks to the surface integral of the flow velocity over the intake or exhaust mouth.

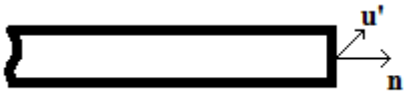


Figure 7.11 – Pulsating volume flow from a pipe opening.

In fact, thanks to the flow velocity it is possible to easily calculate the time derivative of the mass flow. Another example is represented by a loudspeaker when mounted in a box, as depicted in Figure 7.12.

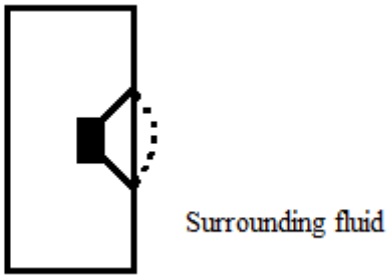


Figure 7.12 – Volume flow produced when a loudspeaker mounted in a box.

In fact, in this case, because of the box a net volume flow is produced in the surrounding medium giving rise to a *monopole field*. This is especially truth for low frequencies, for which the wavelength is greater than the box size. Furthermore, the collapsing cavitation bubbles in liquid are another important example of simple source. The bubbles arise when the local static pressure is below the vapor pressure. Due to their instability, the bubbles may suddenly implode and thanks to the rapid change of volume, the high time derivative $\dot{q}(t)$ may generate high sound levels.

### 7.2.2 Dipole source

Another elementary mechanism of sound generation is represented by a *dipole source* and the corresponding sound field is called *dipole field*[3]. As suggested by eq. (7.30), a pure *dipole field* is, for example, generated when two equal and opposite *monopole sources* are very close to one another. Let consider for example the source distribution $s(\boldsymbol{y}, t)$ as it is schematically shown in Figure 7.13.

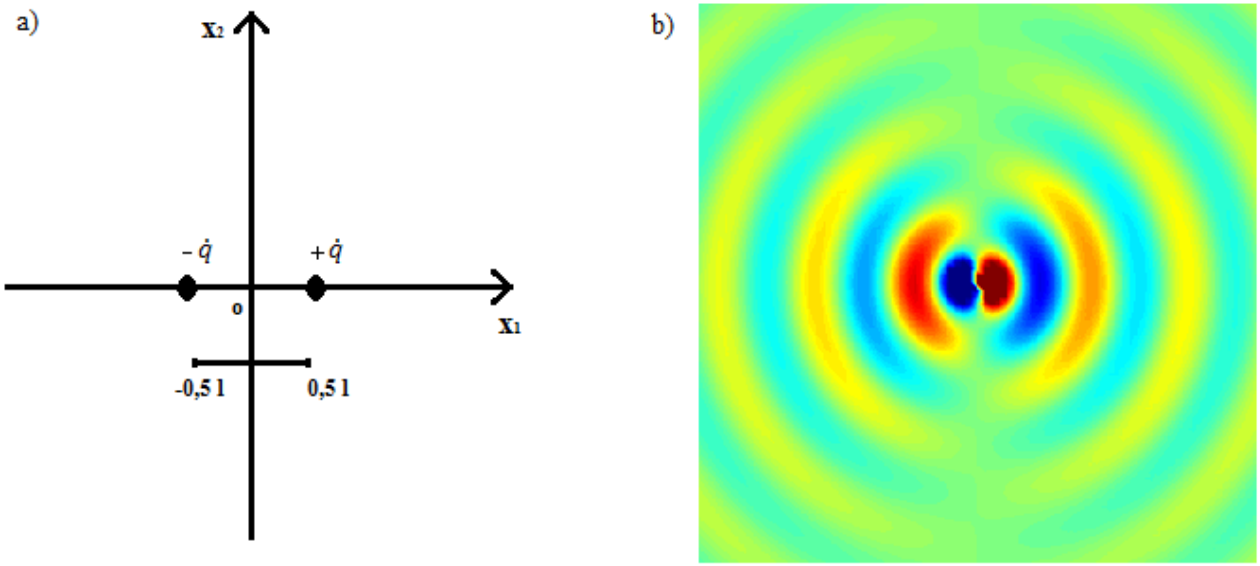


Figure 7.13 - Dipole source a) and corresponding dipole field at 500 Hz b).

Again, in Figure 7.13 b), the red and blue color indicates compression and rarefaction respectively. First thing to note is that, of course, the expression of the sound field is changed with respect to the simple *monopole source*, being a pure *dipole field*[62]. In fact, according to the multipole expansion of the sound field, the distribution of sources is such that both monopole and quadrupole terms ($\widehat{M} = \hat{q} - \hat{q}$ and $\hat{Q}_{11} = \frac{1}{2}[\hat{q}(0{,}5l)^2 + (-\hat{q})(0{,}5l)^2]$) vanish[63]. Consequently, in order to obtain a more suitable expression for pressure fluctuations, consider a particular $i^{th}$ direction, connecting a field point $p$ and the middle of the distance between the two sources, on which apply the multipole expansion formula. Thus, eq. (7.34) yields

$$p'(t,\boldsymbol{x}) = -\left\{-0{,}5l\ cos\vartheta\left[\frac{(-\dot{q})}{4\pi x}\left(-\frac{1}{x}\right) + \frac{(-\ddot{q})}{4\pi x}\left(-\frac{1}{a_0}\right)\right]\right\} - \left\{0{,}5l\ cos\vartheta\left[\frac{\dot{q}}{4\pi x}\left(-\frac{1}{x}\right) + \frac{\ddot{q}}{4\pi x}\left(-\frac{1}{a_0}\right)\right]\right\}$$

$$= -\left(-\frac{\dot{q}}{4\pi x}\frac{1}{x}0{,}5l\ cos\vartheta - \frac{\ddot{q}}{4\pi x}\frac{1}{a_0}0{,}5l\ cos\vartheta\right) - \left(-\frac{\dot{q}}{4\pi x}\frac{1}{x}0{,}5l\ cos\vartheta - \frac{\ddot{q}}{4\pi x}\frac{1}{a_0}0{,}5l\ cos\vartheta\right) \tag{7.46}$$

or

$$p'_D(t,\boldsymbol{x}) = \frac{\dot{q}(t-x/a_0)}{4\pi x}\frac{l\ cos\theta}{x} + \frac{\ddot{q}(t-x/a_0)}{4\pi x a_0}l\ cos\theta \tag{7.47}$$

where the term $l\ cos\theta$ is due to the product of the source positions and the versor of the i-th direction, namely $|\boldsymbol{y_{mi}}|$, and it represents the difference between the distance of point $x$ and the two source positions $r_+$ and $r_-$, both along the chosen i-th direction. This is schematically depicted in Figure 7.14.

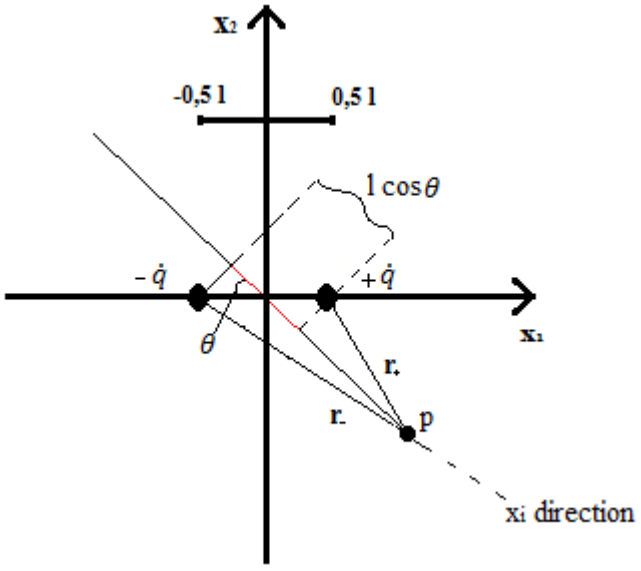


Figure 7.14 - Distances of a point from the source positions along the i-th direction.

[62] The expression of the total sound field would be $p'_D(t,\boldsymbol{x}) = \frac{1}{4\pi x_1}\frac{\partial \dot{m}(t-x_1/a_0)}{\partial t} - \frac{1}{4\pi x_2}\frac{\partial \dot{m}(t-x_2/a_0)}{\partial t}$, being $x_1$ and $x_2$ the distance from the two sources respectively.

[63] $\widehat{D}_1 = \hat{q}\ 0{,}5l + (-\hat{q})(-0{,}5l) = \hat{q}l$ and the sound field may be rewritten as $\hat{p}(\omega,\boldsymbol{x}) = \hat{q}l\frac{\partial}{\partial x_1}\left(\frac{e^{-jkx}}{x}\right)$.

It is that difference in distances from the sources that makes the dipole field not omnidirectional anymore. In fact, as it is possible to appreciate from Figure 7.13 b), there are some directions, say north and south, along which the contributions of the two sources cancel out. In order to understand such behavior, let's look at Figure 7.15, where point $x$ has been chosen on the north direction.

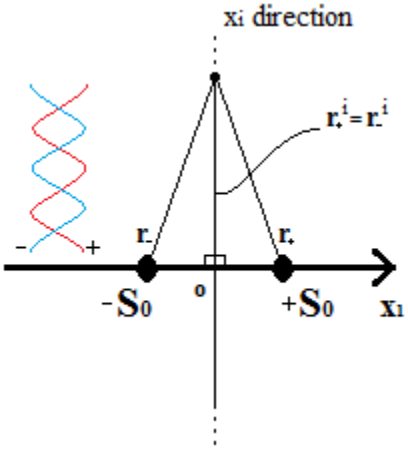


Figure 7.15 - Location of point $x$ along the north direction, with respect to the dipole axis.

In this case, point $x$ has been chosen so that $\left|\boldsymbol{y}_{+}^{\boldsymbol{i}}\right| = \left|\boldsymbol{y}_{-}^{\boldsymbol{i}}\right| = 0$ $(\theta = \pi/2)$ and so the distances from the two sources along the north direction are equal; the considered point is equally spaced with respect to the two sources. This implies that the two sound waves (opposite in phase) travel the same distance in order to reach $x$ and so cancelling out. Consequently, within the left-half plane all the points along each direction are closer to $-S_0$ and so it is its contribution (phase) which dominates the sound field, as shown by Figure 7.16.

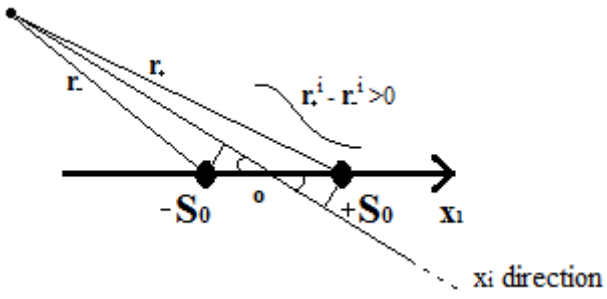


Figure 7.16 - Sound field at a point located in the half-left plane.

Obviously, the contrary happens for the right-half plane (see the differences in Figure 7.13 b)). So, the wavefronts moving to the left and to the right are 180° out of phase with respect to each other. The *far field* directivity plot of a *dipole source* is depicted in Figure 7.17.

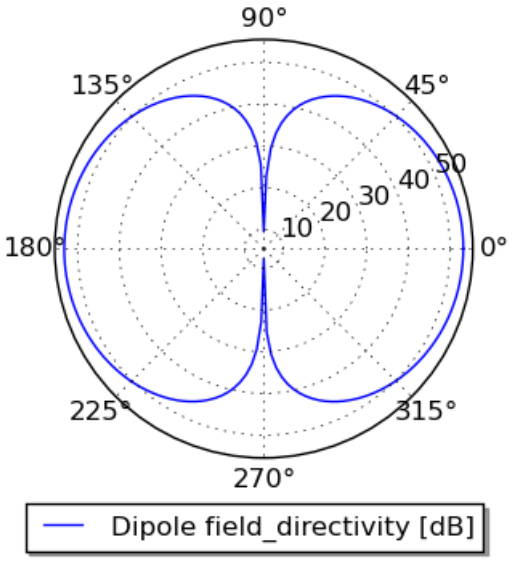


Figure 7.17 – Directivity plot at 500 Hz of a *dipole source* having a unit amplitude. The line refer to a $2m$ of radius from the source ($kr \gg 1$).

Another important thing to note is that, according to eq. (7.37), the source strength equals[64] $\hat{q}l$ and so the same pressure fluctuations would occur if the sources were half as strong but twice as closer to each other. Furthermore, with reference to the *dipole field* expressed by eq. (7.47), the first term (due to the derivative with respect to the $x^{-1}$) represents the *near field* term, whilst the second term (due to the derivative of the time lag $x/a_0$) represents the radiation, or *far field*, term. This subdivision of the sound field in two parts is very useful in understanding the nature of the pressure fluctuations. In fact, by comparing the *dipole field* with the simple (*monopole*) source field, it is easy to find out that the *near field* term scales like $l/x$, whilst the *far field* term scales like the Helmholtz number, namely

$$\frac{p'_{dipole}}{p'_{monopole}} = \frac{l\,cos\theta}{x} + \frac{\omega l\,cos\theta}{a_0} = \frac{l\,cos\theta}{x} + \frac{2\pi l\,cos\theta}{\lambda} \cong \frac{l}{x} + He \tag{7.48}$$

When the Helmholtz number is small, the source region is said to be compact with respect to the wavelength and aerodynamic sources are generally compact (for the characteristic involved frequency scale). Hence, at distances $x$ large compared with the wavelength ($kx \gg 1$), the first term in eq. (7.48) is smaller than the second one which is therefore the only responsible for the acoustic radiation. Here the pressure fluctuations fall off like $1/r$, like the *monopole field*. Closer to the source region than the wavelength ($kx \ll 1$), the *near field* term is predominant and the sound field is quite intense, being induced mainly by the nearest *monopole source*. Therefore, an important result from the above analysis is that although the *near field* is somehow characterized by more intense fluctuations with respect to the *monopole radiation* (at least for distances smaller than source region characteristic length), far less energy is radiated in the *far field*. In other words, the radiation efficiency is reduced, when passing from a *monopole* to a *dipole* radiation, by a factor

[64] In the frequency domain $\dot{q} = \hat{q}e^{j\omega t_e} \Rightarrow \ddot{q} = \frac{\partial \dot{q}}{\partial t} = j\omega\hat{q}e^{j\omega t_e}$. Therefore in eq. (7.35) it is justified the definition of the source strength as $\widehat{D}_i = \sum_m \hat{q}_m(\omega, \boldsymbol{y_m})\,\boldsymbol{y_{mi}} = \hat{q}lcos\theta$.

equal to the Helmholtz number. In fact, a possible way to prove that is by means of eq. (7.48), for which the square of the *far field* pressure fluctuations are given by

$$\left(p'_{dipole}\right)^2 = \left(p'_{monopole}\right)^2 (He)^2 \tag{7.49}$$

This means that the power radiated by a *dipole field* may be expressed as

$$W_{dipole} = \frac{\hat{q}^2}{4\pi\rho a_0}\omega^2(kl)^2 \cong k^4 \tag{7.50}$$

which means that for a given source strength (rate of change of mass flow), the radiated power varies as the fourth power of the wavenumber. Thus, it follows that a dipole is less efficient in radiation low frequency sound with respect to a monopole source. In Figure 7.18, a qualitative comparison between the radiated power by a *monopole* and by a *dipole source* is depicted, for a given source strength, as function of the frequency.

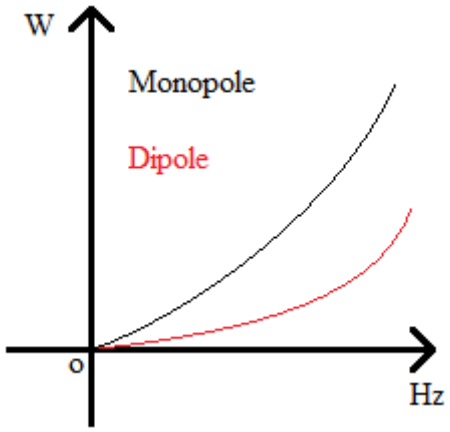


Figure 7.18 – Comparison of the radiated power from both a *monopole* and a *dipole source* at low frequencies.

From the above figure, it is clear that a *dipole source* is less efficient in radiating especially the low frequency sound.

From what has been described in the previous section, a *monopole field* may be generally associated to an unsteady mass injection process. Another process is instead associated with a *dipole field*. To the aim of understanding which process is involved, it is necessary to analyze what happens within the source region. Embedded within this out of phase pulsations there is a fluctuation of the momentum, whose qualitative quantification is possible by considering the mass flow across a disk orthogonal to the distance between the sources[3]. The intuitive trend of such mass flow is depicted in Figure 7.19.

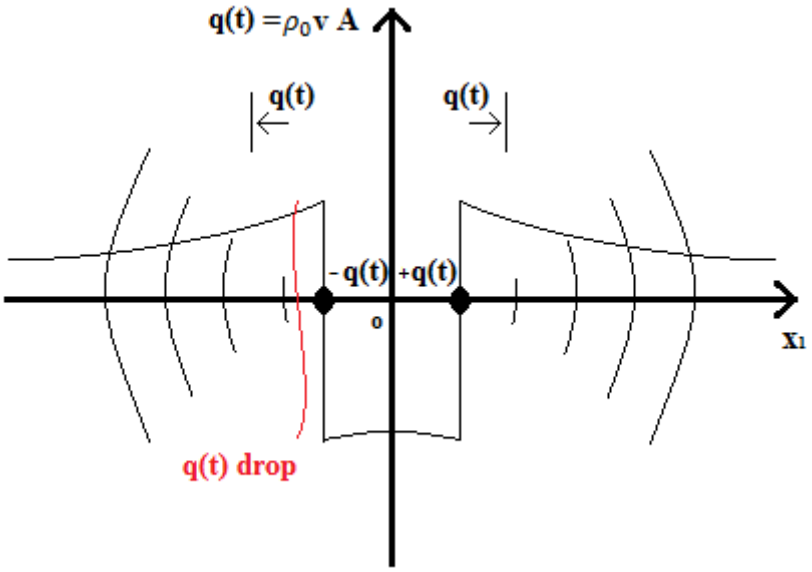


Figure 7.19 – Mass flow trend near the *dipole source*.

Firstly, outside the source region, the mass flow always points outside. Thus, even if the exact trend is unknown, it must suddenly drop by an amount equal to $q(t)$ when approaching $-q(t)$ and it must suddenly rise of the same quantity at the location of $q(t)$. In fact, within the source region, when $-q(t)$ pulses the mass at $q(t)$ flows to the left, which means that it drops by an amount $q(t)$. The contrary happens near $-q(t)$ when $q(t)$ pulses. It follows that the total momentum inside the source region equals the area under the curve mass flow versus position, namely $-q(t)l$. However, no net momentum can be produced by simple sources and so in the external *dipole field* there must be an opposite momentum equal to $q(t)l$. The rate of change of such momentum equals a force which, in this case, acts on the surrounding fluid, namely

$$\dot{q}(t)l = F \tag{7.51}$$

Therefore, according to eq. (7.47), it is possible to point out that a *pure dipole field* is given by the first order spatial derivative of the field associated with a simple source, namely

$$p'_D(t, \boldsymbol{x}) = \frac{\partial}{\partial x}\left(\frac{\dot{q}l}{4\pi x}\right) \tag{7.52}$$

Consequently, by combining eq. (7.51) and (7.52), it is clear how the dipole radiation is due to a force with which the dipole acts on the external fluid. The force's direction is represented by the dipole axis and its orientation (and magnitude) oscillates from the negative to the positive source. In general, there could be also other external forces acting on the fluid, e.g. in case where there is a moving body. In this case the sound field may be seen as composed by a single dipole, whose strength is given by the total force acting on the fluid. This latter must take into account the presence of the moving body, namely

$$F_{tot} = F_{dipole} + \rho_{fluid} V_{body} \dot{u} \tag{7.53}$$

The second term on the right-end side of eq. (7.53) represents the rate of change of momentum of the fluid being displaced by the solid body. Due to the low air density, this term is often not important but it is considered in propeller-noise theory[5].

An important example of pure dipole radiation is represented by a loudspeaker in a fluid.

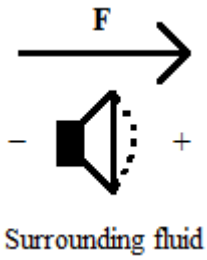


Figure 7.20 – Loudspeaker with no box.

As depicted in Figure 7.20, when the membrane of the loudspeaker vibrates, no net volume flow is produced since when one side of the surrounding fluid in compressed the others is rarefied at the same time. More precisely, while the front is pushing outwards the back is sucking in. This produces an oscillating force on the fluid, whose axis is orthogonal to the membrane. Another very common example of unsteady forces acting of fluid is represented by the periodic flow separation (vortex shedding) when a non-moving solid object appears within a flow as an obstacle. In this flow, vortices are created at the back of the body and detach periodically from either side of it. Thus, the fluid flow past the object creates alternating low-pressure vortices on the downstream side of the object, as schematized in Figure 7.21.

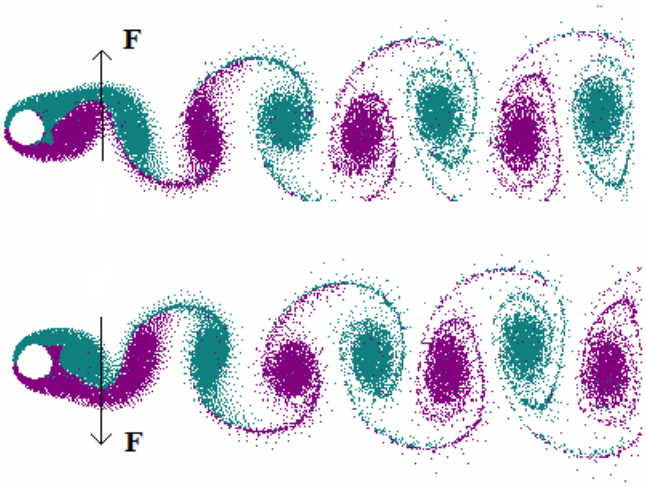


Figure 7.21 – Vortex shedding constituting an acoustic dipole.

Of course, the obstacle will tend to move toward the low-pressure zone. Such fluctuating pressure produces tonal noise with a characteristic frequency corresponding the Strouhal frequency ($St = fl/v$). In addition, if the body' structure is not mounted rigidly and the frequency of vortex shedding matches the resonance frequency of the structure, the structure can begin to resonate, vibrating with harmonic oscillations driven by the energy of the flow. This vibration is the cause for

overhead power line wires "singing in the wind", and for the fluttering of automobile whip radio antennas at some speeds.

### 7.2.3 Quadrupole source

As suggested by the word itself, a *quadrupole source* corresponds to two equal and opposite *dipole sources*, divided by a small distance[3], as depicted in Figure 7.22.

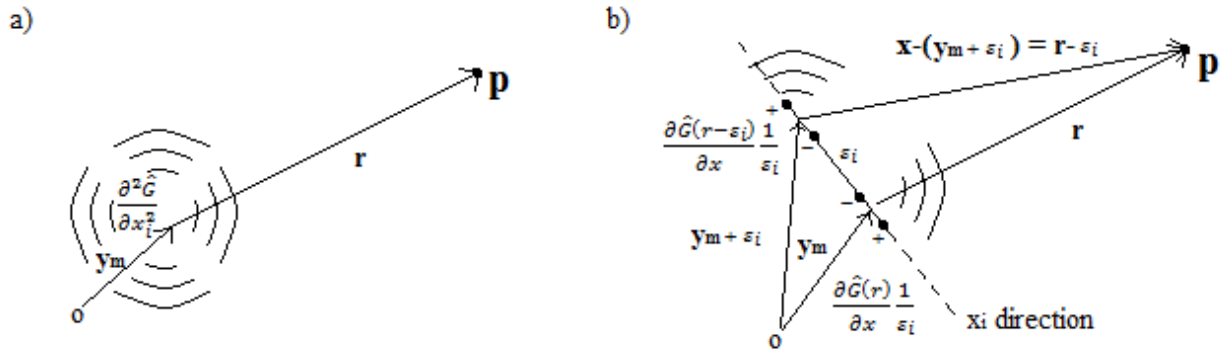


Figure 7.22 – Quadrupole sound field a) and associated multipole expansion in terms of dipoles b).

In fact, in the limit as $\varepsilon_i \to 0$, it is possible to mathematically rewrite a pure *quadrupole field* as two equal and opposite dipoles separated by a small distances, namely

$$\frac{\partial^2 \hat{G}}{\partial x_i^2} = \frac{\partial \hat{G}(r)}{\partial x}\frac{1}{\varepsilon_i} - \frac{\partial \hat{G}(r-\varepsilon_i)}{\partial x}\frac{1}{\varepsilon_i} \tag{7.54}$$

and, obviously, each dipole may be seen as superposition of two monopoles. For example, let consider the sources arrangement which is shown in Figure 7.23. As it will be clear later, this is called *longitudinal quadrupole* because all the sources are arranged in line.

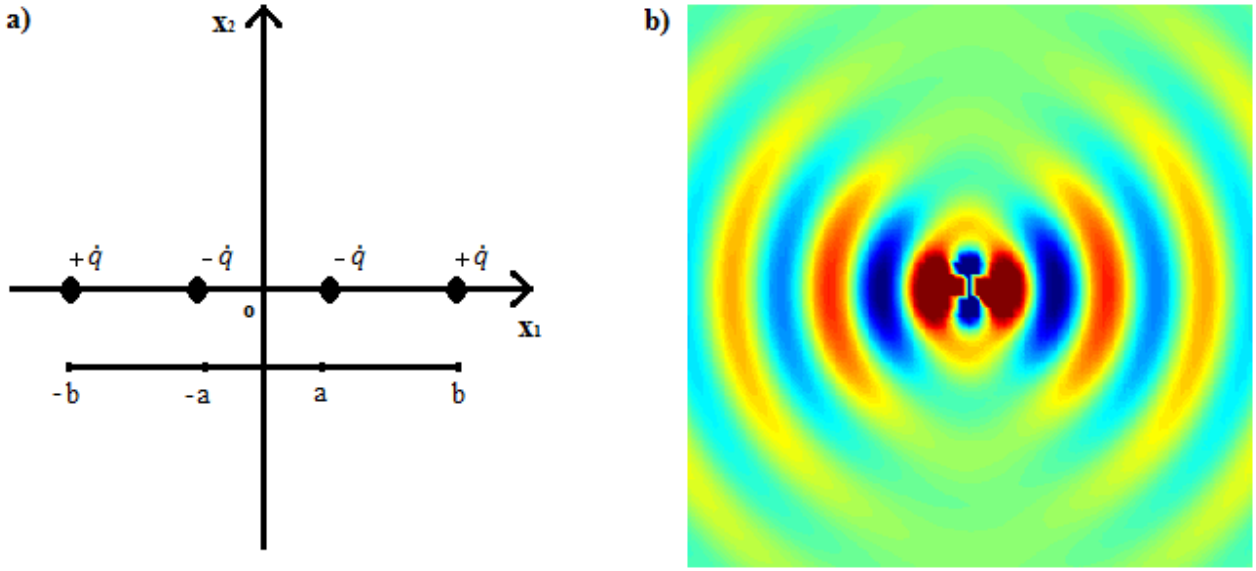


Figure 7.23 – Longitudinal quadrupole a) and corresponding acoustic field at 500 Hz b).

According to the multipole expansion formula, the first non-zero term is the *quadrupole* term, and the time domain expression of the sound field becomes

$$p'(t,\boldsymbol{x}) = \frac{1}{2}\Big\{(-b)cos\theta(-b)cos\theta\left[2\frac{S_{-b}}{4\pi x^3}+\frac{\dot{S}_{-b}}{4\pi x^2}\frac{1}{a_0}+\frac{\dot{S}_{-b}}{4\pi x^2}\frac{1}{a_0}+\frac{\ddot{S}_{-b}}{4\pi x}\frac{1}{a_0^2}\right]+ (-a)cos\theta(-a)cos\theta\left[-2\frac{S_{-a}}{4\pi x^3}-\frac{\dot{S}_{-a}}{4\pi x^2}\frac{1}{a_0}-\frac{\dot{S}_{-a}}{4\pi x^2}\frac{1}{a_0}-\frac{\ddot{S}_{-a}}{4\pi x}\frac{1}{a_0^2}\right]+(a)cos\theta(a)cos\theta\left[-2\frac{S_a}{4\pi x^3}- \frac{\dot{S}_a}{4\pi x^2}\frac{1}{a_0}-\frac{\dot{S}_a}{4\pi x^2}\frac{1}{a_0}-\frac{\ddot{S}_a}{4\pi x}\frac{1}{a_0^2}\right]+(b)cos\theta(b)cos\theta\left[2\frac{S_b}{4\pi x^3}+\frac{\dot{S}_b}{4\pi x^2}\frac{1}{a_0}+\frac{\dot{S}_b}{4\pi x^2}\frac{1}{a_0}+\frac{\ddot{S}_b}{4\pi x}\frac{1}{a_0^2}\right]\Big\} \tag{7.55}$$

or[65]

$$p'(t,\boldsymbol{x}) = cos^2\theta\left(\frac{S}{2\pi x^3}lL+\frac{\dot{S}}{4\pi x^2}\frac{1}{a_0}lL+\frac{\ddot{S}}{4\pi x}\frac{1}{a_0^2}lL\right) \tag{7.56}$$

where $l$ stands for the distance between two opposite *monopoles* (which make a *dipole*) and $L$ is the distance between the two *dipoles*. By comparing the quadrupole field with the simple source field, it comes out that[66]

$$\frac{p'_{quadrupole}}{p'_{monopole}} \cong \left(\frac{L}{x}\right)^2+\frac{L}{x}\frac{2\pi L}{\lambda}+\left(\frac{2\pi L}{\lambda}\right)^2 \tag{7.57}$$

From eq. (7.57) it is easy to find out that the *far field* term scales as the square of the Helmholtz number with respect to the *monopole field*, namely

$$\left(\frac{p'_{quadrupole}}{p'_{monopole}}\right)_{far\ field} = \left(\frac{2\pi l}{\lambda}\right)^2 \tag{7.58}$$

This means that the radiated power by a *quadrupole field* may be expressed as

$$W_{quadrupole} = \frac{\hat{q}^2}{4\pi\rho a_0}\omega^2(kl)^4 \cong k^6 \tag{7.59}$$

which means that for a given source strength (rate of change of mass flow), the radiated power varies as the inverse sixth power of the wavelength. This means that a *quadrupole radiation* should be even less efficient than a *dipole field* in radiating low frequency sound. A very interesting experiment about that may be found in reference[7]. When the distance between the center of the dipoles is orthogonal to the dipole axes, the quadrupole is said to be lateral. In figure below, the far field directivity plots of both longitudinal and lateral quadrupole are shown.

[65] $b^2-a^2=(b-a)(b+a)=lL$.
[66] In the limit of $L \to l$.

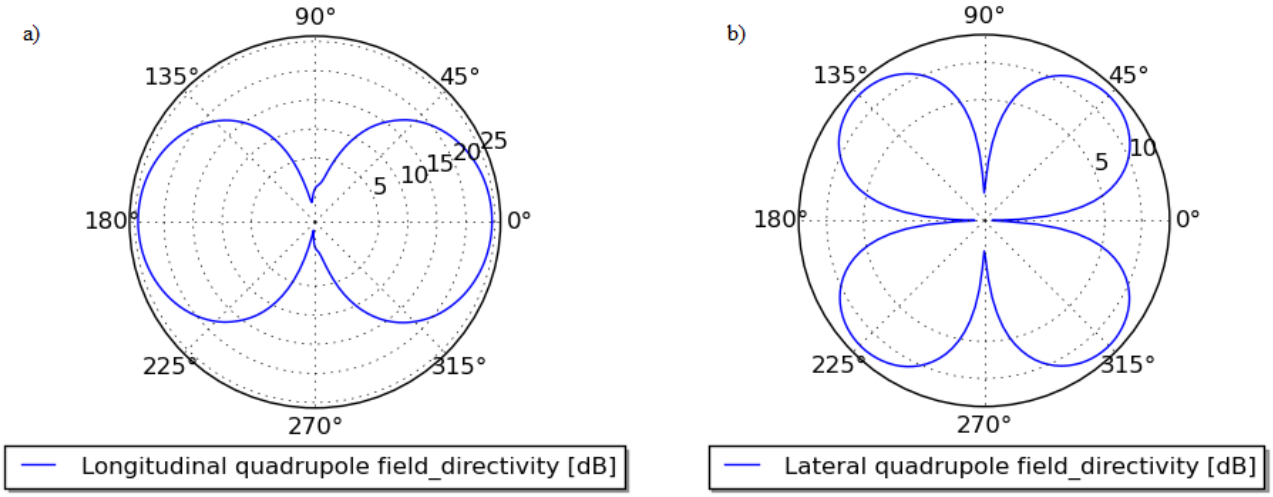


Figure 7.24 – Far field directivity plots of: a) longitudinal and b) lateral quadrupole.

An example of *longitudinal quadrupole* sound source is represented by a tuning fork. In fact, when the two tines vibrate in antiphase, they induce two equal and opposite forces acting on the surrounding medium as schematically depicted in Figure 7.25.

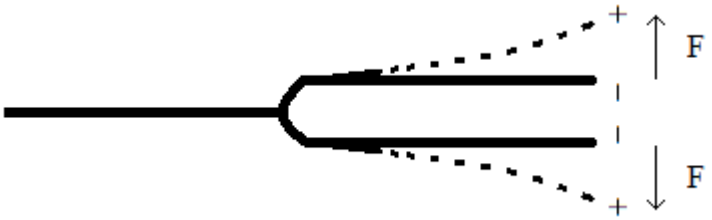


Figure 7.25 – Antiphase oscillating tines of a tuning fork making two equal and opposite *dipoles*.

Another important example of *quadrupole radiation* is represented by a turbulent jet. In fact, in this case there is no time variable rate of introduction of new fluid (there is no rate of change at all), so the *monopole* term equals zero. There are no solid obstacles which can cause unsteady forces on the fluid, so the total *dipole strength* is zero and therefore, neglecting the fact that the jet is hot[67], the radiation is of *quadrupole type*. In order to find out which is the mechanism which generates a *quadrupole*, let's focus on a 2-D turbulent jet, as it is schematically depicted in Figure 7.26.


Figure 7.26 – 2-D turbulent jet representation.

As the above figure suggests, the momentum transport across a fluid element is not only accomplished by pressure gradients but, for example, also by fluctuations of the velocity component

[67] This is equivalent in considering pressure fluctuations due to only adiabatic transformation $p' = \rho' a_0^2$.

orthogonal to the jet direction. Such fluctuations result in two equal and opposite forces ($\rho uvS$), as it is schematically depicted in Figure 7.27.

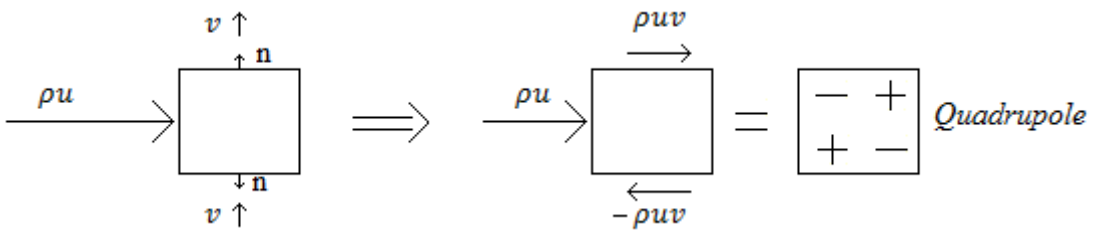


Figure 7.27 – Momentum transport across a fluid element in e turbulent jet.

Such equal and opposite fluctuating forces constitute a *quadrupole* whose strength per unit of volume equals $\rho uv$. In the next section, the way in which the above mentioned *monopole*, *dipole* and *quadrupole radiation* are very useful for understanding the aerodynamic generation of sound will be explained based on the well-known aeroacoustics analogy.

## 7.3 Lighthill's Aeroacoustic Analogy

As briefly mentioned in the introduction, the driving phenomenon which stimulated James Lighthill to formulate an aeroacoustic analogy has been represented by the noise reduction from a propulsion jet[13][2][5]. The basic idea behind the theory is that, in order to approach a sound propagation problem in which source terms are present, the inhomogeneous wave equation is only valid in a limited zone of the acoustic domain, where sound is produced, whilst the propagation obeys to the homogeneous wave equation elsewhere. Such observation led to the subdivision of the acoustic domain in two parts which are called *source field* and *sound field*. Within the *source field* the inhomogeneous wave equation is valid, whilst in the *sound field* the pressure fluctuations satisfy the homogeneous wave equation. Consequently, the main problem was to formulate a model for the *source field*, meaning how to model sound generation due to fluid flow. To this aim, he formulated a so-called aeroacoustic analogy considering the jet noise case, i.e. sound production and propagation due to a stationary, turbulent fluid flow. To the aim of understanding such analogy, let consider a steady fluid flow occupying a limited region of a larger volume of fluid at rest, as schematically depicted in Figure 7.28.

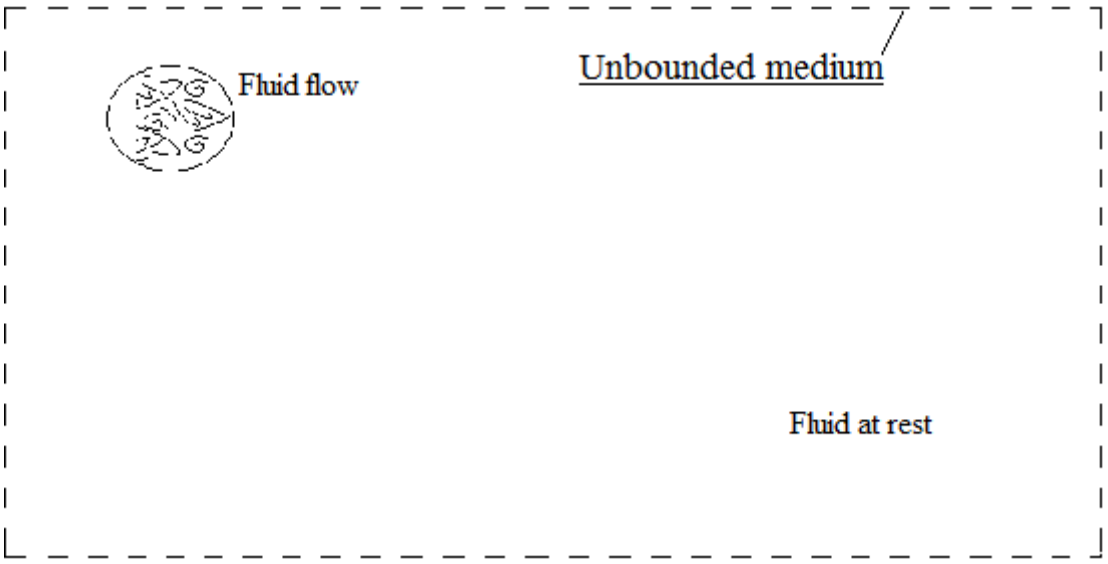


Figure 7.28 – Fluid flow embedded in a very large volume of fluid at rest.

The basic idea of the analogy is ingenious and consists in simply considering the *source field* as an acoustic medium at rest (as the real fluid outside the source region), on which an external force field is acting, known as some quantities in the real flow are known. Therefore, it is necessary to extrapolate from the flow field such equivalent external force field. The main advantage in considering the whole acoustic medium at rest relies on the fact that otherwise, after the sound has been estimated, it would be necessary to consider modification due to turbulence and propagation at variable speed, before the propagation in the surrounding medium may be handled. In this approach, such effects are incorporated within the hypothetical external force field. To the aim of qualitative identify such external force field, let recall the local form of momentum balance equation in Cartesian tensor notation, namely

$$\frac{\partial(\rho V_i)}{\partial t} + \frac{\partial(\rho V_i V_j)}{\partial x_j} - \frac{\partial(T_{ij})}{\partial x_j} = 0 \tag{7.60}$$

where generation of momentum due to external volume forces as been neglected. Such equation expresses that, during a fluid flow, the momentum in the $i^{th}$ direction, contained in a small confined region of space, changes at a rate due to the combined effect of stresses acting on the boundaries (diffusive transport) and momentum flux across them (convective transport). This latter part $(\rho V_i V_j)$, being a divergence term, may be seen as an additional stress system, which is named either *momentum flux tensor* or *instantaneous Reynolds stresses*[68]. Consequently, the rate of change of momentum would be the same if the fluid is considered at rest, under the combined action of the real stresses and the *instantaneous Reynolds stresses*. However, it is not such total stress tensor which must be considered when acoustically modelling the *source region* (or better when modelling the acoustic source term), because it accounts also for the pressure field proportional to density variations through the square of the speed of sound $(\rho a_0^2)$, which is already accounted in the wave equation. Therefore, the equivalent external stress system acting on the fluid at rest in the source region would be given by

[68] In order to not be confused with the Reynolds stresses used in turbulence modelling, which are based on the average of the fluctuating turbulent velocity components.

$$\gamma_{ij} = \rho V_i V_j - T_{ij} - \rho a_0^2 \delta_{ij} \tag{7.61}$$

which accounts not only for the sound generation, but also for its convection with the flow $\left(\rho V_i V_j\right)$, its propagation with variable speed and gradual dissipation by conduction (in part of deviations from adiabatic state of change[69]) and its gradual dissipation by viscosity. In other words, as already seen in chapter 1, the stresses experienced by a fluid at rest are isotropic and given by the following relation

$$T_{ij} = -p_{ij}\delta_{ij} \tag{7.62}$$

where within the right-hand side are involved pressure variations due to both adiabatic state of changes (acoustic ones proportional to density variations through the square of the speed of sound) and non-adiabatic state of changes (e.g. heat releases). On the other hand, when the fluid moves, the stresses experienced by the fluid account also for the presence of viscosity, resulting in a stress tensor equal to

$$T_{ij} = -p_{ij}\delta_{ij} + \tau_{ij} \tag{7.63}$$

Consequently, the stresses experienced by the fluid due only to its motion and eventually non-adiabatic state of change are given by

$$-T_{ij} - \rho a_0^2 \delta_{ij} = p_{ij}\delta_{ij} - \tau_{ij} - \rho a_0^2 \delta_{ij} \tag{7.64}$$

which together with the *momentum flux tensor* represents the equivalent external stress system acting on the acoustic medium at rest, within the source region. In fact, once again, pressure variations due to adiabatic state of change are already accounted in the wave equation itself representing the "internal stress field" experienced when there is sound propagation. The stress system indicated by $\gamma_{ij}$ is called Lighthill tensor.

Lighthill's efforts have focused on estimating, from both qualitative and quantitative points of view[13], the acoustic power output related to the stress system $\gamma_{ij}$[70]. In this regards, he only took into account the source term due to steady fluid flow embedded in an unbounded acoustic medium. However, in the following a more general theory, which involves all the basic aerodynamic sound production mechanisms, will be given.

### 7.3.1 Modelling approach

To the aim of deriving the general inhomogeneous wave equation (valid not only for jet noise) governing the sound generation within the source region, let's start from the local form of the conservation equations with the source terms kept, namely

[69] If $(p' - \rho' a_0^2) \neq 0$ means that pressure variation occurs not only for acoustic phenomena but also for non-adiabatic phenomena like heat release.

[70] The Lighithill's theory for the aerodynamic generation of sound is based on the assumption that the source field is independent from the sound field. Consequently, feedback mechanisms in which the propagation of sound modifies the source region (flow field) cannot be handled.

$$\frac{\partial \rho}{\partial t} + \frac{\partial (\rho V_i)}{\partial x_i} = \dot{\mathcal{M}} \tag{7.65}$$

$$\frac{\partial (\rho V_i)}{\partial t} + \frac{\partial (\rho V_i V_j)}{\partial x_j} = f_{v,i} + \frac{\partial (T_{ij})}{\partial x_j} \tag{7.66}$$

In particular, eq. (7.66) states that in a moving medium, the rate of change of momentum within an elementary control volume is due to momentum flux across the boundary and the combined action of an external stress system $(T_{ij})$ and the volume forces $(f_{v,i})$. However, the same elementary control volume would experience the same rate of change of momentum if it was at rest under the combined action of the same force field plus another stress term $(\alpha_{ij} = \rho V_i V_j)$, namely

$$\frac{\partial (\rho V_i)}{\partial t} = f_{v,i} + \frac{\partial (T_{ij} - \alpha_{ij})}{\partial x_j} \tag{7.67}$$

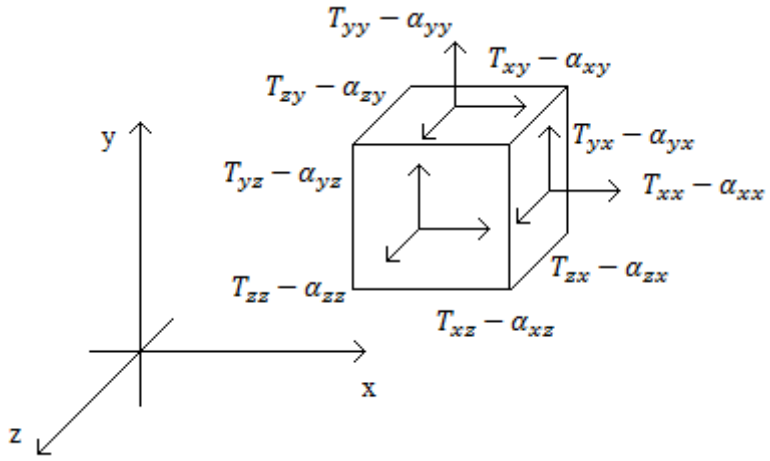


Figure 7.29 – Equivalent (to a flow case) stress system acting on a fluid element at rest.

So, considering the source region as an acoustic medium at rest, the pressure, density and velocity may be expressed as

$$\begin{cases} p(\boldsymbol{r}, t) = p_0 + p'_H(\boldsymbol{r}, t) + \rho'(\boldsymbol{r}, t) a_0^2 \\ \rho(\boldsymbol{r}, t) = \rho_0 + \rho'(\boldsymbol{r}, t) \\ V(\boldsymbol{r}, t) = V'(\boldsymbol{r}, t) \end{cases} \tag{7.68}$$

where both pressure variations due to adiabatic and non-adiabatic state of change have been taken into account[71]. By substituting the relations (7.68) into both eq. (7.65) and (7.67), keeping only linear terms, yields

[71] The heat release effect affects both pressure and density of the acoustic medium. However, despite the effect is the same, it may be seen as a change of stresses (pressure) or, which is the same, change of density. Therefore, when writing the wave equation in density based version, the effect must be taken into account as additional pressure variation. Vice versa, when writing the pressure based version, the effect must be taken into account as additional density variation. It would be erroneous to consider twice the same effect.

$$\begin{cases} \dfrac{\partial \rho'}{\partial t} + \dfrac{\partial (\rho_0 V_i')}{\partial x_i} = \dot{\mathcal{M}} \\ \dfrac{\partial (\rho_0 V_i')}{\partial t} = f_{v,i} - \dfrac{\partial (p_H' + \rho' a_0^2 - \tau_{ij} + \alpha_{ij})}{\partial x_j} \end{cases} \tag{7.69}$$

Then, by performing $\partial(7.69)_1/\partial t - \partial(7.69)_2/\partial x_i$, the following density based wave equation is obtained

$$\frac{\partial^2 \rho'}{\partial t^2} - a_0^2 \nabla^2 \rho' = \frac{\partial \dot{\mathcal{M}}}{\partial t} - \nabla \cdot f_v + \nabla^2 \left( p_H' - \underline{\tau_d} + \underline{\alpha} \right) \tag{7.70}$$

which expresses the complete version of the aeroacoustic analogy first derived by J. Lighthill (density based version) and represents the inhomogeneous wave equation governing the sound production in the source region. The right end side represents the source terms acting on the equivalent acoustic medium at rest. They are known as the flow properties are known. Hence, the main advantage lies in the decoupling of the fluid dynamic problem from the acoustic one, as schematically depicted in Figure 7.30.

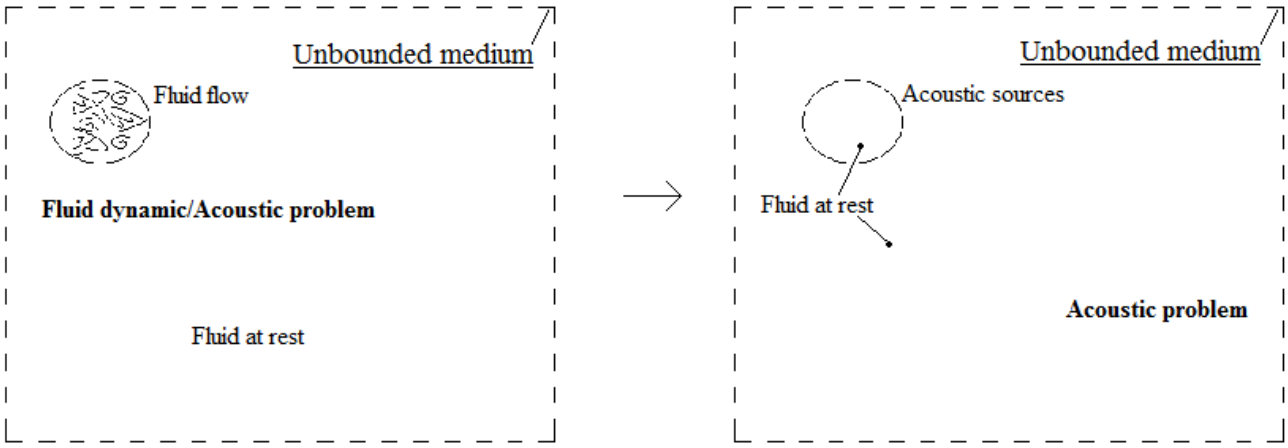


Figure 7.30 – Aeroacoustic analogy.

The pressure based version of the aeroacoustic analogy may be found if, instead of relations (7.68), the following relations are used

$$\begin{cases} p(\boldsymbol{r}, t) = p_0 + p'(\boldsymbol{r}, t) \\ \rho(\boldsymbol{r}, t) = \rho_0 + \dfrac{p'(\boldsymbol{r}, t)}{a_0^2} + \rho_H' \\ V(\boldsymbol{r}, t) = V'(\boldsymbol{r}, t) \end{cases} \tag{7.71}$$

In fact, in this case, non-adiabatic state of changes are taken into account as density variations, leaving the unknown variable $p'(\boldsymbol{r}, t)$ be linked to acoustic phenomena only. The result is represented by the following inhomogeneous wave equation

$$\frac{1}{a_0^2} \frac{\partial^2 p'}{\partial t^2} - \nabla^2 p' = \frac{\partial}{\partial t} \left( \dot{\mathcal{M}} - \frac{\partial \rho_H'}{\partial t} \right) - \nabla \cdot f_v + \nabla^2 \left( -\underline{\boldsymbol{\tau}_d} + \underline{\boldsymbol{\alpha}} \right) \tag{7.72}$$

in which the heat release represents additional mass source term. If there are no deviations from adiabatic state of change the two formulations are equivalent. In Cartesian tensor form, eq. (7.72) becomes

$$\left[\frac{1}{a_0^2}\frac{\partial^2}{\partial t^2}-\frac{\partial^2}{\partial x_i^2}\right]p'=\frac{\partial}{\partial t}\left(\dot{\mathcal{M}}-\frac{\partial \rho_H'}{\partial t}\right)-\frac{\partial f_{v,i}}{\partial x_i}+\frac{\partial^2 \gamma_{ij}}{\partial x_i \partial x_j} \tag{7.73}$$

Considering a situation in which there are not deviations from adiabatic state of change, according to the two formulations, the Lighthill tensor accounts for the *instantaneous Reynolds stresses* (due to momentum transport) and viscous stresses. However, the viscous stresses are mainly important for the damping of sound waves, whilst their contribution for sound production is negligible as the ratio between inertia forces and viscous ones is of the order of the Reynolds number, which is generally very high.

Hence, summarizing, by the examination of the analytic expression of the three source terms, it is found that sound may be produced aerodynamically be means of three elementary mechanisms which are[72]:

i. *Monopole*: unsteady flow process which lead to a fluctuation of the mass in a fixed region of space (or to variation of the rate of change of mass, namely $\frac{\partial \dot{\mathcal{M}}}{\partial t} \neq 0$), as it happens for the pipe openings of internal combustion engines or for a loudspeaker embedded in a very large baffle. From what has been discussed before, this is the simplest and most efficient way of producing sound in fluid flows.
ii. *Dipole*: by forcing the momentum in a fixed region of space to fluctuate (or similarly to force to rate of change of mass flux to vary, namely $\frac{\partial f_{v,i}}{\partial x_i} \neq 0$), as it happens for a loud speaker. Such mechanism corresponds to a fluctuating external force acting on the fluid.
iii. *Quadrupole*: by forcing the net momentum flux across a fixed surface, namely $\frac{\partial(\rho V_i V_j)}{\partial x_j}$, to fluctuate, as it happens when sound is generate aerodynamically with no presence of solid boundaries.

This last source term is also known as Lighthill volume source as it has been first proposed by Lighthill in his aeroacoustic analogy[13]. In the following, the three sound generation mechanisms will be discussed, highlighting the relative importance of each for the sound production.

#### 7.3.1.1 Monopole source term

If a source of mass is present at some point of space, a generation term appear within the mass conservation law (at the right-end side) and, if the mass production fluctuate, that's equivalent to a sound source whose strength per unit of volume equal the rate of change of mass production itself, namely $\dot{q}(\boldsymbol{x},\mathrm{t})$. It therefore corresponds to the first source term in eq. (7.72), namely

$$\left(\frac{1}{a_0^2}\frac{\partial^2}{\partial t^2}-\nabla^2\right)p'(\boldsymbol{x},\mathrm{t})=\frac{\partial m}{\partial t}=\dot{q}(\boldsymbol{x},\mathrm{t}) \tag{7.74}$$

[72] A fluctuation of a quantity implies a non-constant value of its second order derivative.

where $m = \left(\dot{\mathcal{M}} - \rho'_H\right)$ is the mass production term (rate of mass introduction), due to mass injection and non-adiabatic state of changes, namely mass per unit volume per unit of time introduced at $\boldsymbol{x}$ and time instant $t$. According to the nomenclature introduced above, such source is the simplest acoustic source (monopole source) and, from a mathematical point of view, it does not involve spatial derivatives. As it is possible to appreciate from the above equation, it is also confirmed the previously mentioned statement according to which only the rate of change of mass introduction produces sound.

If the acoustic medium is unbounded and sources of mass are distributed around some point of the space, thanks to eq. (7.24), it is possible to express the total monopole field as superposition of monopoles, namely

$$p'(\boldsymbol{x}, \mathrm{t}) = \int_{\mathcal{V}_y} \frac{\dot{q}(\boldsymbol{y}, t_e)}{4\pi|\boldsymbol{x}-\boldsymbol{y}|} d\mathcal{V}_y \tag{7.75}$$

where $\boldsymbol{y}$ stands for the location of a single monopole source and $r$ represent the distance from that source. The quantity $\dot{q}$ is called source strength per unit of volume. If the source region is compact, the variation of the emission time over the sources is negligible ($r = x$) and the total monopole fields becomes

$$p'(\boldsymbol{x}, \mathrm{t}) = \frac{\dot{Q}(\boldsymbol{y}, t_e)}{4\pi x} \tag{7.76}$$

where $\dot{Q}(\boldsymbol{y}, \mathrm{t}_e) = \int_{\mathcal{V}_y} \dot{q}(\boldsymbol{y}, \mathrm{t}_e)\, d\mathcal{V}_y$ is called instantaneous source strength of the compact source region. This may be the case of most exhaust/intake mouths of internal combustion engines, whose characteristic dimension is generally about $2\,cm$. In fact, the monopole spectral components contribution of such systems is prominent a multiple of the engine orders, with a quite rapid decaying. Therefore, it is generally safe to assume that the prominent noise signal spreads until $2\,kHz$. Thus, it is easy to prove that the intake/exhaust mouth generally satisfies the compactness condition fairly enough. Considering the pulsating jet from a pipe opening[5], since the *free field* propagation has been assumed, the sound power radiated may be expressed as

$$W_M = \frac{p'^2}{\rho a_0} 4\pi x^2 = \frac{\dot{Q}^2}{4\pi\rho a_0} \tag{7.77}$$

being $x$ the radius of the wave front. It is important to highlight that the mass flow $m$ scales as $\rho U D^2$ (being $U$ the mean flow speed) and its time derivative $\dot{Q}$ differ by an additional factor $2\pi f$ as already seen by eq. (7.44). Consequently, it is possible to state that the acoustic power output from a monopole source scales as indicated by eq. (7.78)

$$W_M \propto \frac{\rho U^2 D^4 f^2}{a_0} \tag{7.78}$$

which links the power output to typical velocity, frequency, dimension of the source and constants of the medium. Equation (7.78) also shows that the acoustic power output from a monopole source scales as the Mach number. It is also confirmed that, for a given source strength, the radiated power scales as the square of the wavenumber.

### 7.3.1.2 Dipole source term

If a fluctuating external force is present at some point of space, a force per unit of volume term appears on the right-end side of the momentum conservation equation for an acoustic medium at rest. Such term correspond to an acoustic source per unit of volume, equal to the flux of force inwards $-\frac{\partial f_{v,i}}{\partial x_i}$[73]. It therefore corresponds to the second source term in eq. (7.72), namely

$$\left[\frac{1}{a_0^2}\frac{\partial^2}{\partial t^2} - \frac{\partial^2}{\partial x_i^2}\right] p'(\boldsymbol{x}, \mathrm{t}) = -\frac{\partial f_{v,i}}{\partial x_i} \tag{7.79}$$

where $f_{v,i}$ is the fluctuating external force per unit of volume acting on the fluid in the $i^{th}$ direction and $-\frac{\partial f_{v,i}}{\partial x_i}$ represents the source strength per unit of volume. According with the nomenclature introduced above, the corresponding sound field is a dipole field, since the source term involves spatial derivative of first order. In fact, in the limit as $l_i \to 0$, it corresponds to two equal and opposite simple sources of strength $\frac{f_{v,i}}{l_i}$, being $l_i$ the distance between them. For example, the term $-\frac{\partial f_{v,1}}{\partial x_1}$ in the source distribution corresponds to a simple source $\frac{f_{v,1}}{l_1}$ located at $(\bar{x}, y, z)$ and another one $-\frac{f_{v,1}}{l_1}$ located at $(\bar{x} - l_1, y, z)$, both constituting a dipole of strength equal to $f_{v,1}$ along the $x$ axis. So, the entire force field $\boldsymbol{f}_v$ correspond to a volume distribution of dipole sources, each having strength equal to $f_{v,i}$. Then, it is possible to state that a force field $\boldsymbol{f}_v$ produces sound as a volume distribution of dipoles, whose strength vector per unit of volume is $\boldsymbol{f}_v$, as schematically depicted in Figure 7.31.

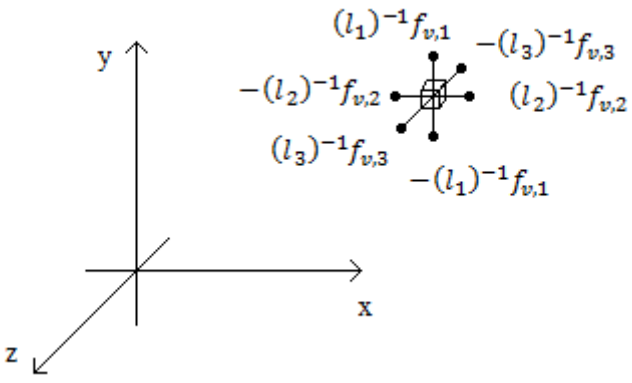


Figure 7.31 – Volume distribution of dipoles corresponding to a force field acting on the elementary volume $d\mathcal{V}_y$.

If the acoustic medium is unbounded and the dipole sources are distributed around some point of the space, thanks to eq. (7.40), it is possible to express the total dipole field as superposition of dipoles, namely

[73]In order to derive the wave equation, a divergence has been applied to the momentum conservation, resulting in a right-end side equal to $\int_{\mathcal{V}} \nabla \cdot \boldsymbol{f}_v \, d\mathcal{V} = \int_S \boldsymbol{f}_v \cdot \boldsymbol{n} \, dS$.

$$p'(\boldsymbol{x},\mathrm{t}) = -\int_{\mathcal{V}_y} \frac{\partial}{\partial x_i}\left[\frac{f_{v,i}(\boldsymbol{y},t_e)}{4\pi|\boldsymbol{x}-\boldsymbol{y}|}\right] d\mathcal{V}_y \tag{7.80}$$

where $\boldsymbol{y}$ stands for the location of a single dipole source which is identified by its center. Equation (7.80) shows explicitly that, although at any time instant the total source strength is zero $\left(f_{v,i}/l_i - f_{v,i}/l_i\right)$, at any point in space the sound field is not zero because the rays of sound, reaching such point at time $t$, were not emitted simultaneously by the simple sources (see Figure7.16). This is taken into account by the emission time appearing into the expression of the sound field. As it has already been described, the dipole field consists of two terms: one due to the derivative with respect to $r$, which falls off like the inverse square of the distance from the source (*near field* term), and another due to derivative of $f_{v,i}$ which falls off like the inverse first power of this distance (*far field* term). Therefore, at large distances from the source the *far field* term dominates the sound radiation, namely[74]

$$p'_{far\ field}(\boldsymbol{x},\mathrm{t}) = \int_{\mathcal{V}_y} \frac{(x_i - y_i)}{4\pi|\boldsymbol{x}-\boldsymbol{y}|^2} \frac{\partial f_{v,i}(\boldsymbol{y},t_e)}{\partial t} \frac{1}{a_0} d\mathcal{V}_y \tag{7.81}$$

For what it has been described when presenting a pure dipole field, since $\frac{\partial f_{v,i}(\boldsymbol{y},t_e)}{\partial t}$ differs from $f_{v,i}(\boldsymbol{y},t_e)$ by a factor equal to $2\pi$ times the considered frequency, the *near field* term is truly negligible if the distance from the source $|\boldsymbol{x}-\boldsymbol{y}|$ is greater than $(2\pi)^{-1}$ times the considered wavelength. If the source region is compact, then the variation of the emission time over it can be neglected and the term $x/|\boldsymbol{x}|^2$ may be placed out of the integral which is with respect to $y$. Since the *free field* propagation has been assumed, the sound power radiated may be expressed as[75]

$$W_D = \frac{\dot{f}_{v,i}^{\,2}}{\rho a_0} 4\pi x^2 = \frac{\dot{f}_{v,i}^{\,2}}{4\pi\rho a_0^3} \tag{7.82}$$

being $x$ the radius of the wave front. Considering the pulsating jet from a pipe opening[5], the external force $f_v$ is represented by the thrust that the flow exercises on the surrounding fluid, and it scales as $\rho U^2 D^2$ (being $U$ the mean flow speed) and its time derivative $\dot{f}_v$ differ by an additional factor $2\pi f$. Consequently, the acoustic power output scales as

$$W_D \propto \frac{\rho U^4 D^4 f^2}{a_0^3} \tag{7.83}$$

which links the power output to typical velocity, frequency and dimension of the source, apart from constants of the medium. Equation (7.83) also shows that the acoustic power output from a dipole source scales as the third power of the Mach number. By comparing eq. (7.78) and eq. (7.83), it is possible to obtain the following scaling law, that is

$$\frac{W_M}{W_D} = \frac{1}{M^2} \tag{7.84}$$

[74] $\frac{\partial f(\boldsymbol{y},t_e)}{\partial x} = -\frac{1}{a_0}\frac{\partial f(\boldsymbol{y},t_e)}{\partial t}\frac{\partial|\boldsymbol{x}-\boldsymbol{y}|}{\partial x} = -\frac{1}{a_0}\frac{\partial f(\boldsymbol{y},t_e)}{\partial t}\frac{(x-y)}{|\boldsymbol{x}-\boldsymbol{y}|}$.

[75] Even if it has been shown the directivity of the dipole field of Figure 7.17, consider the wave front as spherical for simplicity.

according to which, for subsonic flow, a monopole radiation is prominent with respect to a dipole radiation.

### 7.3.1.3 Quadrupole source term

When a fluctuating external stress system acts on some point in space, on the right-end side of the momentum conservation equation an additional fluctuating force per unit of volume appear and it is equal to the flux of stresses inwards, namely $F_{\gamma_{ij}}^{ext} = -\frac{\partial(\gamma_{ij})}{\partial x_j}$. Thus, in total analogy to what has been found for the dipole source, such stress system would produce sound as a dipole whose strength per unit of volume is equal to $F_{\gamma_{ij}}^{ext}$. In fact, such force per unit of volume corresponds to the third acoustic source term in eq. (7.72), which may be expressed as

$$\left[\frac{1}{a_0^2}\frac{\partial^2}{\partial t^2} - \frac{\partial^2}{\partial x_i^2}\right] p'(\boldsymbol{x}, \mathrm{t}) = \frac{\partial^2 \gamma_{ij}}{\partial x_i \partial x_j} \tag{7.85}$$

where $\gamma_{ij}$ is the Lighthill tensor acting on the equivalent acoustic medium at rest. However, according with the nomenclature introduced above, the corresponding sound field is a quadrupole field since the source term involves spatial derivative of second order. This is because, for example, the term $-\frac{\partial(\gamma_{i1})}{\partial x_1}$, actually corresponds to a dipole source $\frac{\gamma_{i1}}{l_1}$ located at $(\bar{x}, y, z)$ and another one $-\frac{\gamma_{i1}}{l_1}$ located at $(\bar{x} - l_1, y, z)$, both constituting a quadrupole source. From another point of view, the divergence of the Lighthill tensor $\frac{\partial(\gamma_{ij})}{\partial x_j}$ represents the resultant force in the $i^{th}$ direction per unit of volume acting on the elementary control volume $d\mathcal{V}$. However this resulting force is due to the combined action of two stresses in the $i^{th}$ direction acting on the surfaces whose normal is $n_j$ and $-n_j$ respectively, as schematized in Figure 7.32.

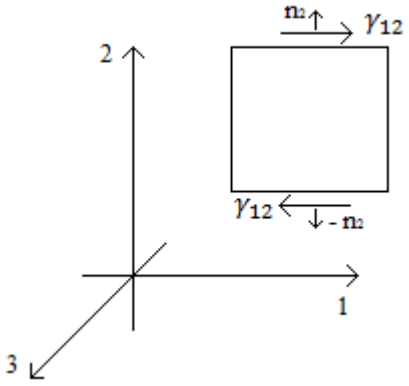


Figure 7.32 – Representation of the force per unit of volume due to the stress system $\gamma_{12}$.

The two forces per unit of volume $\pm\frac{\gamma_{ij}}{\varepsilon_j}$ constitute two acoustic dipoles. If such dipoles are equal and opposite, when $i \equiv j$ the quadrupole is called longitudinal, otherwise it is called lateral. It follows that each of the nine elements of the Lighthill tensor is a quadrupole whose strength is the scalar quantity $\gamma_{ij}$ with axes $i$ and $j$. Hence, there are three longitudinal quadrupoles, e.g. $\gamma_{11}$

having both axis along $x_1$, and three lateral quadrupoles, e.g. $2\gamma_{21}$ having the axes along $x_1$ and $x_2$ directions.

If the acoustic medium is unbounded and the quadrupoles are distributed around some point in space, thanks to eq. (7.40), it is possible to express the total quadrupole field as superposition of quadrupoles, namely

$$p'(\boldsymbol{x},\mathrm{t}) = \int_{\mathcal{V}_y} \frac{\partial^2}{\partial x_i \partial x_j}\left[\frac{\gamma_{ij}(\boldsymbol{y},t_e)}{4\pi|\boldsymbol{x}-\boldsymbol{y}|}\right] d\mathcal{V}_y \tag{7.86}$$

where $\boldsymbol{y}$ stands for the location of the single source. It must be noted that, the order between the spatial derivate and the integration can be interchanged because this latter is with respect with $\boldsymbol{y}$. Again, eq. (7.85) shows explicitly that, although at any time instant the total dipole strength is zero $\left(\frac{\gamma_{ij}}{\varepsilon_j} - \frac{\gamma_{ij}}{\varepsilon_j}\right)$, at any point in space $\boldsymbol{x}$ the sound field is not zero because the rays of sound, reaching such point at time $t$, were not emitted simultaneously by the dipoles.

Now, as it has been already seen, at distances far enough from the flow, such that $|\boldsymbol{x}-\boldsymbol{y}| \gg (2\pi)^{-1}\lambda$, the radiation of sound is only due to the *far field* term, namely

$$p'_{far\ field}(\boldsymbol{x},\mathrm{t}) = \int_{\mathcal{V}_y} \frac{(x_i-y_i)(x_j-y_j)}{4\pi|\boldsymbol{x}-\boldsymbol{y}|^3} \frac{1}{a_0^2} \frac{\partial^2[\gamma_{ij}(\boldsymbol{y},t_e)]}{\partial t^2} d\mathcal{V}_y \tag{7.87}$$

Equation (7.87) is the basic result of the Lighthill's aeroacoustic analogy. Again, if the source region is compact, then the variation of the emission time over it can be neglected and the term $x_i x_j/|\boldsymbol{x}|^3$ may be placed out of the integral which is with respect to $\boldsymbol{y}$.

From what above, the amplitude of the Lighthill tensor's fluctuations mainly scales as $\rho U^2$ (being $U$ the mean flow speed). However, since the *free field* propagation has been assumed, the acoustic power output is equal to[76]

$$W_Q = \frac{\varepsilon_i^2 \varepsilon_j^2 \ddot{\gamma}_{ij}^2}{16\pi^2 x^2 \rho a_0^5} 4\pi x^2 \tag{7.88}$$

and so it is necessary to relate the amplitude of $\gamma_{ij}$ to its second order time derivative. This latter differs by an additional factor equal to $(2\pi f)^2$. Since only fluctuations due to flow instability are taken into account, for a given frequency, the following relation holds[77] for $200 \leq R_e \leq 40000$

$$St = \frac{fL}{U} = 0{,}2 \tag{7.89}$$

It follows that, the second order time derivative of the Lighthill tensor scales as $\rho U^4/L^2$ and therefore, the whole pressure fluctuations expressed by eq. (7.87) are proportional to

[76] $\varepsilon_i = x_i/x$.

[77] Actually, for the particular case of flow around a long cylinder, the Strouhal number is equal to $0{,}198 - 3{,}9R_e^{-1}$ for $250 \leq R_e \leq 200000$[14].

$$\frac{1}{xa_0^2}\frac{\rho U^4}{L^2}L^3 = \frac{\rho U^4 L}{xa_0^2} \tag{7.90}$$

Hence, the acoustic power output scales as indicated by the following relation

$$W_Q \propto \frac{\rho U^8 L^2}{a_0^5} \tag{7.91}$$

which links the power output and typical velocity and dimension of the source, apart from constants of the medium. It is worth noting that the same result is found by means of the already discussed quadrupole power output expressed by eq. (7.59), namely

$$W_{quadrupole} \propto \frac{\rho^2 U^2 L^4}{\rho a_0}\omega^2\left(\frac{2\pi l}{\lambda}\right)^4 \propto \frac{\rho U^8 L^2}{a_0^5} \tag{7.92}$$

Equation (7.91) is known as $U^8$ law[13][3] and it also shows that the acoustic power output from a quadrupole source scales as the fifth power of the Mach numbers, which corresponds also to the efficiency of the aerodynamic sound generation. In fact, a steady flow has a kinetic energy roughly proportional to $\rho U^2 [J/m^3]$, so that the total rate of energy supply is $\rho U^2 (UL^2)$. So the acoustic efficiency, which is a measure of the kinetic energy's fraction converted in acoustic energy, would be

$$\eta_Q = \frac{acoustic\ power}{rate\ of\ kinetic\ energy} \propto M^5 \tag{7.93}$$

The $U^8$ law gives a very good agreement with experimental measurement of the acoustic power output for jet speed whose Mach number is low[3]. At higher Mach number, two phenomena must be taken into account which are a lower turbulence and the Doppler effect. The reduced turbulence level at high Mach number would make the acoustic power output following a $U^6$ law around $M = 1$. However, it is generally recognized that turbulent eddies move at half the jet speed within the atmosphere where they radiate so that, thanks to the Doppler effect, the wavelength of the forward emitted sound is reduced by a factor equal to $(1 - U_e/a_0)$, as schematically depicted in figure below.

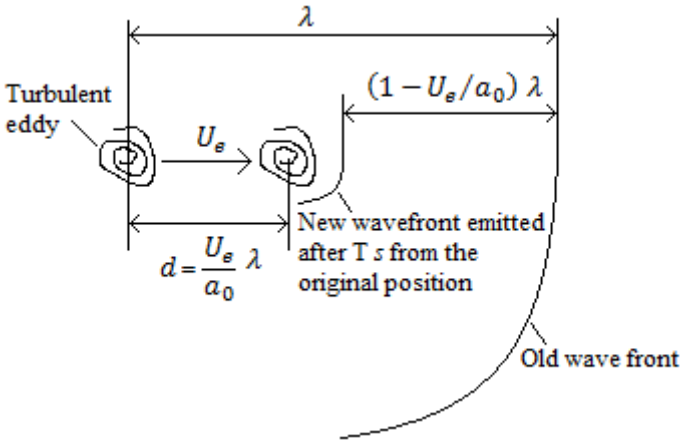


Figure 7.33 – Schematization of Doppler effect of moving eddies.

In particular, since the eddy is moving with velocity $U_e$, after one period of the considered frequency it will move of an amount equal to $d = U_e T = \lambda U_e / a_0$, with a consequence decreasing of the wavelength in the forward direction. Consequently, the Helmholtz number (or compactness ratio) increases restoring the $U^8$ law until about $M = 2$. Around this limit and at higher jet speeds, when the factor $U_e/a_0$ approaches unity[78], the wavelength of the emitted sound reduces without limitation, breaking down the compactness condition of the aerodynamic sources. As a consequence, it is like each eddy carries away its own wave front and the sound field is similar to that of a monopole source. Experimental observations have shown that the power output scales as $U^3$, as it is indicated by Figure 7.34.

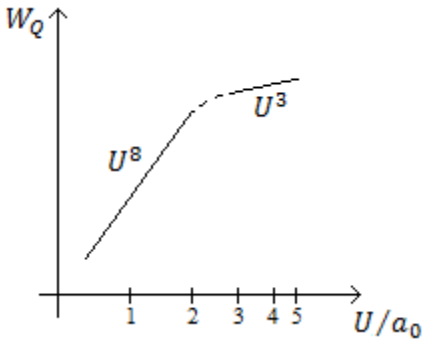


Figure 7.34 – Schematization of the $U^8$ law range of validity (both axis are intended in logarithmic scale).

In conclusion, by comparing eq. (7.78), eq. (7.83) and eq. (7.91) the following scaling law is obtained for the aerodynamic sound generation[5]

$$W_M : W_D : W_Q = 1 : M^2 : M^4 \tag{7.95}$$

which confirms the fact that for low Mach numbers, the monopole source is the most efficient sound generation mechanism.

From the above recalled theory of the aerodynamic generation of sound, it should be clear that, especially for the quadrupole radiation, the complete three-dimensional flow field must be resolved, in order to model the source region as an equivalent acoustic medium at rest. Consequently, it is necessary to take into account the effect of turbulence on the fluid flow and, therefore, the following pages are devoted to give an insight about turbulence modelling.

## 7.4 Introduction to turbulence modelling

In physics, a non-linear system is generally defined as a system in which the output is not directly proportional to the input, so that they may appear chaotic and unpredictable, in opposition to the much simpler linear systems. Mathematically, the evolution of a non-linear system is described by a set of equations in which the unknowns variables appear as a polynomial of degree higher than one. Non-linear problems are of great interest for engineers because most systems are inherently nonlinear in nature. However, sometimes a non-linear system may be considered as linear and the corresponding mathematical description may be linearized, meaning that the governing set of

[78] As just mentioned $U_e \cong U/2$.

equations may be approximated by a polynomial of first order in the unknown variable. This happens for example in linear structural dynamics, where the restoring forces (elastic and damping), due to external excitation, perturbing the equilibrium condition, are linearly dependent on displacement and velocity (at least in the limit of small perturbations)[8]. Fluid flow is an important example of non-linear system where small disturbances may grow rapidly, becoming unstable. However, when the disturbances are assumed to be very small, the system may still be assumed linear, as it happens in linear acoustic theory. As it will be clear in the following, the genesis of the turbulence is the intrinsic non-linearity of fluid flow system.

In spite of the fact that it is a very common phenomenon, there is no rigorous definition for turbulence although it is widespread recognized as a time-dependent chaotic behavior which is seen in many fluid flows. In fact, almost all fluid flows encountered in daily life are turbulent like, for example, the smoke rising from a cigarette, most of the terrestrial atmospheric circulation, flow conditions in many industrial equipment etc.. All these examples are characterized by the fact that, within the flow, many eddies of different size are easily recognizable during the motion. However, from a more rigorous point of view, in fluid dynamics a turbulent flow is a flow regime characterized by chaotic changes in fluid dynamic variables. In this framework, the first thing to mention is that, in contrast to laminar flow, turbulence is associated with high Reynolds numbers[79], where inertial forces dominate over the viscous ones. Moreover, despite there is no general definition for turbulent flow, it has a number of commonly encountered characteristics such as[9]:

- Turbulent flow is *irregular, random and chaotic*. The flow consists of a spectrum (as function of the turbulence wavenumber)[80] of different scales (eddy sizes), where largest eddies are of the order of the flow geometry (i.e. boundary layer thickness, jet width, etc.).
- Turbulent flow is *dissipative*, which means that kinetic energy of the flow is passed down from large eddies to smaller ones until the smallest (dissipative) eddies, in which it is converted into internal energy. This process, which leads to the energy dissipation, is called cascade process. The largest eddies extract their energy from the mean flow. The slightly smaller eddies receive the kinetic energy from the largest eddies and so on.
- Turbulent flow is *high diffusive* meaning that the spreading rate of boundary layers and jets increases. When flow is turbulent, particles exhibit additional transverse motion which enhances the rate of energy and momentum exchange between them.
- Turbulent flow occurs at *high Reynolds number*. For example, the transition from laminar to turbulent flow in pipes occurs at $Re_D \cong 2300$ whilst in boundary layers at $Re_x \cong 10^5$
- Turbulent flow is always *three-dimensional*.

Thus, the chaotic fluctuations of the velocity and other properties of the fluid are the main characteristic of turbulence, representing also the main difficulties encountered in the study of turbulent flows. In fully developed turbulent flows, the field properties become random functions of space and time and, in order to analyze them, it is commonly assumed that each property may be divided into a mean value and a fluctuating one.

[79] The Reynolds number is defined as the ratio of inertial to viscous forces during a fluid flow, namely $Re = \frac{\rho LV}{\mu}$.

[80] In the study of turbulence, the wavenumber is defined as $k = 2\pi/l$ where $l$ indicates the length scale of the considered vortex.

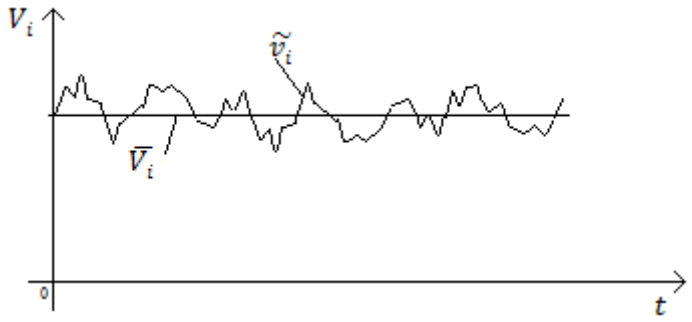


Figure 7.35 – Decomposition of a flow variable into its mean and fluctuating part in case of stationary flow.

Mathematically, when dealing with fully developed incompressible flow, for which the Newtonian fluid model is applicable, such condition may be expressed as

$$\begin{cases} V_i = \overline{V}_i + \tilde{v}_i \\ p = \bar{P} + \tilde{p} \\ \rho = \bar{\rho} \end{cases} \tag{7.96}$$

where the overbar indicates the average value and the fluctuating parts are defined such as their average value is zero[81]. This technique for decomposing the instantaneous motion in its average and fluctuating part is commonly referred as the so-called Reynolds decomposition[10]. It is important to highlight that when dealing with unsteady process the "average" means an ensemble average. Anyway, by substituting the result of the Reynolds decomposition in both the continuity and momentum equation (1.24) and (1.39), yields

$$\frac{\partial(\overline{V}_i+\tilde{v}_i)}{\partial x_i} = 0 \tag{7.97}$$

$$\rho\left[\frac{\partial(\overline{V}_i+\tilde{v}_i)}{\partial t} + \left(\overline{V}_j + \tilde{v}_j\right)\frac{\partial(\overline{V}_i+\tilde{v}_i)}{\partial x_j}\right] + \frac{\partial(\bar{P}+\tilde{p})}{\partial x_i} - \frac{\partial\left(\overline{\tau_{ij}}+\widetilde{\tau_{ij}}\right)}{\partial x_j} = 0 \tag{7.98}$$

In order to obtain the equations for the averaged motion, an averaging[82] operation is required which yields

$$\frac{\partial \overline{V}_i}{\partial x_i} = 0 \tag{7.99}$$

$$\rho\left[\frac{\partial \overline{V}_i}{\partial t} + \overline{V}_j\frac{\partial \overline{V}_i}{\partial x_j}\right] + \rho\left\langle\tilde{v}_j\frac{\partial \tilde{v}_i}{\partial x_j}\right\rangle + \frac{\partial \bar{P}}{\partial x_i} - \frac{\partial \overline{\tau_{ij}}}{\partial x_j} = 0 \tag{7.100}$$

where the brackets $\langle\cdots\rangle$ in the third term indicates averaging operation. Equation (7.100) may be rewritten in order to better understand the interpretation of the third term on the left-hand side. In particular by adding the term $\rho\left\langle\tilde{v}_i\frac{\partial \tilde{v}_j}{\partial x_j}\right\rangle$ which is equal to zero (as it may be seen by combining eq. (7.99) and (7.97)), yields

[81] If the considered field variable is $g$, then the fluctuating part is defined as $\tilde{\tilde{g}} = \frac{1}{T}\int_0^T \tilde{g}\ dt = 0$, being $T$ sufficiently higher than the duration of the fluctuation.

[82] Note that the operations of averaging and differentiation commute, i.e. the average of a derivative is the same as the derivative of the average.

$$\rho\left[\frac{\partial \overline{V_i}}{\partial t}+\overline{V_j}\frac{\partial \overline{V_i}}{\partial x_j}\right]+\frac{\partial \bar{P}}{\partial x_i}-\frac{\partial}{\partial x_j}\left(\overline{\tau_{ij}}-\rho\langle\widetilde{v_i}\widetilde{v_j}\rangle\right)=0 \tag{7.101}$$

First thing to note by the examination of the above equations is that the averaged motion satisfies the same form of the mass conservation equation for the instantaneous motion, as well as the fluctuating motion (consider the new added term in order to found eq. (7.101)), at least for the considered case of incompressible flows. On the other hand, the momentum equation for the average motion is different from the instantaneous one, since an additional fluctuating not-vanishing term appears, which is due, as it has already mentioned, to the intrinsic non-linearity of the system in force of the convective momentum transport. This term has the dimensions of a stress even it is not a stress at all, but simply a re-worked version of the fluctuating contribution to the non-linear acceleration terms. Consequently, it is generally assumed as an additional stress term due to turbulence (fluctuating velocities) and it is called the Reynolds stress tensor (or *Reynold stresses*), which is symmetric and represents the correlations between fluctuating velocities. So, from such brief discussion, it is clear that the turbulence problem arises from the non-linearity of the fluid system. In the limit as the amplitude of the disturbance would be infinitesmal, the additional stresses would vanish (involving products of infinitesimals), and the system of equations would be linearized, as it happens in the standard linear acoustic theory. However, in case of turbulence, the fluctuations continuously extract energy from the mean flow, making small disturbances to grow very quickly. When the amplitudes of the fluctuations can no longer be assumed infinitesimal, the Reynolds stresses cannot be neglected and, as a result, the base flow equations begin to be modified so that the solution to them can no longer be identical to the laminar flow from which it arose[10].

From a modelling point of view, the averaged equations are not closed as there are ten unknowns (three velocity components, pressure, six Reynolds stresses) and only four equations. The simplest idea useful to close the problem would be to write down a set of equations relating the Reynolds stress system to the mean flow field. Although an exact set of such equations has been find (which is called the Reynolds stress equation), unfortunately many new unknowns appear which makes the solution of the problem impossible. Therefore, in order to achieve the closure of the problem, a turbulence model is generally employed[9]. Thanks to the efforts spent during the recent years, a lot of alternatives are available but, however, the most adopted models for achieving industrial goals are represented by the two-equation models, thanks to which two further equations are derived which describe the transport of two scalar quantities related to turbulence. The very basis of such models is represented by a relation linking the Reynolds stress tensor to both the velocity gradients of the average motion and another parameter which is called eddy viscosity. Such relation is generally referred as Boussinesq assumption and may be expressed as[83]

$$\sum_i\sum_j \rho\langle\widetilde{v_i}\widetilde{v_j}\rangle=\sum_i\sum_j -\mu_T\left(\frac{\partial \overline{V_i}}{\partial x_j}+\frac{\partial \overline{V_j}}{\partial x_i}\right)+\frac{2}{3}\delta_{ij}\rho\,\tilde{k} \tag{7.102}$$

where $\mu_T$ stands for the so-called turbulent viscosity (or eddy viscosity). It is important to note that when the suffix $i$ and $j$ are equal, thanks to the conservation of mass, expression (7.102) gives

[83] Actually the general version of the Boussinesq assumption is $\rho\langle\widetilde{v_i}\widetilde{v_j}\rangle=-\mu_T\left(\frac{\partial \overline{V_i}}{\partial x_j}+\frac{\partial \overline{V_j}}{\partial x_i}\right)+\frac{2}{3}\left(\rho\tilde{k}+\mu_T\frac{\partial \overline{V_k}}{\partial x_k}\right)\delta_{ij}$, which coincides with eq. (7.102) in case of incompressible flow[13].

$$\rho\overline{\widetilde{v_1}\widetilde{v_1}} + \rho\overline{\widetilde{v_2}\widetilde{v_2}} + \rho\overline{\widetilde{v_3}\widetilde{v_3}} = 2\rho\tilde{k}$$

where $\tilde{k}$ is consequently defined as average turbulent kinetic energy[84]. Hence, thanks to the Boussinesq assumption, the Reynolds stress tensor is related to two new variables which are eddy viscosity and turbulent kinetic energy. This latter scalar quantity is one parameter on which a further transport equation is generally derived, in order to close the turbulence problem. As an example, in the following paragraph the most used transport equation will be derived which constitutes the basis of the well-known $k-\varepsilon$ turbulence model.

### 7.4.1 Reynolds Stress Equation

The starting point in the derivation of a transport equation for the turbulent kinetic energy is represented by the already mentioned Reynolds stress equation, which historically has been the primary focus for much of the turbulence modelling efforts[10]. It represents the momentum conservation equation for the fluctuating velocity, which may be obtained by subtracting the equation for the instantaneous velocity (7.98) and that of the average motion (7.100), namely

$$\rho\left[\frac{\partial\widetilde{v_i}}{\partial t} + \overline{V_j}\frac{\partial\widetilde{v_i}}{\partial x_j}\right] = -\frac{\partial\tilde{p}}{\partial x_i} + \frac{\partial\widetilde{\tau_{ij}}}{\partial x_j} - \rho\widetilde{v_j}\frac{\partial\overline{V_i}}{\partial x_j} - \rho\left(\widetilde{v_j}\frac{\partial\widetilde{v_i}}{\partial x_j} - \langle\widetilde{v_j}\frac{\partial\widetilde{v_i}}{\partial x_j}\rangle\right) \tag{7.103}$$

where the brackets $\langle..\rangle$ indicates again average quantities. Multiplying the above equation by $\widetilde{v_k}$ and averaging yields[85]:

$$\rho\left[\langle\widetilde{v_k}\frac{\partial\widetilde{v_i}}{\partial t}\rangle + \overline{V_j}\langle\widetilde{v_k}\frac{\partial\widetilde{v_i}}{\partial x_j}\rangle\right] = -\langle\widetilde{v_k}\frac{\partial\tilde{p}}{\partial x_i}\rangle + \langle\widetilde{v_k}\frac{\partial\widetilde{\tau_{ij}}}{\partial x_j}\rangle - \rho\langle\widetilde{v_k}\widetilde{v_j}\rangle\frac{\partial\overline{V_i}}{\partial x_j} - \rho\langle\widetilde{v_k}\widetilde{v_j}\frac{\partial\widetilde{v_i}}{\partial x_j}\rangle \tag{7.104}$$

Both indices $i$ and $k$ are free indices (which means that they are fixed in the equation) and therefore they can be interchanged to yield a second equation, namely

$$\rho\left[\langle\widetilde{v_i}\frac{\partial\widetilde{v_k}}{\partial t}\rangle + \overline{V_j}\langle\widetilde{v_i}\frac{\partial\widetilde{v_k}}{\partial x_j}\rangle\right] = -\langle\widetilde{v_i}\frac{\partial\tilde{p}}{\partial x_k}\rangle + \langle\widetilde{v_i}\frac{\partial\widetilde{\tau_{kj}}}{\partial x_j}\rangle - \rho\langle\widetilde{v_i}\widetilde{v_j}\rangle\frac{\partial\overline{V_k}}{\partial x_j} - \rho\langle\widetilde{v_i}\widetilde{v_j}\frac{\partial\widetilde{v_k}}{\partial x_j}\rangle \tag{7.105}$$

Thus, equations (7.104) and (7.105) can be added together to yield an equation for the Reynolds stress, that is

$$\rho\left[\frac{\partial\langle\widetilde{v_i}\widetilde{v_k}\rangle}{\partial t} + \overline{V_j}\frac{\partial\langle\widetilde{v_i}\widetilde{v_k}\rangle}{\partial x_j}\right] = -\left[\langle\widetilde{v_k}\frac{\partial\tilde{p}}{\partial x_i}\rangle + \langle\widetilde{v_i}\frac{\partial\tilde{p}}{\partial x_k}\rangle\right] + \left[\langle\widetilde{v_k}\frac{\partial\widetilde{\tau_{ij}}}{\partial x_j}\rangle + \langle\widetilde{v_i}\frac{\partial\widetilde{\tau_{kj}}}{\partial x_j}\rangle\right] - \rho\left[\langle\widetilde{v_k}\widetilde{v_j}\rangle\frac{\partial\overline{V_i}}{\partial x_j} + \langle\widetilde{v_i}\widetilde{v_j}\rangle\frac{\partial\overline{V_k}}{\partial x_j}\right] - \rho\left[\langle\widetilde{v_k}\widetilde{v_j}\frac{\partial\widetilde{v_i}}{\partial x_j}\rangle + \langle\widetilde{v_i}\widetilde{v_j}\frac{\partial\widetilde{v_k}}{\partial x_j}\rangle\right] \tag{7.106}$$

To the aim of better understand the nature of the various term involved in eq. (7.106), a little manipulation has to be done. More precisely it is possible to express the first term on the right-hand side as

$$\left[\langle\widetilde{v_k}\frac{\partial\tilde{p}}{\partial x_i}\rangle + \langle\widetilde{v_i}\frac{\partial\tilde{p}}{\partial x_k}\rangle\right] = -\langle\tilde{p}\left[\frac{\partial\widetilde{v_i}}{\partial x_k} + \frac{\partial\widetilde{v_k}}{\partial x_i}\right]\rangle + \frac{\partial\left[\langle\tilde{p}\widetilde{v_i}\rangle\delta_{kj} + \langle\tilde{p}\widetilde{v_k}\rangle\delta_{ij}\right]}{\partial x_j} \tag{7.107}$$

[84] $\tilde{k} = \frac{1}{2}\overline{\widetilde{v_1}\widetilde{v_1}} + \frac{1}{2}\overline{\widetilde{v_2}\widetilde{v_2}} + \frac{1}{2}\overline{\widetilde{v_3}\widetilde{v_3}}$ also called turbulent kinetic energy.

[85] The last term equals zero as the fluctuating components are per definition a zero average ones.

where the first term is generally labeled as pressure strain-rate term whilst the second one, which is a divergence term, is generally called pressure diffusion term. In the same way it is possible to express the second term on the right-hand side of eq. (7.106) as

$$\left[\langle\widetilde{v_k}\frac{\partial\widetilde{\tau_{ij}}}{\partial x_j}\rangle+\langle\widetilde{v_i}\frac{\partial\widetilde{\tau_{kj}}}{\partial x_j}\rangle\right]=-\left[\langle\widetilde{\tau_{ij}}\frac{\partial\widetilde{v_k}}{\partial x_j}\rangle+\langle\widetilde{\tau_{kj}}\frac{\partial\widetilde{v_i}}{\partial x_j}\rangle\right]+\frac{\partial[\langle\widetilde{\tau_{kj}}\widetilde{v_i}\rangle+\langle\widetilde{\tau_{ij}}\widetilde{v_k}\rangle]}{\partial x_j} \tag{7.108}$$

The last term on the right-hand side of eq. (7.106) may be expressed by means of the following relation

$$\frac{\partial\langle\widetilde{v_i}\widetilde{v_j}\widetilde{v_k}\rangle}{\partial x_j}=\langle\widetilde{v_k}\widetilde{v_j}\frac{\partial\widetilde{v_i}}{\partial x_j}\rangle+\langle\widetilde{v_i}\widetilde{v_j}\frac{\partial\widetilde{v_k}}{\partial x_j}\rangle+\langle\widetilde{v_k}\widetilde{v_i}\frac{\partial\widetilde{v_j}}{\partial x_j}\rangle \tag{7.109}$$

the last term being equal to zero since incompressible flow has been assumed. The final form of the Reynolds stress equation is

$$\rho\left[\frac{\partial\langle\widetilde{v_i}\widetilde{v_k}\rangle}{\partial t}+\overline{V_j}\frac{\partial\langle\widetilde{v_i}\widetilde{v_k}\rangle}{\partial x_j}\right]=\langle\tilde{p}\left[\frac{\partial\widetilde{v_i}}{\partial x_k}+\frac{\partial\widetilde{v_k}}{\partial x_i}\right]\rangle+\frac{\partial}{\partial x_j}\{-[\langle\tilde{p}\widetilde{v_i}\rangle\delta_{kj}+\langle\tilde{p}\widetilde{v_k}\rangle\delta_{ij}]+[\langle\widetilde{\tau_{kj}}\widetilde{v_i}\rangle+\langle\widetilde{\tau_{ij}}\widetilde{v_k}\rangle]-$$
$$\rho\langle\widetilde{v_i}\widetilde{v_j}\widetilde{v_k}\rangle\}-\rho\left[\langle\widetilde{v_k}\widetilde{v_j}\rangle\frac{\partial\overline{V_i}}{\partial x_j}+\langle\widetilde{v_i}\widetilde{v_j}\rangle\frac{\partial\overline{V_k}}{\partial x_j}\right]-\left[\langle\widetilde{\tau_{ij}}\frac{\partial\widetilde{v_k}}{\partial x_j}\rangle+\langle\widetilde{\tau_{kj}}\frac{\partial\widetilde{v_i}}{\partial x_j}\rangle\right] \tag{7.110}$$

where the first term is easy recognizable as the rate of change of the Reynolds stress following the mean motion. On the right-hand side the terms appearing are the pressure-strain rate, the turbulence transport (or divergence), the "production" and the "dissipation" respectively, as it will be clear in the following.

However, the prior goal was to find an equation for the kinetic energy and it can be done starting from the Reynolds stress equation. In fact, by contracting the subscripts $i$ and $k$ (which means equaling the indices and so considering the equation for the term $\frac{1}{2}\widetilde{v_i}\widetilde{v_i}=eq.\left(\frac{1}{2}\langle\widetilde{v_1}\widetilde{v_1}\rangle\right)+eq.\left(\frac{1}{2}\langle\widetilde{v_2}\widetilde{v_2}\rangle\right)+eq.\left(\frac{1}{2}\langle\widetilde{v_3}\widetilde{v_3}\rangle\right)$), yields

$$\left[\frac{\partial}{\partial t}+\overline{V_j}\frac{\partial}{\partial x_j}\right]\tilde{k}=\frac{\partial}{\partial x_j}\left\{-\frac{1}{\rho}\langle\tilde{p}\widetilde{v_i}\rangle\delta_{ij}+\frac{1}{\rho}\langle\widetilde{\tau_{ij}}\widetilde{v_i}\rangle-\frac{1}{2}\langle q^2\widetilde{v_j}\rangle\right\}-\langle\widetilde{v_i}\widetilde{v_j}\rangle\frac{\partial\overline{V_i}}{\partial x_j}-\frac{1}{\rho}\langle\widetilde{\tau_{ij}}\frac{\partial\widetilde{v_i}}{\partial x_j}\rangle \tag{7.111}$$

where $q^2=\widetilde{v_1}\widetilde{v_1}+\widetilde{v_2}\widetilde{v_2}+\widetilde{v_2}\widetilde{v_2}$. Equation (7.111) may be further simplified by firstly noting that, for an incompressible Newtonian fluid, the fluctuating part of the deviatoric Cauchy stress tensor may be expressed as

$$\widetilde{\tau_{ij}}=2\mu\,\widetilde{s_{ij}}=\mu\left(\frac{\partial\widetilde{v_i}}{\partial x_j}+\frac{\partial\widetilde{v_j}}{\partial x_i}\right) \tag{7.112}$$

It follows that the equation of transport of the turbulent kinetic energy may be rewritten as

$$\left[\frac{\partial}{\partial t}+\overline{V_j}\frac{\partial}{\partial x_j}\right]\tilde{k}=\frac{\partial}{\partial x_j}\left\{-\frac{1}{\rho}\langle\tilde{p}\widetilde{v_i}\rangle\delta_{ij}+2\upsilon\langle\widetilde{s_{ij}}\widetilde{v_i}\rangle-\frac{1}{2}\langle q^2\widetilde{v_j}\rangle\right\}-\langle\widetilde{v_i}\widetilde{v_j}\rangle\frac{\partial\overline{V_i}}{\partial x_j}-2\upsilon\langle\widetilde{s_{ij}}\frac{\partial\widetilde{v_i}}{\partial x_j}\rangle \tag{7.113}$$

where $\upsilon$ is the kinematic viscosity of the fluid. Moreover, it has already be seen that the deformation-rate tensor (see eq. (1.40)) may be decomposed in symmetric and antisymmetric part and so it is possible to rewrite the last term of eq. (7.113) as

$$\langle \widetilde{s_{ij}} \frac{\partial \widetilde{v_i}}{\partial x_j} \rangle = \langle \widetilde{s_{ij}} \widetilde{s_{ij}^*} \rangle + \langle \widetilde{s_{ij}} \widetilde{s_{ij}} \rangle = \langle \widetilde{s_{ij}} \widetilde{s_{ij}} \rangle$$

since the product of a symmetric and an antisymmetric part of a tensor is equal to zero. Hence, the final form of the turbulent kinetic energy transport equation is

$$\left[\frac{\partial}{\partial t} + \overline{V}_j \frac{\partial}{\partial x_j}\right] \tilde{k} = \frac{\partial}{\partial x_j}\left\{-\frac{1}{\rho}\langle \tilde{p}\widetilde{v_i}\rangle \delta_{ij} + 2\upsilon \langle \widetilde{s_{ij}}\widetilde{v_i}\rangle - \frac{1}{2}\langle q^2 \widetilde{v_j}\rangle\right\} - \langle \widetilde{v_i}\widetilde{v_j}\rangle \frac{\partial \overline{V_i}}{\partial x_j} - 2\upsilon \langle \widetilde{s_{ij}}\widetilde{s_{ij}}\rangle \qquad (7.114)$$

thanks to which it is easier to explain the role of the various term which therein appear. In particular, the first term on the right-hand side, being a divergence term, represents the transport of kinetic energy in an inhomogeneous field due respectively to the pressure fluctuations, the turbulence itself, and fluctuations of the viscous stresses. The second term represents the primary means by which fluctuations extract energy from the mean flow and it is the "generation" of $\tilde{k}$. This may be readily seen by comparing eq. (7.114) with the transport equation for the kinetic energy of the average motion. Following the same procedure described above, starting from the equation for the average motion (7.101), the desired transport equation is obtained, namely

$$\left[\frac{\partial}{\partial t} + \overline{V}_j \frac{\partial}{\partial x_j}\right] \overline{K} = \frac{\partial}{\partial x_j}\left\{-\frac{1}{\rho}\langle PV_i\rangle \delta_{ij} + 2\upsilon \langle S_{ij}\overline{V_j}\rangle - \frac{1}{2}\langle \widetilde{v_i}\widetilde{v_j}\rangle \overline{V_i}\right\} + \langle \widetilde{v_i}\widetilde{v_j}\rangle \frac{\partial \overline{V_i}}{\partial x_j} - 2\upsilon \langle S_{ij}S_{ij}\rangle \qquad (7.115)$$

where $\overline{K} = \frac{1}{2}\overline{V_i}\overline{V_i}$. The first thing to note is that each term has its counterpart in the equation for the average fluctuating kinetic energy. Moreover, the term $\langle \widetilde{v_i}\widetilde{v_j}\rangle \frac{\partial \overline{V_i}}{\partial x_j}$ appears in the equations for the kinetic energy of both the mean motion and the fluctuations. It follows that, whatever is the effect of such term on the kinetic energy of the mean motion, the corresponding effect on the kinetic energy of the fluctuations will be the opposite. Therefore, it represents the mechanism through which energy is exchanged between average motion and turbulence.

Finally, the last term in the equation for the turbulent kinetic energy has been already identified as dissipation term, or the rate of dissipation of the turbulence energy per unit mass. This may be explained by the fact that it is always positive, being the sum of the average of squared quantities[86], and therefore it causes a negative rate of change of kinetic energy. Physically, energy is dissipated because of the work done by the fluctuating viscous stresses in resisting deformation of the fluid material by the fluctuating strain rates (see the last term of the right-hand side of eq.(7.111)). In the following paragraph an insight on the $k-\varepsilon$ turbulence model, which is based on the transport equation of the turbulent kinetic energy, will be given.

### 7.4.2 $k-\varepsilon$ turbulence model

Once the physical interpretation of each term appearing in the transport equation of the turbulent kinetic energy has been introduced, it is necessary to formulate some assumption in order to achieve the closure of the turbulence problem. In fact, as it is possible to appreciate by the examination of the exact eq. (7.114), the turbulent kinetic energy is still related to turbulent quantities when instead, in order to be able to solve the average flow field, it should be dependent only on the average

[86] $\varepsilon = 2\upsilon \langle \widetilde{s_{ij}}\widetilde{s_{ij}}\rangle = 2\upsilon \left[\langle \frac{\partial \widetilde{v_i}}{\partial x_j} + \frac{\partial \widetilde{v_j}}{\partial x_i}\rangle \langle \frac{\partial \widetilde{v_i}}{\partial x_j} + \frac{\partial \widetilde{v_j}}{\partial x_i}\rangle\right]$.

motion. Consequently, the various term appearing in eq. (7.114) have to be related to average quantities. This circumstance is the basis of the most used approach for modelling turbulent flows in the industry, that is the $k-\varepsilon$ turbulence model[9][10]. Thus, it is necessary to relate each term of the right-hand side (divergence, production and dissipation term) to known quantities. However, to this aim it is necessary to make and argue on some assumption about the physics of turbulence. As a consequence, the goal is to find another version of the $\tilde{k}$ equation which is not exact anymore but modelled instead, where all the terms are related to average quantities.

Firstly, as indicated by the divergence term in the exact equation (7.114), the diffusive transport of fluctuating kinetic energy is accomplished thanks to the most intuitively physical transport related to the turbulence itself (and its three-dimensional peculiar behavior) and also by the acceleration of adjacent fluid particles due to both pressure and viscous stresses. In order to model such transport terms, the easiest idea is that these terms allow energy transport only from regions of higher to lower kinetic energy, which means to group all in one term proportional to the gradient of the turbulent kinetic energy, namely

$$-\frac{1}{\rho}\langle\tilde{p}\widetilde{v_i}\rangle\delta_{ij}+2\upsilon\langle\widetilde{s_{ij}}\widetilde{v_i}\rangle-\frac{1}{2}\langle q^2\widetilde{v_j}\rangle=\frac{\upsilon_T}{\sigma_k}\frac{\partial\tilde{k}}{\partial x_j} \tag{7.116}$$

where $\sigma_k$ is a constant which is termed turbulent Prandtl number. Moreover, within the production term, the Reynolds stress tensor is unknown and therefore it is modelled making use of the Boussinesq assumption, namely it is calculated as

$$-\langle\widetilde{v_i}\widetilde{v_j}\rangle\frac{\partial\overline{V_i}}{\partial x_j}=\upsilon_T\left(\frac{\partial\overline{V_i}}{\partial x_j}+\frac{\partial\overline{V_j}}{\partial x_i}\right)\frac{\partial\overline{V_i}}{\partial x_j}-\frac{2}{3}\delta_{ij}\tilde{k}\frac{\partial\overline{V_i}}{\partial x_j}=P_{\tilde{k}} \tag{7.117}$$

At the same time an expression for the turbulent viscosity $\upsilon_T=\mu_T/\rho$ has to be found, otherwise the introduction of such assumption would be useless. As per its definition, the dimension of the kinematic turbulent viscosity is $[m^2/s]$. The same dimension is found by multiplying both a turbulent length and velocity scale, that is[87]

$$\upsilon_T\propto Ul \tag{7.118}$$

The general turbulent velocity scale $U$ may be expressed as $\sqrt{\tilde{k}}$ so that

$$\upsilon_T=c_\upsilon\sqrt{\tilde{k}}\,l \tag{7.119}$$

where another quantity has been introduced which is still unknown, namely the turbulent length scale, and $c_\upsilon$ is an unknown constant. Obviously, there is a wide range of scales in turbulent flow and they are related to one another thanks to the so-called cascade process. This represent a phenomenological explanation of the process thanks to which the energy of the flow is dissipated by turbulence. As it has been already mentioned, the larger scales are of the order of the flow geometry, for example the boundary layer thickness. The kinetic energy of these eddies is passed down, by direct interaction, to slightly smaller scales. In this way, an energy transfer exists from the

[87] Within the algebraic models, in which the Reynolds stress tensor is calculated using only the first two terms appearing in the Boussinesq assumption, the relation for the turbulent kinematic viscosity is $\upsilon_T=l^2\nabla V$, where $l$ is a characteristic length.

large scales of the motion to the smaller ones until a sufficiently small length scale is reached, where there are too large frictional forces due to viscous stresses such that the kinetic energy is dissipated into internal energy[88]. Hence, a first rough approximation of the dissipated energy may be done referring to the larger velocity and length scales, i.e. $U$ and $l$. In fact, according to the cascade process hypothesis, the non-dissipative scales lose their energy during a time proportional to $l/U$, which is commonly referred as large eddy turn over time. It follows that the dissipation term may be thought as

$$\varepsilon \propto \frac{U^3}{l} = \frac{\tilde{k}^{3/2}}{l} \tag{7.120}$$

Thus the turbulent kinematic viscosity may be finally expressed as

$$\upsilon_T = c_\upsilon \frac{\tilde{k}^2}{\varepsilon} \tag{7.121}$$

Consequently, the final form of the modelled equation for the transport of turbulent kinetic energy is the following

$$\left[\frac{\partial}{\partial t} + \overline{V}_J \frac{\partial}{\partial x_j}\right] \tilde{k} = \frac{\partial}{\partial x_j}\left[\frac{\upsilon_T}{\sigma_{\tilde{k}}} \frac{\partial \tilde{k}}{\partial x_j}\right] + P_{\tilde{k}} - \varepsilon \tag{7.122}$$

in which two constants have been defined (and has to be found) and there is still the need to model the dissipation term. Well, in one equation models eq.(7.122) is the only one solved together with the conservation of mass and momentum, and the dissipation term is modelled as suggested by eq. (7.120). Then an algebraic expression is used to calculate the turbulent length scale, e.g. assuming it as proportional to some characteristic length of the flow under investigation. Intuitively, the main disadvantage of such modelling approach lies in the fact that there is not a unique valid expression for the turbulent length scale, which indeed depends on the type of flow itself. Consequently, an equation for the dissipation rate $\varepsilon$ is necessary and, although an exact equation may be derived (introducing many news unknowns), the following modelled equation is commonly adopted

$$\left[\frac{\partial}{\partial t} + \overline{V}_J \frac{\partial}{\partial x_j}\right] \varepsilon = \frac{\partial}{\partial x_j}\left[\frac{\upsilon_T}{\sigma_\varepsilon} \frac{\partial \varepsilon}{\partial x_j}\right] + P_\varepsilon - c_{2\varepsilon} \frac{\varepsilon^2}{\tilde{k}} \tag{7.123}$$

which historically has been obtained using physical reasoning in analogy with eq. (7.122). In fact, again the last two terms on the right-hand side represent the production and dissipation term respectively. The production term is expressed as

$$P_\varepsilon = c_{1\varepsilon} \frac{\varepsilon}{\tilde{k}} P_{\tilde{k}} \tag{7.124}$$

which leads to the final form of the modelled equation for the dissipation rate, namely

$$\left[\frac{\partial}{\partial t} + \overline{V}_J \frac{\partial}{\partial x_j}\right] \varepsilon = \frac{\partial}{\partial x_j}\left[\frac{\upsilon_T}{\sigma_\varepsilon} \frac{\partial \varepsilon}{\partial x_j}\right] + \frac{\varepsilon}{\tilde{k}}(c_{1\varepsilon} P_{\tilde{k}} - c_{2\varepsilon}\varepsilon) \tag{7.125}$$

[88] Of course, the friction forces exist at all scales but they are larger as the dimension of the eddies decreases due to the increase of the velocity gradient. Thus a very small fraction of energy is dissipated at each level and it is assumed that most of the energy is dissipated at the smallest scales.

where other three constants $\sigma_\varepsilon$, $c_{1\varepsilon}$ and $c_{2\varepsilon}$ have to be determined. Thus, eq. (7.122) and eq. (7.125) are the equations used for achieving the closure of the turbulence model in presence of incompressible flow. The values of the five unknowns constants are reported in table below.

| $c_\upsilon$ | $\sigma_{\tilde{k}}$ | $\sigma_\varepsilon$ | $c_{1\varepsilon}$ | $c_{2\varepsilon}$ |
|---|---|---|---|---|
| 0.09 | 1.0 | 1.3 | 1.44 | 1.92 |

Table 8 – Values of the constants for the $k-\varepsilon$ turbulence model.

These default values have been determined from experiments and they have been found to work quite well for a wide range of wall-bounded and free shear flows. The above described turbulence model has been firstly proposed by Launder and Spalding[13] and it is also known as standard $\mathrm{k}-\varepsilon$ turbulence model[11]. It has become the workhorse for many practical engineering flow calculations but, nevertheless, it has some limited predicting capabilities mainly due to the modelling of the transport of the dissipation rate. For these reasons, other two versions have been developed which are the RNG and realizable model.

The first has been developed using a statistical technique called re-normalization group (RNG) theory[12], in order to account for the effects of smaller scales of motion. In fact, in the standard $\mathrm{k}-\varepsilon$ model the eddy viscosity is determined from a single turbulence length scale (see eq.( 7.118)) and so the calculated turbulent diffusion is that which would occur only at the specified scale. However, in reality all scales of motion will contribute to the diffusive transport. Thus, the RNG approach results in a differential equation for turbulent viscosity and a modified form of the epsilon equation, in order to take into account how the effective turbulent diffusive transport varies with the effective Reynolds number (or eddy scale), thanks to changes in the production term[12]. It follows that, the RNG model allows to better handle low-Reynolds-number and near-wall flows. On the other hand, the realizable model contains an alternative formulation for both the turbulent viscosity and transport equation for the dissipation rate. The name realizable derives from the fact that this latter equation is based on the dynamic equation of the mean-square vorticity fluctuation, so that the model respects certain mathematical constraints on the Reynolds stresses, consistent with the physics of turbulent flows. The equation for the eddy viscosity is the same as eq. (7.121) apart from the fact that $c_\upsilon$ is not constant. The deeper study of the peculiarity of each model is left to more specific books.

## Bibliography


[1] Lighthill, M. J. (1952). "On sound generated aerodynamically. I. General theory". Proceedings of the Royal Society A. 211 (1107): 564–587, doi:10.1098/rspa.1952.0060.

[2] Lighthill, M. J. (1954). "On sound generated aerodynamically. II. Turbulence as a source of sound". Proceedings of the Royal Society A. 222 (1148): 1–32, doi:10.1098/rspa.1954.0049.

[3] J. L. Lumley, "Aerodynamic Generation of Sound", reference materials for the National Committee for Fluid Mechanics Films movie series, available at http://web.mit.edu/hml/notes.html .

[4] S. Sami, T. Carmody, and H. Rouse, "Jet diffusion in the region of flow establishment," Journal of Fluid Mechanics, vol. 27, pp. 231–252, 1967.

[5] M. Abom, "An Introduction to Flow Acoustics", Publisher: KTH-The Royal Institute of Technology, ISBN: ISRN/KTH/AVE/N-06/04-SE.

[6] Fine Acoustics Theoretical Manual, Release 5.2.3, July 2014.

[7] Russell DA, Titlow JP, Bemmen YJ. Acoustic monopoles, dipoles, and quadrupoles: An experiment revisited. Am J Phys. 1999;67:660–664.

[8] Krodkiewski, J. M. (2008), "Mechanical vibration", Melbourne: The University of Melbourne.

[9] L. Davidson, "An Introduction to Turbulence Models", Chalmers University of Technology, January 2003.

[10] William K. George, "Lectures in Turbulence for the 21st Century", Chalmers University of Technology.

[11] Bardina, J.E., Huang, P.G., Coakley, T.J. (1997), "Turbulence Modeling Validation, Testing, and Development", NASA Technical Memorandum 110446.

[12] Notes about turbulence modelling available at https://www.cfd-online.com/Wiki/K-epsilon_models .

[13] Ansys Fluent V. 14, Theory Guide, Ansys Inc., 2011.

[14] A. K. Ghosh, "INTRODUCTION TO MEASUREMENTS AND INSTRUMENTATION", Publisher: Prentice-Hall of India Pvt.Ltd, ISBN10: 8120346254.

# Chapter 8

# Geometric Optimization

## Introduction

In the present chapter several comprehensive analyses of the intake system under investigation are described. These are aimed to the enhancement of the acoustic attenuation properties in order to lower the gas-dynamic noise emissions. Some of the presented results derive from the preliminary studies corresponding to the following articles:

*Siano D., D'Agostino D., "Optimization of an intake acoustic behavior by geometry CAD modifications", presented at ATI 2015 Meeting "Internal Combustion Engines", Rome (Italy), September 9-11, 2015*

*Siano D., Aiello R., D'Agostino D., "Transmission loss assessment and optimization of an intake system for automotive application", International Journal of Mathematics and Computers in Simulation, Vol. 10, 2016, Pages 82-89, ISSN: 1998-0159*

In chapter 6, a gas-dynamic noise analysis of the air induction system under investigation has been presented. Both experimental and numerical outcomes have been compared, in order to achieve a second validation step of the three-dimensional purely acoustic model. Such aspect is particularly important within the design and optimization cycle of a system. In fact, once a realizable model exists which is capable of reproducing the response of the actual system, it is possible to numerically study the effect of whatever new geometric configuration on the acoustic properties.

On this idea, the acoustic performance of the studied system has been enhanced by means of geometrical modifications, and the results will be shown in the present chapter. In fact, on the basis of the previous performed Transmission Loss analysis, some new design configurations have been realized, to the aim of improving the noise attenuation characteristic. As it is schematized in Figure 8.1, the preliminary step in the above mentioned process is represented by the availability of an experimentally validated numerical model. Once such target is achieved, it is possible to execute a loop procedure in which it is possible to investigate the effect that several geometric changes have on the noise attenuation characteristics.

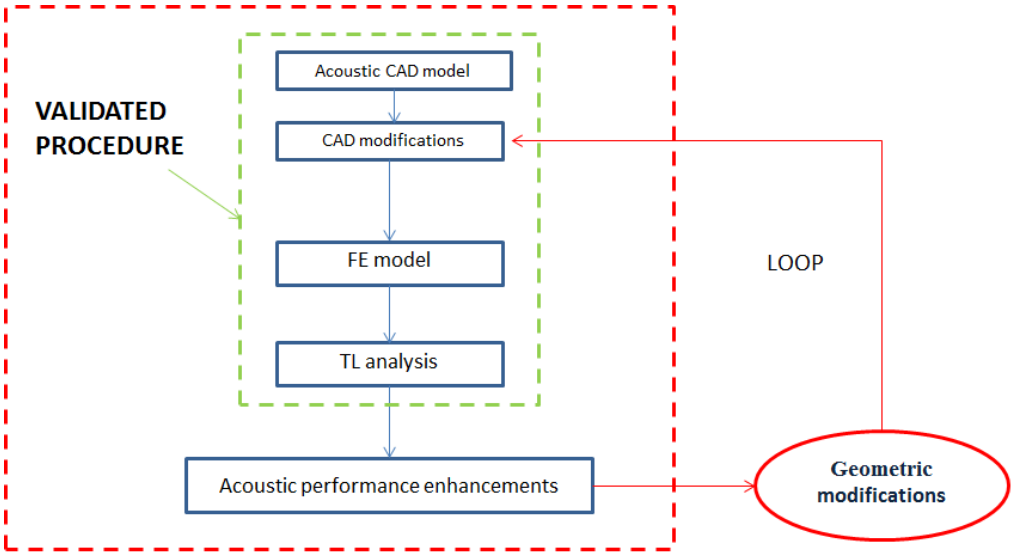


Figure 8.1 - Flow chart of the Transmission Loss enhancement analysis.

In general, at the current state of art, three ways exist for improving the sound attenuation within duct systems which rely on dissipative mechanisms, reflective mechanisms or noise cancelling mechanisms respectively. This latter is the most expensive one, as it directly relies on the use of an external sound source. Roughly speaking, the sound attenuation is realized by means of the installation, at certain point in the system, of internal speakers which produce a noise with a phase shift of $\pi$ radians with respect to the noise component to be deleted. This results in a sound attenuation, as schematically depicted in Figure 8.2.

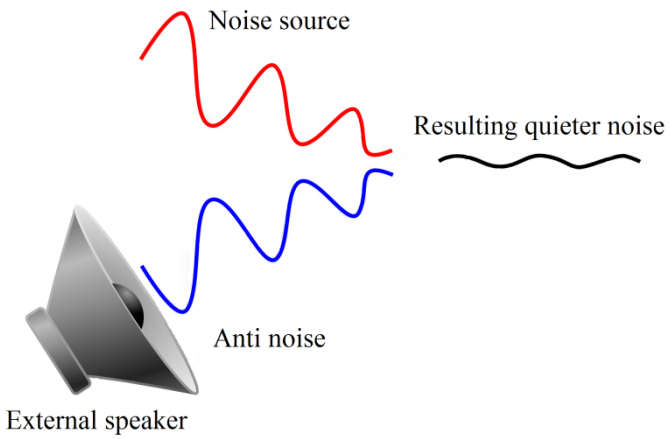


Figure 8.2 - Schematization of the noise active control methodology.

On the other hand, the use of sound dissipative mechanisms, such as insulation with porous material, is forbidden in intake systems as a considerable pressure loss may occur with a decrease in the volumetric efficiency. Hence, the choice is generally based on reflective related noise attenuation mechanisms. In this regards, the simplest way to improve the Transmission Loss of a system is represented by the project (ex novo) of external chambers which may act as acoustic resonators. In this framework, the most common choice is represented by both Helmholtz resonators and Quarter wavelength resonators. As already mentioned, an acoustic resonator is a very common element for duct systems which does not allow sound transmission downstream at

certain frequencies. In particular, when the excitation frequency equals the resonant frequency of the resonator, the acoustic impedance at the inlet section of the resonator equals zero, being the air inside the resonator comparable to a mass of a single degree of freedom system, vibrating and injecting acoustic energy into the duct system. This choice, despite the fact that is quite cheap and simple to realize, may result in a significant change of the original size of the system[1]. As an example, two air induction systems, for commercial vehicles, having acoustic resonators are reported in Figures 8.3 and 8.4.


Figure 8.3 - Engine bay a) and air induction system b) of the Toyota FT8.


Figure 8.4 - Engine bay a) and air induction system b) of a Hyundai vehicle.

As it is possible to appreciate from the above pictures, solutions which rely on the project of external resonators certainly do not save space in the engine bay. Consequently, alternatives of this type cannot be always pursued, especially for small size engines, due to some compactness requirements which must be respected. This is the case of the studied system, for which the engine bay is depicted in Figure 8.5.


Figure 8.5 - Engine bay hosting the studied system.

As it is possible to appreciate from the above photo, the available space for eventually realized modifications is close to zero. In such cases, the alternative is represented by a rearrangement of the available volumes, where and if possible. However, once several modifications have been tested, in terms of acoustic attenuation characteristics enhancement, another step must be taken before proceeding with the prototype creation and related experimental testing, since important aspects must be carefully considered.

Firstly, it is necessary to confirm that the eventually achieved goals in terms of Transmission Loss optimization are confirmed when dealing with the actual noise emissions. As already mentioned, the Transmission Loss analysis represents the stand-alone study of the system and, as such, it represents just a qualitatively assessment of its noise attenuation performances. To the aim of establishing the amount of noise, namely the "quantum", it is required a completely different approach which takes into account also the component of noise due to the turbulence inside the system, when this latter is coupled with the engine. Hypothetically, it could happen that the geometric change under consideration, although resulting in an increase of the Transmission Loss, may as well result in an increment of noise emissions due to an increase of turbulence inside the new system.

Secondly, but not less important, it is mandatory to take into account the effect of new configurations on the engine performances. In fact, a re-design of the air induction system may directly affects the power output and engine efficiency, as its prior task is to maximize the cylinders filling. As an example, it could happen that a new configuration resulting in a decrease of noise emission may result in significant increase of the pressure drop across the boundary of the system, with related decrease of the volumetric efficiency. Therefore, sometimes a trade-off between acoustic emissions and engine performances must be achieved and each of the new design configurations must be carefully investigated from many points of view.

In the following pages, the focus will be on the in depth investigation of three geometric changes, which have been realized on the previously validate acoustic model. The guidelines for the realization of such geometric modifications have been based on the well understood Transmission Loss trend, which has been very useful for understanding the influence of each parts the system consists of (expansion chambers, resonators etc.) on the frequency dependent noise attenuation characteristic. So, the focus will be on firstly improve the Transmission Loss within the low frequency range, where the noise signature is expected to be prominent. Then, subsequent gas-dynamic noise analyses, accounting for both noise contributions (namely engine pulses and flow noise) to

the overall acoustic emissions, will be presented in order to assess the effectiveness of the supposed modifications with respect to the amount of noise emitted in an engine condition, namely $2100\ rpm$ WOT, which has been judged to be critic. In fact, treating the intake system of a small size engine which is equipped on a city car, such rotational speed is the most commonly encountered in road-traffic conditions[89], whilst other rpm conditions are only representative of higher vehicle speeds when other, more prominent, noise sources are present such as road noise, aerodynamic noise etc.. Besides, the impact on the engine performances will be also evaluated. In the whole simulation process, namely CFD (1D\3D) and 3D FE acoustic model, the presence of the air filter has been neglected, on the basic idea that its influence is the same for each of the investigated system configurations. In this way it has been possible to overcome the 3D CFD modelling difficulties described in chapter 6.

## 8.1 Transmission Loss enhancement

In this paragraph it will be shown how the acoustic performance of the intake system depicted in Figure 5.5 has been optimized, in terms of its Transmission Loss, by means of several geometrical changes applied on the validated 3D FE model. It is worth noting that such model does not take into account the structural participation since, in chapter 5, it has been found that the system seems to be quite rigid in the investigated constraint conditions, which are even less constraining than those the air intake is subjected when mounted on the engine block (see Figure 5.40). This model has been validated by means of a comparison with available experimental data and therefore it is safe to assume that the effects of geometric changes (applied on the model) on the TL would be unaltered, if the system is actually modified. More precisely, the results of the numerical simulations have showed a fully satisfactory agreement with the experimental findings, demonstrating the potentiality of the numerical 3D acoustic model eventually to be used in optimization procedures.

The optimization loop merely follows the flow chart depicted in Figure 8.1, consisting of different modifications, applied to the original CAD model of the acoustic cavity (see Figure 5.16), with the aim of improving its acoustic performances within the investigated frequency range. In order to explain the logic behind the different CAD modifications, it is necessary to recall and understand how the original system acoustically works. To this aim, in the figure below the Transmission Loss in rigid wall configuration is depicted. The analysis has been executed within the range $[20;\ 2000]\ Hz$, with a frequency step equal to $10\ Hz$.

[89] Actually, road-traffic conditions correspond to low engine load. However, dealing with a VVA engine, the throttle is almost always completely open, the load control being regulated by the VVA system itself.

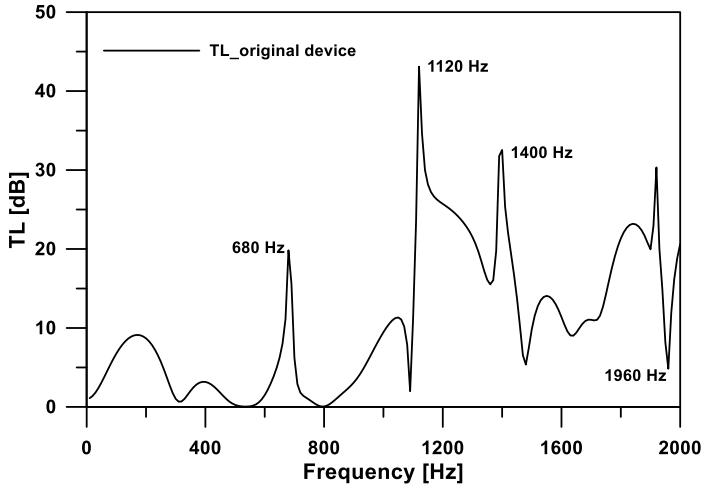


Figure 8.6 - Transmission Loss results in rigid wall configuration.

Such particular profile may be explained by the examination of the original geometry. As an example, the basic shape is similar to the Transmission Loss profile of two expansion chambers in series. This is particularly true in the low frequency region, say below $600\ Hz$, where there are no other influences on the TL profile, such as resonators. To prove that, in the figure below the Transmission Loss of two consecutive expansion chambers is depicted.

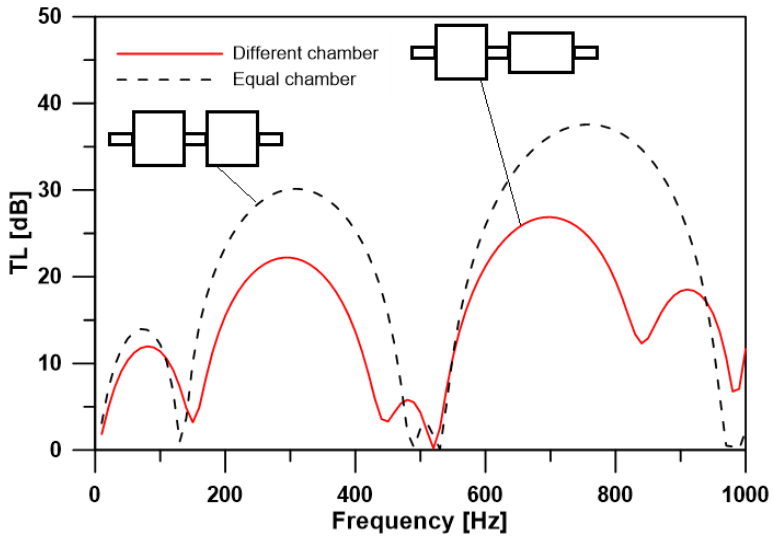


Figure 8.7 - Transmission Loss of consecutive expansion chambers.

From the above figure it is also important to note that there is a clear trend of the basic shape to be repeated with higher amplitudes, as the frequency is increased. The same kind of tendency is observable in the Transmission Loss profile of Figure 8.6. Such similarity is due to the fact that the system may be schematized as made of two main volumes which constitute, from an acoustic point of view, two expansion chambers with different cross section ratios and characteristics lengths. More precisely, the various elementary acoustic elements, which may be recognized within the air induction system, may be schematized as reported in figure below. All together form the total volume of the system which is equal to $4{,}636\ L$.

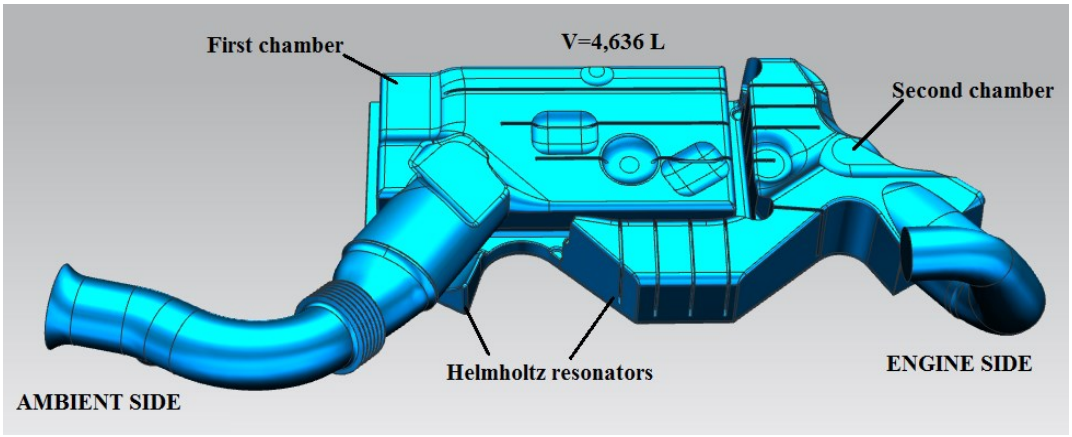


Figure 8.8 – Acoustic CAD model of the original system.

The frequency at which the two resonators work are easily recognizable from Figure 8.6. Here, as already pointed out, the two peaks located at 680 $Hz$ and 1120 $Hz$ are due to two cavities which indeed act as an Helmholtz resonators. To confirm that, in figure below the pressure distributions inside the system, at the two above mentioned frequencies, are depicted. Here the red and blue colors represent compression and rarefaction of the acoustic medium respectively, whilst the green color indicates the nodal points. Thus, thanks to the color map, it is possible to appreciate how the sound transmission is blocked in correspondence of the resonators.

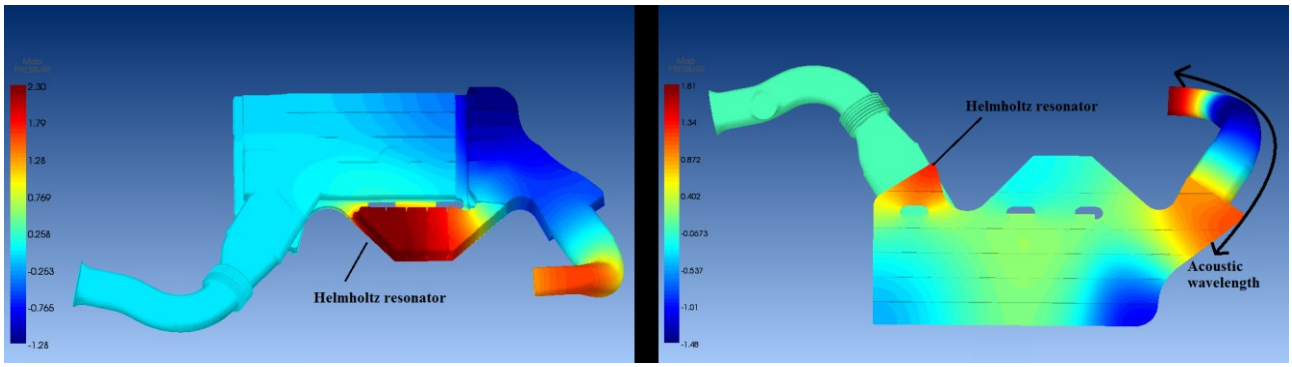


Figure 8.9 - Pressure distribution of the forced response analysis (TL) at a) 680 and b) 1120 Hz.

Moreover, it has also already been shown that the ninth acoustic mode at 1394 $Hz$ (see table 6[90]) is responsible for the peak in sound attenuation at 1400 $Hz$. Such evidence has been confirmed by the comparison of the pressure distribution at 1400 $Hz$ and that corresponding to the above mentioned acoustic mode (see Figure 5.37, chapter 5). The same explanation holds for the Transmission Loss peak located at 1960 $Hz$, where the response of the system is dominated by the nineteenth acoustic mode which occurs at 1954 $Hz$, as depicted in Figure 8.10. Here the color map is expressed in $dB$ scale, in order to highlight the nodal lines. So, red points correspond to maximum pressure oscillation, whilst green-like one indicates poor fluctuations.

[90] The resonant frequency of the ninth acoustic mode is slightly shifted because of the fact that table 6 makes reference to the modified cavity depicted in Figure 5.17 b).

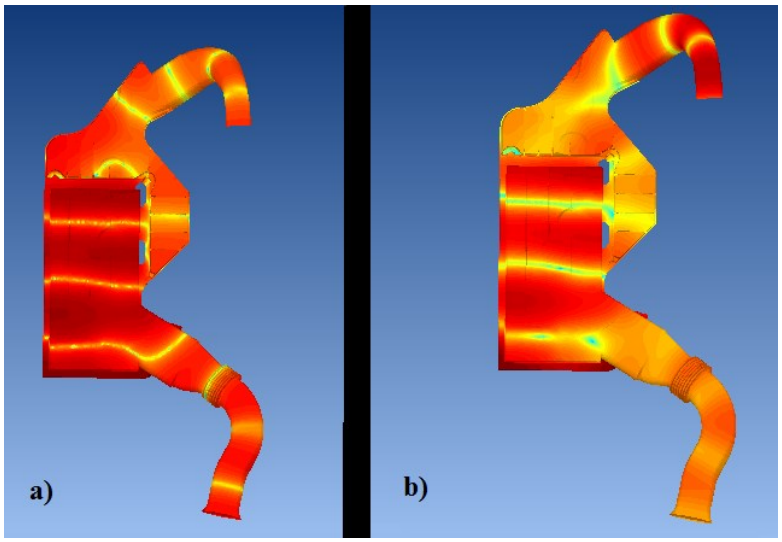


Figure 8.10 - Acoustic pressure distribution a) acoustic mode at 1954 Hz; (b) system response at 1960 Hz.

As it is possible to appreciate from the above picture, the pressure distribution at $1960\ Hz$ is such that almost the same magnitude of pressure oscillation occurs at the excitation port (on the top) with respect to the anechoic termination (at the bottom), justifying the low value of the Transmission Loss.

Once the acoustic behavior of the system has been fully investigated and understood, it has been possible to proceed with the realization of several CAD modifications, aimed to improve the sound attenuation properties. To this purpose, the focus is on the low frequency range, say below $1000\ Hz$, where the system seems to exhibit the lowest Transmission Loss. In fact, as it is evident from Figure 8.6, within the frequency range $[20;\ 1000]\ Hz$, the system seems to not ensure an high sound attenuation, being the average attenuation equal to $3{,}6\ dB$. This in principle may represent a critical conditions for systems like that, since it is expected that the most prominent noise sources radiate at multiple of the engine firing frequency which is, for example, equal to $92\ Hz$ at $5500\ rpm$ (see eq. (1)). However, it is important to recall that the actual attenuation is higher, especially at very low frequencies, since, when the air induction system is working, the energy associated with sound waves travelling toward the external ambient are partly reflected at the inlet mouth thanks to the external acoustic load represented by the radiation impedance. This latter, as it is already mentioned at the end of chapter 6, is responsible for a non-zero reflection coefficient with amplitude decreasing as the frequency increases. Nevertheless, the focus is on the low frequencies range as it is the most difficult to control.

Thus, the basic intent on the realization of the modifications has been to not modify the size of the original system. Consequently, the only possible guidelines for the modifications to be realized have to rely on parts of the foam material which is attached behind the system, as it is depicted in figure below. More precisely, such foam material is supposed to primarily act as a damper for the vibrations related to the engine block-intake system interaction, in order to lower the plastic-to-plastic impact related noise. However, if a more performant isolator could be used, which means more thin, part of the new volume available could be used to appropriately modify the air volume, in order to reach the desired acoustic performance enhancement. In particular, as it is highlighted in Figure 8.11, a lot a space could serve the purpose. However, it is very important to note that each of

the new design configurations of the intake system must be carefully examined, as every change in the volume available for travelling sound waves, directly affects the cavity modes and the corresponding resonant frequencies.

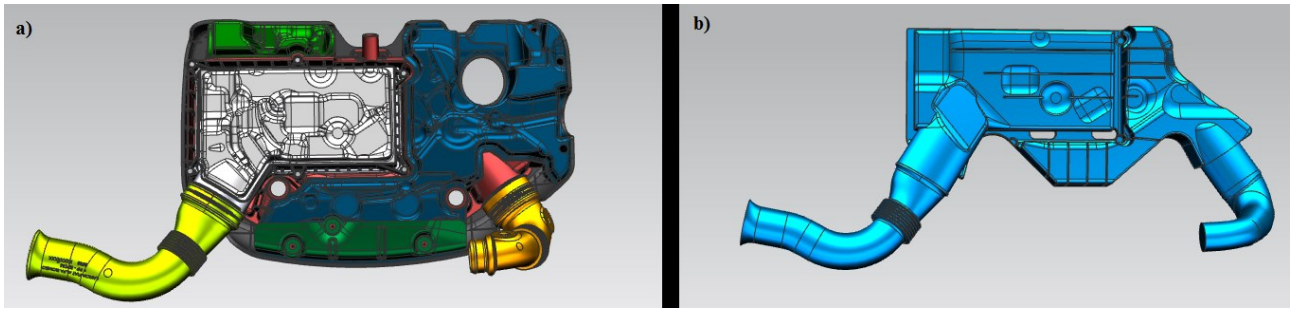


Figure 8.11 – CAD model comparison: a) structural and b) acoustic.

In this framework, as it is possible to appreciate from Figure 8.11 a), both white and blue colored foam material may be used in order to realize the desired CAD modifications. Thus the first CAD modification has relied on a re-design of the volume available within the filter box, considering part of the foam (colored in white within Figure 8.11 a)) there attached, as embedded in the acoustic medium. According to the schematization of the system, as mainly composed by two expansion chambers in series, such geometrical change would be equivalent in increasing the area ratio of the first chamber (refer to Figure 8.8). The resulting available volume within the air induction system is depicted in figure below, where it is compared with that of the original device.

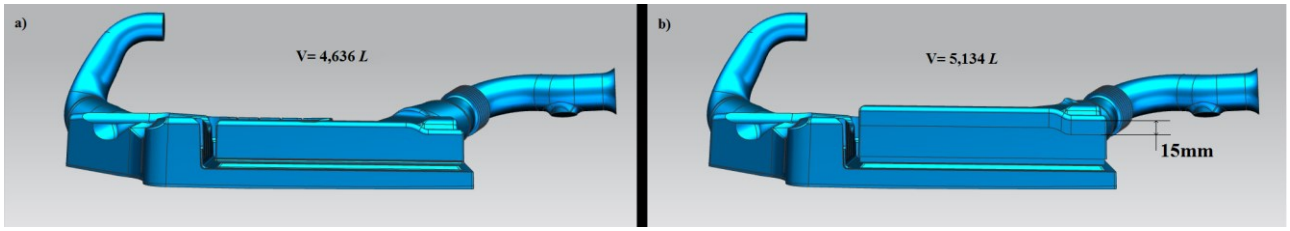


Figure 8.12 – CAD model comparison: a) Original device and b) first modification.

As it is possible to appreciate from the above figures, the applied modification to the filter box results in a slight increment of the total volume. In fact, by simply incrementing the height of the filter box of an amount equal to $1{,}5\ cm$, the total volume of the system changes from $4{,}636$ to $5{,}134\ L$, namely an increase of the $10{,}7\%$. Besides, the modification has been realized in a way such that the resulting volume is almost completely embedded within the foam, which is attached behind the filter box in its original configuration. Such circumstance is highlighted in figure below, where it is possible to appreciate that the CAD model of the foam material, which has been colored in white, is almost completely outside the new volume corresponding to the higher filter box.

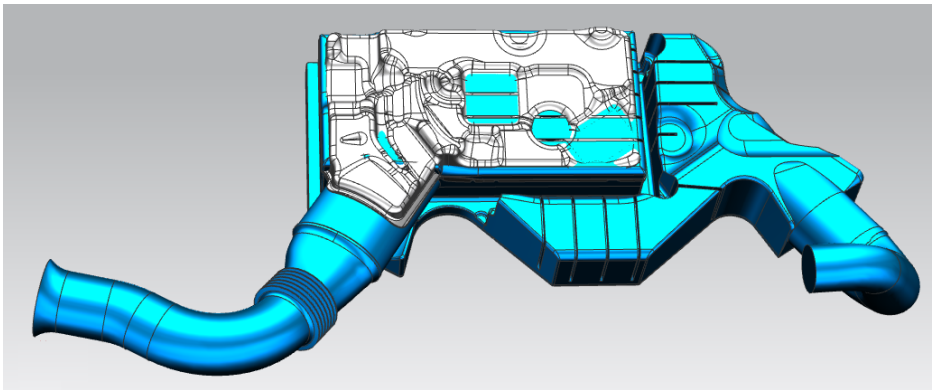

Figure 8.13 – CAD model comparison between the volume occupied by the foam (white) and the volume occupied by the first modification.

The corresponding acoustic mesh is depicted in figure below and it consists of 58797 solid elements (Tetra 10-noded) and 95499 nodes, allowing acoustic analysis until 5000 $Hz$ considering a spatial resolution of six points per wavelength.

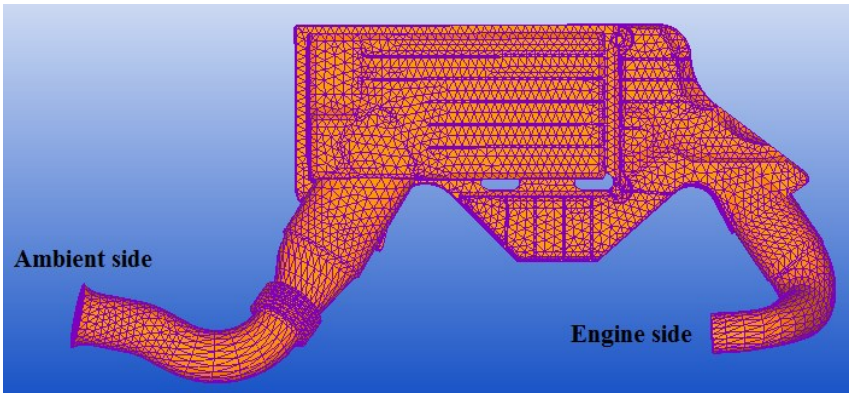


Figure 8.14 - Acoustic mesh corresponding to the first CAD modification.

By executing a Transmission Loss analysis of the system depicted in Figure 8.12 b), corresponding to the first geometrical modification, it is obviously expected that the position of the first two peaks occurring at 680 and 1120 $Hz$ will not change as they are due to resonators, whilst the position of the peaks located at 1400 and 1960 $Hz$ will probably change. This is reasonable since, as already proved above, the sharp values of the Transmission Loss achieved at these two frequencies are due to system's resonances. In fact, a change in the volume of the cavity will also probably change the acoustic natural modes and the corresponding natural frequencies. In Fig. 8.15, both the original and the new TL trends have been reported as function of frequency, where the black continuous and red dashed lines refer to the original and modified configuration of the system respectively. The analysis has been carried out within the range $[20;\ 2000]\ Hz$, with a frequency step equal to 10 $Hz$.

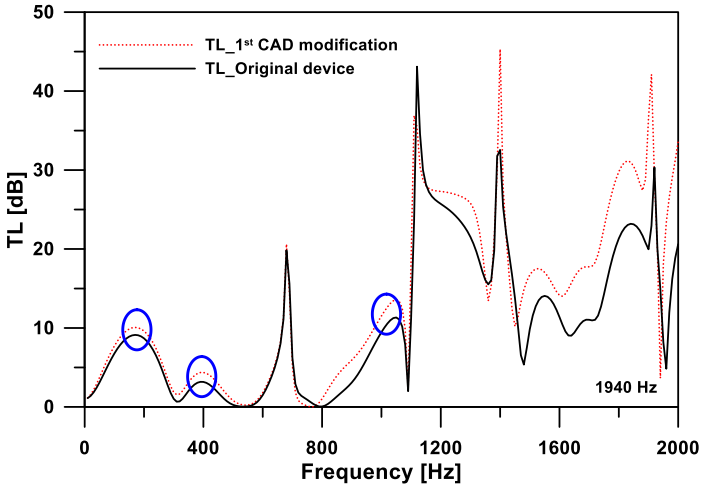


Figure 8.15 - Effect of the first CAD modification on the Transmission Loss.

As it has been expected, the sound attenuation of the new system is increased within the entire considered frequency range, as it is highlighted by the blue circles in Figure 8.15. This effect could be easily understood by recalling the analytic expression of the Transmission Loss for a single expansion chamber[3], namely:

$$TL = 10Log\left[1+\frac{1}{4}\left(\frac{S_c}{S_i}-\frac{S_i}{S_c}\right)^2 \sin^2\left(kl_c\right)\right] \tag{8.1}$$

where $S_c$ and $S_i$ are the cross sections of the chamber and inlet/outlet pipes, whilst $k$ is the wave number and $l_c$ in the chamber's length. Even if eq. (8.1) represents the analytic expression of the TL in the case of plane wave propagation, it is conceptually clear that increasing the area of the expansion chamber, the TL increases as well. From a purely acoustic point of view, this is justified by the fact that, increasing the cross section ratio will result in a stronger impedance mismatch and so stronger acoustic reflections at the chamber's interfaces. Moreover, as it is previously anticipated, the location of the first two peaks has not changed, whilst that of the second two peaks has changes. To confirm the above explanation, according to which such shift is due to a change in the natural frequencies, table 9 reports the natural frequencies of the first 19$^{th}$ acoustic modes for both original and modified device. It is worth noting the different natural frequencies for the original device with respect to those indicate in table 6 of chapter 5. This is due to the fact that, during the analyses of this chapter, the inlet and outlet tubes have not been modified as it has been done during the Transmission Loss analysis in chapter 5.

| Mode number | Resonant frequency $[Hz]$ Original device | Resonant frequency $[Hz]$ Firstly modified device |
|---|---|---|
| 1 | 233 | 239 |
| 2 | 326 | 319 |
| 3 | 474 | 477 |
| 4 | 642 | 645 |
| 5 | 675 | 675 |
| 6 | 781 | 781 |
| 7 | 879 | 864 |
| 8 | 1072 | 1078 |

| | | |
|---|---|---|
| 9 | 1124 | 1128 |
| 10 | 1159 | 1157 |
| 11 | 1351 | 1349 |
| 12 | 1394 | 1384 |
| 13 | 1439 | 1415 |
| 14 | 1533 | 1514 |
| 15 | 1625 | 1621 |
| 16 | 1723 | 1718 |
| 17 | 1783 | 1779 |
| 18 | 1908 | 1894 |
| 19 | 1954 | 1939 |

Table 9 - First 19th natural frequency of the acoustic cavities depicted in Figure 8.12.

As it is possible to appreciate from the table above, starting from the tenth natural mode, a clear negative frequency shift exists when the geometry is modified according to Figure 8.12 b), which confirm the explanation above. This in particular explains why the Transmission Loss curve depicted in red in Figure 8.15 has a small negative shift with respect to the black one starting from about $1300\ Hz$.

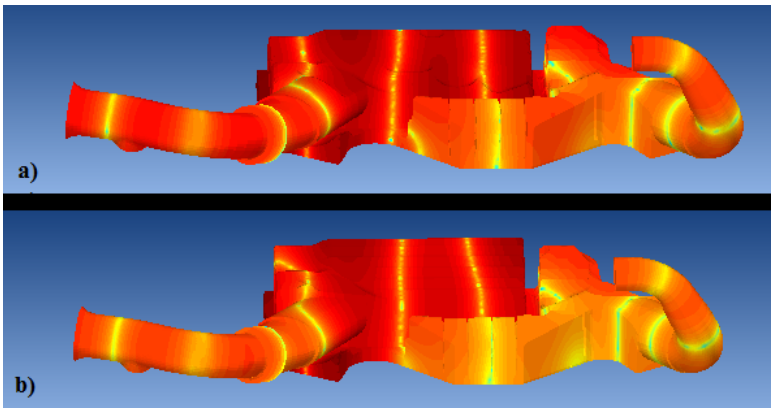


Figure 8.16 – 19th Acoustic mode comparison: a) Original device and b) first modification.

However, still a Transmission Loss value below $5\ dB$ within the range $[300;\ 600]\ Hz$ is achieved. This is not the best situation from an acoustic performance point of view, since within this range multiple of prominent engine orders may still appear in the noise signature (see Figure 6.14 in chapter 6). It follows that, another modification aimed to improve the acoustic attenuation in such frequency range would be necessary. Thus, it is possible to take into account another part of the foam attached to the original system (part of that depicted in blue within Figure 8.11 (a), in order to increase the volume of the cavity which is responsible for the peak around $680\ Hz$. This would certainly lower the critical frequency of the Helmholtz resonator, for which the greater the volume the lower the resonant frequency according to eq. (3.63)[3]. Thus, after this further geometry modification, the air volume embedded within the system should look as depicted in Figure 8.17.

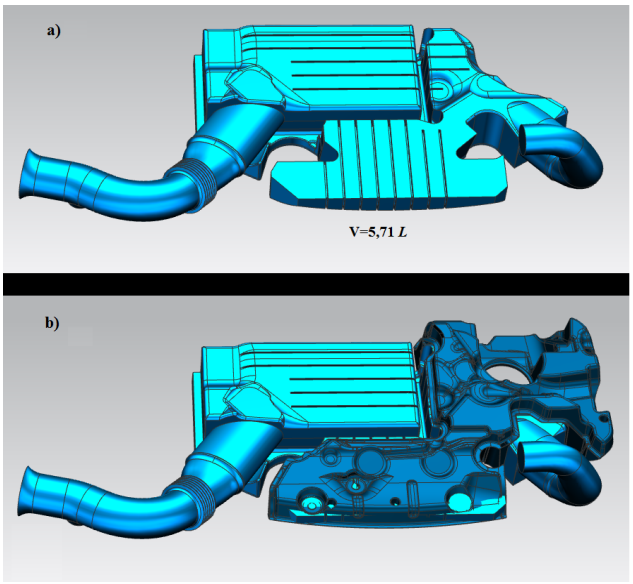


Figure 8.17 - Second CAD modification: increased volume of the resonator.

As it is possible to appreciate by the examination of the above figure, the volume of the new Helmholtz resonator is almost completely embedded within the foam which is attached behind the air box in its original configuration. The total volume of the system would reach $5{,}71\ L$, which corresponds to an increase of the $23\%$ with respect to the original size. The corresponding acoustic mesh is depicted in figure below and it consists of 64954 solid elements (Tetra 10-noded) and 105479 nodes, allowing acoustic analysis until $5000\ Hz$ considering a spatial resolution of six points per wavelength.

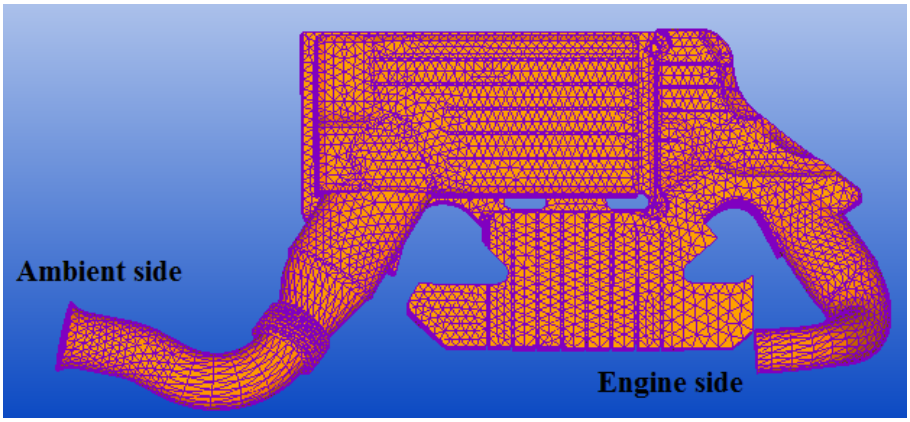


Figure 8.18 - Acoustic mesh corresponding to the second CAD modification.

The corresponding effect on the Transmission Loss profile is depicted in Figure 8.19, in which the black continuous and the red dashed lines refer to the original and modified geometry respectively. Even in this case the analysis has been carried out within the range $[20;\ 2000]\ Hz$, with a frequency step equal to $10\ Hz$.

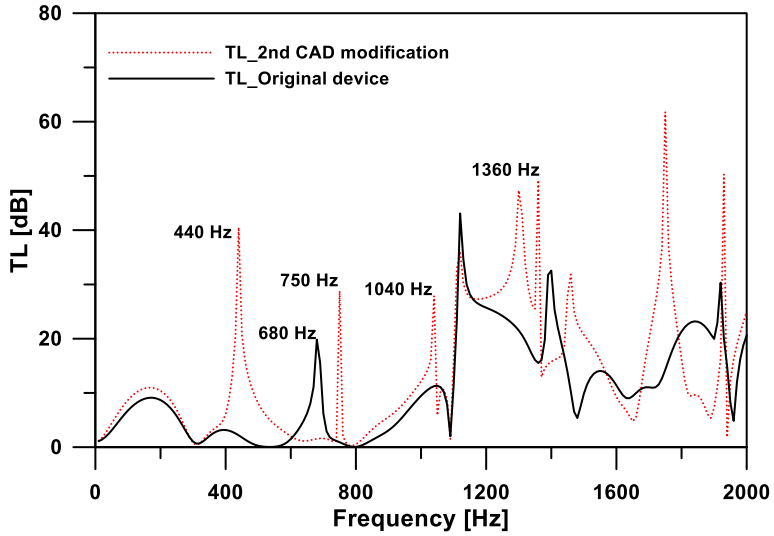


Figure 8.19 - Effect of the second CAD modification on the Transmission Loss.

As expected, the combined effect of the two CAD modifications has improved the TL in the low frequency range, e.g. 40,5 $dB$ at 440 $Hz$. More precisely, as highlighted in Figure 8.19, the peak due to the resonant cavity has moved from 680 to 440 $Hz$. Such behavior perfectly agrees with the analytic expression of the resonant frequency of an Helmholtz resonator, considering the different volumes highlighted in Figure 8.20. In fact, even if it is extremely difficult to exactly individuate the length and cross section of the resonator neck, as the whole three-dimensional geometry is very complex, the resonant frequency corresponding to the modification may be found by means of the knowledge of the volume of the cavity. Such information is reported in Figure 8.20, where it has been highlighted that the volume of the resonator has been increased from 0,383 to 0,957 $L$.

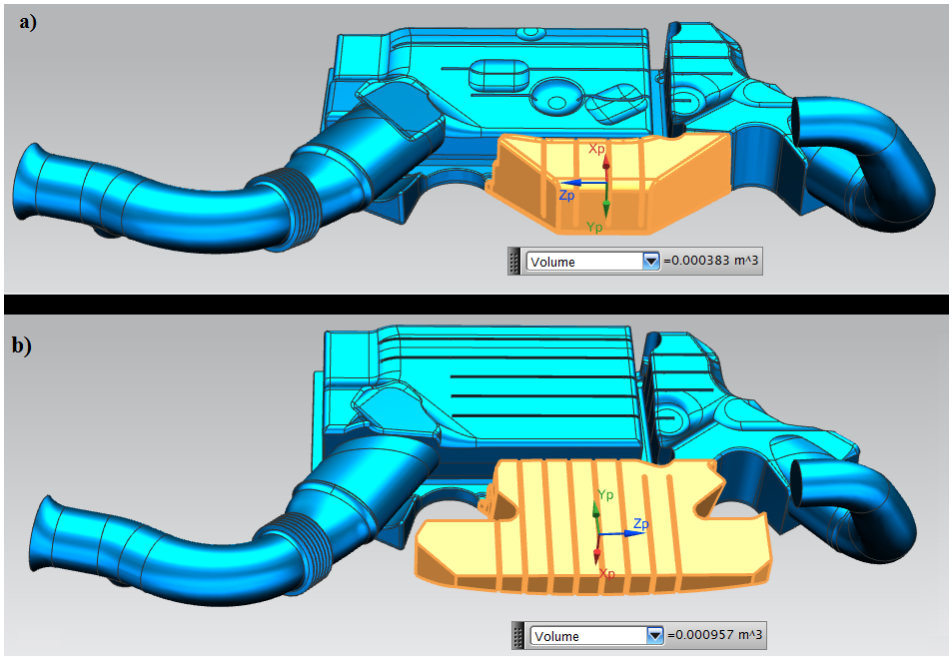


Figure 8.20 - Comparison between the volumes of the resonator: a) before and b) after the second CAD modification.

Thus, in the hypothesis that the acoustic length of the resonator's neck does not change when modifying the geometry, according to the analytic expression of the resonant frequency for an Helmholtz resonator, the new resonance would occur at

$$f_2 = \frac{a_0}{2\pi}\sqrt{\frac{S}{LV_1}}\sqrt{\frac{V_1}{V_2}} = f_1\sqrt{\frac{V_1}{V_2}} \cong 430\ Hz \tag{8.2}$$

where $a_0$ is the speed of sound, $V$ is the volume of the cavity whilst $S$, $L$ are the neck's cross section and length respectively. Obviously, the analytical result does not coincide exactly with the simulation finding, as a change in the shape would also affect the acoustical length of the cavity's neck. Moreover, as it has been expected, new peaks appear in the TL profile, since new cavity modes characterize the new configuration. As an example confirming such statement, in Figure 8.19 three peaks have been highlighted at $750$, $1040$ and $1360\ Hz$. The acoustic response at these frequencies are clearly influenced by the presence of cavity modes occurring at $747$, $1045$ and $1360\ Hz$ respectively, as indicated within the Figures below.

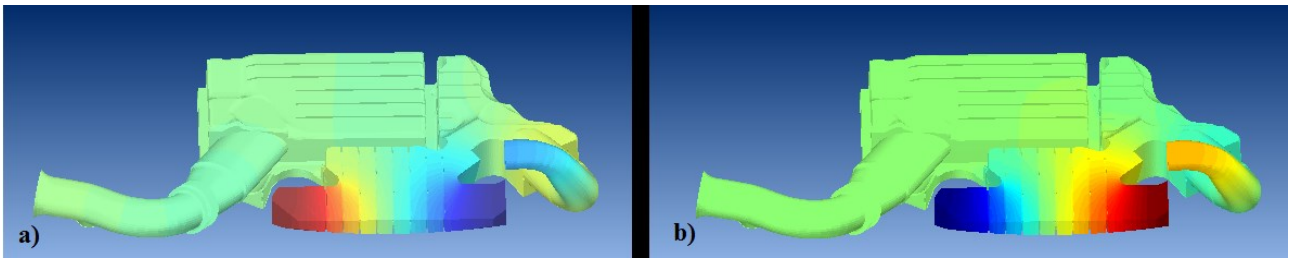


Figure 8.21 - Pressure distribution of a) the acoustic modes at 747 Hz and b) system response at 750 Hz.

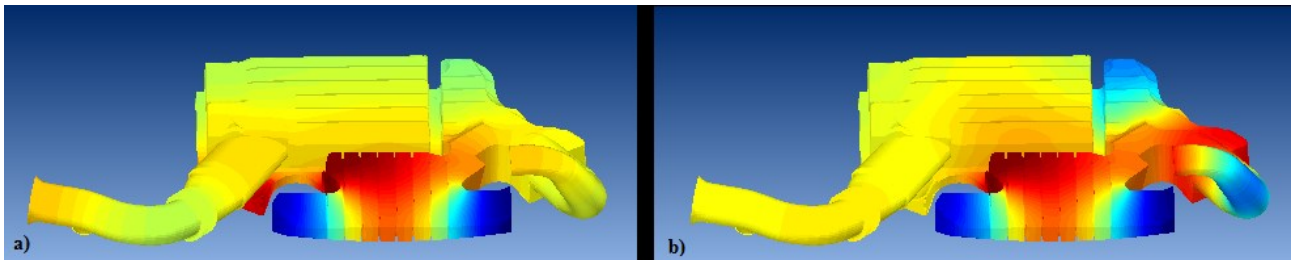


Figure 8.22 - Pressure distribution of a) the acoustic modes at 1045 Hz and b) system response at 1040 Hz.

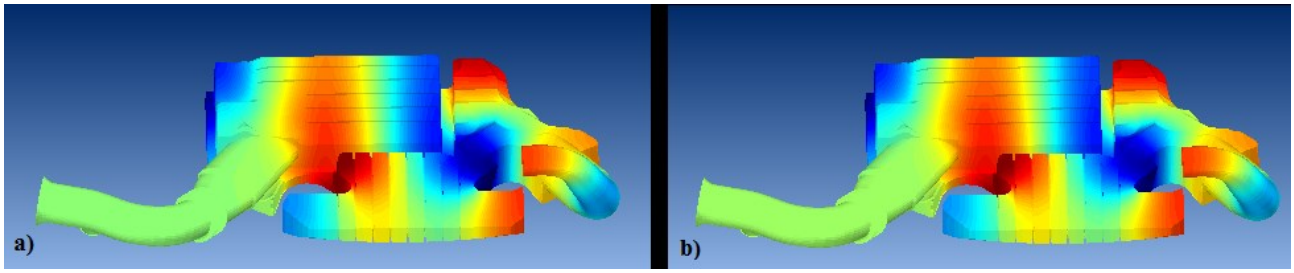


Figure 8.23 - Pressure distribution of a) the acoustic modes at 1360 Hz and b) system response at 1360 Hz.

In spite of the fact that the lowering of the resonant frequency of the main resonator ensure a better acoustic performance at low frequencies, a very poor attenuation holds so far in the frequency range $[600;\ 900]\ Hz$. In fact, within this range, only the very sharp peak occurring at $750\ Hz$ ensures sound attenuation. Therefore, a further geometrical modification might be necessary, which is

highlighted in Figure 8.24 a). Even in this case, the foam has still been used as the previous modifications to improve the volume of the air cavity. More precisely, such modification would increase the cross section ratio of the second volume indicated in Figure 8.8.

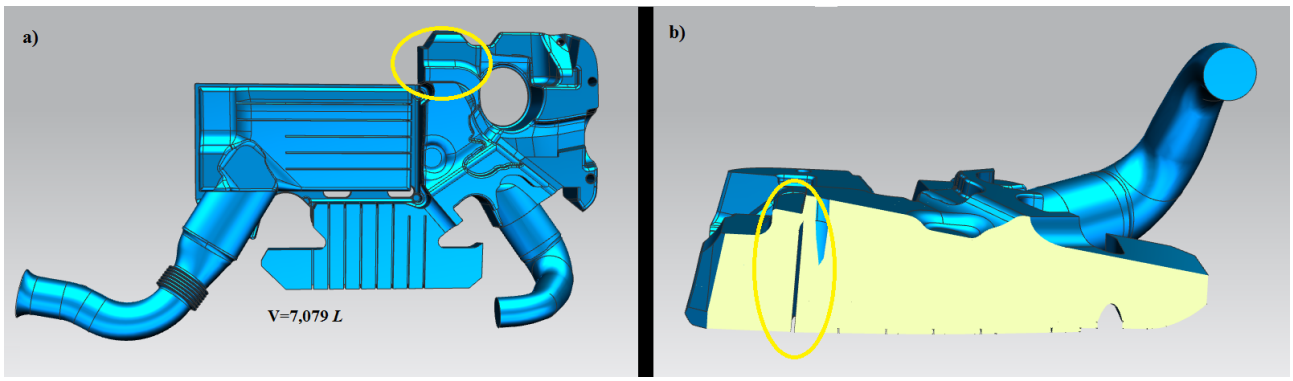


Figure 8.24 - Third CAD modification: Added volume to the outlet (engine side) chamber.

As it is possible to appreciate from the examination of the above figure, the foam has been attached to the air volume in a way such that the cavity, highlighted in Figure 8.24 a) by a yellow circle, would represent an additional resonator (see the separation within the yellow circle in Figure 8.24 b)). In figure below, the original CAD model of the foam has been compared with the volume of the acoustic system after the three modifications.

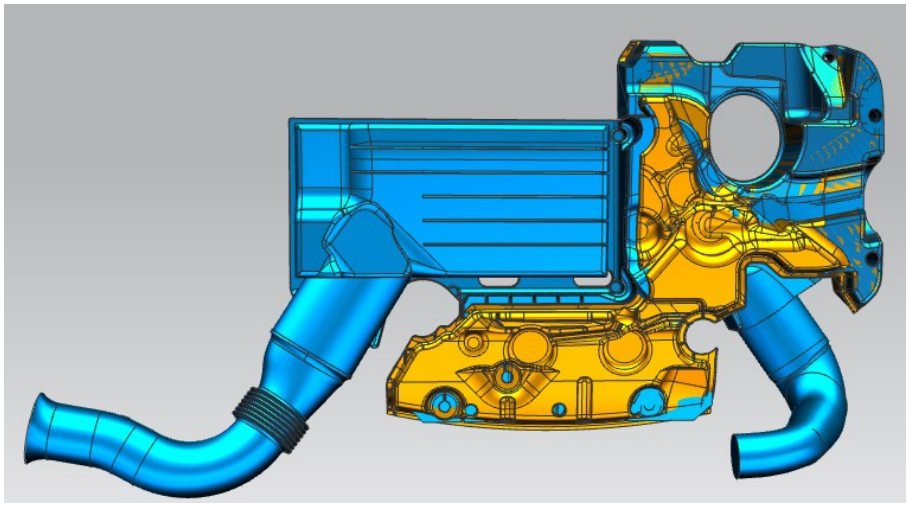

Figure 8.25 - Third CAD modification: Added volume to the outlet chamber.

As it is possible to appreciate by the examination of the above figure, even in this case the volume of the new air induction system is almost completely embedded within the foam which is attached behind the air box in its original configuration (depicted in yellow in the above figure). The total volume of the system reaches $7{,}079\ L$, which corresponds to an increase of the $52{,}7\%$ with respect to the original size. The corresponding acoustic mesh is depicted in figure below and it consists of 88143 solid elements (Tetra 10-noded) and 142207 nodes, allowing acoustic analysis until $5000\ Hz$ considering a spatial resolution of six points per wavelength.

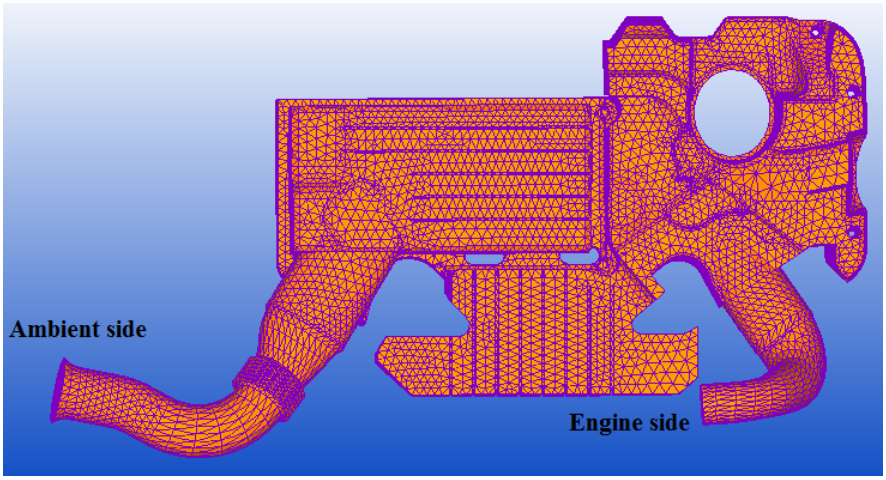


Figure 8.26 - Acoustic mesh corresponding to the third CAD modification.

The corresponding effect on the Transmission Loss is shown in Figure 8.27, where the black continuous line refers to the original device whilst the red dashed line to the modified system according to Figure 8.24. Even in this case the analysis has been carried out within the range $[20;\ 2000]\ Hz$, with a frequency step equal to $10\ Hz$.

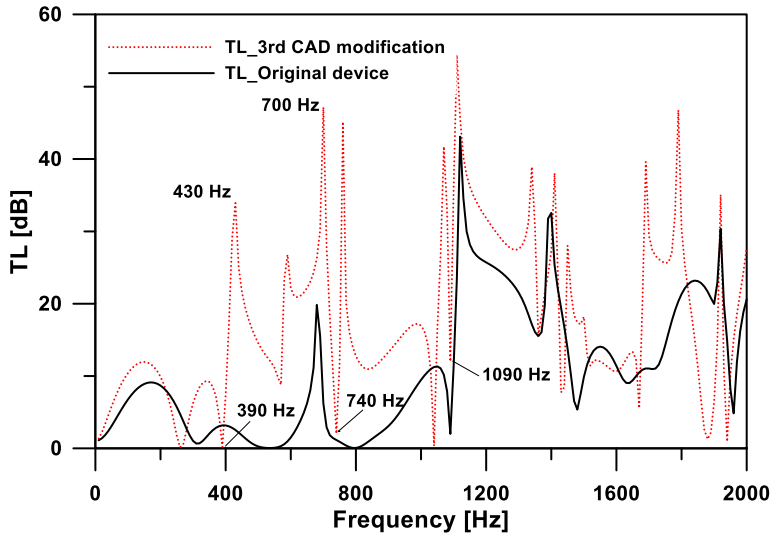


Figure 8.27 - Effect of the third CAD modification on the Transmission Loss.

As it is possible to point out from the above depicted curves, the last geometry change ensures a great increase in the acoustic performance of the intake system within the whole investigated frequency range. In particular, the main gain has been obtained within the range $[400;\ 1000]\ Hz$. In particular, the peak at $700\ Hz$ is due to the resonance of the new cavity, as it is possible to appreciate by the pressure distribution depicted in Figure 8.28.

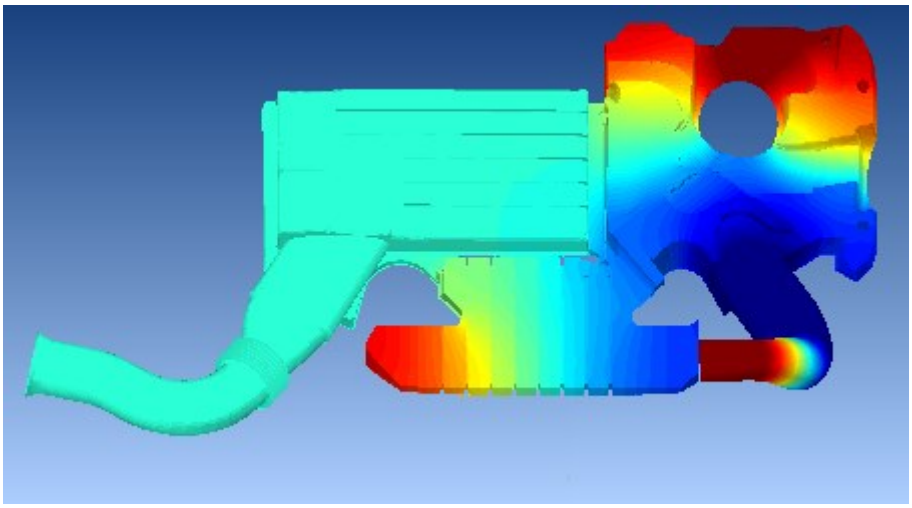

Figure 8.28 - Sound pressure distribution at 700 Hz.

Furthermore, as expected, the effect of the previously modified resonator is not changed, apart from a little frequency shift which makes the resonance occurring at $430\ Hz$ instead of $440\ Hz$. This may be probably due to a change radiation condition outside the resonator for which a different acoustical length characterizes the resonator's neck.

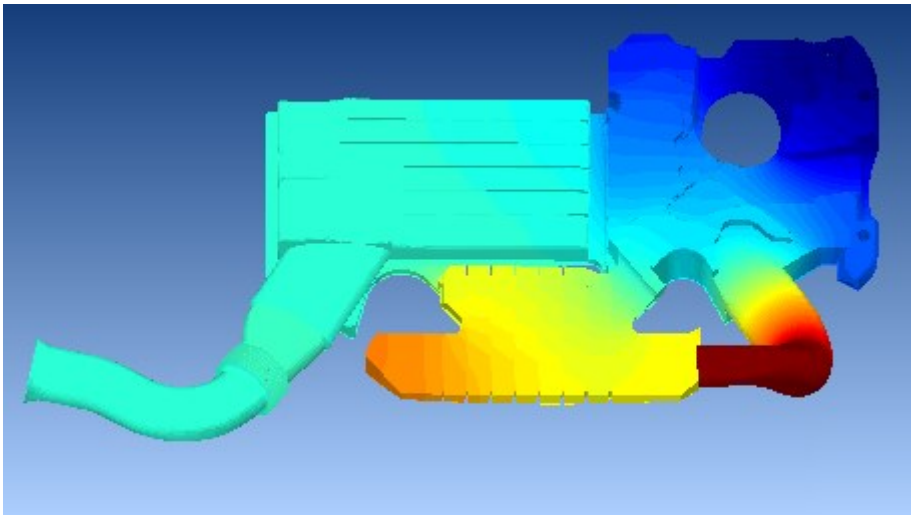

Figure 8.29 - Sound pressure distribution at 430 Hz.

However, there are still some frequencies at which the system does not work very well, e.g. at $390$ and $740\ Hz$, as it has been highlighted in Figure 8.27. Such behavior is easily explainable from the examination of the acoustic modes of the system in this new configuration. More precisely, after performing an acoustic modal analysis aimed to extract all the mode shapes until $2000\ Hz$, it has been found that the response of the system at the two mentioned frequencies is mainly influenced by the presence of two mode shapes, occurring at $394$ and $761\ Hz$ respectively. This is evident by the examination of Figures 8.30 and 8.31, where the pressure distributions of both acoustic mode and forced response, in the two cases, are depicted. The color map is expressed in $dB$ scale in order to highlight as much as possible the nodal lines.

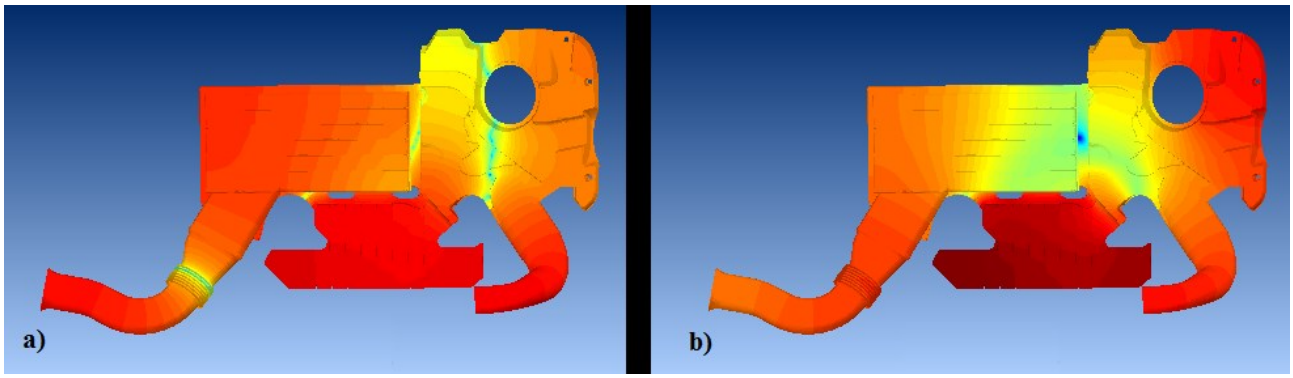


Figure 8.30 - Pressure distribution of a) the acoustic modes at 394 Hz and b) system response at 390 Hz.

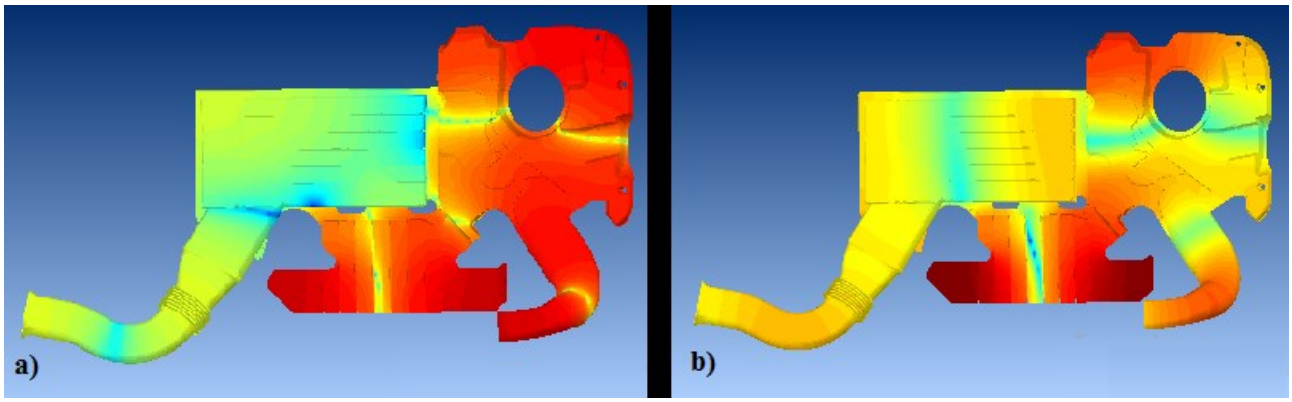


Figure 8.31 - Pressure distribution of a) the acoustic modes at 761 Hz and b) system response at 740 Hz.

As it is possible to appreciate from the contour plot of the above figures, both sound pressure distributions in correspondence of the two acoustic modes, clearly highlight almost the same magnitude at the inlet and outlet sections. Therefore, the low TL values at both $390$ and $740\ Hz$ are justified by the prominent influence of the two above depicted modes on the system's response. Thus, in spite of the fact that, at some frequency, the presence of new cavity modes lowers the sound attenuation characteristic, the Transmission Loss has been globally highly improved. Besides, as it is possible to appreciate by Figure 8.27, a lot of new peaks are present in the new TL profile, all occurring in correspondence of new natural modes. As an example, the response of the system at $1090\ Hz$ is due to the presence of a cavity mode occurring at $1091\ Hz$, as it is possible to appreciate from the figure below.

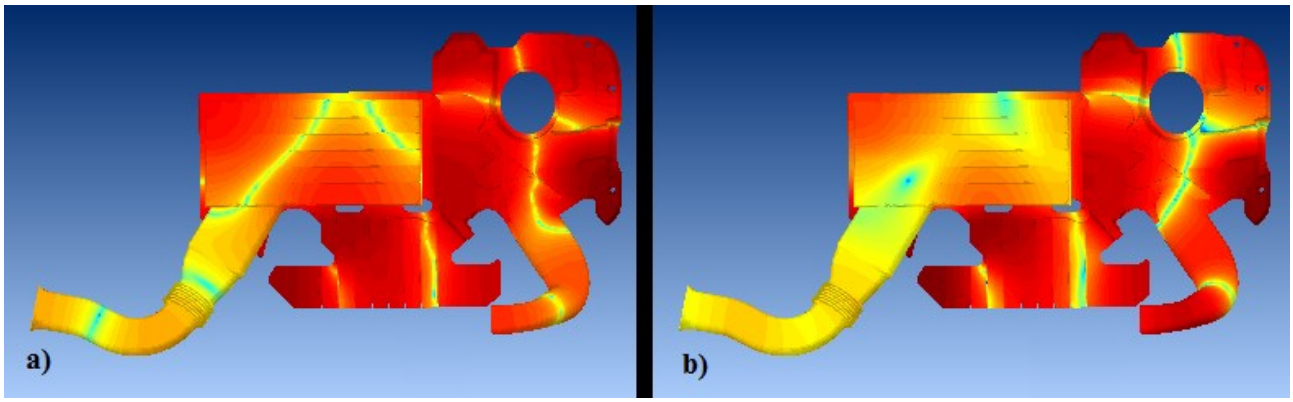


Figure 8.32 - Pressure distribution of a) the acoustic modes at 1091 Hz and b) system response at 1090 Hz.

Moreover, the same thing happens for the system's response at $1040\,Hz$ which is drastically influenced by the presence of an acoustic mode occurring at $1040\,Hz$, as it is shown in figure below.

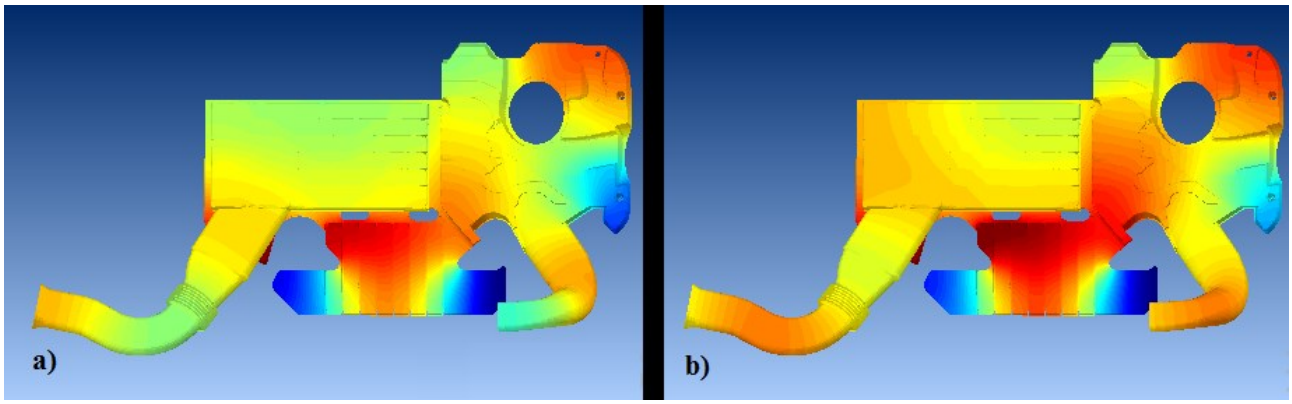


Figure 8.33 - Pressure distribution of a) the acoustic modes at 1040 Hz and b) system response at 1040 Hz.

Actually, it is important to note that the mode depicted in Figure 8.33 a) is not a new natural mode, whose presence is due to a change in the volume of the system. In fact, the same mode shape exists for the second version of the intake system depicted in Figure 8.17 a), as it is possible to appreciate by comparing the color maps of both Figure 8.22 a) and 8.33 a).

In conclusion of this paragraph, it has been shown how the acoustic performance of the investigated intake system may be significantly improved by means of geometric modifications, without changing the overall size of the system, which represents a very important restriction for the considered engine. More precisely, starting from previously discussed studies, in which a numerical model has been validated by means of experimental investigations, the Transmission Loss in rigid wall condition has been numerically evaluated, in order to assess the improvements coming from various geometric changes. Thus, it has been demonstrated that opportunely realized modifications in the volume distribution may considerably increase the TL profile, within the investigated frequency range. Of course, further analyses have to be executed, in order to verify that the amount of noise emitted in real working conditions is effectively diminished, when considering the three proposed versions of the modified system. Besides, the effects of such modifications on the engine performance must be evaluated as well. Consequently, in the following paragraph, the gas-dynamic analyses of the new configurations of the air induction system will be in depth discussed.

## 8.2 Gas-dynamic noise Analysis

### 8.2.1 Problem statement

Once it has been found that the realized geometric modifications have a positive impact on the acoustic Transmission Loss of the original device, another analysis has to be carried out in order to assess the real effectiveness of the new design configurations. In fact, it is necessary to verify that the amount of noise emitted when the new configurations of the air induction system are working will be reduced and, at the same time, that no decrease in the engine performances would occur. To this aim, a more complicated gas-dynamic analysis has to be performed which takes into account all the involved acoustic contributions. Such circumstance arises from the fact that, as already highlighted, when the engine is running the overall noise emission (intake side) is mainly due to

two contributions. In fact, for systems like that, two major sources of sound exist, as it is schematically depicted in Figure 8.34[8].

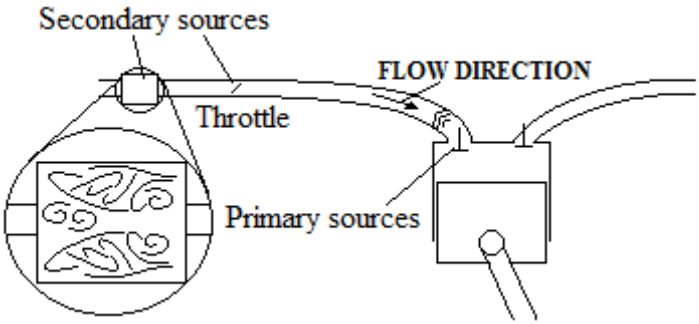


Figure 8.34 - Sound source of the intake and exhaust gas-dynamic noise.

As it has been already mentioned, the major contribution to the engine gas-dynamic noise is represented by the so-called engine pulses and it is due to pressure fluctuations induced by periodic valves opening at the IVO crank angle positions. Thus, the periodic air flow through the valves represents a monopole source term. The main spectral components are concentrated within the low frequency range, corresponding to the first engine orders. Such circumstances make the primary source of noise to be modelled starting from information available from a one-dimensional fluid dynamic code (according to the flow chart of Figure 6.2 in chapter 6) which, as it has already been shown, could also give a first approximate estimation of the noise emitted in various engine running conditions.

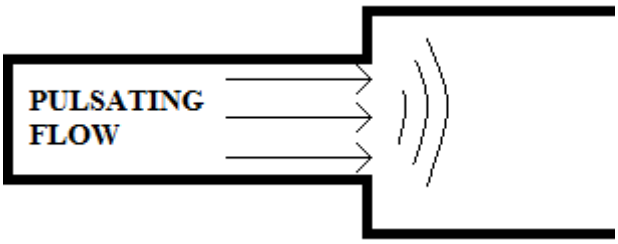


Figure 8.35 - Pulsating flow due to periodic valve opening as primary source of sound.

However, another quite important contribution to the overall noise emitted by the intake mouth is represented by the flow instabilities induced noise (flow noise), which represents a broad band noise due to turbulence inside the system. In fact, aerodynamic processes associated with the cyclic flow through the valves, fluid separation and vortex generation at junction of expansion sections, constitute an additional source of intake and exhaust noise as well. Such contribution, which corresponds to a quadrupole source term, is generally associated with almost every aerodynamic process and it is present even in stationary fluid flow, as it is schematically depicted in figure below.

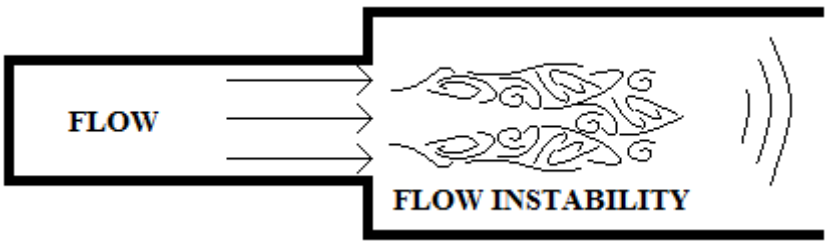


Figure 8.36 - Fluid flow and corresponding turbulence as secondary source of sound.

Obviously, treating turbulence induced sources of sound, the full three-dimensional flow field developed inside the air induction system must be resolved with the help of a 3D CFD code. Thus, the problem to be dealt with is a computational aero-acoustics one, for which several solving strategies may be used. They rely on the use of direct methods, hybrid methods and semi-empirical methods.

As regards the direct methods, both the fluid dynamic and the acoustic part of the problem are solved by the 3D CFD code. However, some drawbacks are encountered such as for example that the CFD solvers work in time domain whilst acoustic is a frequency dependent phenomena dealing with natural frequencies (acoustic and structural), frequency dependent material properties (e.g. damping) etc.. Besides, the CFD boundary conditions are not appropriate for acoustic simulations. As an example, it is possible to consider that a zero pressure[5] boundary condition does not reproduce an acoustic free field condition in acoustics. Moreover, the finite volume CFD spatial schemes is highly dissipative and the acoustic perturbations, which are infinitely small with respect to the flow perturbations, are generally numerically damped for the sake of convergence. Consequently, the accurate prediction of an acoustic field with a direct approach is a difficult objective to be reached, which makes the CFD analysis more complex, very time-consuming and so not appropriate for industrial goals.

Concerning the hybrid methods, they are based on the decoupling, as it is described in the Lighthill's theory[13], between aerodynamically generated sound and its propagation. Such assumption implies that there is no feedback mechanism between acoustic field and propagation field. The acoustic sources are related to the turbulence within the flow but the corresponding acoustic field does not modify the flow. Consequently, such hybrid solutions rely on two basic steps in which the acoustic problem is decoupled from the fluid dynamic one, by letting the flow field to be solved by a 3D CFD solver, whilst the equivalent acoustic sources calculation and their propagation is left to the 3D acoustic solver. The equivalent source terms are reconstructed starting from the resolved flow field, thanks to aeroacoustic analogies such as the aerodynamic generation of sound by Lighthill or Möhring's analogy[5].

As regards the semi-empirical methods, they also rely on a two steps procedure. As an example, a SNGR (stochastic noise generation and radiation) technique may be used to reconstruct a synthetic unsteady velocity field, starting from steady 3D CFD RANS data and isotropic turbulence theory[6][10]. Then, similarly to what happens for hybrid methods, the source terms are computed using aeroacoustic analogies applied to the unsteady synthetic velocity field. However, this method may lead to a not accurate approximation of the acoustic sources and their corresponding frequency spectrum, as the process starts from steady CFD results.

In this thesis it has been chosen to model the turbulence induced acoustic sources by means of an hybrid method, modelling the additional contribution on the basis of the Lighthill equivalent source term. The whole gas-dynamic analysis process merely follows the flowchart of Figure 6.1 and it is reported below.

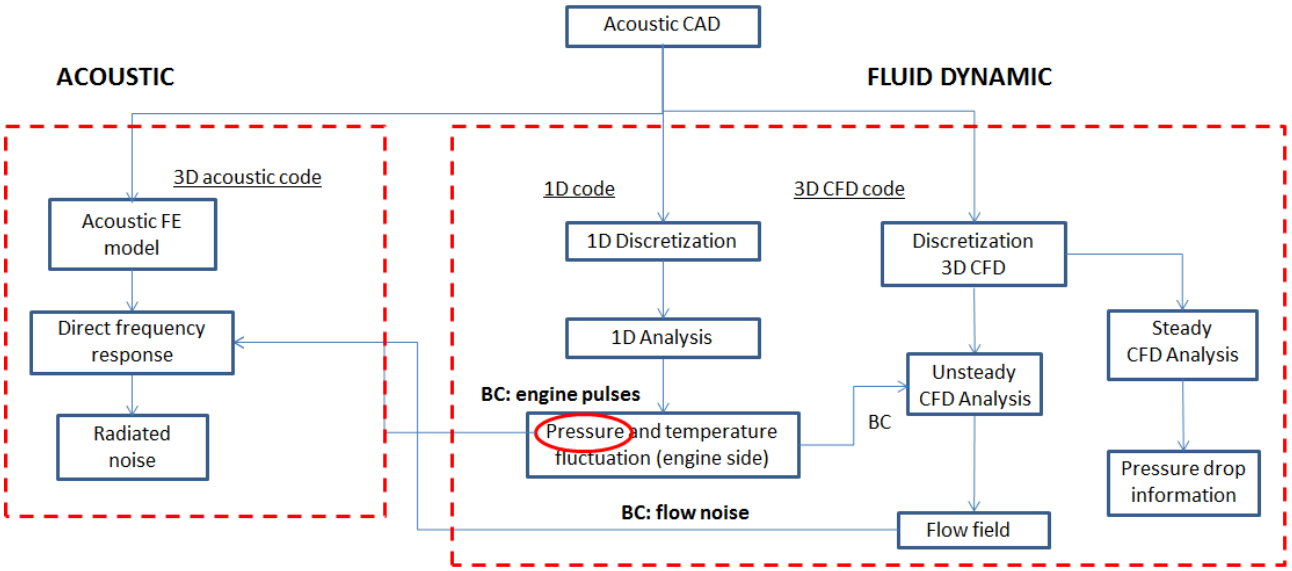


Figure 8.37 – Flow chart of hybrid procedure useful for the gas-dynamic noise analysis.

More precisely, besides what has been described in chapter 6, three-dimensional CFD analyses have been executed in order to resolve the flow field inside the various investigated versions of the system (original and new configurations respectively). To the aim of obtaining suitable boundary conditions for the 3D CFD analysis, the previously discussed one-dimensional engine map has been used. The only difference lies in the fact that the one-dimensional schematization process of the air induction system has been obviously repeated, for each of the new configurations. Then, in correspondence of the engine running point at WOT $2100\ rpm$[91], the pressure and temperature fluctuations, calculated in a section of the 1D map just after the compressor (referring to Figure 6.7 of chapter 6), represent the main excitation of the 3D CFD solver. Once the flow field is completely resolved, it is given to the acoustic solver which reconstructs the equivalent additional acoustic source term, consisting of the spectrum of the Lighthill stress tensor.

However, within the whole above described process, the presence of the paper sheets composing the air filter inside the air induction system has not been taken into account, for each of the new investigated device's configurations, due to the already mentioned lack of information necessary to model the fluid dynamic of porous material within the 3D CFD software. Despite of this modelling issue, it is expected that the validity of the results is not affected by such defection, as the air filter would be the same for each of the new designed devices.

[91] As already mentioned in the introduction of this chapter, the $2100\ rpm$ has been chosen because it is representative of the most common $rpm$ condition encountered at low vehicle speeds, where the intake noise represents a prominent noise source. Besides, it is reasonable to assume that if good results are found at WOT condition, even lower noise emission would be found at lower engine loads. At higher rpm, which corresponds to high vehicle speeds, there are other more prominent noise contributions, e.g. aerodynamic noise.

In the following, the setting up process, for the analyses which are schematized in Figure 8.37, will be presented with particular focus on the discussion of the results. Firstly, the one-dimensional analysis will be briefly described, giving a first insight about the impact of the air system modifications on the engine overall performances. In particular, a comparison among information about power, fuel consumption and volumetric efficiency will be presented, for each of the new configurations. Then, the building-up procedure for the three-dimensional CFD models will be presented and two analyses will be discussed. The first is an unsteady analysis useful for resolving the three-dimensional flow field, developed at $2100\ rpm$ WOT, whilst the second is a steady flow analysis useful for examining the pressure drop trend, as function of the mass flow rate, which would be realized across the inlet and outlet section of each system' configurations. Finally, a comparison will be made about the noise emissions, simulated with the aim of the 3D acoustic model, in terms of frequency spectrum and overall levels, in order to establish the effectiveness of the presented new versions of the studied system.

## 8.2.2 Analysis process

### 8.2.2.1 One-dimensional CFD analysis

According to the schematization of Figure 8.37, when evaluating the gas-dynamic noise within the whole shape-optimization process, the first step to be made has been the one-dimensional schematization of the modified systems, followed by a 1D analysis aimed to obtain the proper set of boundary conditions for both 3D CFD and 3D acoustic model. Once again, in order to obtain an as much as possible suitable one-dimensional representations of the various versions of the intake system, the useful tool GEM 3D has been used. As it has already outlined, the starting point for the model preparation is represented by the available topological information in terms of CAD models. Thus, all the three new CAD models have been firstly divided into parts which could better represent one dimensional flow components. The first analysis has been about the original device, because that described in chapter 6 has taken into account the presence of the air filter which has been modelled as a simple orifice connection (see Figure 6.7). However, in order to respect the coherence with three-dimensional CFD analysis, the presence of the air filter has to be neglected. Hence, the new one-dimensional discretization is depicted in Figure 8.38.

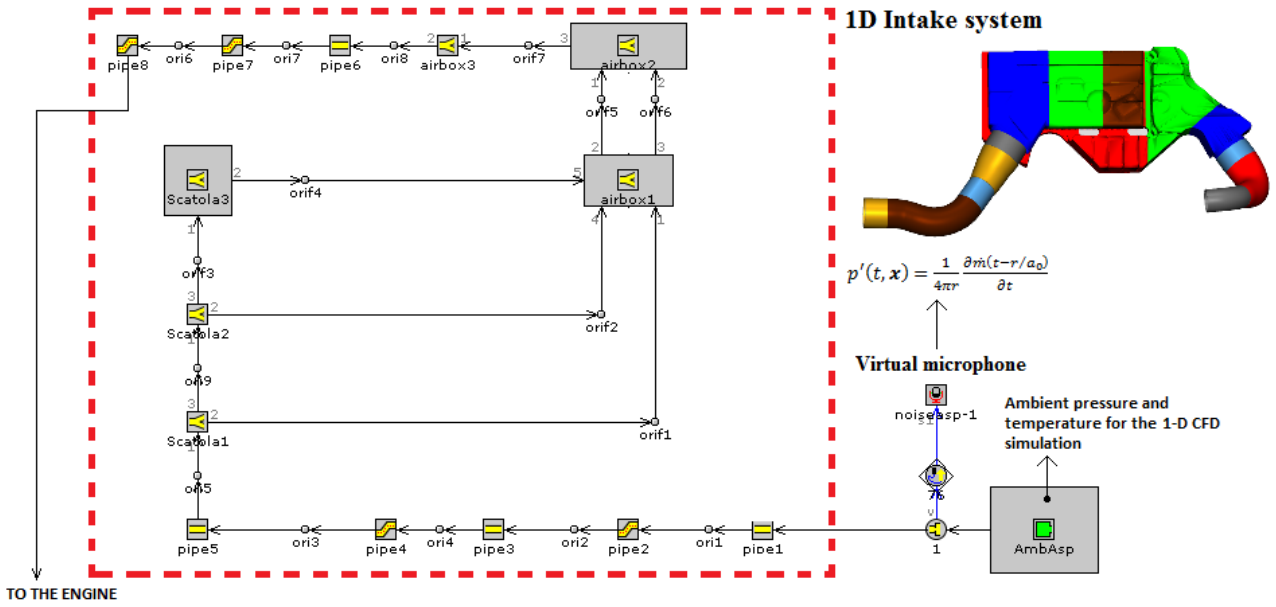


Figure 8.38 - 1D schematization of the original device (without the air filter).

By comparing the above picture with Figure 6.7 of chapter 6, it is possible to appreciate that the only difference is represented by the absence of the air filter. The same process has been executed for the three investigated versions of the original device and, as an example, the corresponding 1D representation of the first CAD modification is depicted in Figure 8.39.

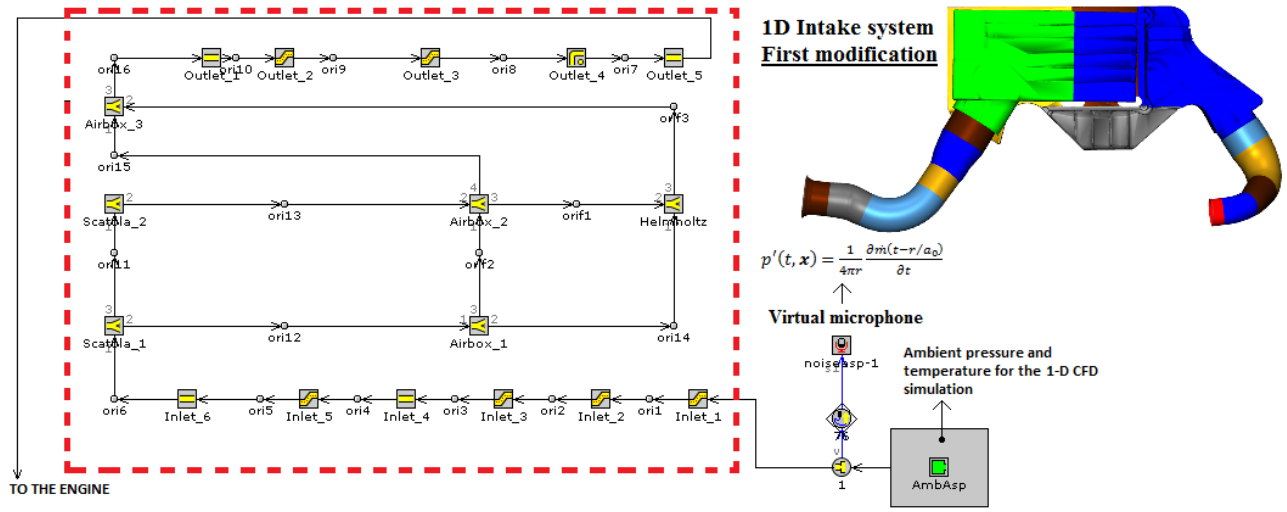


Figure 8.39 - 1D schematization of the first CAD modification.

As it is possible to appreciate from the above figure, a more detailed description of the air induction system has been realized. As an example, it is possible to note the presence of a flow component schematizing the main Helmholtz resonator. Such increase of details has been realized in order to easily reproduce the geometric changes, leaving unaltered the 1D representation of the other parts. As an example of the effectiveness of such modelling strategy, in the figure below the one-dimensional representation of the second CAD modification is shown.

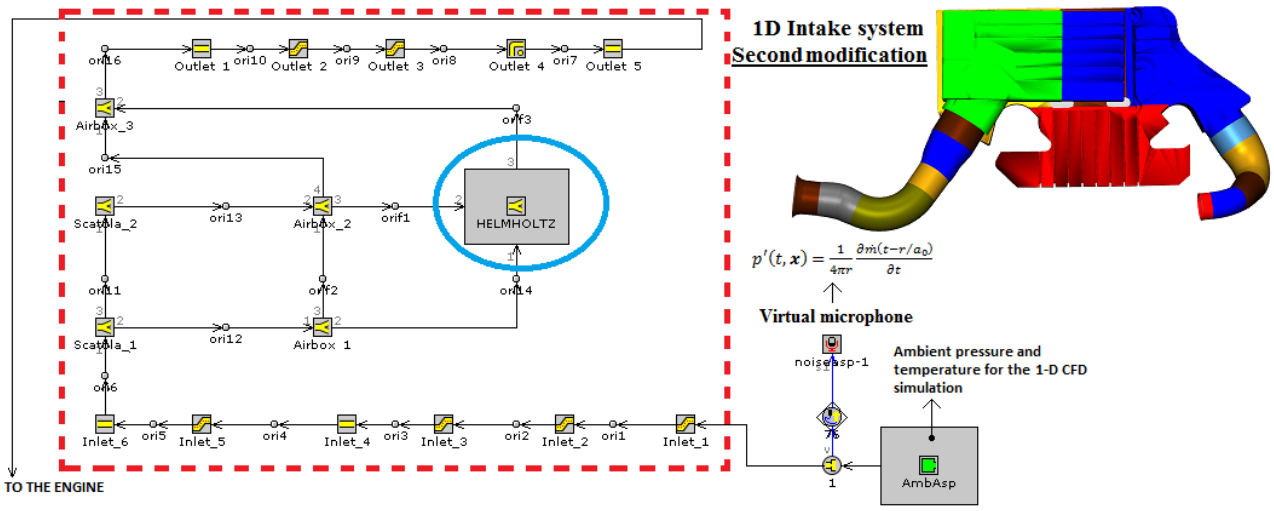


Figure 8.40 - 1D schematization of the second CAD modification.

As it is schematically indicated by the blue circle in the figure above, the only change occurring in the 1D scheme is represented by the flow component describing the Helmholtz resonator, which is the only change realized between first and second geometric modification. It is also possible to appreciate that the other flow components are exactly the same. This should ensure that the output of the 1D simulations are affected only by the effective modification in the CAD models and not by different modelling strategies. In Figure 8.41, the one-dimensional representation of the CAD model corresponding to the third investigated version of the studied system is shown.

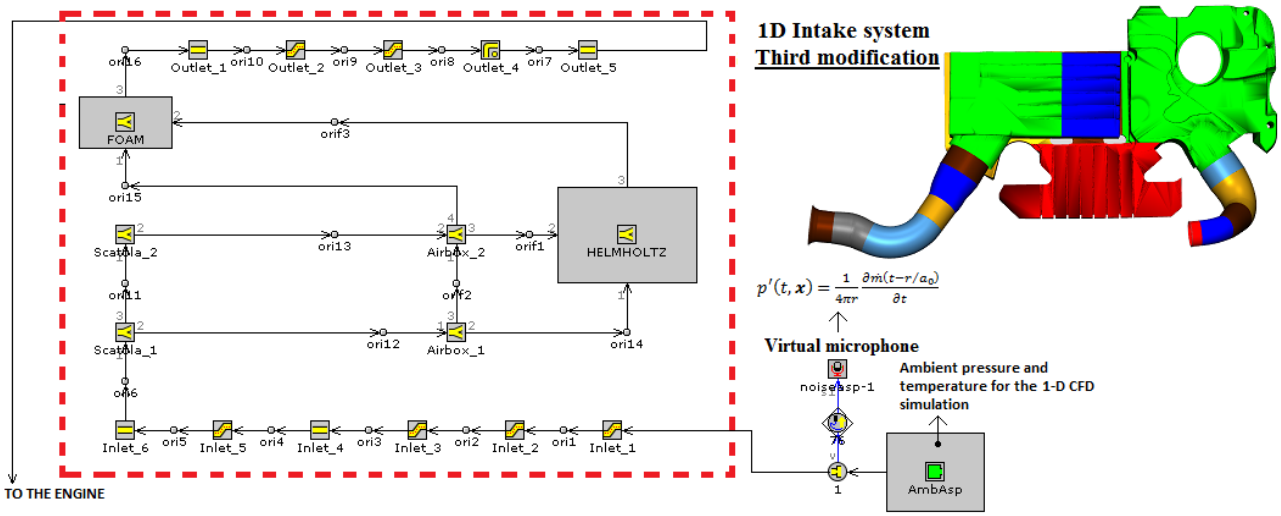


Figure 8.41 - 1D schematization of the third CAD modification.

As regards the analysis output, the main information is represented by the pressure and temperature fluctuations at the outlet of the system (engine side), which are mandatory for the further three-dimensional analyses. However, it is important, before proceedings with further investigations, to compare the effects that the various modified versions of the air induction system have on the engine performances. From such a viewpoint, an indication may be obtained by comparing power, fuel consumption and volumetric efficiency accomplished during each 1D simulations of the coupled system (engine-intake). Such information have been reported in the figures below.

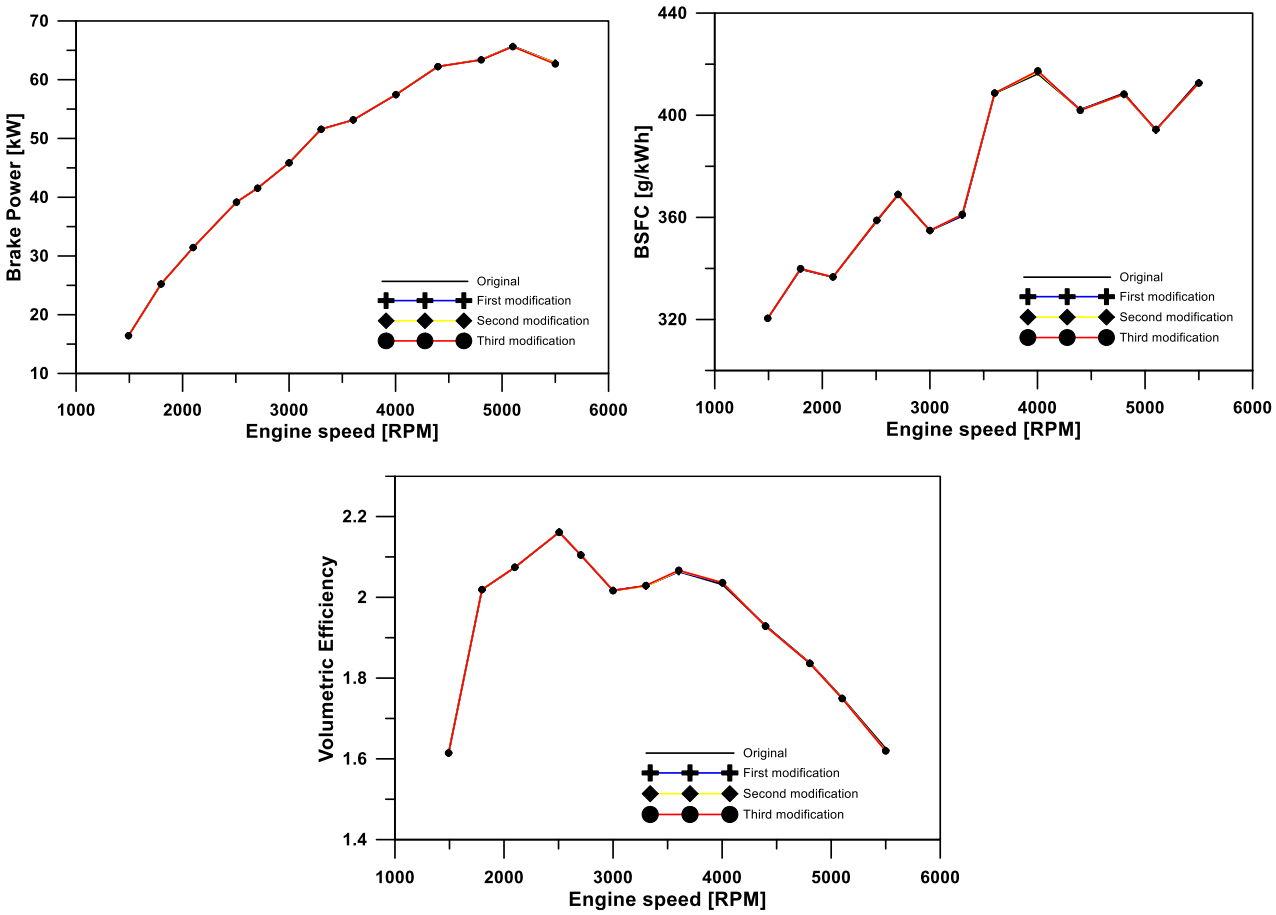


Figure 8.42 - Engine performance comparison.

As it is possible to appreciate from the above figures, the curves corresponding to each of the investigated system's configuration are practically indistinguishable. It follows that the main engine performance parameters should remain unchanged when each of the investigated new versions of the intake system is coupled to the engine. Nevertheless, a more accurate analysis would also take into account the pressure drops occurring across the inlet and outlet sections of the systems. Such aspect has been further investigated with the aim of a three-dimensional CFD code, as it will be described in the following. However, before deepening the investigations, it is interesting to assess the influence of the various changes in the 1-D discretization on the pressure fluctuations, in a section just before the inlet of the compressor, which will be useful for the successive analyses. To this aim, in figure below, the incident pressure fluctuations, calculated by means of eq. (6.2), occurring in 720 crank angle degrees and corresponding to each of the new investigated configurations of the air induction system are shown.

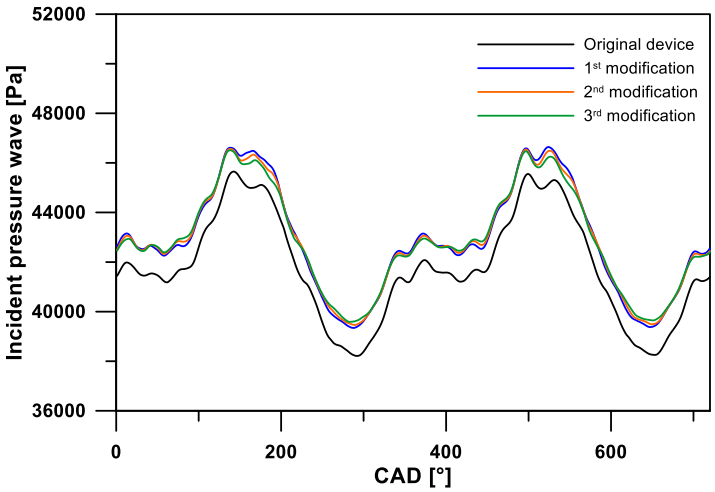


Figure 8.43 - Incident pressure waves into the various version of the air induction system.

As it is possible to appreciate from the above figure, there are not significant changes in the incident pressure wave, when the modifications are applied to the one-dimensional representation of the air induction system. More precisely, it is possible to point out that, as the basic waveform does not change, it is expected that the spectrum information at low frequency would be practically unaltered. Some change in the spectrum would certainly occur at high frequency where, however, small amplitudes components are present whose contribution to the overall sound emission is negligible.

### 8.2.2.2 Three-dimensional CFD analysis

As it has been already mentioned, the main result of the one-dimensional analysis is represented by the fluid dynamic state at the outlet of the air induction system (engine side), just before the inlet of the turbocharger group. In fact, once such information is available, it is possible to set up the proper boundary conditions in order to perform a 3D CFD unsteady analysis, aimed to resolve the entire flow field which is developed inside the system, in various engine running points. Thus, the 3D CFD analyses have been executed with the aim of a commercial software for fluid dynamic simulations. It is very important to underline that, especially in the case of a CFD analysis, the crucial step for the model preparation has been represented by the mesh creation. In order to ease the discretization process, the CAD models have been opportunely divided in at least four parts. As an example, Figure 8.44 shows the various parts composing the intake system in its original configuration, which are inlet (grey), filter box (light blue), airbox (green), outlet (light orange).

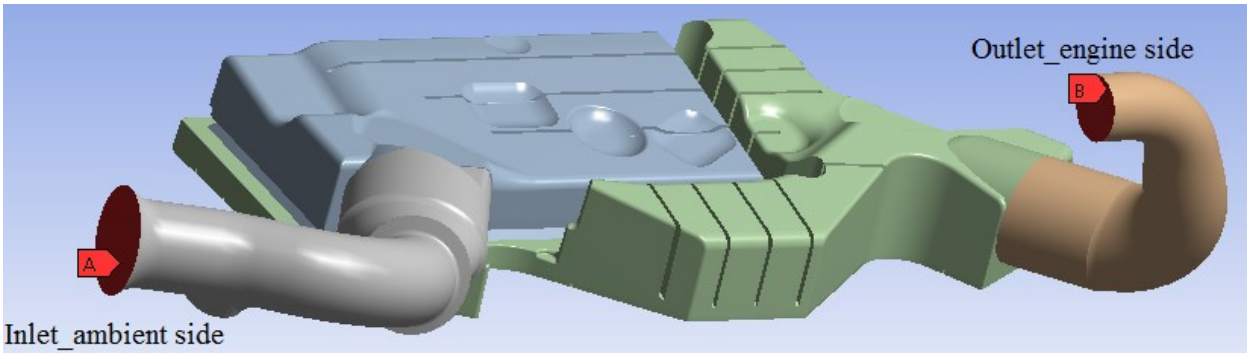


Figure 8.44 - Input CAD model for the 3D CFD analysis.

In the above figure, both the inlet and outlet section have been highlighted, as the boundary conditions have been applied on the elements corresponding to them. It is important to note that particular attention has been spent for the meshes generation processes since the quality of the grid drastically affects the convergence of the incompressible flow simulation. In the figure below, the CFD mesh for the original system configuration is shown. Here, it is possible to recognize the four different meshes of the parts composing the assembly depicted in Figure 8.44. For simplicity, a TET-based discretization process has been executed, such that the final mesh consists of 1135896 elements (Tetra 4-noded) and 224534 nodes.

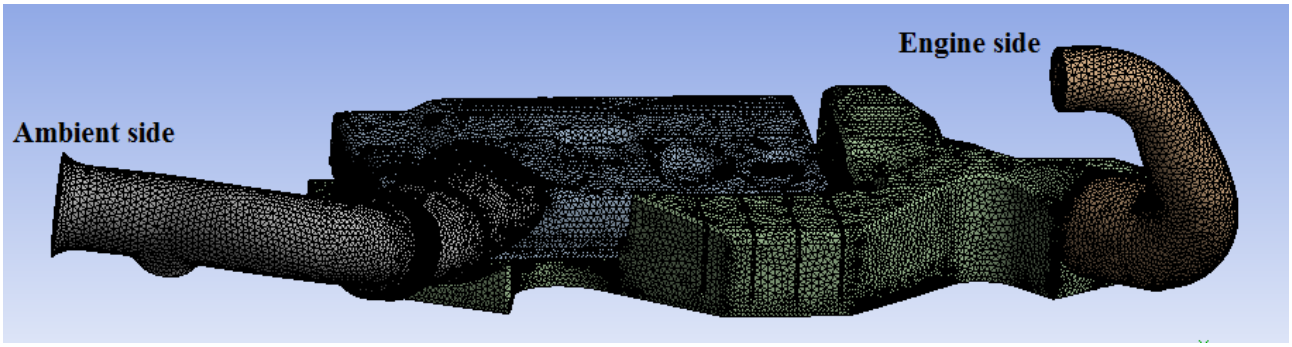


Figure 8.45 - 3D CFD mesh for the original device configuration.

As already mentioned, on the elements constituting the system's termination at the engine side, a fluctuating pressure and temperature profile have been imposed, which have been extracted from the engine map depicted in Figure 8.38, after the 1D simulation. As an example, in the figure below, the pressure and temperature profile imposed when simulating the $2100\,rpm$ wide-open throttle condition are depicted.

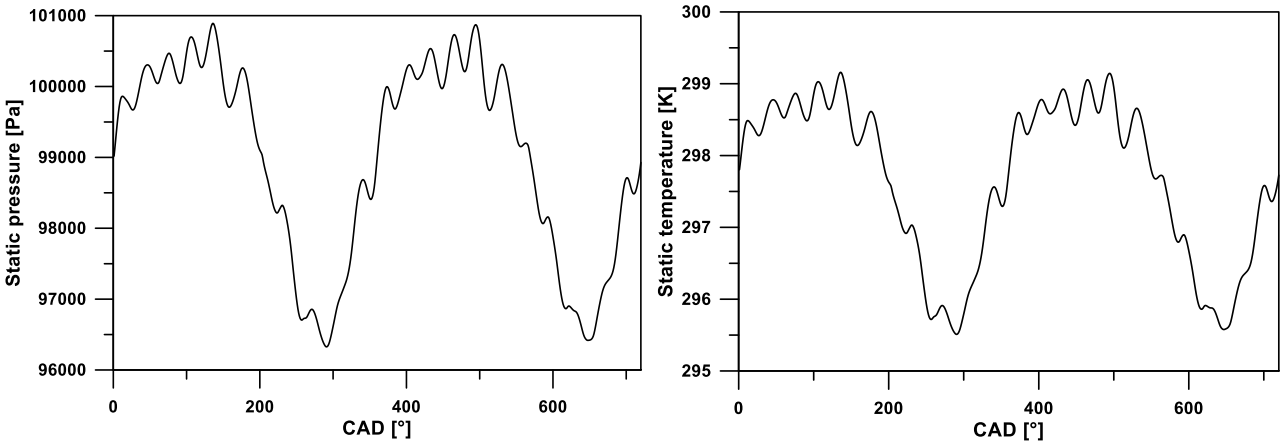


Figure 8.46 - Boundary conditions in terms of pressure and temperature fluctuations for the 3D CFD model.

At the same time, a constant static pressure and temperature have been imposed at the intake mouth, in order to reproduce the thermodynamic conditions within the external ambient. From a modelling point of view, apart from the above mentioned boundary conditions, a turbulence model had to be specified, which is necessary in order to express the Reynolds stress tensor as function of the average flow field, allowing the closure of the fluid dynamic problem to be reached, as it has been already mentioned at the end of chapter 7.

A two equation model has been employed, corresponding to the standard k-epsilon, which has been used for all the simulations. Then, the time step has been fixed corresponding to the information given by the 1D solver, namely every crank angle degree. To the aim of determining the minimum number of cycles to be simulated, necessary for considering the solution as fully converged, a sensitivity analysis have been executed. Hence, five consecutive cycles (corresponding to 3600 time step) have been simulated, in correspondence of the engine running point at 2100 $rpm$ WOT. The main output of such unsteady CFD simulation is represented by the three-dimensional flow field developed inside the system, which has been used as additional input in the acoustic model. As an example, the velocity field within the original device at 2100 $rpm$ is reported in figure below.

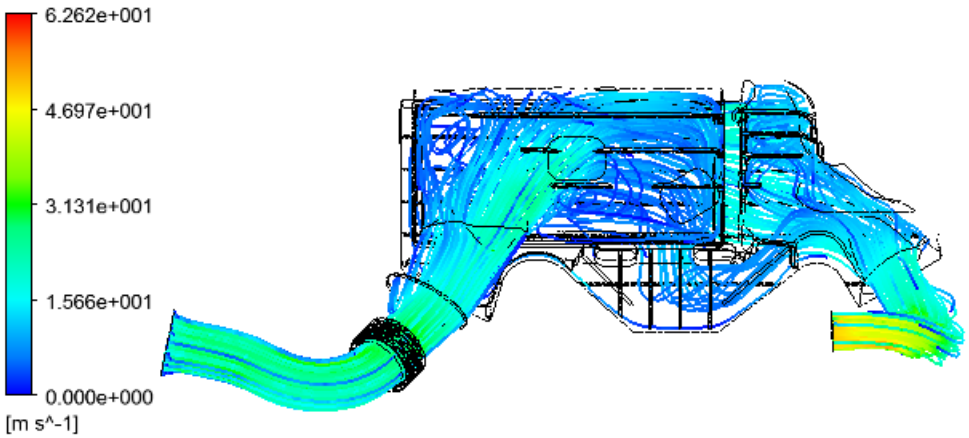


Figure 8.47 - Velocity streamline at the last time step of the simulation at 2100 rpm WOT.

In the figure above, the higher the velocity magnitude the more red-like the color map. Such output information is necessary to model the turbulence induced additional acoustic sources according to the aeroacoustics analogy, as described in chapter 7. For completeness, the CFD discretizations corresponding to each of the investigated versions of the air induction system have been reported in Figure 8.48.

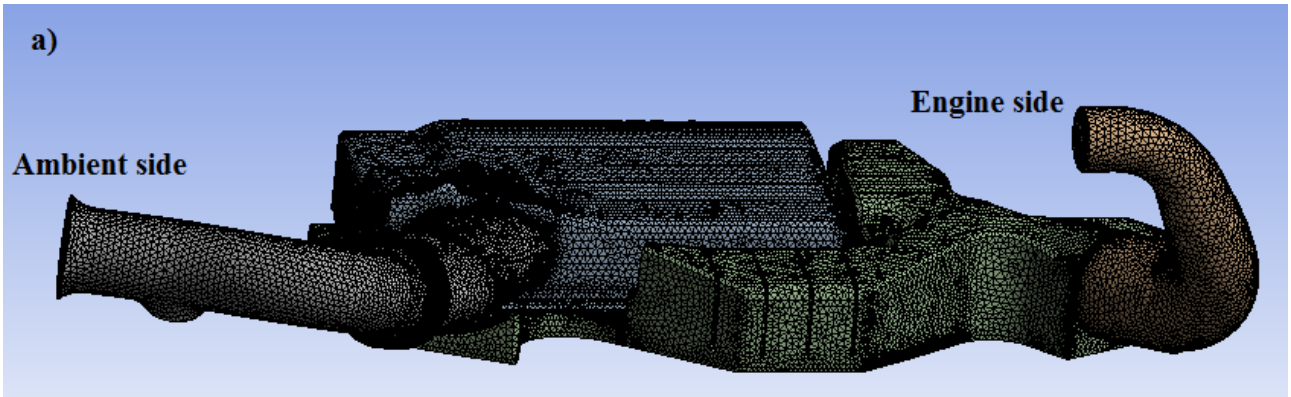

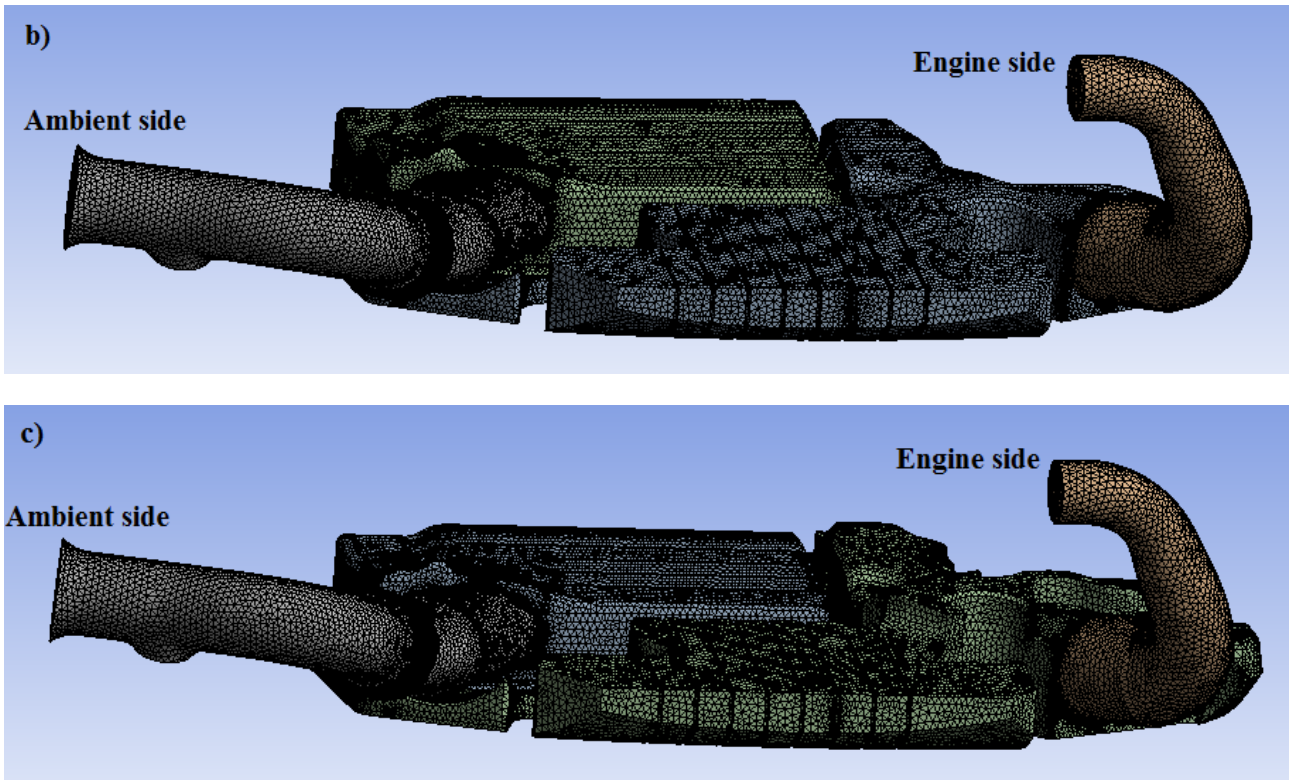


Figure 8.48 - 3D CFD mesh corresponding to a) first, b) second and c) third modification respectively.

Even in those cases, a TET-based mesh creation process has been executed, due to its simplicity in representing very complex geometries and the results, in terms of number of elements and nodes, are reported in the table below.

| Geometry | Number of elements (Tetra 4-noded) | Number of nodes |
|---|---|---|
| First modification | 1176859 | 229917 |
| Second modification | 1488162 | 288359 |
| Third modification | 1532437 | 298620 |

Table 10 - Mesh characteristic for the modified versions of the intake system under investigation.

Obviously, by the examination of the data within table 10, it is clear that the number of elements is increased as the volume of the considered geometry increases. Such aspect directly affects the computational time of each simulation.

Another important aspect, which highlights the importance of a three-dimensional fluid dynamic code, is represented by the fact that it allows the accurate calculation of the pressure drop which is realized across the boundaries of the computational domain. Thus, the above described models have been used also for steady state flow simulations, aimed to calculated the pressure drop of each systems as function of the mass flow rate. In particular, the mass flow rates, corresponding to each engine points, have been extracted from the 1D maps after the simulations and have been used as boundary conditions for such steady state analyses. The results are summarized in Figure 8.49, where the red, black, blue and green line refer to the pressure drop realized across the boundary of the original device, first, second and third modification respectively.

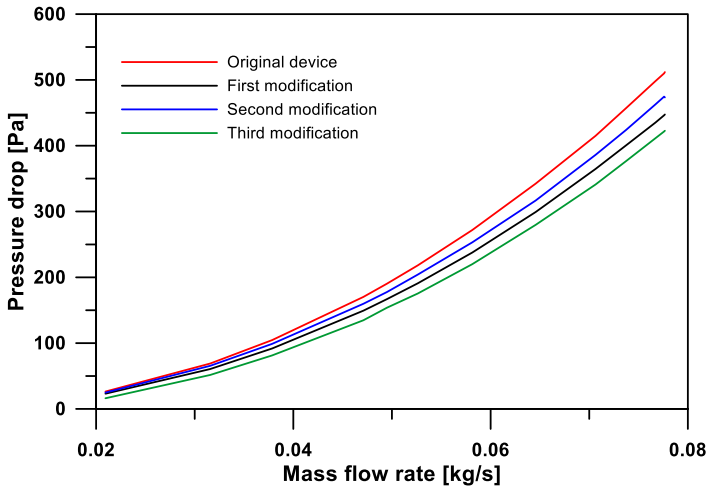


Figure 8.49 - Static Pressure drops computed with the aim of the 3D CFD code as function of the mass flow rate.

Firstly, it is important to note that, as expected, the static pressure drop has a quadratic trend as function of the mass flow rate[7]. Secondly, by the examination of the curves depicted in the above figure, it is possible to point out that all the investigated geometric modifications would not increase the static pressure drop, which would result in a decrease of both the air density and consequently the volumetric efficiency. On the contrary, the pressure drop would decrease if the various geometric changes would be applied to the original device.

Once the flow field inside the air induction system has been resolved, it is possible to feed the acoustic model with the additional boundary condition, which is necessary to model the flow noise contribution to the overall noise emission. Thus, in the following, the three-dimensional acoustic model and the corresponding outcomes will be presented and discussed.

### 8.2.2.3 Three-dimensional acoustic analysis

Even in this case, the analyses have been conducted by using the commercial software Actran release 15.1, powered by Free Field Technology. Following the flow chart of Figure 8.37, the three-dimensional acoustic analyses have been executed in order to estimate the gas-dynamic noise related to the various new configurations of the air induction system, with the target of evaluating the effectiveness of the proposed modifications in terms of emitted noise. To this aim, both engine pulses and flow noise contributions have to be taken into account and, consequently, the acoustic model building-up procedure has been slightly different with respect to that described in chapter 6. Apart from the absence of the air filter model, the main difference relies of course in an additional boundary condition, necessary to model the flow noise contribution within the air induction systems, which has been imposed by means of aeroacoustics analogy. As it should be clear from the theory reported in chapter 7, the basic idea for formulating such analogy is to start from the basic equations of the fluid dynamics, make as few assumptions as possible and manipulate the equations to reveal the wave propagation operator and the right source term. This has been done referring to the aeroacoustics analogy formulated by Lighthill, according to which the source region may be considered as an equivalent acoustic medium at rest, on which the Lighthill stress system acts, this latter being known once some properties in the flow region are known.

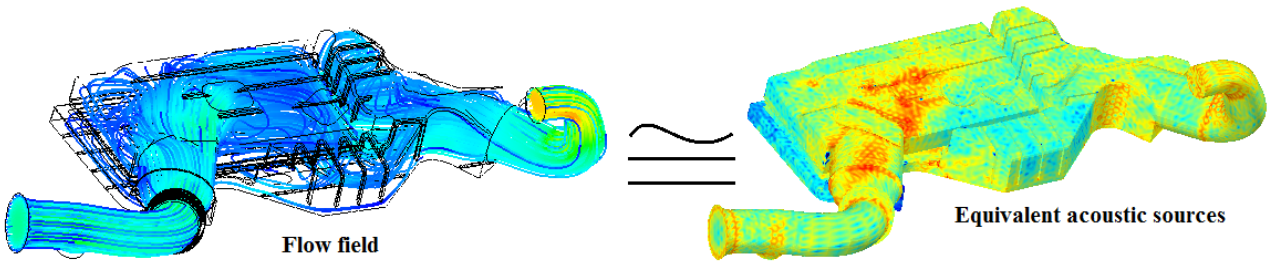


Figure 8.50 - Aeroacoustics analogy applied to the air induction system.

This means that, apart from the element at the outlet of the system (engine side) where an incident plane wave field has been specified, in order to simulate the acoustic presence of the valve openings, inside the acoustic cavity the equations to be solve is

$$\left[\frac{1}{a_0^2}\frac{\partial^2}{\partial t^2} - \frac{\partial^2}{\partial x_i^2}\right] p' = \frac{\partial^2 \gamma_{ij}}{\partial x_i \partial x_j} \tag{8.3}$$

where the term on the right-hand side represents the additional sound source contribution to be added to the model. According to the nomenclature introduced in chapter 7, such term is the so-called Lighthill stress tensor and in general it is expressed in Cartesian tensor form as

$$\gamma_{ij} = \rho V_i V_j - T_{ij} - \rho a_0^2 \delta_{ij} \tag{8.4}$$

As it is possible to appreciate by eq. (8.4), it is important to recall that, in general, the stresses embedded within the Lighthill tensor are due to the momentum convective flux, pressure fluctuations due to non-adiabatic state of change and viscous stresses. However, considering that within the fluid dynamic of intake systems no relevant entropy variations are present as well as those arising in heat release processes and, neglecting the effect of the viscous stresses on the generation of sound[92], only the first term on the right-hand side of eq. (8.4) has to be considered. As a consequence, once the developed flow field inside the system has been resolved by the three-dimensional CFD analysis, it is possible to evaluate the flow noise related source term to be added as additional boundary condition within the 3D acoustic model according to eq. (8.3). Actually, the acoustic code solves the wave equation within the frequency domain, which implies that for the propagation of the additional flow noise source term the equation to be solved in the flow region (the air induction system) is the Helmholtz equation with the right-hand side equal to the Fourier transform of the Lighthill tensor, namely

$$(\nabla^2 + k^2)\hat{p}(\omega, \boldsymbol{x}) = -\hat{\gamma}(\omega, \boldsymbol{x}) \tag{5.5}$$

where $\hat{p}$ is the complex valued amplitude of the sound wave whilst $\hat{\gamma}$ is the amplitude of the additional source, both at the angular frequency $\omega = 2\pi f$.

Thus, several aeroacoustics simulations have been performed at full load operation and for the engine speed $2100\ rpm$, based on the coupled information coming from both the 1D (useful for

[92] The identification of the relative magnitude between momentum convective and diffusive (due to viscous stresses) fluxes may be accomplished thanks to the Reynolds number (representing the ratio of inertial forces to viscous ones) which in general is far greater than unity.

characterizing the engine pulses contribution) and 3D CFD analysis (useful for characterizing the flow noise contribution). The way in which the data, imported from the 1D analysis, is used has been already described in chapter 6, whilst that coming from the 3D CFD solution, since the flow has been assumed incompressible, it is represented by the velocity field in each CFD cell. Such information has been exported every two time steps, that is every two crank angle degrees. This has been necessary in order to equal the frequency domain information of each of the two noise contributions[5], which means having two spectra spreading in the same frequency range with the same frequency step equal to half the first engine order. Finally, the 3D acoustic model corresponding to the original device is reported in figure below, where it is possible to distinguish among the different applied boundary conditions.

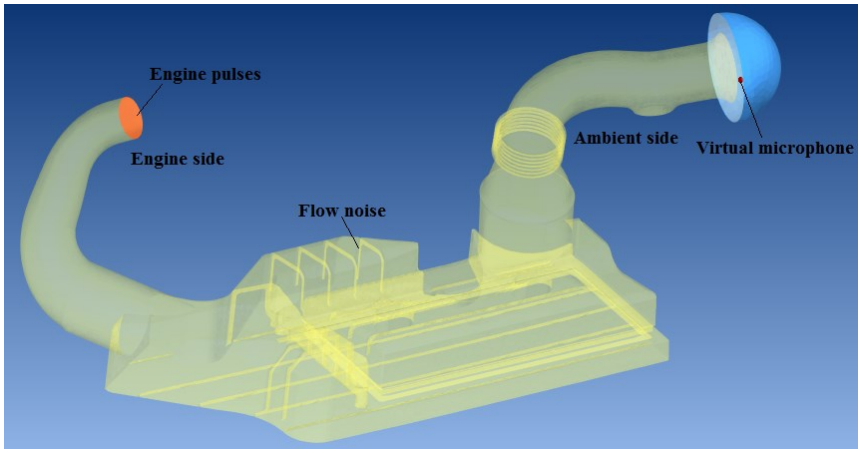


Figure 8.51 - 3D acoustic model of the original device.

In particular, different colors are recognizable in Figure 8.51 indicating various model "components". The elements simulating the presence of the primary sound source are depicted in red whilst the whole cavity mesh, on which the flow noise sources belong, is depicted in yellow. Moreover, similarly to what has been described in chapter 6, the two-dimensional mesh supporting the infinite elements, simulating the non-reflecting boundary condition, is depicted light blue. A virtual microphone has been placed at 1 cm away from the inlet mouth, whose location within the acoustic model is highlighted by a red point in the above figure. As previously mentioned, the frequency step of the simulated engine running point has been fixed accordingly with the spectral content of the two modelled sound sources, so that the frequency range of each analyses extends from $\Delta f$ up to $2\,kHz$, with a frequency step equal to $17{,}5\,Hz$. In the figure below, the three-dimensional acoustic models, corresponding to each of the modified versions of the air induction system, are shown.

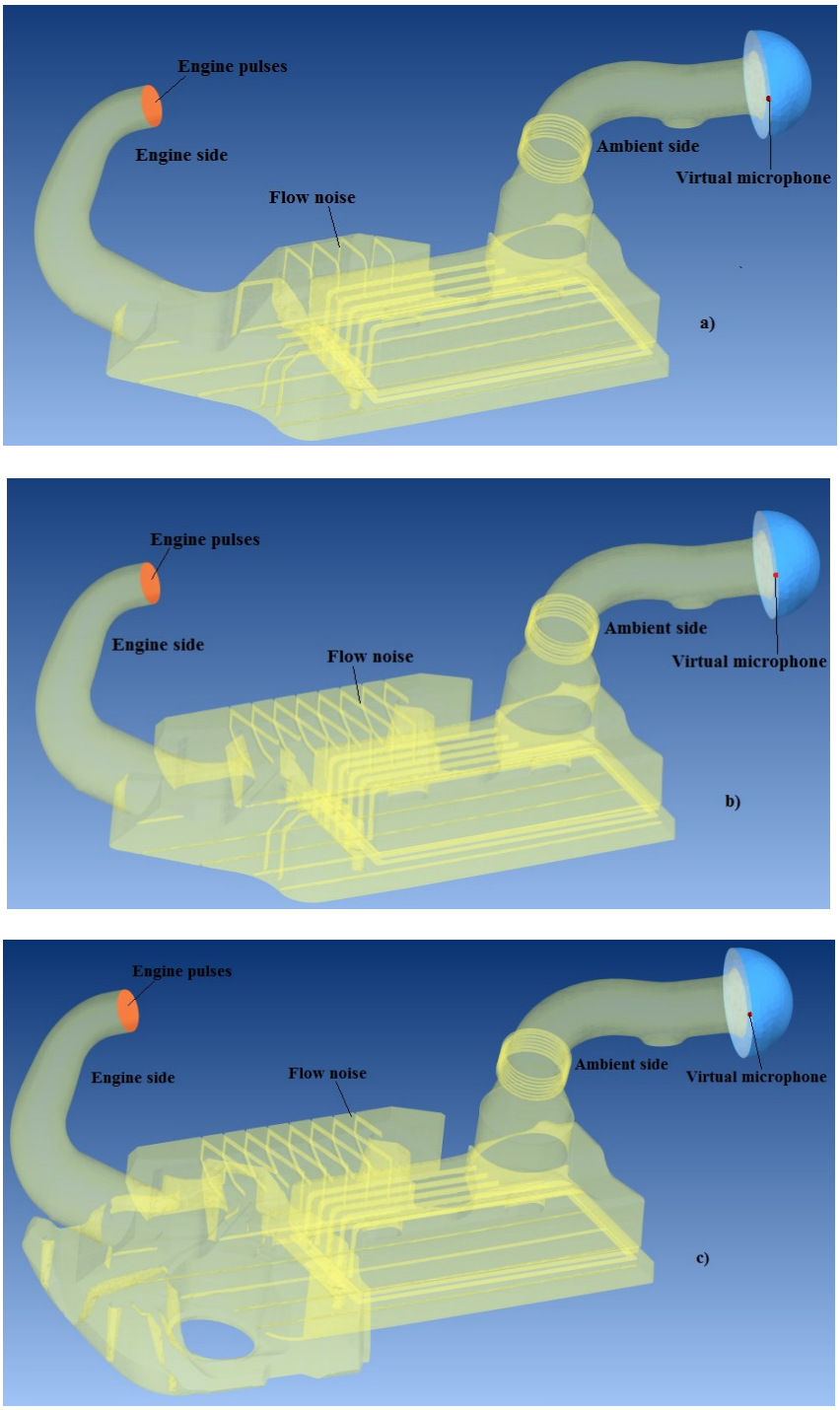


Figure 8.52 - 3D acoustic model corresponding to: a) first, b) second and c) third modification.

The output of each acoustic analysis is represented by the gas-dynamic noise emitted, in terms of sound pressure level spectrum, and the corresponding overall level at the virtual microphone location. In particular, since linear theory holds, it has been possible to examine the contribution to the total sound pressure level of each of the imposed noise sources (engine pulses and flow noise). As an example, in figure below the sound pressure level spectrum corresponding to the primary and secondary noise sources at $2100\,rpm$ is shown for the original device. Here, the black and blue curves represent the engine pulses and flow noise contribution respectively, whilst the red curve represents the total sound pressure level.

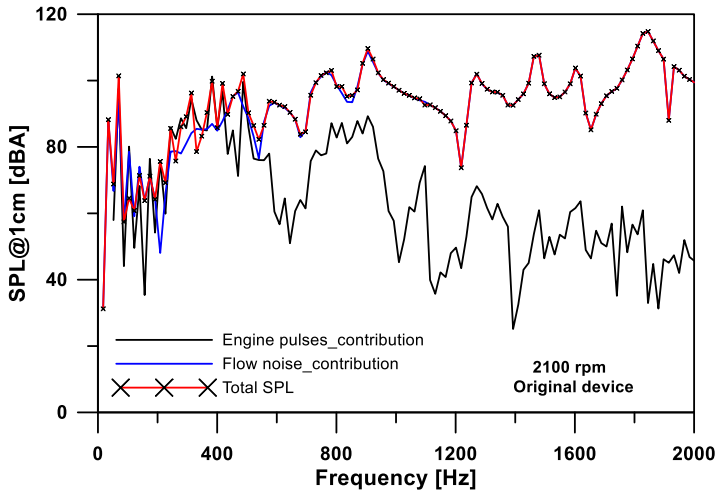


Figure 8.53 - Engine pulses vs Flow noise contribution for the original device @ 2100rpm WOT.

By the examination of the above figure, it is very interesting to appreciate how, as expected, the flow noise contribution represents the main source of noise at high frequency. As it has been already mentioned, such contribution mainly consists of a broad-band noise, due to various turbulent scales indeed. Consequently, the total sound pressure level which would be perceived at the microphone location is dominated at low frequency by the engine pulses contribution whilst, at high frequency, by the flow noise contribution. In Figure 8.54, the comparison between the total sound pressure levels, at $2100\ rpm$, corresponding to the original device and first modification is shown as function of the frequency.

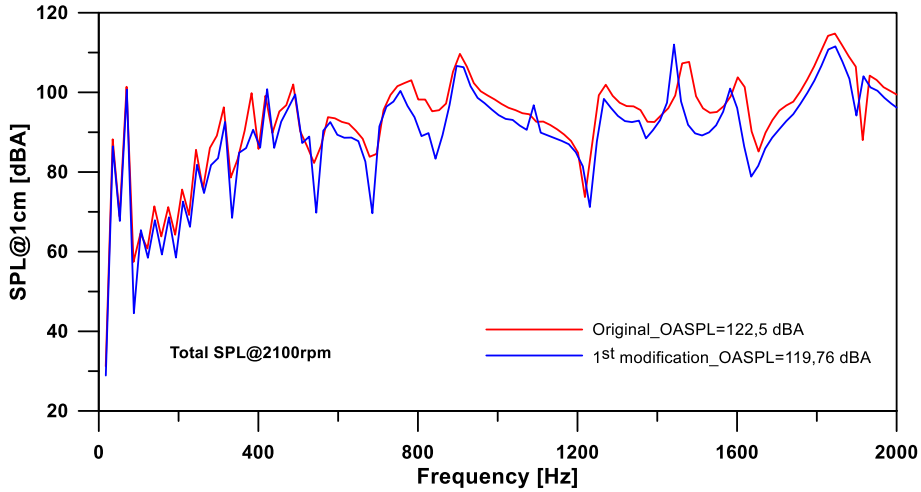


Figure 8.54 - Total A-weighted SPL comparison at 2100rpm: original device and first modification.

In the figure above, the red and blue curves represent the analysis output corresponding to the original device and modified (first) device respectively. As it is qualitatively possible to appreciate by the examination of the two trends, the noise emission corresponding to the first geometric modification of the air induction system would decrease. This is also confirmed by the calculation of the overall A-weighted sound pressure levels (OASPL) (see eq. (2.11)), which highlights a decrease in the noise level of $2{,}74\ dBA$, up to $2\ kHz$. However, in order to deeply understand such result, it is necessary to examine the single components of each of the total SPL of the above figure.

To this aim, in Figure 8.55 the noise emissions due to only the primary sound sources are shown as function of the frequency, where the same color legend of Figure 8.54 has been used.

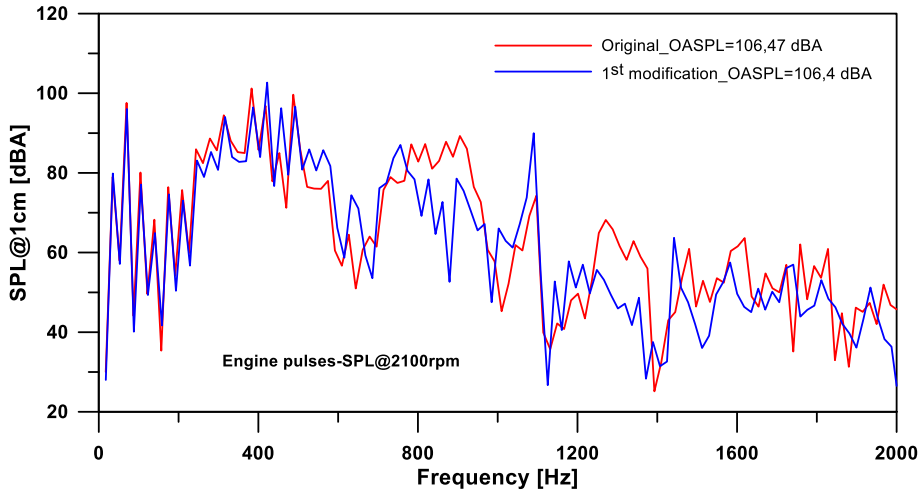


Figure 8.55 - A-weighted SPL comparison at 2100rpm WOT (engine pulses contribution): original device and first modification.

By the examination of the above figure, it is possible to point out that the two contributions are almost equivalent in terms of energy content, as it is testified by the same values of the OASPL. This is due to the fact that, changes in the pressure fluctuations, calculated during the one-dimensional analysis in a section just before the entrance of the compressor, do not affect the low frequency content of the signals, which are the most prominent. In particular, as it has already mentioned, the basic waveform of the pressure fluctuation is unaltered, indicating that the low frequency content is not significantly changed. To prove that, the spectrums of the incident waves, which have been applied as excitation (engine pulses) for the models depicted in Figure 8.51 and Figure 8.52 a), are shown below.

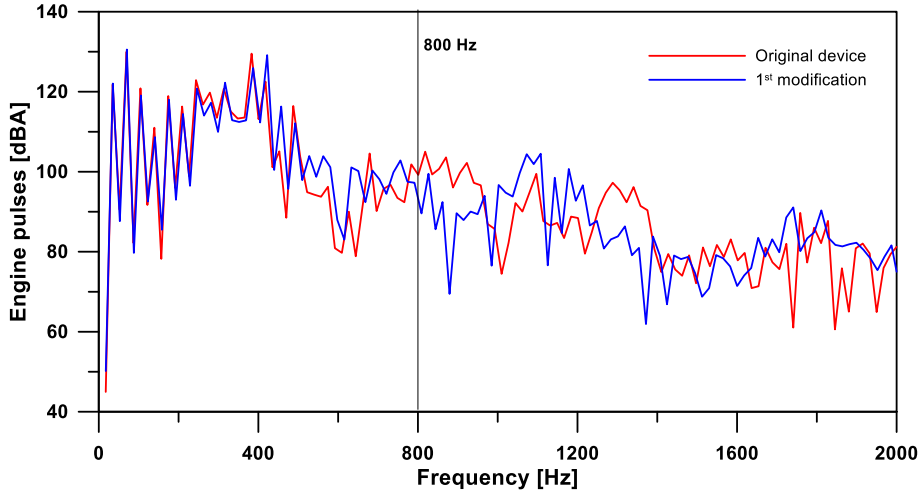


Figure 8.56 - Frequency domain representation of the engine pulses excitation.

As it is possible to appreciate, the two spectra are almost equivalent, at least at low frequencies. In fact, important differences between the two trends are only observable after $800\,Hz$ where, however, the sound pressure levels (SPL) are lower and do not represent a prominent contribution to the overall levels. Such circumstance is also observable in Figure 8.55. It follows that, in spite of

the fact that the high frequency noise attenuation characteristic increases with the aim of the first CAD modification, as it is indicated by the TL comparison of Figure 8.15, the benefits in terms of overall sound pressure levels due to the primary sound source are not evident, as there are no significant low frequency changes in the excitation spectrum coming from the one-dimensional analysis. In the figure below, the comparison between the flow noise contribution has been reported where, again, the same color legend has been adopted.

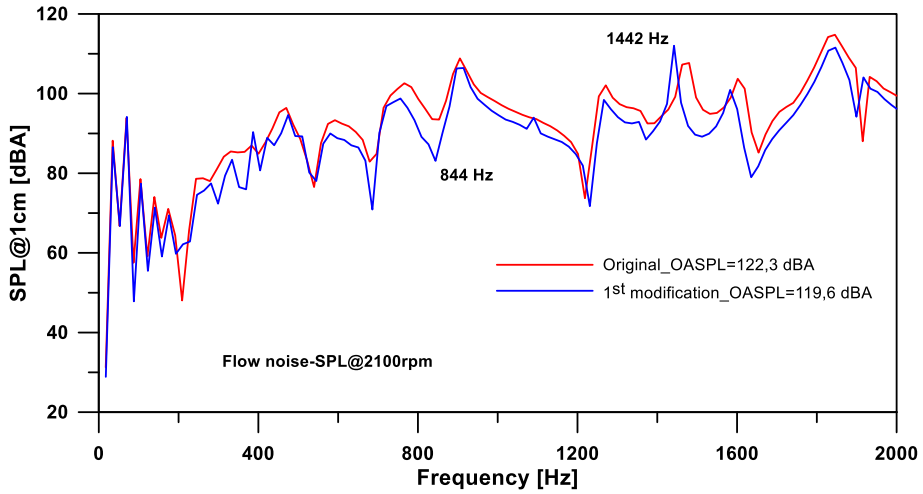


Figure 8.57 - A-weighted SPL comparison at 2100rpm WOT (flow noise contribution): original device and first modification.

By the examination of the above figure, it is clear that the reduction of 2,74 $dBA$ on the total sound pressure level, between the original device and the first modification, is mainly due to a decrease in the flow noise contribution, as it is also testified by the reported overall A-weighted SPL. In fact, within the whole investigated frequency range, the blue curve is fair below the red one, apart from some isolated frequency, e.g. at 1442 $Hz$. Here, the higher SPL related to the first modification is due to different attenuation characteristic at such frequency. To prove that, in Figure 8.58, the noise attenuation curve in real engine working condition has been reported as function of the frequency, where the red and blue curves refer to original device and first modification respectively.

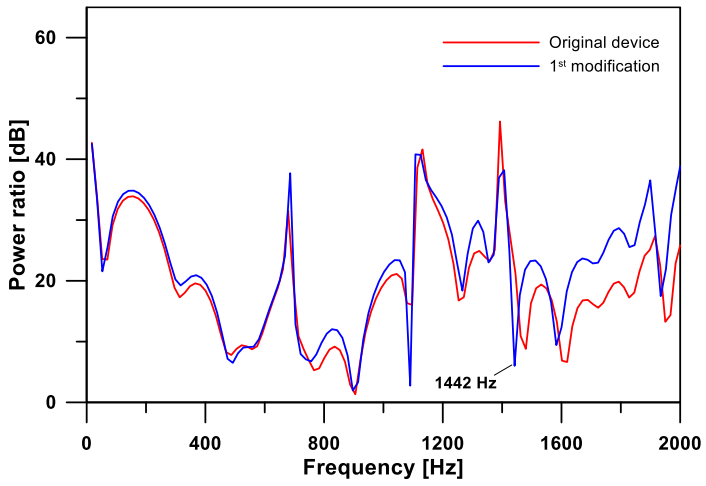


Figure 8.58 - Sound power ratio comparison.

As it has been highlighted in the above figure, at $1442\ Hz$, the noise attenuation of the original device is higher with respect to that of the first modification, which results in a lower sound pressure level at such frequency.

However, the fact that the two spectra of Figure 8.57 are very similar in shape, but with quite different amplitudes in some frequency range, suggests that the turbulent characteristics of the flow field inside the two devices are similar, but with different turbulence intensity levels. As an example, it is possible to compare the response of the systems around $840\ Hz$. Around such frequency, Figure 8.57 indicates a prominent noise level corresponding to the original device (which is about $10\ dBA$ higher than the other one). This is easily explainable by the examination of the intensity of the flow noise related source term, namely the laplacian of the Lighthill tensor, which is depicted in figure below. Here, the color scales have been standardized in a way such that, for each figure, the more red-like the color the higher the intensity.

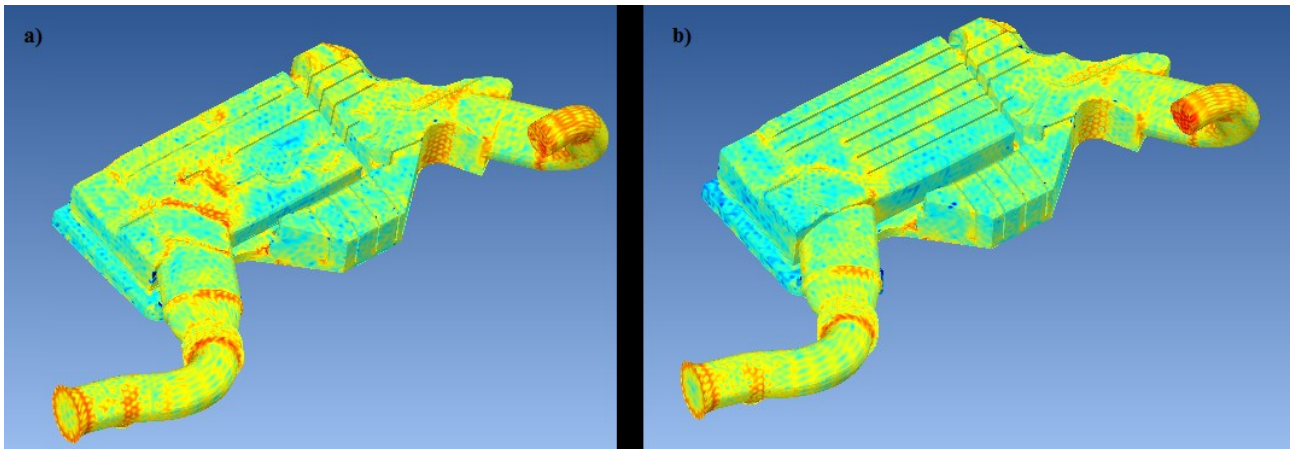


Figure 8.59 - Intensity plot of the Lighthill tensor's divergence at 841 Hz: a) original device and b) first modification.

As it is possible to appreciate from the above color plot, the intensity level of the Lighthill source term at $841\ Hz$ is globally higher for the original device, especially in zones of the acoustic mesh near and inside the inlet tube of the air induction system. Moreover, the fact according to which lower levels of flow instabilities are related to the first geometric modification is confirmed by the lower level of velocity magnitude and turbulent kinetic energy, as it is reported in Figure 8.60 and 8.61 respectively.

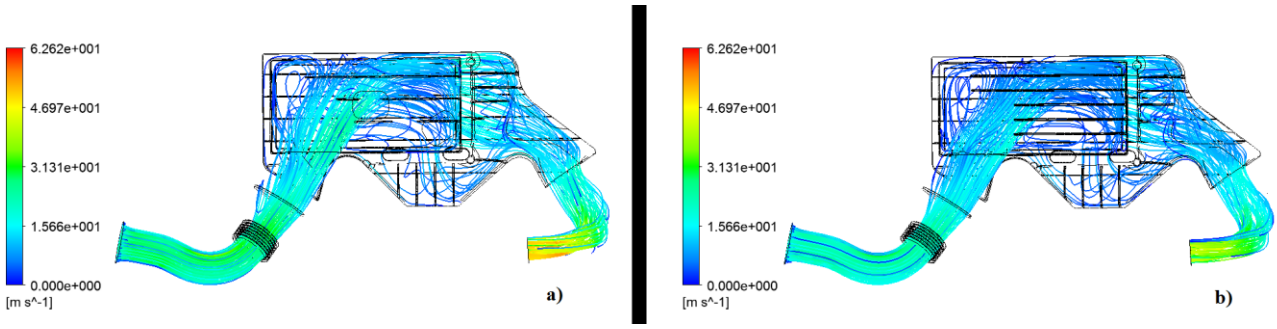


Figure 8.60 - Intensity plot of the velocity streamline at 2100 rpm WOT: a) original device and b) first modification.

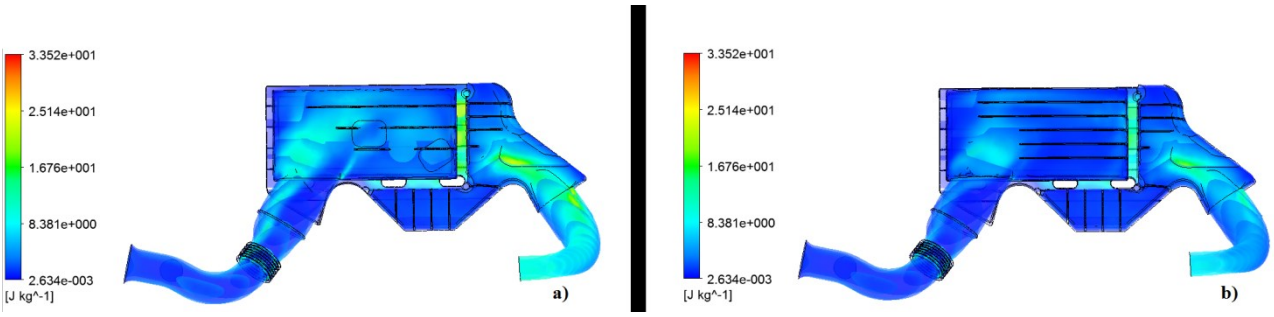


Figure 8.61 - Intensity plot of the turbulent kinetic energy at 2100 rpm WOT: a) original device and b) first modification.

Regarding the second version of the air induction system, in Figure 8.62 the total sound pressure level comparison is shown. The red and green curves represent the response of the original device and second modification respectively.

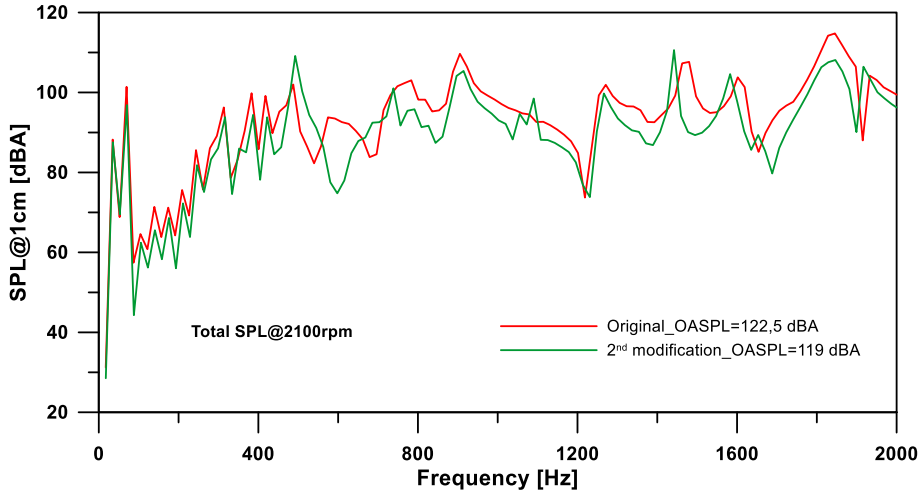


Figure 8.62 - Total A-weighted SPL comparison at 2100 rpm WOT: original device and second modification.

Even in this case, the noise emission corresponding to the second geometric modification of the air induction system would further decrease. In fact, the OASPL comparison shows a decrease of 3,5 $dBA$, up to 2 $kHz$, with respect to the original device. In figure below, the noise emissions due to only the primary sound sources are shown as function of the frequency, where the same color legend of Figure 8.62 has been used.

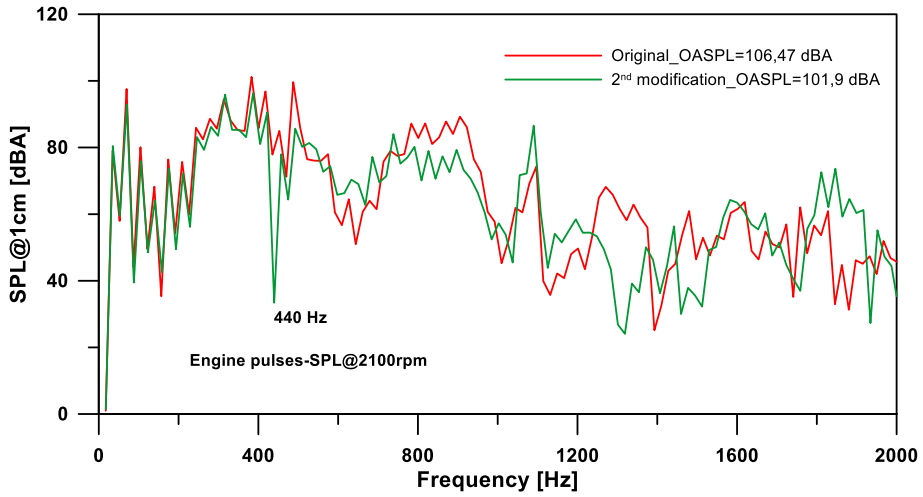


Figure 8.63 - A-weighted SPL comparison at 2100rpm (engine pulses contribution): original device and second modification.

So, as it is possible to appreciate from the two above depicted spectra, the engine pulses contribution to the total sound pressure level is quite lower for the second modification. In fact, the difference in the OASPL is equal to $4{,}57\ dBA$ up to $2\ kHz$. Such result is mainly due to the fact that, as it happens for the case of the first modification, the pressure excitation coming from the one-dimensional analysis is practically unaltered at low frequencies with respect to that corresponding to the original device. This is highlighted in figure below, where it is possible to appreciate how the two signals are almost equivalent up to $500\ Hz$.

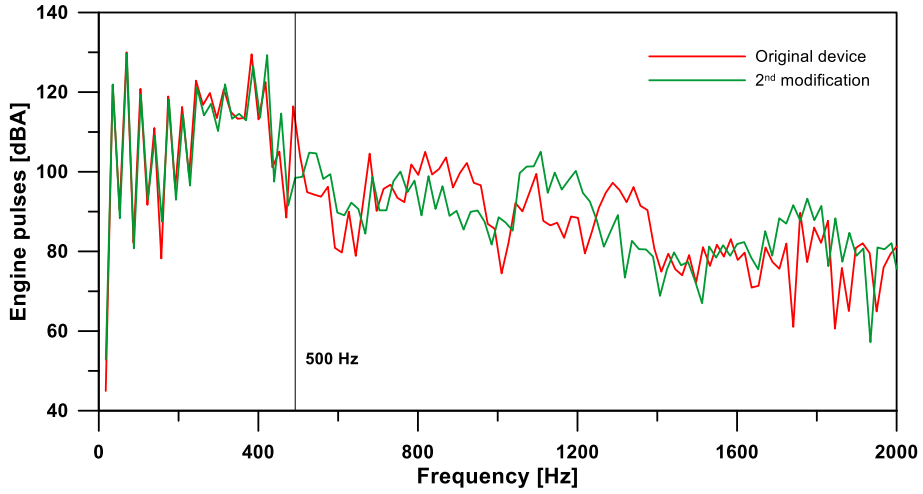


Figure 8.64 - Frequency domain representation of the engine pulses excitation.

Nevertheless, as it is indicated by Figure 8.19, the noise attenuation characteristics at low frequencies are highly increased with respect to the first modification, thanks to the increase of the main resonator's volume, allowing a lower OASPL to be achieved (see also the SPL drop achieved at $440\ Hz$ in Figure 8.61). Thus, even if the prominent frequency content (at low frequency) in not changed, the resulting sound pressure level is decreased due to the higher noise attenuation characteristic. As regards the flow noise contributions, these are reported in figure below, where the same color legend of Figure 8.62 has been used.

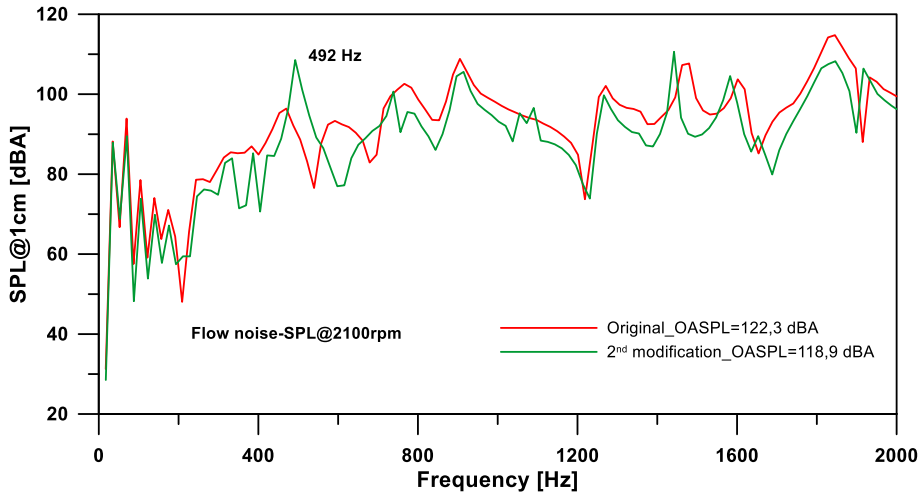


Figure 8.65 - A-weighted SPL comparison at 2100 rpm WOT (flow noise contribution): original device and second modification.

By the examination of the above figure, it is clear that even in this case there is a significant reduction in the noise emissions, as it is also testified by the reported overall A-weighted SPLs. So, since the two spectra are very similar in shape but with different amplitudes, the same kind of already discussed considerations may be spent for this case. Besides, the peak response achieved at $492\ Hz$, is certainly due do the fact that, as the volume of the resonator has been increased, the sound attenuation in the range immediately after the new resonant frequency is very low, as it has been described in the previous paragraph. To strengthen such evidence, in Figure 8.66 the sound power ratios are shown with the same color legend of Figure 8.65.

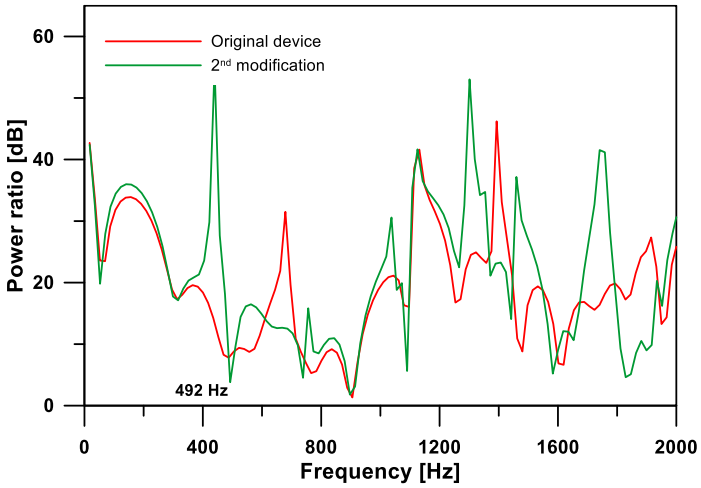


Figure 8.66 - Sound power ratio comparison.

As it is possible to appreciate by the examination of the above figure, the lowering of the resonant frequency, discussed in the previous paragraph, leaves a very low sound attenuation around $500\ Hz$. In spite of such high peak response, the flow noise contribution is globally below that corresponding to the original device as it is testified by the lower overall A-weighted sound pressure level which is $3{,}4\ dBA$ lower than that corresponding to the original device.

Regarding the results corresponding to the last geometric modification, the total SPL has been depicted in figure below. Here, the red and black curves represent the response of the original device and second modification respectively.

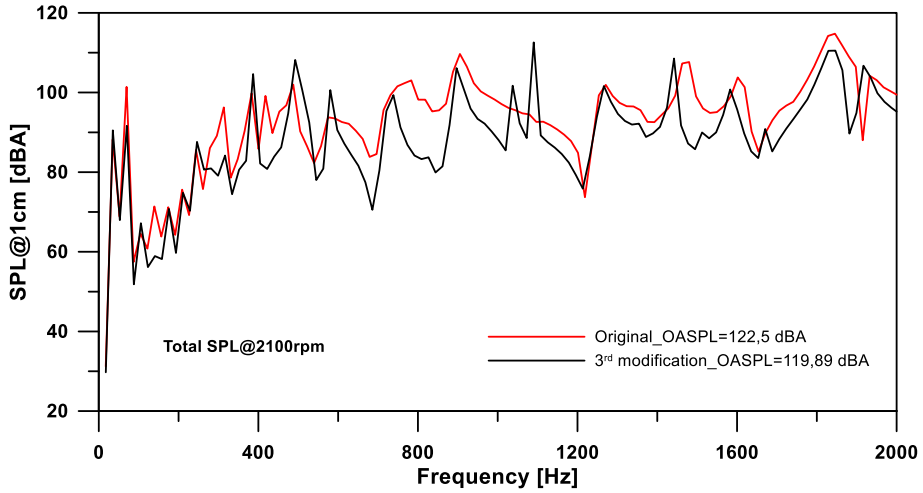


Figure 8.67 - Total A-weighted SPL comparison at 2100 rpm WOT: original device and second modification.

As it is possible to appreciate from the above figure, the noise emissions at the virtual microphone location would decrease with respect to the original device. However, by comparing the overall sound pressure levels, it follows that such reduction is the lowest among those examined so far ($2{,}61\ dBA$). In order to understand why, it is necessary to examine the contribution from primary and secondary noise sources. To this aim, in Figure 8.68 the engine pulses related noise emissions are compared making use of the same color legend of the above figure.

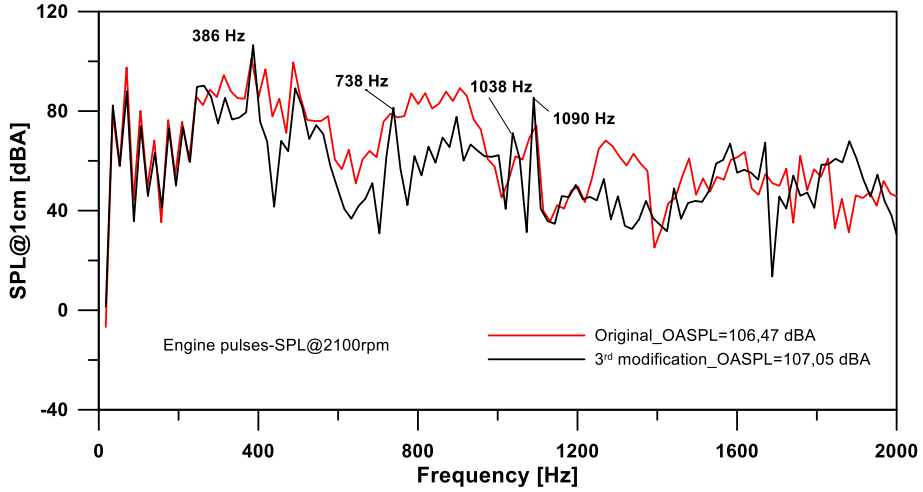


Figure 8.68 - A-weighted SPL comparison at 2100 rpm WOT (engine pulses contribution): original device and third modification.

As it is possible to appreciate from the above figure, the OASPL of the engine pulses contribution is higher in case of the third modification ($0{,}58\ dBA$ with respect to the original device). In spite of the globally lower amplitudes, this is mainly due to the peak responses occurring at the four highlighted frequencies, namely 386, 738, 1038 and 1090 $Hz$, which are not due to changes in the excitation. In fact, as regards the information about the pressure fluctuations from the one-

dimensional analysis, event in this case the spectra are almost the same up to $500\,Hz$, as it is possible to appreciate from the figure below.

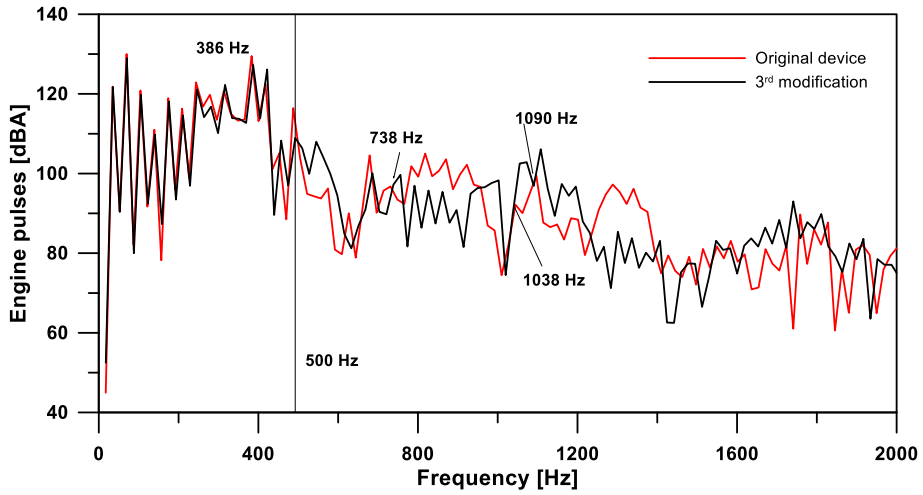


Figure 8.69 - Frequency domain representation of the engine pulses excitation.

Besides, it is important to note that the amplitudes of the incident waves at 386, 738, 1038 and $1090\,Hz$ are practically the same for the two devices. However, as it has already mentioned in the previous paragraph, the third modification is such that new cavity modes are present which mainly influence the response of the system in terms of Transmission Loss at the above mentioned frequencies. The same behavior is observable when the system radiates into free field, as it is indicated in figure below, where the so-called sound power ratios are shown.

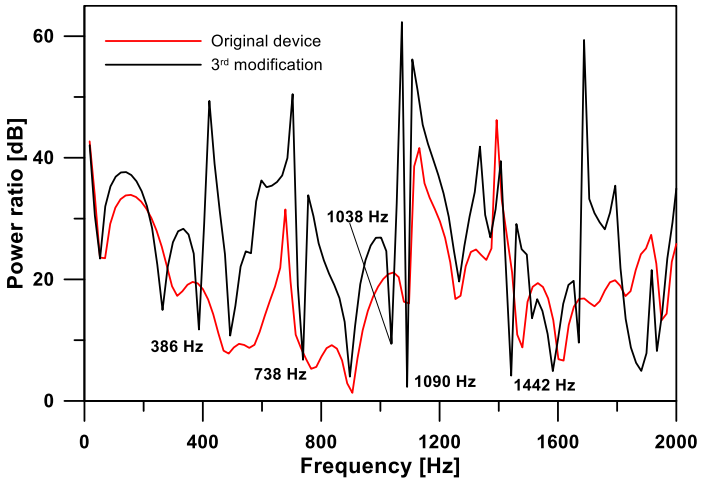


Figure 8.70 - Sound power ratio comparison.

Consequently, it is possible to state that the higher SPL due to primary sound source is mainly due to the poor sound attenuation which is achieved in correspondence of the new cavity modes occurring at the above mentioned frequencies. For what concerns the flow noise contribution, the comparison in terms of A-weighted sound pressure level is depicted in figure below, where the same color legend of Figure 8.67 has been used.

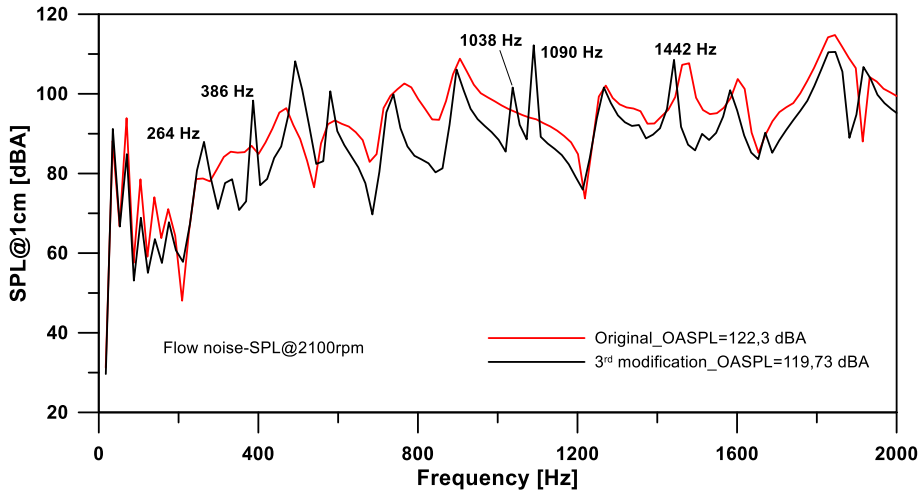


Figure 8.71 - A-weighted SPL comparison at 2100 rpm WOT (flow noise contribution): original device and second modification.

Thanks to the comparison in the above figure, it is possible to point out that the contribution from the aeroacoustics sources is effectively lower in comparison to that corresponding to the original device. In fact, the comparison of the OASPL shows a decrease of 2,57 $dBA$. Even in this case, in spite of the fact that the black curve is globally lower that the red one, the effect of the above mentioned new cavity resonances is present and evident thanks to some localized peak response. In fact, at such frequency locations, the sound pressure level emitted by the third version of the modified system is higher with respect to that of the original device.

In conclusion to this chapter, it has been demonstrated that opportunely realized modifications on the original design configuration of the studied air induction system may effectively enhance its acoustic performances. Such statement relies on the fact that it has been shown that all the three investigated versions of the intake system allow an higher level of Transmission Loss to be reached and, at the same time, a lower level of emitted gas-dynamic noise to be achieved, without decreasing the engine performances. In particular, thanks to a one-dimensional fluid dynamic analyses, it has been shown that the main engine performance parameters remain unchanged, whilst more accurate 3D CFD analyses have shown that all the investigated new geometries are such that a lower value of the pressure drop across inlet and outlet is achieved. Such aspect is particularly positive, as it would directly imply an higher value of the volumetric efficiency.

From an acoustic point of view, it has been shown that the acoustic attenuation characteristics are always globally improved, even if, as expected, the results in terms of Transmission Loss are locally affected by the presence of new cavity modes which characterize the various new investigated configurations. The same tendency is found when dealing with the emitted gas-dynamic noise, which makes the third investigated modification to be not considered for future developments, as the lowest improvement is reached together with the maximum increase of the volume of the system. In this framework, the presented second version of the air induction system is probably the best as it ensures the maximum benefit in term of emitted gas-dynamic noise, with a decrease of 3,5 $dB$ on the A-weighted overall sound pressure level up to 2 $kHz$, in the investigated engine condition. Thus, it is possible to state that the second modification depicted in Figure 8.17 a) is such that the best trade-off between acoustic performance and entity of the modification (the increase of

volume being equal to the 23% with respect to the volume of the original device) is achieved. Such circumstance makes it more suitable for further developments and improvements.

## Bibliography


[1] Siano, D., Teodosio, L., De Bellis, V., and Bozza, F., "Analysis and Design of an Intake Filter Box for a Downsized VVA Engine," SAE Technical Paper 2014-01-1693, 2014, doi:10.4271/2014-01-1693.

[2] M. Abom, “An Introduction to Flow Acoustics”, Publisher: KTH-The Royal Institute of Technology, ISBN: ISRN/KTH/AVE/N-06/04-SE.

[3] M. L. Munjal, “Acoustics of Ducts and Mufflers with Application to Exhaust and Ventilation System Design”, John Wiley & Sons.

[4] Actran 15.1 User’s Guide,Volume 1 “Installation, Operations, Theory and Utilities”, April 2015.

[5] Ansys Fluent V. 14, User’s Manual, Ansys Inc., 2011.

[6] Fine Acoustics Theoretical Manual, Release 5.2.3, July 2014.

[7] R. della Volpe, M. Migliaccio, “Motori a combustione interna per autotrazione”, Publisher Liguori, ISBN: 9788820701932.

[8] P.O.A.L. Davies, K.R. Holland, “I.C. ENGINE INTAKE AND EXHAUST NOISE ASSESSMENT”, Journal of Sound and Vibration, Volume 223, Issue 3, 10 June 1999, Pages 425–444.

[9] Lighthill, M. J. (1952). "On sound generated aerodynamically. I. General theory". Proceedings of the Royal Society A. 211 (1107): 564–587, doi:10.1098/rspa.1952.0060.

[10] P. Di Francescantonio, P. Ferrante, T. Deconinck, and C. Hirsch. "Assessment of SNGR Method for Robust and Efficient Simulations of Flow Generated Noise", 19th AIAA/CEAS Aeroacoustics Conference, Aeroacoustics Conferences, (AIAA 2013-2264).

# Chapter 9

# Conclusions and Future Developments

The main practical objective of this thesis has been the development and optimization, from an acoustic point of view, of a Finite Element numerical model of an air induction system for a commercial spark ignition engine. During the entire duration of the PhD course, in order to achieve such a goal, a lot of efforts have been spent for trying to first understand the basic principles which are involved in such huge analysis process and then approaching the very fascinating world of the Computer Aided Engineering, in order to achieve the above mentioned target. In fact, as already mentioned, acoustic related phenomena may be extremely complex, as various different physics are involved. For this reason, after studying the necessary subjects from many different references, a lot of patient has been spent for grouping all the necessary background in the theoretical chapters of this thesis. Such an understanding is indeed the minimum fundamental to ensure that simulations are correctly set up and to be able to properly analyze the corresponding outcomes.

In order to achieve the prescribed final goal, various steps have been addressed one after another. Firstly, a Finite Element Model of the studied system has been created and a comprehensive acoustic characterization analysis, aimed to calculate its acoustic attenuation properties in terms of Transmission Loss, has been performed and described in chapter 5. The same analysis has been also experimentally executed, thanks to a collaboration with the University of Florence. Thus, the Transmission Loss of the intake system has been calculated and measured in different operating conditions, accounting for both structural participation and the presence of the air filter. From the comparison between the whole numerical and experimental set of results, a very good correlation has been found, thanks to which the model has been considered as fully representative of the qualitative acoustic behavior of the real system. In fact, as it has been mentioned many times above, a Transmission Loss analysis represents just a qualitative information about the acoustic response of the system under investigation, giving no information about real working conditions to which it is subjected when coupled with the internal combustion engine.

For this reason, before thinking to proceed with an acoustic optimization, another validation step has been pursued and described in chapter 6, aimed to confirm the goodness of the numerical modelling procedure when dealing also with amount of noise emitted in various engine running points. This in turn requires a completely different kind of approach, which involves also one-dimensional and three-dimensional fluid dynamic analyses useful for setting up the right boundary conditions for the 3D acoustic model. Nevertheless, due to lack of information necessary for modelling the air filter during the 3D CFD analyses, only information coming from the 1D CFD analysis has been considered in the acoustic model. Moreover, despite the modelling difficulties due to intrinsic errors related to the one-dimensional analysis and absence of information about the engine acoustic impedance, the comparison between numerical results and available experimental data has given a quite satisfactory level of agreement. Consequently, the whole acoustic modelling procedure has been considered as fully validated, being able to reproduce both the qualitative and

the quantitative acoustic behavior of the actual system, representing a very important tool, eventually to be used for optimization procedures.

In fact, thanks to the availability of a validated numerical model of the studied system, it has been possible to deeply investigate its acoustic behavior, in order to choose the best strategy useful for achieving the desired improvements. Consequently, a refinement process of the air induction system's design has been investigated, and three modified versions have been designed and studied. The guidelines, which have been followed for the realization of the CAD modifications, have relied on an improvement of the acoustic attenuation curve, together with the geometrical constraint represented by the necessity of not changing the overall size of the system in its original configuration. In order to respect such geometrical constraint, all the modifications have relied on the partial use of foam material which is attached behind the original system, in direct contact with the engine block, in order to probably lower the impact related noise (plastic-engine head).

Thus, it has been firstly shown in chapter 8 that the opportunely realized geometric modifications may highly enhance the Transmission Loss, so that subsequent gas-dynamic noise analyses have been executed in order to verify that the amount of noise, which would be emitted if the modifications are actually realized, would effectively decrease. Among all the available engine running points, it has been decided to focus on the $2100\ rpm$ WOT condition for several reasons. Firstly, for the studied engine, the condition of wide open throttle is almost always encountered, being the control of the load mainly achieved thanks to the VVA system. Secondly, $2100\ rpm$ is a frequent engine regime encountered in road traffic conditions, when the vehicle speed is low enough such that the intake noise represents a prominent noise source. In fact, considering the class of the vehicle on which the intake system is installed, higher regimes are reasonably encountered only at higher vehicle speeds when, however, more prominent noise sources exist such as road noise, aerodynamic noise etc.. Then, it is reasonable safe to assume that if lower noise levels are found at such regime and high engine load, similar results would be found at lower $rpm$ and lower loads. At the same time, the analysis at high load operation gives the possibility to verify the effects of the modification on the engine performance.

In fact, before proceeding with the acoustic analyses, CFD studies have been carried out on all the versions of the air induction system, to the aim of firstly evaluating the corresponding effects on the engine performances. Therefore, it has been found that, according to the results coming from 1D CFD analyses, all the three new design configurations are such that the main engine performance parameters all remain unchanged (brake power, brake specific fuel consumption). Besides, thanks to more detailed 3D CFD steady state analyses, it has been possible to evaluate the pressure drops realized across the inlet and outlet of each system. As a result, the pressure drop, which would be realized across the fluid dynamic boundaries of each of the three new intake systems, is always lower than that corresponding to the original device. This is a particular positive result, as the pressure drop is directly related to the engine power by means of the volumetric efficiency.

From what concerns the gas-dynamic noise analyses, the information coming from both 1D and 3D CFD unsteady analyses have been used as boundary conditions for the acoustic models, in order to model both engine pulses and flow noise contribution to the overall sound emission. This has been possible because the presence of the air filter has been neglected on the hypothesis that its influence is the same for each system's configuration. As results, it has been found that all the three

investigated modified versions of the air induction system allow lower level of noise to be emitted. More precisely, the lowest overall sound pressure level corresponds to the second modification, to which a decrease in the OASPL equal to $3{,}5\ dBA$ corresponds. Consequently, such second geometric change has been judged as representative of the best trade-off among lower acoustic transparency, lower pressure drop and lower volume change of the air induction system (this latter corresponding to an increase of the $23\%$ with respect to the volume of the original size). Therefore, according to the author, such design configuration should be considered for further studies and, eventually, the development of a prototype.